TWO-DIMENSIONAL ANALYTICAL PREDICTIVE MODELING OF SCHOTTKY BARRIER SOI AND MULTI-GATE MOSFETS

Mike Schwarz

Dipòsit Legal: T.456-2013

ADVERTIMENT. L'accés als continguts d'aquesta tesi doctoral i la seva utilització ha de respectar els drets de la persona autora. Pot ser utilitzada per a consulta o estudi personal, així com en activitats o materials d'investigació i docència en els termes establerts a l'art. 32 del Text Refós de la Llei de Propietat Intel·lectual (RDL 1/1996). Per altres utilitzacions es requereix l'autorització prèvia i expressa de la persona autora. En qualsevol cas, en la utilització dels seus continguts caldrà indicar de forma clara el nom i cognoms de la persona autora i el títol de la tesi doctoral. No s'autoritza la seva reproducció o altres formes d'explotació efectuades amb finalitats de lucre ni la seva comunicació pública des d'un lloc aliè al servei TDX. Tampoc s'autoritza la presentació del seu contingut en una finestra o marc aliè a TDX (framing). Aquesta reserva de drets afecta tant als continguts de la tesi com als seus resums i índexs.

ADVERTENCIA. El acceso a los contenidos de esta tesis doctoral y su utilización debe respetar los derechos de la persona autora. Puede ser utilizada para consulta o estudio personal, así como en actividades o materiales de investigación y docencia en los términos establecidos en el art. 32 del Texto Refundido de la Ley de Propiedad Intelectual (RDL 1/1996). Para otros usos se requiere la autorización previa y expresa de la persona autora. En cualquier caso, en la utilización de sus contenidos se deberá indicar de forma clara el nombre y apellidos de la persona autora y el título de la tesis doctoral. No se autoriza su reproducción u otras formas de explotación efectuadas con fines lucrativos ni su comunicación pública desde un sitio ajeno al servicio TDR. Tampoco se autoriza la presentación de su contenido en una ventana o marco ajeno a TDR (framing). Esta reserva de derechos afecta tanto al contenido de la tesis como a sus resúmenes e índices.

WARNING. Access to the contents of this doctoral thesis and its use must respect the rights of the author. It can be used for reference or private study, as well as research and learning activities or materials in the terms established by the 32nd article of the Spanish Consolidated Copyright Act (RDL 1/1996). Express and previous authorization of the author is required for any other uses. In any case, when using its content, full name of the author and title of the thesis must be clearly indicated. Reproduction or other forms of for profit use or public communication from outside TDX service is not allowed. Presentation of its content in a window or frame external to TDX (framing) is not authorized either. These rights affect both the content of the thesis and its abstracts and indexes.

UNIVERSITAT ROVIRA I VIRGILI
TWO-DIMENSIONAL ANALYTICAL PREDICTIVE MODELING OF SCHOTTKY BARRIER SOI AND MULTI-GATE MOSFETS
Mike Schwarz
Dipòsit Legal: T.456-2013

TWO-DIMENSIONAL ANALYTICAL PREDICTIVE MODELING OF SCHOTTKY BARRIER SOI AND MULTI-GATE MOSFETS

$$\Delta x \cdot \Delta p \geq \hbar$$

Schwarz, Mike

Doctoral Thesis
2012

Department of Electronic, Electric and Automatic Engineering

Universitat Rovira i Virgili

UNIVERSITAT ROVIRA I VIRGILI
TWO-DIMENSIONAL ANALYTICAL PREDICTIVE MODELING OF SCHOTTKY BARRIER SOI AND MULTI-GATE MOSFETS
Mike Schwarz
Dipòsit Legal: T.456-2013

UNIVERSITAT ROVIRA I VIRGILI
TWO-DIMENSIONAL ANALYTICAL PREDICTIVE MODELING OF SCHOTTKY BARRIER SOI AND MULTI-GATE MOSFETS
Mike Schwarz
Dipòsit Legal: T.456-2013

UNIVERSITAT ROVIRA I VIRGILI
TWO-DIMENSIONAL ANALYTICAL PREDICTIVE MODELING OF SCHOTTKY BARRIER SOI AND MULTI-GATE MOSFETS
Mike Schwarz
Dipòsit Legal: T.456-2013

Mike Schwarz

TWO-DIMENSIONAL ANALYTICAL PREDICTIVE MODELING OF SCHOTTKY BARRIER SOI AND MULTI-GATE MOSFETS

DOCTORAL THESIS

Supervised by Dr. Benjamín Iñíguez
and Dr. Alexander Kloes

Department of Electronic,
Electrical and Automatic Control Engineering

UNIVERSITAT ROVIRA I VIRGILI

Tarragona
2012

UNIVERSITAT ROVIRA I VIRGILI
TWO-DIMENSIONAL ANALYTICAL PREDICTIVE MODELING OF SCHOTTKY BARRIER SOI AND MULTI-GATE MOSFETS
Mike Schwarz
Dipòsit Legal: T.456-2013

UNIVERSITAT ROVIRA I VIRGILI
TWO-DIMENSIONAL ANALYTICAL PREDICTIVE MODELING OF SCHOTTKY BARRIER SOI AND MULTI-GATE MOSFETS
Mike Schwarz
Dipòsit Legal: T.456-2013

UNIVERSITAT ROVIRA I VIRGILI
TWO-DIMENSIONAL ANALYTICAL PREDICTIVE MODELING OF SCHOTTKY BARRIER SOI AND MULTI-GATE MOSFETS
Mike Schwarz
Dipòsit Legal: T.456-2013

Statement of Supervision

Department of Electronic, Electric
and Automatic Engineering (DEEEA)
Av. Paisos Catalans 26, Campus Sescelades
43007, Tarragona, Spain
Phone: +34 977 558524
Fax: +34 977 559605

I STATE that the present study, entitled "Two-Dimensional Analytical Predictive Modeling of Schottky barrier SOI and Multi-Gate MOSFETs", presented by Mike Schwarz for the degree of Doctor, has been carried out under my supervision at the Department of Electronic, Electrical and Automatic Control Engineering of this university, and that it fulfils all the requirements to be eligible for the European Doctorate.

Tarragona (Spain), July 15th, 2012

Dr. Benjamín Iñíguez, Doctoral Thesis Supervisor

Dr.-Ing. Alexander Kloes, Doctoral Thesis Co-Supervisor

UNIVERSITAT ROVIRA I VIRGILI
TWO-DIMENSIONAL ANALYTICAL PREDICTIVE MODELING OF SCHOTTKY BARRIER SOI AND MULTI-GATE MOSFETS
Mike Schwarz
Dipòsit Legal: T.456-2013

Declaration

Device Modeling Research Group
Wiesenstraße 14, Campus Gießen
35390, Gießen, Germany
Phone: +49 641 3091948
Fax: +49 641 3092901

I STATE that the dissertation is my original work and that I have not received outside assistance. Only the sources cited have been used in this draft. Parts that are direct quotes or paraphrases are identified as such.

Gießen (Germany), July 15th, 2012

Mike Schwarz, M.Eng.

UNIVERSITAT ROVIRA I VIRGILI
TWO-DIMENSIONAL ANALYTICAL PREDICTIVE MODELING OF SCHOTTKY BARRIER SOI AND MULTI-GATE MOSFETS
Mike Schwarz
Dipòsit Legal: T.456-2013

UNIVERSITAT ROVIRA I VIRGILI
TWO-DIMENSIONAL ANALYTICAL PREDICTIVE MODELING OF SCHOTTKY BARRIER SOI AND MULTI-GATE MOSFETS
Mike Schwarz
Dipòsit Legal: T.456-2013

Acknowledgment

This dissertation would not have been possible without the guidance and the help of several individuals who in one way or another contributed and extended their valuable assistance in the preparation and completion of this study.

First and foremost, I offer my sincerest gratitude to my supervisors, Prof. Benjamín Iñíguez and Prof. Alexander Kloes, who supported me throughout my dissertation with their patience and knowledge and in particular by their support of always independent and demanded working.

I also thank Reinaldo Vega from University of California, Berkeley (USA) for the many discussions on Schottky barrier diodes with the resulting effects. He has been sharing his knowledge without any demand and is a really friendly and kind researcher.

I gratefully acknowledge Muthupandian Cheralathan and Ghader Darbandy from the University Rovira i Virgili in Tarragona (Spain)for their valuable inputs and discussion during the many meetings at different conferences. Especially, the fruitful conversations about occurring physical effects inside semiconductors influenced this research.

Many individuals provided input data, i.e., parsers, TCAD simulation studies and other. Thomas Holtij from THM in Giessen (Germany), as well as various exchange students, like Justin Bare from the University of Maryland in Washington D.C. (USA), Melissa Hickson, Kerri Wait, Dejan Subaric, and Adrian Frost from Griffith University in Brisbane (Australia).

I would like to offer special thanks to my colleagues Mark Weber and Matthias Loth from THM in Giessen (Germany) for the many discussions on mathematically problems and providing ideas solving these.

Furthermore, I would like to offer my special thanks to Chris Volkmar from THM in Giessen (Germany), Juergen Bornmann from Grundschule Sachsenberg (Germany), and Erhard Freitag from Hollingsworth & Vose GmbH (Germany) for their support during the correction of the grammar and language in this dissertation.

Finally, I would like to express my deep appreciation to many friends and family who provided so much support and encouragement throughout this process, especially to my parents for their untiring support and promotion during my entire training. Not at least I would like to thank my girlfriend Ms. Sabrina Czepa for her patience, consideration and support which she brought during the entire time of this work.

UNIVERSITAT ROVIRA I VIRGILI
TWO-DIMENSIONAL ANALYTICAL PREDICTIVE MODELING OF SCHOTTKY BARRIER SOI AND MULTI-GATE MOSFETS
Mike Schwarz
Dipòsit Legal: T.456-2013

Nomenclature

Symbol	Description
a	function parameter
A	amplitude
	Airy function parameter
	diode area
	smoothing parameter
$\mathrm{A_i}$	Airy function
A^*	conjugate amplitude
	effective Richardson constant
A^{**}	reduced effective Richardson constant
b	function parameter
B	Airy function parameter
	smoothing parameter
$\mathrm{B_i}$	Airy function
c	function parameter
	speed of light
C	Airy function parameter
	circle
	conformal mapping parameter
	integration constant
$\overline{\mathrm{C}}$	circle in complex plane
$\mathrm{C'_{ox}}$	oxide capacitance
d	function parameter
D	Airy function parameter
	integration constant
$\mathrm{D_{it}}$	interface-trap density
$\mathrm{D_{ox}}$	dielectric displacement
$\mathrm{D_x, D_y}$	components of the dielectric flow
e	function parameter
$\vec{\mathrm{e}}_x$	unit vector in x-direction
$\vec{\mathrm{e}}_y$	unit vector in y-direction

Symbol	Description
E	electric field (scalar)
$\underline{E}$	electric field (complex)
$\vec{E}$	electric field (vector)
$E_\perp$	electric field (normal component)
E_f	Fermi level
E_{fm}	Fermi energy metal
E_{fs}	Fermi energy semiconductor
E_g	band gap
E_{ox}	electric field of oxide
E_x	x-component of electric field
E_y	y-component of electric field
E_0	electric field at $Si - Si0_2$ interface
	vacuum level
E_C	conduction band
E_V	valence band
f	conformal mapping function
f_P	quantum mechanical tunneling and reflection parameter
f_Q	quantum mechanical tunneling and reflection parameter
f^{-1}	inverse conformal mapping function
f_m	Fermi-Dirac distribution metal
f_s	Fermi-Dirac distribution semiconductor
F	image force
i	counter
i_{in}	incoming flow
i_r	reflected flow
i_t	transmitted flow
I	(total) current
I_{off}	leakage current
I_{on}	drive current
I_{therm}	thermionic emission current
I_{tun}	tunneling current
I_{DD}	drift/diffusion current
I_{TTE}	model current $I_{tun} + I_{therm}$
j	imaginary value $\sqrt{-1}$
J	Current density
J_{therm}	thermionic emission current density
J_{tun}	tunneling current density

Symbol	Description
k	Boltzmann constant
	wave vector
l_{ch}	channel length
Δl_{ch}	coordinate in y-direction of a point within the channel
L_D	length of depletion region
m	mass for holes and electrons
m^*	effective mass for holes and electrons
m_0	electron rest mass
n_i	intrinsic carrier concentration
N	number vertices of a polygon
N_A	acceptor impurity concentration
N_B	impurity concentration in (n or p-type) bulk silicon
N_C	effective density of states in conduction band
N_D	donor impurity concentration
N_V	effective density of states in valence band
$\vec{p}$	impulse
P	complex potential function
	general model parameter
	probability particle
q	elementary charge
Q_{dep}	depletion charge
Q_{inv}	inversion charge
Q_M	surface-charge density in metal
Q_{SC}	surface-charge density in semiconductor
Q_{SS}	interface-trap charge
r	gradient
	radius of a circle
R	reflection
	region of a z-plane
R^*	region of a w-plane
t	time
t_{ch}	channel thickness
Δt_{ch}	coordinate in x-direction of a point within the channel
t_{ox}	gate oxide thickness
$\tilde{t_{ox}}$	transformed gate oxide thickness
T	absolute temperature
	transmission, tunneling probability

Symbol	Description
u	coordinate within the complex plane
$\overline{u}$	coordinate within the complex plane w with an infinitesimal gap
$\overline{u}_a$	integration boundary
$\overline{u}_b$	integration boundary
$u(x)$	function for Airy functions
v	coordinate within the complex plane
	velocity
v_D	diffusion velocity
v_G	group velocity
v_R	recombination velocity
V	potential
	voltage
V_b	potential barrier
V_d	drain potential
V_{ds}	drain-source voltage
V_{fb}	flat band voltage
V_g	gate potential
V_{ox}	voltage drop across the oxide
V_s	source potential
V_t	thermal voltage
V_{th}	threshold voltage
w	coordinate within the complex plane
w^*	conjugate complex coordinate within the complex plane
w_{ch}	channel width
x	coordinate within the complex plane
x_m	position of barrier peak
y	coordinate within the complex plane
$\overline{y}_{i,top}$	array which changes coordinates from $2\tilde{t}_{ox} \rightarrow \tilde{t}_{ox}$
$\overline{y}_{i,bottom}$	array which changes coordinates from $0 \rightarrow \tilde{t}_{ox}$
z	coordinate within the complex plane
z_s	Airy function parameter
z'	Airy function parameter
$\overline{z}$	point within the complex plane
z_0	Airy function parameter
	singularity within the complex plane
α	parameter of complex potential theory, identifies direction of Δz
	adjusting parameter for the electrostatic potential of SB-UTB-MOSFET

Symbol	Description
χ	electron affinity
δ	absolute error
	interfacial layer thickness
Δ	Laplace operator
$\Delta\phi$	change in barrier height due to Schottky barrier lowering
$\Delta \mathrm{x}$	length of a linear shaped boundary
$\Delta \mathrm{y}$	geometry parameter of the conformal mapping
ϵ	dielectric permittivity
ϵ_0	dielectric permittivity of vacuum
ϵ_{ox}	dielectric permittivity of insulator/dielectric
ϵ_{Si}	dielectric permittivity of silicon
Θ	mobility degradation
ϕ	electric potential
ϕ_{B}	barrier height
$\phi_{\mathrm{B,eff}}$	effective barrier height for dopant segregation
ϕ_{bi}	built-in potential
ϕ_{Bn}	barrier height for electrons
ϕ_{Bn0}	barrier height for electrons (without image-force lowering)
ϕ_{Bp}	barrier height for holes
ϕ_{Bp0}	barrier height for holes (without image-force lowering)
ϕ_{bnd}	boundary parameter
ϕ_{m}	metal work function
ϕ_{ms}	contact or built-in potential
ϕ_{n}	energy difference between $\mathrm{E_C}$ and $\mathrm{E_f}$
ϕ_{p}	distance between midgap and $\mathrm{E_f}$
ϕ_{s}	semiconductor workfunction
ϕ_0	neutral level of interface states
Φ	electric potential or real part of complex potential
φ	potential solution Laplace equation
$\varphi(\overline{\mathrm{u}})$	boundary condition
$\varphi(\mathrm{z})$	potential solution in z-plane
Γ	curve in complex plane
κ	quantity of Schrödinger equation
λ	wavelength
Λ	potential across interfacial layer
μ	mobility of charge carriers
ν	index

Symbol	Description
ρ	space charge density
σ	parameter of the compact solution of the electric field
$\sigma(\mathrm{x}, \mathrm{y})$	absolute deviation
σ_1	parameter of the compact solution of the electrostatic potential
σ_2	parameter of the compact solution of the electrostatic potential
σ_3	parameter of the compact solution of the electrostatic potential
σ_4	parameter of the compact solution of the electrostatic potential
ς	parameter of the complex plane
ξ	carrier energy
$\xi(\mathrm{x})$	carrier energy at position x
Ξ	imaginary part of complex potential
∇	Nabla operator
h	Planck constant
$\hbar$	reduced Planck constant, $h/2\pi$
ψ	wave function
ω	wave frequency

International Publications

Journals

M. Weidemann, A. Kloes, **M. Schwarz**, B. Iñíguez: Two-dimensional analytical model for channel length modulation in lightly-doped DG FETs, Electronics and Telecommunications Quarterly published by Committee of Electronics and Telecommunication of the Polish Academy of Sciences, Vol. 55, No. 4, 2009

M. Schwarz, M. Weidemann, A. Kloes, B. Iñíguez: 2D Analytical Calculation of the Electrostatic Potential in Lightly Doped Schottky Barrier Double-Gate MOSFET, Solid-State Electronics, Vol. 54, No. 11, 2010

A. Kloes, M. Weidemann, **M. Schwarz**: Analytical Current Equation for Short-Channel SOI Multigate FETs Including 3D Effects, Solid-State Electronics, Vol. 54, No. 11, 2010

M. Schwarz, T. Holtij, A. Kloes, B. Iñíguez, 2D Analytical Calculation of the Electric Field in Lightly Doped Schottky Barrier Double-Gate MOSFETs and Estimation of the Tunneling/Thermionic Current, Solid-State Electronics, Vol. 63, No. 1, 2011

M. Schwarz, T. Holtij, A. Kloes, B. Iñíguez: Analytical Compact Modeling Framework for the 2D Electrostatics in Lightly Doped Double-Gate MOSFETs, Solid-State Electronics, Vol. 69, No. 1, 2012

A. Kloes, **M. Schwarz**, T. Holtij: MOS^3: A New Physics-Based Explicit Compact Model for Lightly-Doped Short-Channel Triple-Gate SOI MOSFETs, IEEE Transactions on Electron Devices, Vol. 59, No. 2, 2012

M. Schwarz, T. Holtij, A. Kloes, B. Iñíguez: Complex 2D Electric Field Solution in Undoped Double-gate MOSFETs, IETE Journal of Research, Vol. 38, No. 3, 2012

T. Holtij, **M. Schwarz**, A. Kloes, B. Iñíguez: 2D Analytical Calculation of the Parasitic Source/Drain Resistances in DG-MOSFETs Using the Conformal Mapping Technique, IETE Journal of Research, Vol. 38, No. 3, 2012

M. Schwarz, T. Holtij, A. Kloes, B. Iñíguez: Compact Modeling Solutions for SOI Short-Channel Schottky Barrier MOSFETs, submitted to Solid-State Electronics, 2012

Conferences

M. Weidemann, **M. Schwarz**, A. Kloes, B. Iñíguez: Analytical 2D Modelling of Channel Length Modulation in DG FETs, ESSDERC, Edinburgh, Scotland, 2008

M. Schwarz, M. Weidemann, A. Kloes, B. Iñíguez: 2D Analytical Model of the Potential Distribution in Lightly Doped Schottky Barrier DG-MOSFET, Graduated Student Meeting on Electronic Engineering, Tarragona, Spain, 2009

A. Kloes, M. Weidemann, **M. Schwarz**, T. Holtij: Design Considerations for Undoped FinFETs Based on a 3D Compact Model for the Potential Barrier, ULIS, Aachen, Germany, 2009

A. Kloes, M. Weidemann, **M. Schwarz**: Analysis of 3D current flow in undoped FinFETs and approaches for compact modeling, MIXDES, Lodz, Poland, 2009

M. Weidemann, A. Kloes, **M. Schwarz**, B. Iñíguez: 2D physics-based compact model for channel length modulation in lightly doped DG FETs, MIXDES, Lodz, Poland, 2009

M. Schwarz, M. Weidemann, A. Kloes, B. Iñíguez: 2D Analytical Solution of Potential in Lightly Doped Schottky Barrier Double-Gate MOSFET, ESSDERC, Athens, Greece, 2009

M. Weidemann, A. Kloes, **M. Schwarz**, B. Iñíguez: 2D physics-based compact model of channel length modulation for asymmetrically biased double-gate MOSFETs, ESSDERC, Athens, Greece, 2009

A. Kloes, M. Weidemann, **M. Schwarz**: Closed-form current equation for short-channel triple-gate FETs, MOS-AK Workshop at ESSDERC, Athens, Greece, 2009

M. Schwarz, M. Weidemann, A.Kloes, B. Iñíguez: Two-Dimensional Model for the Potential Profile in a Short Channel Schottky Barrier DG-FET, ISDRS, University of Maryland, USA, 2009

M. Weidemann, A. Kloes, **M. Schwarz**, B. Iñíguez: Analysis and Modeling of the Pinch-Off Point in a Lightly Doped Asymmetrically Biased Double Gate MOSFET, ISDRS, University of Maryland, USA, 2009

M. Schwarz, A.Kloes, B. Iñíguez: 2D Closed-Form Model for the Source/Drain Orthogonal Electric Field in Lightly Doped Schottky Barrier Double-Gate MOSFET, ULIS, Glasgow, 2010

M. Schwarz, A.Kloes, B. Iñíguez: Analytical 2D Model for the Channel Electric Field in Undoped Schottky Barrier DG-MOSFET, MIXDES, Wroclaw, Poland, 2010

UNIVERSITAT ROVIRA I VIRGILI
TWO-DIMENSIONAL ANALYTICAL PREDICTIVE MODELING OF SCHOTTKY BARRIER SOI AND MULTI-GATE MOSFETS
Mike Schwarz
Dipòsit Legal: T.456-2013

M. Schwarz, A. Kloes, B. Iñíguez: Closed-Form 2D Analytical Model for the Electric Field in Lightly Doped Schottky Barrier Double-Gate MOSFET, Graduated Student Meeting on Electronic Engineering, Tarragona, Spain, 2010

M. Schwarz, A. Kloes, B. Iñíguez: 2D Analytical Calculation of the Tunneling Current in Lightly Doped Schottky Barrier Double-Gate MOSFET, ESSDERC, Seville, Spain, 2010

T. Holtij, **M. Schwarz**, A. Kloes: Analytical two-dimensional model for the parasitic source/drain resistance in DG-MOSFETs, MOS-AK Workshop at ESSDERC, Seville, Spain, 2010

M. Schwarz, A. Kloes, B. Iñíguez: 2D Analytical Calculation of the Current in Lightly Doped Schottky Barrier Double-Gate MOSFET, EUROSOI, Granada, Spain, 2011

M. Schwarz, T. Holtij, A. Kloes, B. Iñíguez: 2D Analysis of Source/Drain Carrier Tunneling in Lightly Doped Schottky Barrier DG-MOSFETs Using a Fully Analytical Model, ULIS, Cork, Ireland, 2011

T. Holtij, **M. Schwarz**, A. Kloes, B. Iñíguez: 2D Analytical Calculation of the Source/ Drain Access Resistance in DG-MOSFET Structures, ULIS, Cork, Ireland, 2011

M. Schwarz, T. Holtij, A. Kloes, B. Iñíguez: 2D Analytical Framework for Compact Modeling of the Electrostatics in Undoped DG MOSFETs, MIXDES, Gliwice, Poland, 2011

M. Schwarz, T. Holtij, A. Kloes, B. Iñíguez: I-V Model for Lightly Doped Schottky Barrier DG-MOSFETs Including 2D Effects, ESSDERC, Helsinki, 2011

T. Holtij, **M. Schwarz**, A. Kloes, B. Iñíguez: 2D Analytical Modeling of the Potential in Doped Multiple-Gate-FETs Including Inversion Charge, ESSDERC, Helsinki, 2011

A. Kloes, **M. Schwarz**, T. Holtij: Compact DC Model for Lightly-Doped Short Channel Triple-Gate MOSFETs, MOS-AK Workshop at ESSDERC, Helsinki, 2011

M. Schwarz, T. Holtij, A. Kloes, B. Iñíguez: Macro Model for Drift/Diffusion Effects in Short-Channel Undoped Schottky Barrier DG-MOSFETs, MOS-AK Workshop at ESS-DERC, Helsinki, 2011

A. Kloes, **M. Schwarz**, T. Holtij: Physics-Based, Closed-Form DC Model for Lightly-Doped Short Channel Triple-Gate MOSFETs Including Three-Dimensional Effects, IS-DRS, University of Maryland, 2011

M. Schwarz, T. Holtij, A. Kloes, B. Iñíguez: 2D Analytical DC Model for Nanoscale Schottky Barrier DG-MOSFETs, ISDRS, University of Maryland, 2011

M. Schwarz, T. Holtij, A. Kloes, B. Iñíguez: Explicit Model Equations for the Tunneling Current Density in Schottky Barrier Double-Gate MOSFETs, EUROSOI, Montpelier, 2012

T. Holtij, **M. Schwarz**, A. Kloes, B. Iñíguez: 2D Analytical Modeling of the Potential within Juntionless DG MOSFETs in the Subthreshold Regime, EUROSOI, Montpelier, 2012

M. Schwarz, T. Holtij, A. Kloes, B. Iñíguez: Explicit Model Equations for the Tunneling Current Density in Schottky Barrier Double-Gate MOSFETs, ULIS, Grenoble, 2012

T. Holtij, **M. Schwarz**, A. Kloes, B. Iñíguez: 2D Analytical Potential Modeling of Junctionless DG MOSFETs in Subthreshold Region Including Proposal for Calculating the Threshold Voltage, ULIS, Grenoble, 2012

T. Holtij, **M. Schwarz**, A. Kloes, B. Iñíguez: V_T Based Current Modeling Within Highly Doped Short-Channel Multigate FETs, Graduated Student Meeting on Electronic Engineering, Tarragona, Spain, 2012

M. Schwarz, T. Holtij, A. Kloes, B. Iñíguez: Scaling Behavior Investigation of Schottky Barrier DG-MOSFETs Using a 2D Analytical Model, , Graduated Student Meeting on Electronic Engineering, Tarragona, Spain, 2012

M. Schwarz, T. Holtij, A. Kloes, B. Iñíguez: Two-dimensional Physics-based Modeling of Dopant-segregated Schottky Barrier UTB MOSFETs, MIXDES, Warsaw, Poland, 2012

T. Holtij, **M. Schwarz**, A. Kloes, B. Iñíguez: Analytical 2D Modeling of Junctionless and Junction-Based Short-Channel Multigate MOSFETs, ESSDERC, Bordeaux, 2012

M. Schwarz, T. Holtij, A. Kloes, B. Iñíguez: Investigation of Scaling Behavior of Schottky Barrier Double-Gate MOSFETs Using a 2D Analytical Model, ESSDERC, Bordeaux, 2012

UNIVERSITAT ROVIRA I VIRGILI
TWO-DIMENSIONAL ANALYTICAL PREDICTIVE MODELING OF SCHOTTKY BARRIER SOI AND MULTI-GATE MOSFETS
Mike Schwarz
Dipòsit Legal: T.456-2013

"If you want to build a ship, don't drum up people together to collect wood and don't assign them tasks and work, but rather teach them to long for the endless immensity of the sea."

Antoine de Saint-Exupéry

UNIVERSITAT ROVIRA I VIRGILI
TWO-DIMENSIONAL ANALYTICAL PREDICTIVE MODELING OF SCHOTTKY BARRIER SOI AND MULTI-GATE MOSFETS
Mike Schwarz
Dipòsit Legal: T.456-2013

UNIVERSITAT ROVIRA I VIRGILI
TWO-DIMENSIONAL ANALYTICAL PREDICTIVE MODELING OF SCHOTTKY BARRIER SOI AND MULTI-GATE MOSFETS
Mike Schwarz
Dipòsit Legal: T.456-2013

Contents

1. Introduction **2**
1.1. History . . . 2
1.2. Technologies, Circuit Design and Compact Modeling . . . 4
1.2.1. Technologies . . . 4
1.2.2. Circuit Design and Compact Modeling . . . 7
1.3. State of the Art . . . 10
1.4. Primary objective of the Doctoral Thesis . . . 13

2. Theoretical and Physical Basics **16**
2.1. The Quantum Mechanical Tunneling Effect . . . 16
2.1.1. Wave-particle duality . . . 16
2.1.2. Schrödinger Equation . . . 18
2.1.3. Potential Well . . . 20
2.1.4. Transmission and Reflection, Tunneling Effect . . . 21
2.2. Metal-Semiconductor Contacts . . . 22
2.2.1. Schottky Barrier Formation . . . 23
2.2.2. Current Transport Processes . . . 28
2.3. Quantum Mechanical Tunneling Models . . . 32
2.3.1. Tunneling Mechanisms . . . 33
2.3.2. Transmission Coefficient Modeling . . . 33
2.4. Operation Principle of Schottky Barrier MOSFETs . . . 38

3. Mathematical Basics **42**
3.1. Poisson's and Laplace's Equation . . . 42
3.2. Complex Potential Theory . . . 43
3.2.1. Differentiation . . . 43
3.2.2. Integration . . . 45
3.2.3. Complex Potential Theory of Electrostatics . . . 45
3.3. Conformal Mapping . . . 47
3.3.1. Transformation of a Potential . . . 47
3.3.2. Points of Non-conformality of Mapping . . . 47

UNIVERSITAT ROVIRA I VIRGILI
TWO-DIMENSIONAL ANALYTICAL PREDICTIVE MODELING OF SCHOTTKY BARRIER SOI AND MULTI-GATE MOSFETS
Mike Schwarz
Dipòsit Legal: T.456-2013

3.3.3. Mapping of the Inside of Closed Polygons . . . 49
3.4. Potential Solutions for Boundary Conditions of First Kind . . . 50
3.4.1. Potential Solution Single Vertex . . . 50
3.4.2. Solution for Arbitrary Boundary Conditions . . . 51

4. General Modeling Simplifications **54**
4.1. Area Definition . . . 54
4.2. Simplifications . . . 55
4.2.1. Poisson's Equation . . . 55
4.2.2. Oxide Transformation . . . 56
4.3. Boundary Conditions . . . 57
4.4. Decomposition Strategy . . . 57

5. Modeling Approaches for the Electrostatics **60**
5.1. Boundary Conditions . . . 60
5.1.1. Special Case: Boundary Condition Single Vertex . . . 61
5.2. Conformal Mapping of the Structure . . . 62
5.2.1. Special Case: Conformal Mapping Single Vertex . . . 65
5.3. Electrostatic Potential . . . 66
5.3.1. Single Vertex Approach . . . 66
5.3.2. Square Root Approximation Approach . . . 68
5.3.3. Electrostatic Potential Results . . . 74
5.4. Electric Field . . . 83
5.4.1. Single Vertex Approach . . . 83
5.4.2. Electric Field Results . . . 87
5.5. Conclusion . . . 93

6. Analytical Numerical Modeling Approach (ANMA) for the Currents **96**
6.1. Simplification & Definition . . . 96
6.2. Tunneling Current . . . 98
6.2.1. Tunneling Probability Estimation . . . 98
6.2.2. Tunneling Current Density . . . 99
6.2.3. Tunneling Current Calculation . . . 102
6.3. Thermionic Current . . . 103
6.3.1. Thermionic Current Density . . . 103
6.3.2. Thermionic Current Calculation . . . 104
6.4. Transition; Thermionic to Tunneling Current . . . 104
6.5. Results $I_d - V_g$ . . . 105

UNIVERSITAT ROVIRA I VIRGILI
TWO-DIMENSIONAL ANALYTICAL PREDICTIVE MODELING OF SCHOTTKY BARRIER SOI AND MULTI-GATE MOSFETS
Mike Schwarz
Dipòsit Legal: T.456-2013

6.6. Results $I_d - V_{ds}$ . . . 115
6.6.1. Analyses . . . 116
6.6.2. Macro Model Approach . . . 118
6.6.3. Results . . . 119
6.7. Investigation of the Scaling Behavior of Schottky Barrier Double-Gate MOSFETs . . . 121
6.8. Conclusion . . . 127

7. 2D Analyses of the Current Components 130
7.1. Analyses of the TCAD Tunneling Generation Rate . . . 130
7.2. Analyses of the Model Tunneling Generation Rate . . . 137
7.2.1. Tunneling Probability . . . 138
7.2.2. Carrier Distributions . . . 141
7.2.3. Tunneling Generation Rate . . . 142
7.3. Analyses of the Model Current Densities . . . 151
7.4. Conclusion: Where are we? Where should we go? . . . 154

8. Analytical Closed-form Modeling Approach (ACFMA) for the Currents 156
8.1. Tunneling Current Density . . . 156
8.1.1. Analytical Approximation of the Tunneling Current Density . . . 157
8.1.2. Mapping of Distribution Function . . . 158
8.1.3. Closed-Form Solution of Tunneling Current Density . . . 161
8.1.4. Estimation of x_{E_f} . . . 163
8.2. Parabolic Current Approximation . . . 164
8.2.1. Closed-Form Solution of Currents . . . 166
8.3. Smoothing; Thermionic to Tunneling Current . . . 167
8.4. Results . . . 168
8.5. Conclusion . . . 169

9. Measurement Data for dopant-segregated SB-UTB-MOSFETs 172
9.1. Device Physics . . . 172
9.2. Area Definition, Boundary Conditions, Conformal Mapping & Simplifications . . . 179
9.3. Electrostatics . . . 181
9.3.1. Electrostatic Potential Solution . . . 182
9.3.2. Electric Field Solution . . . 187
9.4. Currents . . . 188
9.5. Results . . . 189

UNIVERSITAT ROVIRA I VIRGILI
TWO-DIMENSIONAL ANALYTICAL PREDICTIVE MODELING OF SCHOTTKY BARRIER SOI AND MULTI-GATE MOSFETS
Mike Schwarz
Dipòsit Legal: T.456-2013

9.6. Conclusion 190

10. Conclusion **192**
10.1. Summary 192
10.2. Future Research Prospects 194
10.3. Conclusions 195

A. The Quantum Mechanical Tunneling Effect **198**
A.1. Infinite Potential Well 198
A.2. Finite Potential Well 200

B. The WKB Approximation **202**

C. The Square Root Approximation **204**

D. Closed-form Equation Package **208**

Bibliography **212**

UNIVERSITAT ROVIRA I VIRGILI
TWO-DIMENSIONAL ANALYTICAL PREDICTIVE MODELING OF SCHOTTKY BARRIER SOI AND MULTI-GATE MOSFETS
Mike Schwarz
Dipòsit Legal: T.456-2013

UNIVERSITAT ROVIRA I VIRGILI
TWO-DIMENSIONAL ANALYTICAL PREDICTIVE MODELING OF SCHOTTKY BARRIER SOI AND MULTI-GATE MOSFETS
Mike Schwarz
Dipòsit Legal: T.456-2013

Chapter 1.

Introduction

"The complexity for minimum component costs has increased at a rate of roughly a factor of two per year... Certainly over the short term this rate can be expected to continue, if not to increase. Over the longer term, the rate of increase is a bit more uncertain, although there is no reason to believe it will not remain nearly constant for at least 10 years. That means by 1975, the number of components per integrated circuit for minimum cost will be 65,000. I believe that such a large circuit can be built on a single wafer." - Gordon Moore, 1965 [1]

Moore's law, named after Intel co-founder Gordon E. Moore, states that the complexity of integrated circuits with minimum component costs regularly doubles itself; depending upon the source every 18 or 24 months. Gordon Moore understood complexity as the number of circuit components on a computer chip. Occasionally, the device complexity is supposed to duplicate, thus the number of transistors per unit area doubles. This technology progress forms a substantial basis "of the digital revolution". Originally, Moore spoke of a duplication every year, however, in 1975 he corrected his statement on a duplication every two years. At that time Moore's Intel colleague David House introduced an duplication cycle of 18 months [2] which is the most common variant of the Moore's law today and also forms the framework for the semiconductor industry. In reality the achievement of new computer chips doubles itself on the average about every 20 months.

Since Moore it has been the target of researchers to increase performance, energy efficiency, and size. Complying with Moore's law [1] is the official goal of semiconductor industry. Today, those goals are defined in the International Technology Roadmap for Semiconductors (ITRS) [3].

1.1. History

In 1925 Julius Edgar Lilienfeld announced the first patents of the principle of the transistor [4,5]. Lilienfeld describes an electronic element which exhibits characteristics of an

electron tube, and in the broadest sense is comparable to today's designated field-effect transistor. At his time it was technically not possible to realize field-effect transistors practically.

Ten years later, in 1934, the German physicist Oskar Heil patented and designed the first field-effect transistor which acts as a semiconductor FET with insulating gate [6]. In 1938 Boris Davydov [7], Nevill Mott [8], and Walter Schottky [9] independently explained rectification.

The first practical realized JFET with a pn-junction and a gate as electrode was evolved by Herbert F. Mataré, Heinrich Welker and indepently by William B. Shockley and Walter H. Brattain in the 1945 [10].

In 1947 the first bipolar transistor, a point-contact transistor, was invented by Bell Laboratories' researchers Shockley, Bardeen and Brattain [11,12,13,14]. The first bipolar junction transistor followed three years later in 1951 [15].

The first integrated circuit (IC), a flip-flop, was developed by Jack Kilby in 1958 [16]. It consisted of two bipolar transistors which were fastened on a germanium substrate and connected by gold leads. Furthermore, in 1958 Esaki developed the tunnel diode [17]. Esaki or tunnel diode (named by the quantum-mechanical tunneling effect), offers fast switching speed with very low power consumption.

The first metal-oxide-semiconductor field-effect transistor (MOSFET) was reported by Kahng and Atalla in 1959 [18, 19]. Four years later Frank Wanlass at Fairchild Semiconductor originated and published the idea of complementary-MOS (CMOS) [20, 21] and "Silicon Valley" was born.

In 1965 Moore predicted with Moore's Law the future of integrated circuits [1]. One year later in 1966 IBM engineers pioneered computer-aided electronic design automation tools. Integrated circuits began to incorporate hundreds of gates and thousands of transistors, therefore tools were needed for reducing errors and decreasing design time [22].

From 1968 until 1971 the first microprocessors appeared from Garrett AiResearch's Central Air Data Computer (CADC) in 1968 [23] Texas Instruments (TI) the TMS 1000 in 1971 [24], and Intel's 4004 in 1971 which generally is regarded as the first commercially available microprocessor [25].

Eight years later in 1979, California Institute of Technology Professor Carver Mead and Xerox Corp. computer scientist Lynn Conway wrote a manual of chip design called "Introduction to VLSI Systems" [26].

Fundamentally, it is the MOSFET which is scaled down to allow an exponentially grown number of devices on a chip. The best way of showing the ongoing down-scaling is to present the number of transistors on commercial microprocessors in Table 1.1.

UNIVERSITAT ROVIRA I VIRGILI
TWO-DIMENSIONAL ANALYTICAL PREDICTIVE MODELING OF SCHOTTKY BARRIER SOI AND MULTI-GATE MOSFETS
Mike Schwarz
Dipòsit Legal: T.456-2013

A continuous growth of the number of transistors is observed, since the MOSFETs have been scaled down to 45 nm. Then manufacturers reached the first limits of the planar MOSFET technology. These challenges forced the microprocessors industry to change architectures of microprocessor, e.g. Dual Core or Quad Core to name a few. As mentioned before, a continuous growth of the transistors number can be observed in Table 1.1, the huge amount of transistors for the Dual-Core Itanium 2 microprocessor diverges from the trend. This processor includes a 24 MB Cache and doubled die feature size which effectively results in a comparable amount as for the Core i7.

Nevertheless, the scaling continued with new technologies, e.g. high-k materials, to squeeze the planar MOSFET technology. Intel's Core i7 3930K is based on 32 nm Sandy Bridge technology, still manufactured on planar MOSFET technology [27]. At the end of 2011 Intel published the Ivy Bridge technology for Intel's 22 nm die shrink of the Sandy Bridge micro architecture based on Triple-Gate ("3D") transistors [28]. First microprocessors are expected to be built in 2012. As scaling is expected to reach the 20 nm barrier soon, Multi-Gate MOSFETs become more and more important.

1.2. Technologies, Circuit Design and Compact Modeling

The challenge to pass the 20 nm barrier continues in various research groups day by day. It is the aim to scale down the MOSFET to allow an exponentially grown number of devices on a chip, to raise e.g. the clock frequency of commercial microprocessors, or the storage density of memories. However, at the same time the power consumption has to be reduced. This target forces worldwide research groups to find new methods, materials and even new circuit design to fulfill the requirements. To pass the 20 nm barrier soon, Multi-Gate MOSFETs become more and more important, as the industry showed at the end of 2011, when Intel changed their architecture for microprocessors to Triple-Gate ("3D") base transistors [28].

Beside the boost in the technology area, an improvement of design tools is necessary. The evolved technologies have to be included in electronic design automation tools as well as in circuit design tools. Designer's need the full spectrum of state-of-the-art technological possibilities.

1.2.1. Technologies

With the introduction of Triple-Gate transistors to the production of commercial microprocessors by Intel, the proposed importance of Multi-Gate FETs for channel lengths in the 20 nm area has been fulfilled. Some more popular and promising candidates are the Double-Gate FET [36], Triple-Gate FET [37], and the Quadruple-Gate FET [38],

UNIVERSITAT ROVIRA I VIRGILI
TWO-DIMENSIONAL ANALYTICAL PREDICTIVE MODELING OF SCHOTTKY BARRIER SOI AND MULTI-GATE MOSFETS
Mike Schwarz
Dipòsit Legal: T.456-2013

Table 1.1.: Evolution of transistors in commercial microprocessors [29, 30, 31, 32, 33, 34, 35].

processor	number of transistors	year	manufacturer
Intel 4004	2250	1971	Intel
Intel 8008	3500	1972	Intel
Intel 8080	4500	1974	Intel
6502	5000	1975	MOS Technology
Intel 8088	29.000	1979	Intel
Motorola 68000	68.000	1979	Motorola
Intel 80286	134.000	1982	Intel
Intel 80368	275.000	1985	Intel
Intel 80486	1.200.000	1989	Intel
Pentium	3.100.000	1993	Intel
AMD K5	4.300.000	1996	AMD
Pentium II	7.500.000	1997	Intel
AMD K6	8.800.000	1997	AMD
Pentium III	9.500.000	1999	Intel
AMD K6-III	21.300.000	1999	AMD
AMD K7	22.000.000	1999	AMD
Pentium 4	42.000.000	2000	Intel
Itanium	25.000.000	2001	Intel
Barton	54.300.000	2003	AMD
Intel Pentium M	77.000.000	2003	Intel
AMD K8	105.900.000	2003	AMD
Itanium 2	220.000.000	2003	Intel
Itanium 2 (9 MB Cache)	592.000.000	2004	Intel
Cell	241.000.000	2006	Sony/IBM/Toshiba
Core 2 Duo	291.000.000	2006	Intel
Core 2 Quad	582.000.000	2006	Intel
G80 (GPU)	681.000.000	2006	nVIDIA
Dual-Core Itanium 2 (24 MB Cache)	1.700.000.000	2006	Intel
Power 6	789.000.000	2007	IBM
Core i7	731.000.000	2008	Intel
AMD K10	785.000.000	2009	AMD
RV870, Cypress (GPU)	2.154.000.000	2009	AMD ATI
Intel Core i7 2600K	995.000.000	2010	Intel
AMD Bulldozer	1.200.000.000	2011	AMD
Intel Core i7 3930K	2.270.000.000	2011	Intel

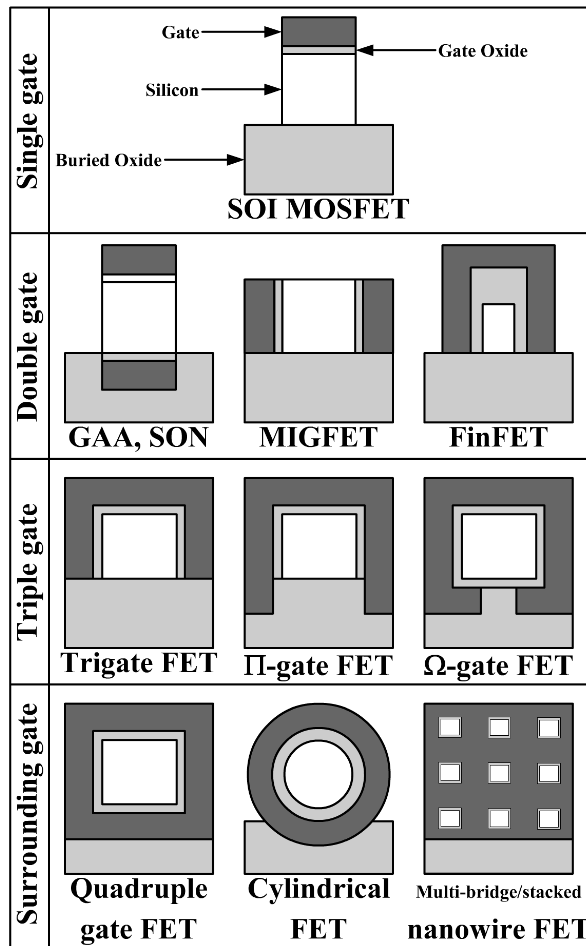

Figure 1.1.: Different gate structures [41].

published by Colinge [39]. With these alternative device designs on SOI, substrate short-channel effects are reduced dramatically [40] and gate control is improved (Fig. 1.1).

Various Multi-Gate SOI MOSFETs have been introduced [42, 43]. These are FinFET [44,45], Pi-Gate [46], Surrounding-Gate or Gate-All-Around [38], Omega-Gate [47] along with many others [41]. The manufacturing of those structures is still a challenge, as most studies are based on device simulations.

High doping and steep doping gradients are needed to scale Single-Gate MOSFETs below 100 nm while the current minimum of the gate length is approximately 3 nm [48]. However, high doping and steep doping gradients are harmful for charge carrier mobility. Using Multi-Gate MOSFETs fully depleted body with low doping is possible [49].

There are a lot of approaches to optimize MOSFET devices in the sub-100 nm area. One approach describes the introduction of Schottky barrier (SB) MOSFET devices, proposed in 1968 [50] which are one of the promising structures due to their high scalability even down to the sub-10 nm region and good process compability with the current

standard Si technologies [51, 52]. The main benefit of Schottky barrier devices is the low specific resistance [53] of the metallic source/drain (S/D) electrodes. Furthermore, due to the work function difference between the metallic S/D electrodes and the channel region, channel doping is no longer necessary.

However, the performance of a Schottky barrier MOSFET is limited by its Schottky barrier height at the silicide-to-silicon interface. A more promising approach towards the Schottky barrier MOSFET is the dopant-segregated Schottky barrier MOSFET, proposed in 2004 [54]. A shallow, heavily-doped region lies adjacent to the silicide region to reduce the Schottky barrier height.

Another approach which increases transistor density, is 3D die stacking by vertically integrating two or more dies with a dense, high-speed interface [55]. The stacking enables the construction of circuits using multiple layers of active silicon bonded with low-latency, high-bandwidth and very dense vertical interconnects [56,57]. Furthermore, the stacking enables mixing dissimilar process technologies such as high-speed CMOS with high-density DRAM. Stacking DRAM directly on top of a processor significantly improves the performance and is a way to attack the Memory Wall problem [58].

However, all these approaches of downscaling and increasing the density on a wafer and at least a single chip have to take account for effects of variations and statistical variability, dopant fluctuations, surface roughness, reliability, and others which results during the manufacturing process and from the before described methods of improvements [59, 60, 61, 62].

By introducing Multi-Gate MOSFETs and various technological optimization approaches the understanding of their behavior and their modeling are much more difficult. In case of Multi-Gate MOSFETs the additional gates influence the field lines in a more dimensional way compared to Single-Gate transistors. Nowadays, a lot of research is done and as already mentioned the border of the sub-20 nm has almost been reached since the Triple-Gate introduction of Intel [28]. All these effects and optimizations of new technologies have to be taken into account for compact models which might be implemented in state of the art design tools and circuit simulators.

1.2.2. Circuit Design and Compact Modeling

In the 1960's and early 1970's, when integrated circuits began to incorporate hundreds of gates and thousands of transistors, computer-aided electronic design automation tools were required to reduce errors and decrease design time [22]. The first commercial microprocessor 4004 from Intel in 1971 already consisted of 2250 transistors [25] which was quite complicated to build manually by the designer. Today an Intel Core i7 3930K microprocessor consists of more than 2 billion transistors [29].

UNIVERSITAT ROVIRA I VIRGILI
TWO-DIMENSIONAL ANALYTICAL PREDICTIVE MODELING OF SCHOTTKY BARRIER SOI AND MULTI-GATE MOSFETS
Mike Schwarz
Dipòsit Legal: T.456-2013

During the last 40 years the amount of transistors has been increasing rapidly, thus design tools with an improved performance are required to handle the new chip designs. Especially the design of new integrated circuits involves the use of several electronic design automation tools for high-level digital design. Furthermore, simulation and modeling of discrete devices is very important for the design of new integrated circuits.

Both systems, analogue and digital, are simulated countless times to ensure the functionality of the circuit in all conceivable cases, e.g. power supply variation.

Device Simulations

Repeating manufacturing challenges of new device structures force research groups to study the new structure on device simulators, e.g. Silvaco ATLAS [63], Synopsys TCAD (Technology Computer-Aided Design) Sentaurus [64] or Minimos-NT [65]. These device simulators use a mesh on 2D surfaces or 3D volumes and solve each grid point iteratively with the help of a partial differential equation solver. Depending on the mesh refinement and the resulting number of points a simulation of one device can take several hours up to several weeks.

These device simulators offer a wide variety of parameters to change, such as various materials and their parameters. Additionally, the parameter variations seem to be endless for the various existing models in the device simulators. Furthermore, device simulations can predict and offer insight into the device physics of novel devices. Without device simulations the development costs for new devices raise to infinity.

However, besides all the advantages which are given to the device designers, these kind of numerical device simulations are not applicable in circuit simulators [66].

Circuit Simulations

In contrast to device simulations and device designers the physics of the various elements of a circuit are of minor interest for circuit designers. From a circuit designer's point of view the function, verification, and tests of simple and complex analogue and digital circuits is more important. However, a condition for correct behavior of the circuit is that the real device elements are modeled sufficiently exact with the implementation of the simulation software. In result this saves time and costs for the development of electronic circuits and on the other hand helps to understand electronics including various misbehaviors.

Today, the most famous circuit simulators are SPICE (Simulation Program with Integrated Circuit Emphasis) [67] and Eldo [68]. SPICE, mostly a derivative of the CANCER program [69], was first presented at a conference in 1973. Eldo, as many others, is a derivative of SPICE. Today, almost all circuit simulators have their origin in CANCER.

Models for Circuit Simulators

A circuit simulator is only as good as its included models for the device elements. Therefore, a wide range of models for devices exists. Depending on the case whether the circuit for the most effective or most exact model is chosen. Older models are only valid in particular regions of operation, connected mathematically, to provide continuous solutions. These models are often treated as threshold-based models, because the threshold voltage is the key parameter. Newer models have to take for shorter channel lengths and the resulting reduced supply voltages into account because MOS devices now often operate in moderate and weak inversion regions. Therefore, these models differ from threshold-based models and apply two main approaches. These depend on inversion charge or surface potential as well as inversion-charge based and surface-potential based models [70].

Older models are BSIM 3v3 [71], PCIM [72], Motorola Model [73] and EKV [74]. Newer models for more advanced devices are BSIM 4 [75], BSIM 5 [76, 77], BSIM 6 [78], BSIMSOI [78], BSIMCMG [78], PSP [79, 80] and HiSIM [81, 82, 83, 84].

In general, these kinds of models for circuit simulators can be divided in three types of models [85, 86], namely physical-based models, numerical-fit models, and empirical models.

Physical-based models try to use physics-based equations to describe the behavior of the transistor with the advantage that they are able to predict the behavior of scaled devices. These types of models do not introduce empirical fitting parameters [66]. However, a disadvantage is that the equations are often not continuous for all transistor operation regions and often not accurate enough compared to other model-types [70, 87]. These models are often used to describe the behavior of long-channel devices [88].

Numerical-fit models have no relation to the principle basics of the device. The equations of these models consist of a countless number of fitting parameters where every change of physical device parameters requires a complete new set of fitting parameters [66].

Empirical models are in-between physical-based and numerical-fit models. These models use physic-based equations and introduce several fitting parameters to simplify and improve the models. However, these fitting parameters reduce the ability to predict the behavior of transistors with changed physical characteristics [66].

All these models have to fulfill the same requirements [88, 89]. The behavior of the device has to be described as exactly as possible. The application specifies the accuracy; analogue circuits need higher accuracy one compared to digital circuits [90]. The models in circuit simulators should consist of analytical closed-form equations which are called compact models. These are needed to save time, because electrical connections in a

UNIVERSITAT ROVIRA I VIRGILI
TWO-DIMENSIONAL ANALYTICAL PREDICTIVE MODELING OF SCHOTTKY BARRIER SOI AND MULTI-GATE MOSFETS
Mike Schwarz
Dipòsit Legal: T.456-2013

circuit simulator are solved with iterative methods [66]. Furthermore, due to convergence reasons a continuous first derivative of the models is required. Additionally, it is desirable to use one set of parameters which can be applied to the various devices in modern circuit simulators [91].

1.3. State of the Art

In this section, a brief overview of the state of the art for Schottky barrier devices is given. Both, current technologies and models are presented.

The Schottky barrier MOSFET device-fabrication literature provides several different topics for improvements like Schottky barrier device architectures, height engineering, and integration of new silicides [53].

A bulk 27 nm channel length PtSi Schottky barrier device, with a drive-current of 350 µA/µm, was demonstrated 1999 by Wang et al. [92]. This device set standard for the drive-current performance for highly scaled Schottky barrier MOSFET technology.

In 2000, sub-25 nm SOI Schottky barrier PMOSFET and Schottky barrier NMOSFET devices were demonstrated by Kedzierski where the off-state performance of the PtSi Schottky barrier PMOSFET and $ErSi_x$ Schottky barrier NMOSFET devices was significantly improved by using SOI substrate [93, 94, 95].

Various Schottky barrier MOSFET short-channel literature deals with a silicide source/drain architecture on either bulk or SOI substrate without using interfacial layers to improve performance [53].

Beside of these approaches, Tsui and Lin presented a FinFET device with an interfacial layer placed between the metal source/drain and the channel region provided by an "implant-to-silicide" technique, known as dopant segregation (DS). With this technique Tsui reported a drive-current of 250 µA/µm and an on-off current ratio of 10^9 [96].

Various methods are reported in literature to improve the drive current as well as the leakage current. One method is to improve the carrier injection which is determined by the Schottky barrier between source and the channel. A reduction of the Schottky barrier height can be achieved by techniques as Fermi level depinning with an insulator between the metal and semiconductor [97, 98], low Schottky barrier silicides [99], and dopant segregation [96, 100].

For instance, the dopant segregation effect results in a thin highly doped layer which causes a strong band bending at the silicide-to-silicon interface and hence in an increased tunneling probability for the carriers due to the effectively reduced Schottky barrier height [101]. Promising results with a "steep" subthreshold behavior are reported for nanowire and planar UTB SOI Schottky barrier MOSFETs with dopant segregation by Knoll [102].

Another approach, the use of several silicides for the source/drain formation, was reported by Zhu et al. in 2004 [99]. Zhu announced a barrier height of 0.27 eV for $YbSi_x$, more than the typically reported 0.28 eV for $ErSi_x$. Furthermore, Zhu reported that Ytterbium provides an improvement of the I_{on} performance by 240 % and an I_{on}/I_{off} ratio improvement of two to three orders of magnitude [53].

Some debate about the optimal Schottky barrier height became evident. To get an acceptable performance, several opinions exist for the barrier height while simulation studies suggest a finite positive barrier of 0.06 eV-0.1 eV is needed for Schottky barrier PMOSFET and Schottky barrier NMOSFET [53].

The problem which still exists, is the fabrication of these devices. This is a challenge, because of the stringent requirement that the Schottky barrier has to be ideal. Otherwise, if the Schottky barrier is influenced by e.g. surface roughness effects, interfacial states, traps, etc., the drive current is low [103] and the off state leakage is large [104]. This results into a poor subthreshold behavior and an on-state performance inferior to conventional MOSFETs.

Beside the Schottky barrier device architectures, Schottky barrier height engineering, and Schottky barrier integration also the topic of modeling is of worldwide interest. The existing models for Schottky barrier MOSFETs can be divided into two kinds, the self-consistent numerical iterative models for commercial state-of-the-art device simulators like Synopsys TCAD Sentaurus [64] or Silvaco ATLAS [63], and the analytical modeling approaches for future applications in circuit simulators. Here, two kinds of approaches for analytical modeling are introduced. These are the analytical numerical and the analytical closed-form or compact models.

The device simulators Synopsys TCAD Sentaurus and Silvaco ATLAS are in principle based on similar numerical iterative models. Mainly they are based on the proposed expression known as the Tsu-Esaki model [105].

Synopsys TCAD Sentaurus offers three models which can be applied to solve the tunneling current in Schottky barrier devices. The most versatile tunneling model is the non-local tunneling model based on Ieong's work [106]. Beside the non-local model a powerful direct tunneling model based on Schenk [107] and a simple Fowler-Nordheim model [108] can be applied in the device simulator. Furthermore, there band-to-band tunneling models included in TCAD.

Silvaco ATLAS also offers various kinds of tunneling models. It offers various non-local tunneling models for heterojunctions or quantum barriers, a Fowler-Nordheim model based on Zaidman [109], and various band-to-band tunneling model based on [110, 111, 112, 113].

The models accuracy depend on the description of the transmission coefficient. Various methods for prediction exist in TCAD Sentaurus and Silvaco ATLAS. The simplest

UNIVERSITAT ROVIRA I VIRGILI
TWO-DIMENSIONAL ANALYTICAL PREDICTIVE MODELING OF SCHOTTKY BARRIER SOI AND MULTI-GATE MOSFETS
Mike Schwarz
Dipòsit Legal: T.456-2013

model for both device simulators is based on the Wentzel-Kramers-Brillouin (WKB) approximation [114,115,116]. In TCAD enhancements of the WKB are given by Fei [117] and Register [118] as well as enhanced transmission coefficient models for TCAD and ATLAS e.g. Schrödinger equation-based tunneling probability. Additionally, in ATLAS an Airy function approach for the tunneling coefficient estimation is available which is implemented in the direct tunneling model based on Schenk [107] in TCAD.

Beside the commercial state-of-the-art device simulators several free device simulators exist also at the nanoHUB community. The Resonant Tunneling Diode Simulation with NEGF from [119] simulate 1D RTDs using non-equilibrium Green's function (NEGF), a Schottky-Barrier Carbon Nanotub (CN) FET Simulation from [120, 121], a Quantum and Semi-classical Electrostatics Simulation of SOI Trigates from [122, 123] to name a few with relation to the quantum mechanical tunneling.

Another state-of-the-art device simulator, the MINIMOS-NT [124], developed by the Institute for Microelectronics from Vienna University, is mainly based on analytical numerical modeling approaches. MINIMOS-NT is a generic simulator accounting for a variety of materials, including group IV semiconductors, III-V compound semiconductors and their alloys, and non-ideal dielectrics. The models are verified against statistically analyzed measured data [125]. Especially a wide variety of tunneling models have been included in the MINIMOS-NT by the work of Gehring [126].

A huge amount of various models exists from several research groups worldwide. Analytical closed-form or compact models are rare. Nevertheless, some approaches in literature present very promising results for new methods of predicting the tunneling current in Schottky barrier devices. In general, two kinds of compact models are provided in literature, sub-circuit-based compact models or macro models and physics-based compact models, depending on the geometry. Beside the two kind of compact models, only a few compact models provide 2D approaches. Mostly, the presented approaches are suitable for Nanotube FETs or long channel where 1D solutions are accurate enough.

A circuit-based compact model was presented by Prégaldiny [127] in 2006 and explains a modified circuit compact model for Carbon Nanotube FET applications for analogue and digital circuits based on the work of Raychowdhury [128].

Physics-based compact models are presented by Frégonèse in 2010 and 2011, who developed an electrical compact model for the Double-Gate Carbon Nanotube FET, a 1D physics-based model which include the most significant mechanism such as electrostatics, band-to-band tunneling effect and quasi-ballistic transport [129, 130].

A non-iterative physics-based compact model of a Carbon Nanotube Transistor based on a closed-form linear approximation for the surface potential is presented by Sinha [131] which is still a 1D approach. However, Sinha applies the WKB approximation with the Fabry-Pérot cavity model which takes reflections into account.

UNIVERSITAT ROVIRA I VIRGILI
TWO-DIMENSIONAL ANALYTICAL PREDICTIVE MODELING OF SCHOTTKY BARRIER SOI AND MULTI-GATE MOSFETS
Mike Schwarz
Dipòsit Legal: T.456-2013

In 2008 Zhu presented a Schottky barrier Double-Gate MOSFET model, based on a quasi-2D surface-potential solution for the energy band model and the Miller-Good tunneling method for the terminal current [132]. 2009 Zhu applied the proposed quasi-2D approach onto a compact model for undoped silicon Nanowire MOSFETs with Schottky barrier source/drain including the Schottky barrier lowering effect for channel lengths down to 65 nm [133]. In [134] Zhu published an analytical device model and an unique sub-circuit approach for a compact model with dopant-segregated Schottky gate-all-around Si-Nanowire MOSFETs excluding the Schottky barrier lowering effect. Results are presented for channel length down to 40 nm which are quite in a good agreement to measurement data.

In 2010 Balaguer reported an analytical compact model for Schottky-Barrier Double Gate MOSFETs [135] which is valid for long-channel devices. The model is a modification, based on the work of Moldovan [136].

1.4. Primary objective of the Doctoral Thesis

In this dissertation a new way to calculate the current in Schottky barrier Double-Gate MOSFETs is presented. The aim is to simplify the model and include first order effects, to receive a compact model for an accurate current estimation. In contrast to previous works of other research groups, the approach presented here describes a fully functional 2D model for electrostatics and current calculations. Due to this circumstance the model is able to predict the current behavior even for short-channel lengths down to 22 nm quite accurately. Throughout this dissertation all results are compared to the numerical device simulator TCAD Sentaurus [64]. The results of a modification for a Schottky barrier ultra-thin body (UTB) MOSFET are compared with measurement data.

In chapter one a brief overview into the history is given. Afterwards, a brief overview in technologies, the circuit design, and compact modeling are is given. Finally, the state of the art in technologies and models are presented.

Chapter two primarily focuses on the theoretical background and physical basics. First, the necessary quantum mechanical tunneling effect is introduced. Secondly, the metal-semiconductor contacts are explained with the main current transport processes. Afterwards, various tunneling models are presented and the operation principle of Schottky barrier devices is introduced.

In chapter three the necessary mathematical basics which are used are introduced. The conformal mapping technique which is used to solve 2D electrostatics in closed form, is described in detail. With the help of the Schwarz-Christoffel transformation [137, 138] a z-plane is mapped into the upper half of a w-plane and the equations can be determined.

UNIVERSITAT ROVIRA I VIRGILI
TWO-DIMENSIONAL ANALYTICAL PREDICTIVE MODELING OF SCHOTTKY BARRIER SOI AND MULTI-GATE MOSFETS
Mike Schwarz
Dipòsit Legal: T.456-2013

Chapter four presents the general modeling simplifications that define the area which is to be solved. Furthermore, the applied boundaries are defined and described in detail and a decomposition is introduced which keeps the mathematics as simple as possible.

The closed-form solutions for electrostatics are derived in chapter five. Two approaches for the electrostatic potential are explained first and then compared to each other. Afterwards, the electric field solution is derived in closed form. A comparison of all approaches versus TCAD Sentaurus is made.

In chapter six the derived solution for the electrostatics is applied to the analytical numerical modeling of the currents in the Schottky barrier device. First, further simplifications are defined, then the approach for the calculation of the tunneling current is introduced. Afterwards, the thermionic emission current is described in detail followed by the introduction of a transition area between both current components. The results are compared to TCAD Sentaurus for both current characteristics. Finally, an investigation of the scaling behavior of Schottky barrier Double-Gate devices is made with the here presented current modeling approach.

Chapter seven deals with detailed 2D analyses of the current components. In the first step the TCAD Sentaurus current components are analyzed. Secondly, the current components of the model approach are analyzed and compared with the ones from TCAD Sentaurus. Afterwards, an analysis of the model current densities is done. Finally, the main contributions of the current components are highlighted for the definition of a compact model.

The analytical closed-form solution for the currents is presented in chapter eight with the analyses from chapter seven. An analytical approach for the tunneling current density is introduced. Then an approach for the currents itself is presented. Finally, a smoothing from the thermionic to the tunneling operation area is explained. The presented approaches are compared to simulation results from TCAD Sentaurus in a last step.

Chapter nine compares the analytical numerical modeling approaches described in chapter six with measurement data for dopant-segregated Schottky barrier UTB MOSFETs. Therefore, the electrostatics for Double-Gate MOSFET devices from chapter five are converted to electrostatics for UTB MOSFETs.

Chapter ten summarizes the dissertation and gives an outlook into the future research prospects. Finally, it concludes the work of the dissertation.

In the appendix the quantum mechanical tunneling effect is introduced in detail. Furthermore, the calculation of the WKB approximation is explicitly explained. Additionally, the introduced square root approximation from chapter five for the electrostatic potential is verified on performance. Finally, an equation package summarizes all necessary equations to calculate the current in Schottky barrier Double-Gate devices.

UNIVERSITAT ROVIRA I VIRGILI
TWO-DIMENSIONAL ANALYTICAL PREDICTIVE MODELING OF SCHOTTKY BARRIER SOI AND MULTI-GATE MOSFETS
Mike Schwarz
Dipòsit Legal: T.456-2013

Chapter 2.

Theoretical and Physical Basics

In this chapter a brief overview of the necessary physics and effects in Schottky barrier devices is given. First, an excursion into the quantum mechanics and keywords like wave-particle duality, Schrödinger equation, potential well, transmission and reflexion are discussed. Afterwards, the metal-semiconductor contacts with the Schottky barrier formation and their current transport processes follow and finally the operation principle in Schottky barrier MOSFET devices is presented.

2.1. The Quantum Mechanical Tunneling Effect

The quantum mechanical tunneling effect is one of the most important phenomena that exists in our universe. Without this effect, life on earth in a way we know today would not be possible. The tunneling effect allows nuclear fusion of hydrogen to helium within the sun, with the sun's current temperature and size. Otherwise, without this effect the sun would have to be much larger and hotter that nuclear fusion can take place. Therefore, life on earth would never be the same as it is today [139].

This consideration shows that there are phenomena which can not be described by the classical physics, i.e., Newton's axioms or Maxwell's equations. They have to be described by quantum mechanics. Classical physics fulfill macroscopic space while quantum mechanics are suitable for the microscopic space, as in semiconductors. Furthermore, quantum mechanics are based on postulates from a large amount of experimental observations [140].

2.1.1. Wave-particle duality

Classical physics and quantum mechanics are described by two quantities, particles and/or waves. Classical particles are small objects which can be described by several physical properties such as volume or mass while waves are disturbances or oscillations which travel through the space and the time, accompanied by the transfer of energy.

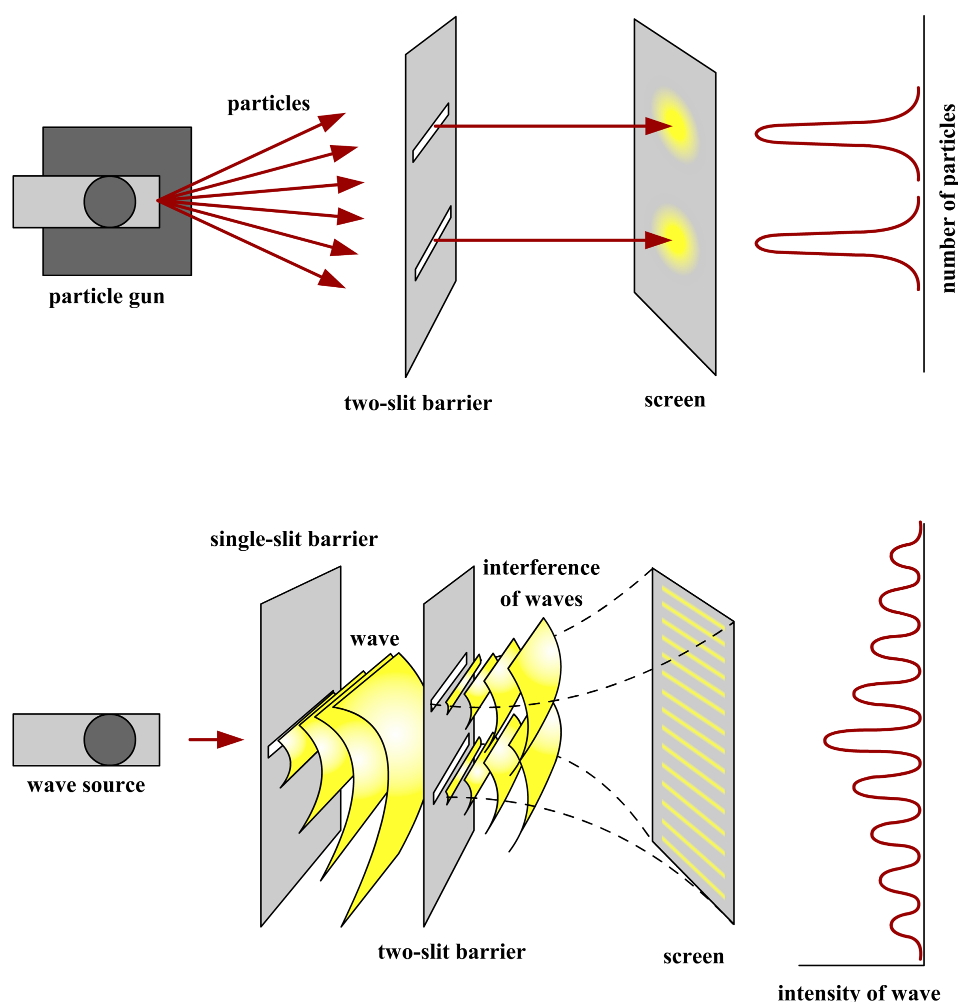

Figure 2.1.: In some experiments electrons behave like particles, e.g., light → photoelectric effect and in other experiments like waves, e.g., light → double-slit diffraction and interference [141].

In classical physics particles are used for the description while in the quantum mechanics the behavior of a "microscopic" particle can be described by both. In some experiments (Fig. 2.1) "microscopic" particles behave like waves, e.g. light → double-slit diffraction and interference [142]. In other experiments like a particle, e.g. light → photoelectric effect [143].

The wave-particle duality postulates that all particles exhibit both wave and particle properties. In 1924 De-Broglie [144] elaborated the hypothesis that if light can be described as a particle as well as a wave, hence particles, e.g. electrons, could be described by waves. The proof followed with the double-slit experiment with electrons. Due to this circumstance also material shows the properties of particles and waves, depending on the experiment. This is a very important fact for nanotechnology [145, 146, 147].

UNIVERSITAT ROVIRA I VIRGILI
TWO-DIMENSIONAL ANALYTICAL PREDICTIVE MODELING OF SCHOTTKY BARRIER SOI AND MULTI-GATE MOSFETS
Mike Schwarz
Dipòsit Legal: T.456-2013

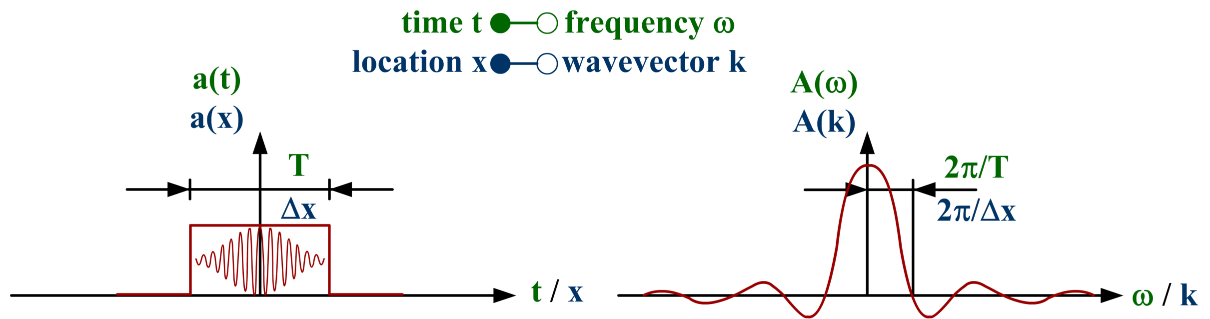

Figure 2.2.: The broader the amplitude spectrum $A = A(k)$ is, the more exact the localization of a wave packet appears. A comparison between time t and frequency ω with help of the Fourier transform explains the behavior between location x and the wave vector $\vec{k}$.

2.1.2. Schrödinger Equation

In 1926 Schrödinger [148] had the idea to interpret elementary particles as wave packets. One must superpose many waves with slight amplitude of different wavelength. Then the amplitude of the resulting wave is zero, except the place of the wave packet itself due to the interference. A light particle, a photon, is handled as such a wave packet, also the velocity of the wave packet along the path of the wave is the so-called group velocity v_G [145, 146, 147].

The wave function of a particle is defined as

$$\psi(\vec{x}, t) = A \cdot \exp(j(\vec{k}\vec{x} - \omega t)) \tag{2.1}$$

with amplitude A, wave frequency $\omega = c \cdot k$, the speed of light c, and wave number $k = |\vec{k}| = 2\pi/\lambda$. The wavelength λ in the potential well results from the standing waves where $\lambda_n = 2L/n$ due to the fact that only waves with an integral of the multiples half wavelength exist. The impulse $\vec{p} = \hbar\vec{k}$ where $\hbar$ describes the Planck constant, of a particle and its wavelength are coupled.

A moving particle can be interpreted as a wave packet which results from the superposition of waves with different wavelengths. The wave packet is moving with the classical particle velocity v through space. The wavelength of a particle decreases with increasing mass [145, 146, 147].

The broader the amplitude spectrum $A = A(k)$ is, the more exact the localization of a wave packet appears. A comparison is given in Fig. 2.2 with the help of the Fourier transform.

Therefore follows, if within a length Δx an electron exist, the uncertainty wavelength amounts at least

$$\Delta k = \frac{2\pi}{\Delta x} \text{ or } \Delta\frac{1}{\lambda} = \frac{1}{\Delta x}. \tag{2.2}$$

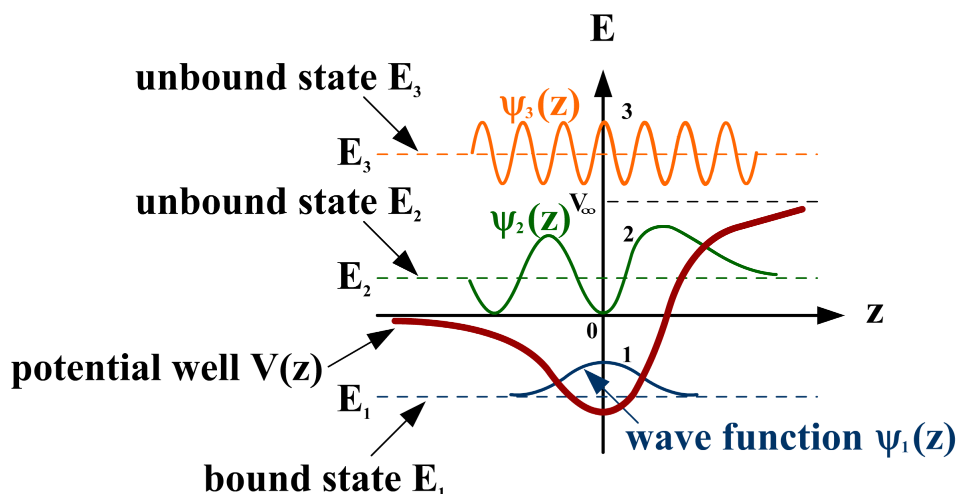

Figure 2.3.: Three types of solutions of the Schrödinger equation for an one-dimensional well of arbitrary form [145].

With $p = \hbar/\lambda$ the Heisenberg uncertainty principle [149] is introduced

$$\Delta x \cdot \Delta p \geq \hbar, \tag{2.3}$$

which says that, when the position x is exactly defined, only an inaccurate state of the impulse is possible and vice versa [147].

The square of the absolute value of the wave function at position x yields the probability to find a particle at position x [145, 146, 147, 148]

$$P = |\psi(x,t)|^2 = \psi(x,t) \cdot \psi^*(x,t). \tag{2.4}$$

The following normalization has to be satisfied [147, 148]

$$\int_{-\infty}^{+\infty} |\psi(x,t)|^2 \, dx = 1. \tag{2.5}$$

For a free electron with the wave function of one wavelength the identical probability at each position is derived [145, 146, 147, 148]

$$\psi(x,t) \cdot \psi^*(x,t) = A \exp(j(kx - \omega t)) \cdot A^* \exp(-j(kx - \omega t)) = AA^* = \text{const}. \tag{2.6}$$

The uncertainty principle results in $\Delta p \to 0 \Rightarrow \Delta x \to \infty$.

For a localized electron within Δx the impulse is undefined! The uncertainty principle results in $\Delta x \to 0 \Rightarrow \Delta p \to \infty$.

Wave functions are described by the Schrödinger equation (Fig. 2.3), here in its one-dimensional form [145, 146, 147, 148]

$$-\frac{\hbar^2}{2m} \cdot \frac{\partial^2 \psi(x)}{\partial x^2} + V(x) \cdot \psi(x) = \xi \cdot \psi(x) \tag{2.7}$$

UNIVERSITAT ROVIRA I VIRGILI
TWO-DIMENSIONAL ANALYTICAL PREDICTIVE MODELING OF SCHOTTKY BARRIER SOI AND MULTI-GATE MOSFETS
Mike Schwarz
Dipòsit Legal: T.456-2013

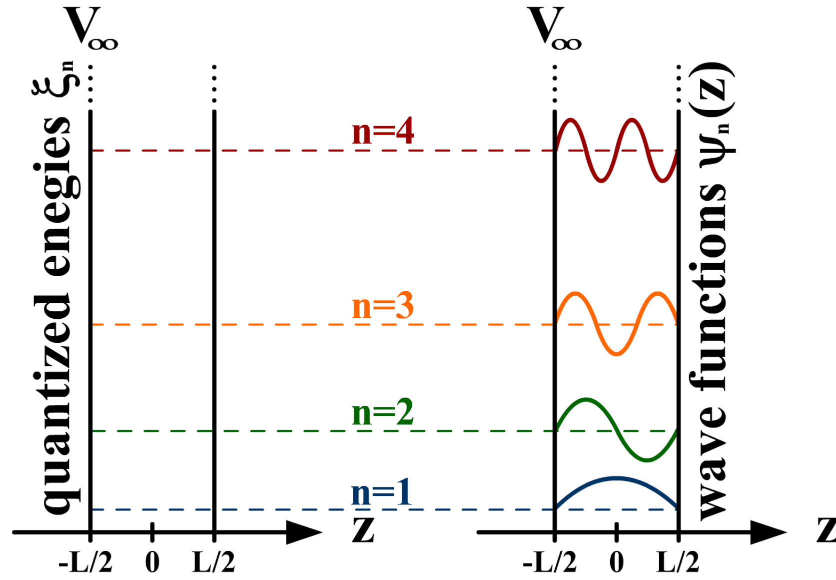

Figure 2.4.: Solutions of the Schrödinger equation for a quantum well with infinite barriers. Eigenenergies, ξ_n, are defined as $\xi_n = n^2\xi_1$ where $\xi_1 = \hbar^2\pi^2/(2mL^2)$ [145].

where $\psi(x,t) = \psi(x) \cdot \exp(-j\omega t)$ is the time description, $\psi(x)$ the time independent description, $V(x)$ is the potential energy, m the mass of a charge carriers and ξ the energy of an electron in x-direction [145, 146, 147, 148].

2.1.3. Potential Well

With the help of the Schrödinger equation and the defined wave functions it is possible to demonstrate the existence of the tunneling effect. Therefore, two contemplations with the potential well are made where the calculations can be found in the Appendix A.1 and A.2.

If an infinite potential well is assumed, the potential wells are impenetrable and then the stationary solutions result in standing waves. The forward- and backward moving wave results in the group velocity $v_G = 0$, but with the energy of an electron (Fig 2.4)

$$\xi = \frac{p^2}{2m} = \frac{h^2}{\lambda^2}\frac{1}{2m} = \hbar\omega. \tag{2.8}$$

Energy states with quantized energies are allowed with $n = \pm 1; \pm 2; \pm 3; \ldots$

$$\xi_n = \frac{\hbar^2}{2m}\frac{\pi^2}{L^2}n^2. \tag{2.9}$$

If a finite potential well is assumed, the potential wells are penetrable and it is valid for $|x| \geq \frac{L}{2}$ with $\kappa_b = \sqrt{2m(V_b - \xi)/\hbar^2}$ (Fig 2.5)

$$\psi(z) = A\exp\left(\mp\kappa_b\left(x \mp \frac{L}{2}\right)\right). \tag{2.10}$$

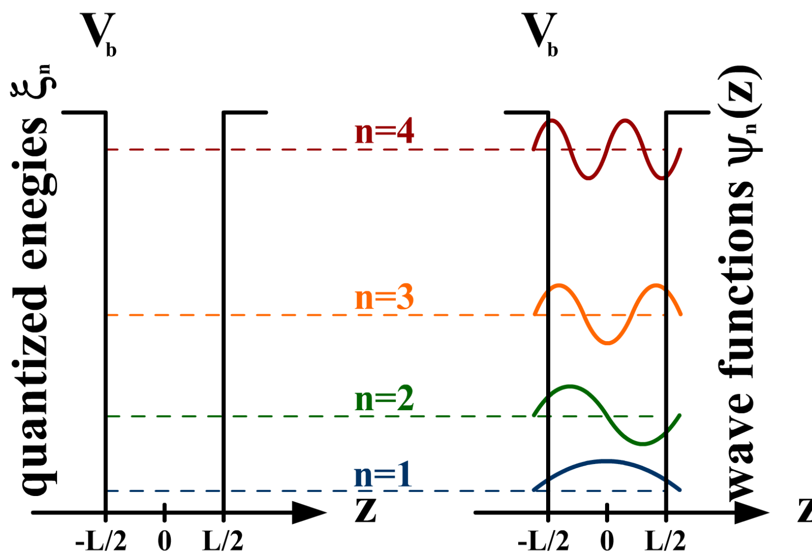

Figure 2.5.: Solutions of the Schrödinger equation for a quantum well with finite barriers. Eigenenergies, ξ_n, are defined as $\xi_\mathrm{n} = \mathrm{n}^2\xi_1$ where $\xi_1 = \hbar^2\pi^2/(2\mathrm{mL}^2)$ [145].

Within the potential well quantized energies are allowed. An exponential fading wave function in the barrier is observed which results in a probability that a particle can be found outside the potential well. This effect is referred as the tunneling effect [145, 146, 147, 148].

2.1.4. Transmission and Reflection, Tunneling Effect

If an electron with energy ξ moves towards a barrier with height $\mathrm{V_b}$ and thickness L the following connection between the incoming flow $\mathrm{i_{in}}$, the reflected flow $\mathrm{i_r}$, and the transmitted flow $\mathrm{i_t}$ results as shown in Fig. 2.6

$$\mathrm{R}(\xi) = \mathrm{i_r}/\mathrm{i_{in}}, \tag{2.11}$$

$$\mathrm{T}(\xi) = \mathrm{i_t}/\mathrm{i_{in}}. \tag{2.12}$$

If $\mathrm{L} >> \lambda$, (classical behavior) the outcome is

$$0 < \xi < \mathrm{V_b} \rightarrow \mathrm{R} = 1; \mathrm{T} = 0, \tag{2.13}$$

$$\mathrm{V_b} < \xi \rightarrow \mathrm{R} = 0; \mathrm{T} = 1. \tag{2.14}$$

The transmission coefficient or tunneling probability T which can be understood as the probability that an electron penetrates (Fig. 2.7) the barrier, can be calculated for $\xi < \mathrm{V_b}$ with the following equation [145, 146, 147, 148]

$$\mathrm{T} \approx \frac{16\mathrm{k}^2\kappa^2}{(\mathrm{k}^2+\kappa^2)^2}\exp(-4\kappa\mathrm{L}) \tag{2.15}$$

UNIVERSITAT ROVIRA I VIRGILI
TWO-DIMENSIONAL ANALYTICAL PREDICTIVE MODELING OF SCHOTTKY BARRIER SOI AND MULTI-GATE MOSFETS
Mike Schwarz
Dipòsit Legal: T.456-2013

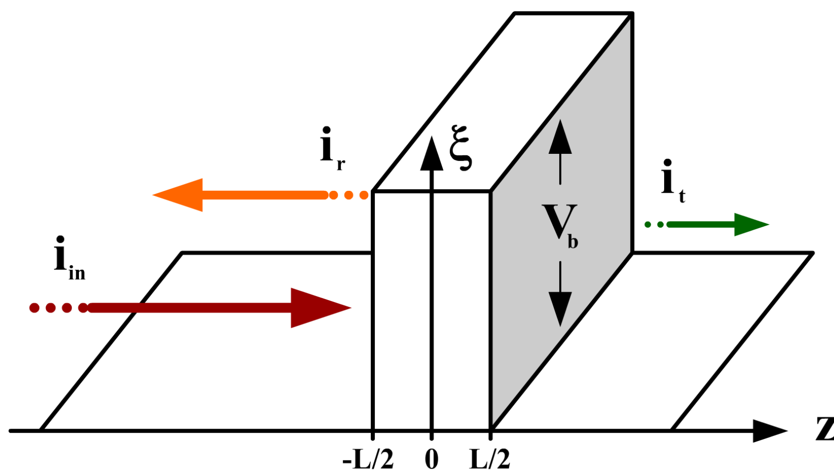

Figure 2.6.: If an electron with energy ξ moves towards a barrier with height V_b and thickness L an incoming flow i_{in}, a reflected flow i_r, and a transmitted flow i_t describe the transmission and reflection through the barrier [145].

with $\kappa = \sqrt{2m(V_b - \xi)/\hbar^2}$ and $k = \sqrt{2m\xi/\hbar^2}$. $\xi > V_b$ yields

$$T \approx 1. \tag{2.16}$$

Certainly, the shown barrier is a construct and in real semiconductor devices the barrier itself depends on the material and other factors. Therefore, the equation for the transmission will be another one as discussed here. In principle, the same quantum mechanical effects occur in semiconductor devices and can be described by the Schrödinger equation. The resulting tunneling equations or models will be discussed in the next sections.

2.2. Metal-Semiconductor Contacts

The first time in history that the rectifying characteristics of metal-semiconductor contacts have been observed was in 1874 by Ferdinand Braun [151]. In the beginning, the metal-semiconductor junctions consisted of point-contacts. In 1904 they found practical applications. In 1938 Walter Schottky [9] applied the transport theory of semiconductors based on the band theory of solids [152] to metal-semiconductor contacts and suggested that the potential barrier could arise from stable space charges in the semiconductor alone without the presence of a chemical layer. Since this model was introduced, metal-semiconductor contacts have been designated as Schottky barrier. Beside Schottky also Mott devised a model in 1938 [8]. These models have been enhanced by Bethe in 1942 [153], as well as by Crowell, Sze, Fowler, and Rhoderick to give a few examples.

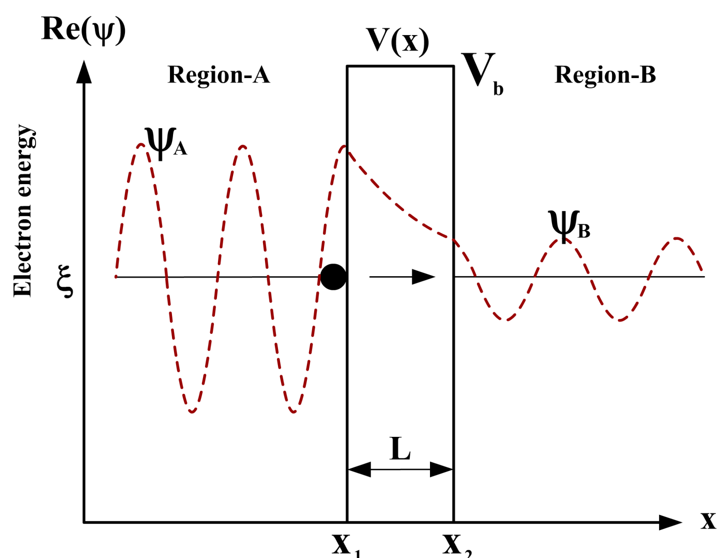

Figure 2.7.: Wave function shows electron tunneling through a rectangular barrier [150].

Finally, the point-contact was replaced by metallic thin-film which today is the standard for Schottky diodes [150].

In the following, the theory of an ideal Schottky diode is explained. Afterwards, the influences which lead to non-ideal behavior are presented. Then the occurring main transport processes and ways to model these are discussed.

2.2.1. Schottky Barrier Formation

A barrier is formed at the metal-semiconductor interface, when a metal comes in contact with a semiconductor. This is responsible for the current control as well as for the behavior of the capacitance.

Ideal Schottky Diode

Figure 2.8(a) shows the electronic energy relations of a high work-function metal and a n-type semiconductor which are in separate systems and not in contact with each other. If they are brought into contact, electrons leave the semiconductor and leave a positive charge of fixed ions behind which create an electric field in negative direction. Electrons flow into the metal until thermal equilibrium is established which means the Fermi levels on both sides line up [150].

Contrary to a semiconductor which has a valence energy band edge E_V, a conduction band edge E_C, and a Fermi level E_f between E_V and E_C, metals only have a Fermi level. In relation to the Fermi level in the metal, the Fermi level in the semiconductor is lowered by an amount equal to the difference between the two work functions [150].

UNIVERSITAT ROVIRA I VIRGILI
TWO-DIMENSIONAL ANALYTICAL PREDICTIVE MODELING OF SCHOTTKY BARRIER SOI AND MULTI-GATE MOSFETS
Mike Schwarz
Dipòsit Legal: T.456-2013

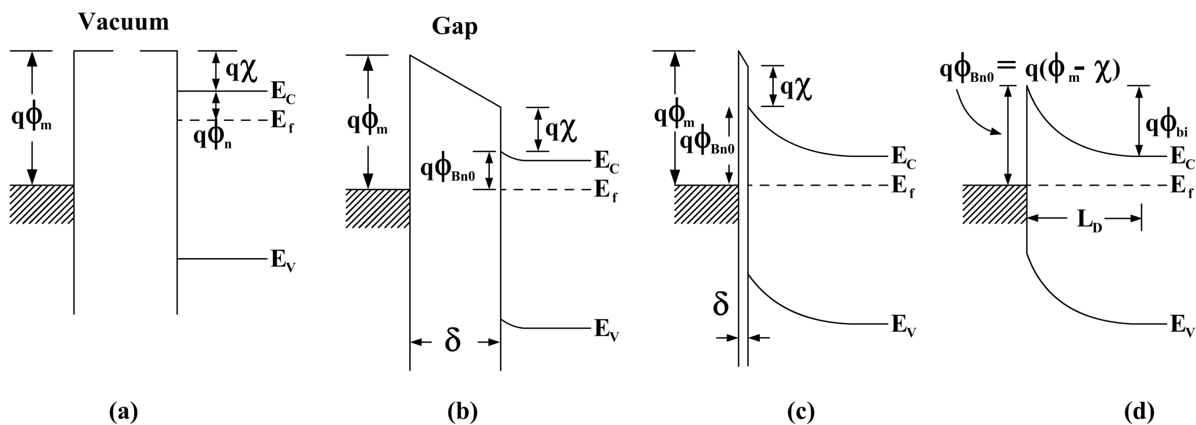

Figure 2.8.: Energy-band diagrams of metal-semiconductor contacts. Metal and semiconductor (a) in separated systems, and (b) connected in one system. As the gap δ (c) is reduced and (d) becomes zero [150].

$q\phi_{\mathrm{m}}$ is the metal work function, i.e., the voltage necessary to remove one electron from the metal, expressed as the difference between E_f and the vacuum level E_0. It varies from metal to metal while different metals exhibit different work functions. $q\phi_s = q(\chi + \phi_n)$ is the semiconductor work function where $q\chi$ is the electron affinity, i.e., the voltage necessary to remove one electron from the conduction band of the semiconductor and $q\phi_n$ the energy difference between the conduction band E_C and the Fermi level E_f. The work function is the energy difference between the vacuum level E_0 and the Fermi level E_f. The potential difference between the two work functions is called the contact potential $\phi_{ms} = \phi_m - \phi_s$ or built-in potential ϕ_{bi} [150].

When the gap distance δ decreases, the electric field in the gap increases and an increasing negative charge is built up at the metal surface. An equal opposite charge exists in the depletion region of the semiconductor. The potential variation behavior within the depletion layer is similar to that of one side of a pn-junction. When δ is low, comparable to atomic distances, the gap becomes transparent to electrons and the case shown in Figure 2.8(d) is obtained. The limiting value of the barrier height $q\phi_{Bn0}$ is given by [150]

$$q\phi_{Bn0} = q(\phi_m - \chi). \tag{2.17}$$

The Schottky barrier height is then defined as the difference between the metal work function and the semiconductor electron affinity. Hence, for an ideal contact between a metal and a p-type semiconductor, the Schottky barrier height $q\phi_{Bp0}$ is given by [150]

$$q\phi_{Bp0} = E_g - q(\phi_m - \chi) \tag{2.18}$$

where E_g is the band gap. The sum of the barrier for electrons and holes of a semiconductor equals the band gap [150]

$$E_g = q(\phi_{Bp0} + \phi_{Bn0}). \tag{2.19}$$

If for n-type silicon, for example, the metal work function is lesser than the silicon work function, then the metal-semiconductor junction becomes an ohmic junction for electrons under forward bias conditions while a Schottky barrier still exists, though, electrons do not experience an ohmic contact under reverse bias [150].

Schottky diodes are considered to be majority carrier devices while forward bias majority carriers are injected from the semiconductor to the metal and minority carriers are injected from the metal to the semiconductor. The opposite occurs under reverse bias conditions. In both biasing conditions the majority carrier current is significantly greater than the minority carrier current [154].

Note that this model of the Schottky barrier or Schottky diode, respectively, is only valid for ideal conditions. In reality, the barrier height is determined by interface states. ϕ_{Bn0} is strongly influenced by the Fermi level pinning effect which is mainly caused by metal induced gap states (MIGS) or defects associated with physical non idealization of the interface. Alongside the interface states the Schottky barrier is influenced by an effect known as the Schottky effect (Schottky barrier lowering) or image-force lowering [150].

Interface States

As already mentioned, a Schottky barrier is influenced by so-called interface states. If metal is deposited onto a semiconductor in all likelihood a non-ideal Schottky diode is formed. Surface states at the semiconductor surface of the metal-semiconductor junction will modify the surface potential, thus modifying the extent of band bending as well a the dimensions of the Schottky barrier. These effects are the so-called metal induced gap states (MIGS). It is stressed again that the Schottky barrier height depends primarily on the surface potential where the built-in voltage of a given Schottky diode depends on the difference of this potential to the potential of the semiconductor [154].

As the source of surface states that can alter the surface potential, interfacial oxides or other interfacial layers at non-silicided metal-semiconductor junctions are responsible [154]. This behavior is shown in Fig. 2.9 for a n-type semiconductor where the states below the Fermi level are filled with electrons while those above are empty. The interfacial layer is in the order of a few atomic layers. Here, ϕ_m presents the work function of metal, ϕ_{Bn0} the barrier height (without image-force lowering), ϕ_0 the neutral level of interface states, Λ the potential across interfacial layer, χ the electron affinity of semiconductor, ϕ_{bi} the built-in potential, δ the thickness of interfacial layer, Q_{SC} the

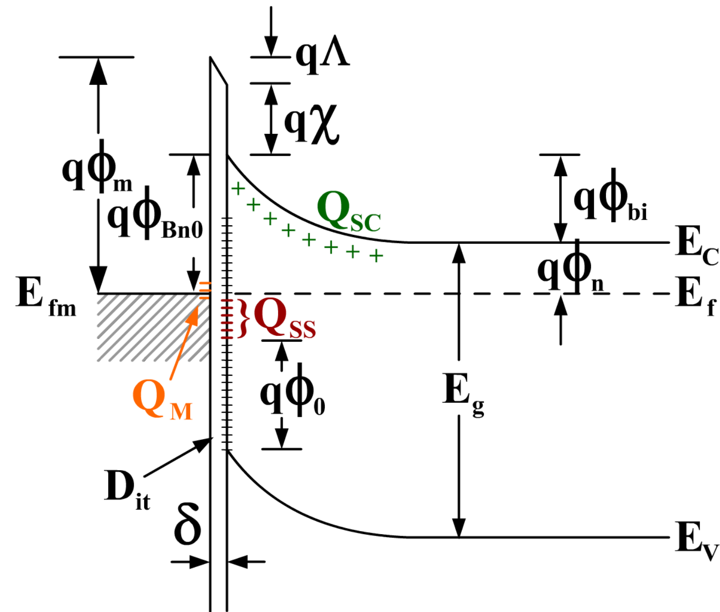

Figure 2.9.: Metal-semiconductor junction with an interfacial layer [150]. The interfacial layer is responsible at the source of surface states, and thus the Fermi pinning effect takes place.

space-charge density in semiconductor, Q_{SS} the interface-trap charge, Q_M the surface-charge density on metal, and D_{it} the interface-trap density. The density of the surface states and their distribution around the semiconductor band gap determine the energy for which the Fermi band at the interface gets "pinned" [154].

The interfacial layer theory is invalid for metal silicides, because this layer is consumed during the silicidation process and therefore the interface is almost a metal-semiconductor interface. Therefore, the interfacial layers are not the only contributor to the energy states at the metal-semiconductor interface. The metal-induced gap states (MIGS) are responsible for the influence [150, 154, 155].

Schottky Barrier Lowering

At a metal-semiconductor junction, ionized dopants, defects, and empty or filled gap states provide a charge within the semiconductor. These charges generate electric field lines which end at the metal due to an "image" charge that is generated for each charge in the semiconductor which lies within the depletion region. The image charge creates an image field which is directed opposite to the field of the energy bands, in the semiconductor near the interface. The actual potential profile of the Schottky barrier is therefore a function of the two superposed electric fields which results in a lowering of the potential at the top of the barrier [154].

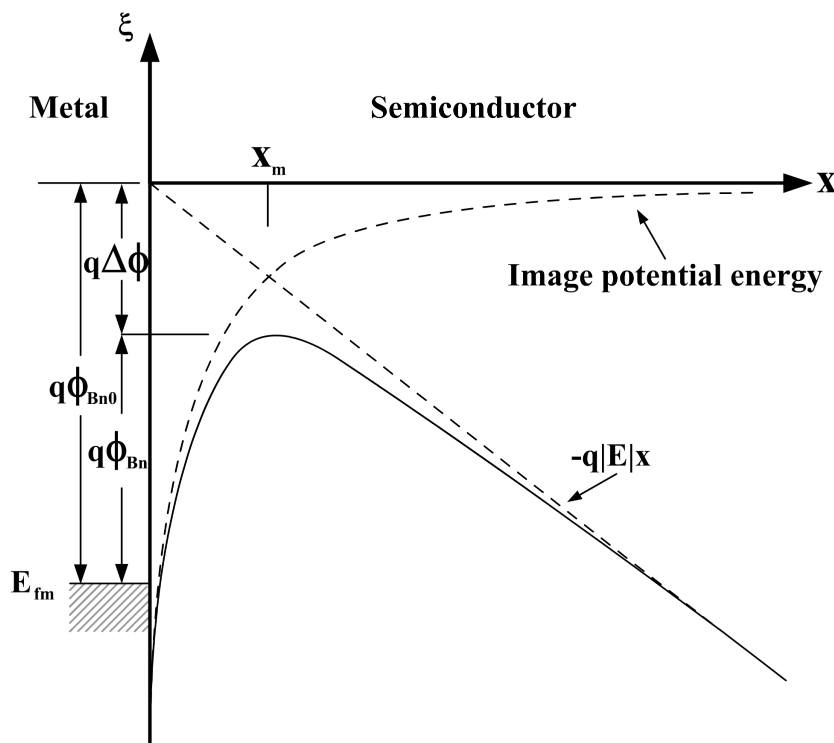

Figure 2.10.: Energy band diagram of Schottky barrier lowering between a metal surface and a semiconductor [150].

In other words, an electron that approaches the boundary surface creates a positive image (mirror) charge in the metal and will lower its potential energy due to the developed electrostatic attraction. The attractive force toward the metal, called the image force, is known as Schottky barrier lowering and is illustrated in Fig. 2.10 where x_m is the position of the peak, $\Delta\phi$ is the change in the barrier height due to Schottky barrier lowering, the "Image potential energy" is the extended electron energy from the metal surface due to the image force, and $-q|E|x$ is the extended electron energy from an ideal Schottky barrier height into the bulk region where the electric field is negative.

While the electric field at the metal-semiconductor junction increases negatively, the extent of barrier lowering increases. Furthermore, this field can also emerge from gate-induced changes in the energy band structure. The image force is calculated by [150]

$$F = \frac{-q^2}{16\pi\epsilon_0 x^2} \tag{2.20}$$

where q is the elementary charge, ϵ_0 the permittivity of free space, and x the distance to the metal. Because of the bent band edges in the space charge region, the effective electron barrier is lowered which is proportional with its field intensity [150]

$$\Delta\phi = \sqrt{\frac{qE}{4\pi\epsilon_s}} \tag{2.21}$$

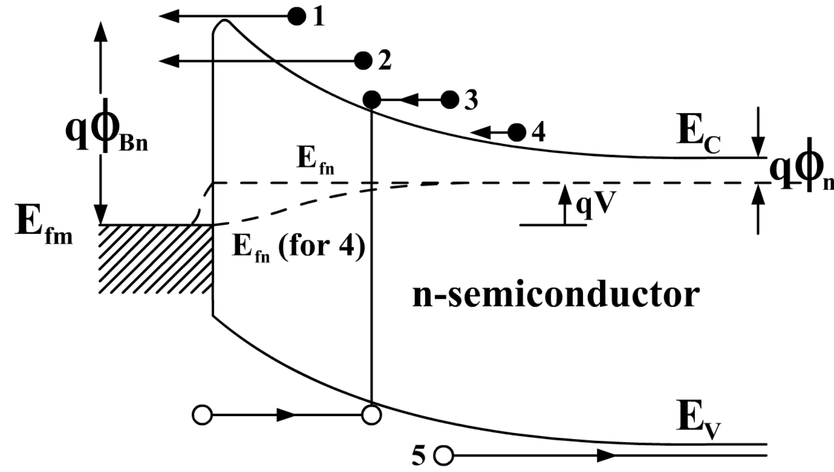

Figure 2.11.: Five basic transport processes under forward bias [150].

where ϵ_{s} is the permittivity of the semiconductor and E is the external applied electric field.

The length $\mathrm{L_D}$ of the depletion region is similar to the one-sided abrupt (e.g. $\mathrm{p^+n}$) junction [150]

$$\mathrm{L_D} = \sqrt{\frac{2\epsilon_0\epsilon_{\mathrm{si}}}{\mathrm{qN_D}}\left(\phi_{\mathrm{bi}} - \mathrm{V} - \frac{\mathrm{kT}}{\mathrm{q}}\right)} \tag{2.22}$$

where ϵ_{si} is the dielectric constant of Si, k is the Boltzmann constant, T is the Temperature in Kelvin, $\mathrm{N_D}$ is the donor impurity concentration, V is the applied voltage, and ϕ_{bi} is the built-in potential. The length of the depletion region depends on the doping concentration and the applied voltage. With increasing doping concentration, $\mathrm{L_D}$ decreases. If the doping concentration is larger than $10^{20}\,\mathrm{cm^{-3}}$, $\mathrm{L_D}$ is in the order of a few nanometers [156].

2.2.2. Current Transport Processes

The current transport in metal-semiconductor contacts is mainly defined by majority carriers, in contrast to pn-junctions where the minority carriers are responsible. Fig. 2.11 shows a Schottky diode under forward bias conditions including the relevant carrier transport mechanisms which are [150, 153]:

1. Thermionic emission: Electrons overcome the Schottky barrier and travel from the semiconductor into the metal by thermal emission.

2. Tunneling: Electrons pass through the barrier by quantum-mechanical tunneling.

3. Recombination: Electrons and holes recombine in the space-charge region.

4. Diffusion of electrons: Diffusion of electrons in the depletion region.

5. Diffusion of holes: Holes are injected from the metal into the semiconductor.

The overall current can approximately be modeled via a combination of the thermal emission current and the tunneling current assuming a high mobility and low density of defect states. In this case the other currents (3 to 5) can be neglected. In the following, the mechanisms are explained for the case of electrons.

Thermionic Emission Current

A dominant current conduction mechanism for Schottky diodes with moderately doped semiconductors (e.g. $\mathrm{N_B} < 10^{17}\,\mathrm{cm^{-3}}$) is the thermionic emission. The thermionic theory by Bethe [153] describes that only carriers with energies larger than $\mathrm{q}\phi_{\mathrm{Bn}}$ or $\mathrm{q}\phi_{\mathrm{Bp}}$ can overcome the Schottky barrier and contribute to the transport from the metal to the semiconductor or vice versa. By increasing the forward bias, the metal Fermi energy remains at the same potential. The Fermi energy of the semiconductor is shifted to higher levels due to the applied voltage. This results in a lowering of the barrier. Hence, the current from the semiconductor to the metal increases significantly. At the same time, the electron current from the metal to the semiconductor is very small due to the high and constant potential barrier between them. Similarly, under reverse bias the current from the semiconductor to the metal is decreased significantly, because the potential barrier is increased. While the electron current from the metal to the semiconductor is almost voltage independent, the total current for forward and reverse bias can be different [156]. The sum of both current contributions is given by [150, 157]

$$\begin{aligned} \mathrm{J_n} &= \left[\mathrm{A^*T^2}\exp\left(-\frac{\mathrm{q}\phi_{\mathrm{B}}}{\mathrm{kT}}\right)\right]\left[\exp\left(\frac{\mathrm{qV}}{\mathrm{kT}}\right)-1\right] \\ &= \mathrm{J_{TE}}\left[\exp\left(\frac{\mathrm{qV}}{\mathrm{kT}}\right)-1\right] \end{aligned} \tag{2.23}$$

where

$$\mathrm{J_{TE}} = \mathrm{A^*T^2}\exp\left(-\frac{\mathrm{q}\phi_{\mathrm{B}}}{\mathrm{kT}}\right). \tag{2.24}$$

ϕ_{B} denotes the barrier height, T the temperature, k the Boltzmann constant, V the applied voltage, and

$$\mathrm{A^*} \equiv \frac{4\pi \mathrm{qm^*k^2}}{h^3} \tag{2.25}$$

is called the effective Richardson constant [157] for thermionic emission with h the Planck constant, neglecting the effects of optical-phonon scattering and quantum-mechanical reflection [150]. It's a function of the effective mass $\mathrm{m^*}$ with $\frac{110\mathrm{A}}{\mathrm{cm^2K^2}}$ for electrons and

$\frac{40\mathrm{A}}{\mathrm{cm}^2\mathrm{K}^2}$ for holes. For free electrons ($\mathrm{m}^* = \mathrm{m}_0$) the Richardson constant A is $\frac{120\mathrm{A}}{\mathrm{cm}^2\mathrm{K}^2}$. Furthermore, note that, when the image-force lowering is considered, the barrier height ϕ_{Bn} is reduced by $\Delta\phi$ from equation (2.21) [150].

Diffusion Current

The diffusion theory by Schottky [9] is a further mechanism in Schottky diodes. It has been derived from the assumptions that the barrier height is much larger than kT and electron collisions within the depletion region are neglected, i.e., diffusion, is included. Furthermore, the carrier concentrations at $x = 0$ and $x = L_D$ are unaffected by the current flow and the impurity concentration is non degenerated [150].

Neglecting image-force effects the current density for the diffusion is given by [150]

$$\begin{aligned} J_n &\approx q\mu_n N_C E \exp\left(-\frac{q\phi_B}{kT}\right)\left[\exp\left(\frac{qV}{kT}\right) - 1\right] \\ &\approx J_D\left[\exp\left(\frac{qV}{kT}\right) - 1\right] \end{aligned} \tag{2.26}$$

with N_C the density of states for electrons, μ_n the mobility of the electrons, and E the electric field at the boundary. The current density expression of the diffusion theory is basically very similar to the one of the thermionic emission theory.

Thermionic Emission Diffusion Current

A synthesis of both approaches is proposed by Crowell and Sze [150,158]. The approach was derived from the boundary condition of a thermionic recombination velocity v_R near the metal-semiconductor interface [150].

In the end, the following equation was developed for the thermionic emission diffusion theory [150]

$$J_{TED} = \frac{qN_C v_R}{1 + (v_R/v_D)} \exp\left(-\frac{q\phi_B}{kT}\right)\left[\exp\left(\frac{qV}{kT}\right) - 1\right] \tag{2.27}$$

where the relative values v_R and v_D determine the relative contribution of thermionic emission versus diffusion. The parameter v_D can be approximated by $v_D \approx \mu_n E$ and v_R yields [150]

$$v_R = \sqrt{\frac{kT}{2m^*\pi}} = \frac{A^*T^2}{qN_C}. \tag{2.28}$$

It can be seen that if $v_D >> v_R$ the pre-exponential term is dominated by v_R and the thermionic emission theory applies ($J_{TED} = J_{TE}$). If $v_D << v_R$ the diffusion process is the limiting factor ($J_{TED} = J_D$) [150].

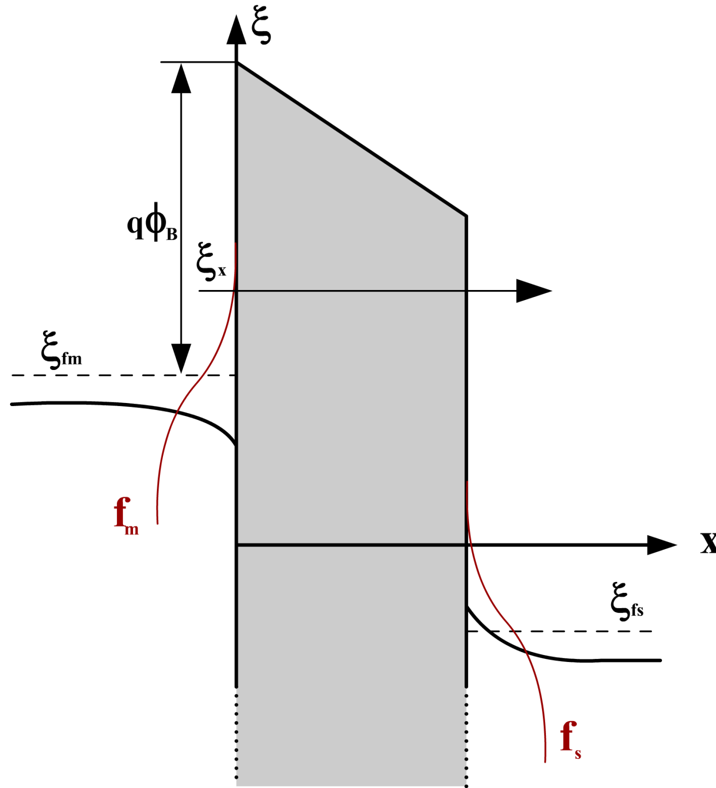

Figure 2.12.: Energy barrier with two electrodes which can be used to describe electron conduction band or hole valence band processes [126].

Also considering quantum-mechanical tunneling and reflection which are taken into account by the factor f_P and f_Q yields [150, 159]

$$J = A^{**}T^2 \exp\left(-\frac{q\phi_B}{kT}\right)\left[\exp\left(\frac{qV}{kT}\right) - 1\right] \tag{2.29}$$

where

$$A^{**} = \frac{f_P f_Q A^*}{1 + (f_P f_Q v_R / v_D)}. \tag{2.30}$$

The impact results in a reflected and reduced effective Richardson constant from A^* to A^{**} [150].

Tunneling Current

The tunneling current is also a non negligible transport process which becomes more significant for heavily doped semiconductors and ohmic contacts. However, for lower doped devices this mechanism can not be neglected [150].

The tunneling current is proportional to the quantum transmission coefficient multiplied with the occupation probability in the semiconductor and the unoccupied prob-

UNIVERSITAT ROVIRA I VIRGILI
TWO-DIMENSIONAL ANALYTICAL PREDICTIVE MODELING OF SCHOTTKY BARRIER SOI AND MULTI-GATE MOSFETS
Mike Schwarz
Dipòsit Legal: T.456-2013

ability in the metal for forward biased Schottky diodes. The behavior for reverse biased Schottky diodes is vice versa. For a forward biased Schottky diode this results in [150, 159]

$$J_{tun,s\rightarrow m} = \frac{A^*T}{k} \int_{E_{fm}}^{q\phi_{Bn}} f_s T(\xi)(1 - f_m) d\xi. \tag{2.31}$$

f_s and f_m are the Fermi-Dirac distribution functions for the semiconductor and the metal, respectively. $T(\xi)$ represents the tunneling probability which depends on the width of the barrier at a particular energy (Fig. 2.12). The net current density is the sum of both results, from metal to semiconductor and vice versa.

This expression is also known as Tsu-Esaki formula. Proposed by Duke [160], the model was used by Tsu and Esaki for the modeling of tunneling current in resonant tunneling devices [105].

Generally, in equation (2.31) the domain of integration reaches from $-\infty$ to $+\infty$. Taking into account the band gap and the distribution function for the electrons, the integration domain starts from the Fermi level of the metal E_{fm} and stops at the Schottky barrier height $q\phi_{Bn}$ at the junction.

2.3. Quantum Mechanical Tunneling Models

This section deals with the in section 2.1 discussed quantum-mechanical tunneling effects. Especially, with the transmission coefficient $T(\xi)$ from equation (2.31) which can generally be described by the Schrödinger equation. Further, the different tunneling mechanisms, such as direct-, Fowler-Nordheim, and trap-assisted tunneling can be approximated with the help of the Schrödinger equation by several models.

As explained above, the transmission coefficient can be found by Schrödinger's equation. There exist a lot of methods and models to describe the transmission coefficient although some are more or less accurate. Many of them are discussed and covered in [140]. The Wentzel-Kramers-Brillouin (WKB) approximation and Gundlach method are the most common models which are used to model the tunneling current. They have several approximations and are often referred to as semi-classical approximations. To cover the transmission through arbitrary shaped barriers, the need of advanced models is necessary, such as the transfer-matrix methods as well as the quantum transmitting boundary method (QTBM) [126].

Here, a brief overview into the existing models is given while in the thesis the Wentzel-Kramers-Brillouin (WKB) approximation due to its relative simplicity is used to receive a closed-form solution for the tunneling current.

UNIVERSITAT ROVIRA I VIRGILI
TWO-DIMENSIONAL ANALYTICAL PREDICTIVE MODELING OF SCHOTTKY BARRIER SOI AND MULTI-GATE MOSFETS
Mike Schwarz
Dipòsit Legal: T.456-2013

2.3.1. Tunneling Mechanisms

In a silicon-dielectric-silicon structure a variety of tunneling mechanisms can be observed (Fig. 2.13). Fowler-Nordheim (FN) tunneling and direct tunneling (DT) can be observed for higher energies. Trap-assisted tunneling (TAT) results in different processes at different energies. In between, electrons from the conduction band (ECB), electrons from the valence band (EVB), and holes from the valence band (HVB) might tunnel. If electrons tunnel from the valence band to the conduction band, free carriers at both sides of the dielectric are created which for MOS transistors, gives rise to increased substrate current. This mechanism is referred as the EVB process. As stated before, the TAT results in different processes. It can be elastic which means that the energy of the carrier is conserved or inelastic where the carrier loses its energy due to the emission of phonon's. Furthermore, in dielectrics with a very high defect density, hopping conduction via multiple defects may occur [126].

2.3.2. Transmission Coefficient Modeling

The transmission coefficient $\mathrm{T}(\xi)$ is defined as the ratio of the quantum-mechanical current due to an incident wave and a transmitted wave

$$\mathrm{T}(\xi) = \frac{\mathrm{k_1 m_1}}{\mathrm{k_n m_n}} \frac{|\mathrm{A_n}|^2}{|\mathrm{A_1}|^2} \tag{2.32}$$

where

$$\begin{aligned} \psi_1(\mathrm{x}) &= \mathrm{A_1} \exp(\mathrm{jk_1 x}), \\ \psi_\mathrm{n}(\mathrm{x}) &= \mathrm{A_n} \exp(\mathrm{jk_n x}). \end{aligned} \tag{2.33}$$

The wave functions' amplitudes $\mathrm{A_1}$ and $\mathrm{A_n}$ can be found by solving the Schrödinger equation by various methods, Fig. 2.14. The Wentzel-Kramers-Brillouin (WKB) approximation can be applied either analytically for a linear barrier or numerically for arbitrary barriers. Gundlach's method can be applied for a single linear energy barrier while the transfer-matrix and quantum transmitting boundary methods are used for arbitrary shaped barriers [126].

The Wentzel-Kramers-Brillouin Approximation

One of the most frequently used assumption for the quantum-mechanical wave function is the Wentzel-Kramers-Brillouin (WKB) approximation which has been implemented in several device simulators like Synopsys TCAD Sentaurus [64] or Silvaco ATLAS [63].

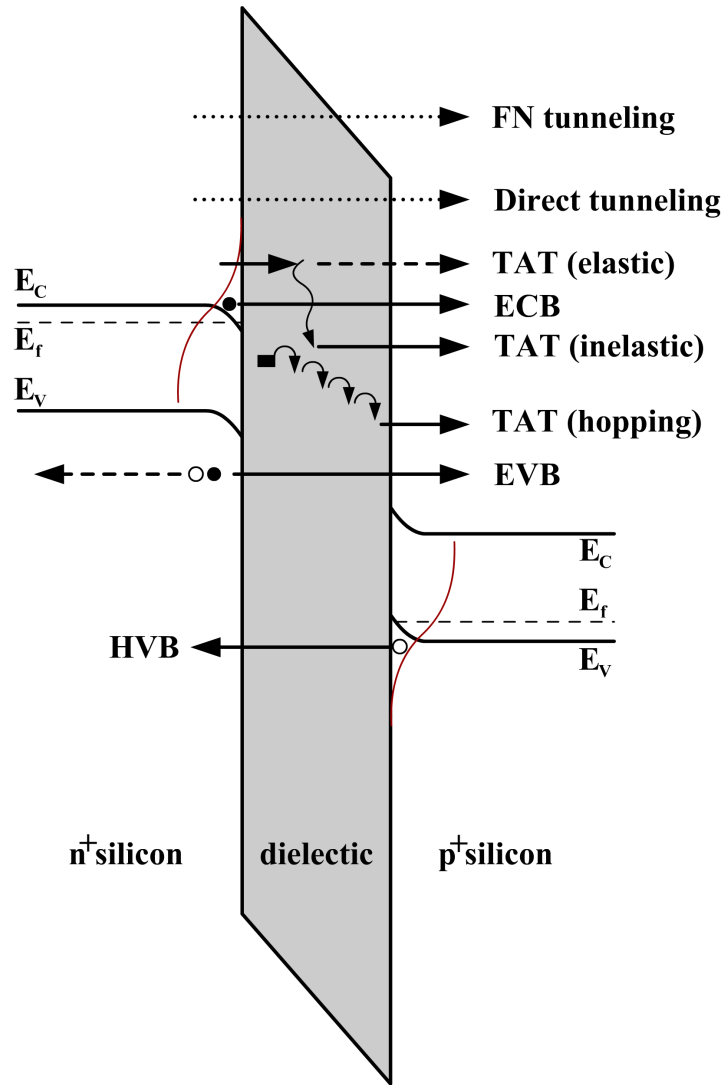

Figure 2.13.: Schematic of the tunneling processes in a silicon-dielectric-silicon structure [126].

The transmission coefficient for the Wentzel-Kramers-Brillouin (WKB) approximation is [114, 115, 116, 126, 140]

$$T(\xi) = \exp\left(-\frac{2}{\hbar}\int_{x_1}^{x_2}\sqrt{2m(V(x)-\xi)}dx\right). \tag{2.34}$$

In appendix B the Wentzel-Kramers-Brillouin (WKB) approximation is shown in detail. Integration takes place between the classical turning points x_1 and x_2 where $\xi \leq V(x)$ and (2.34) is real. Therefore, the decaying part of the wave function is considered. If the barrier is linearly shaped, an analytical solution is possible. However, a separation

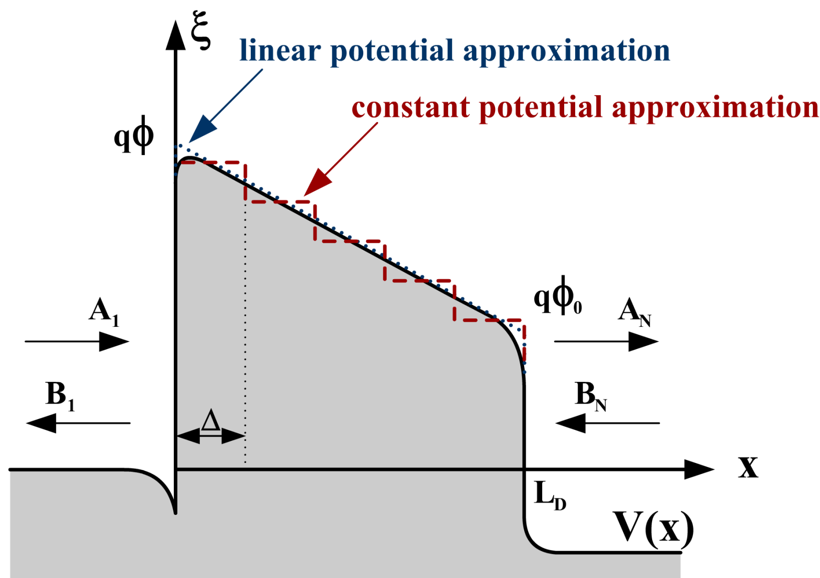

Figure 2.14.: The energy barrier of a single-layer dielectric. The potential energy V(x) may either be the conduction band or the valence band energy, depending on the tunneling process. The linear and constant potential approximations refer to the transfer-matrix method [126].

between Fowler-Nordheim tunneling and direct tunneling is necessary. In the direct tunneling regime $\xi < q\phi_0$ holds (Fig. 2.14). The transmission coefficient

$$T(\xi) = \exp\left(-\frac{2}{\hbar}\int_0^{L_D}\sqrt{2m(q\phi - qEx - \xi)}dx\right) \tag{2.35}$$

results in

$$T(\xi) = \exp\left(-4\frac{\sqrt{2L_D}}{3\hbar qE}\left((q\phi-\xi)^{3/2}\right) - (q\phi_0 - \xi)^{3/2}\right) \tag{2.36}$$

with E is the electric field, $\hbar$ is the reduced Planck constant, and m is the electron mass in the region. ϕ and ϕ_0 are the upper and lower barrier heights. ϕ_0 is calculated assuming a linear potential in the barrier

$$\phi_0 = \phi - E \cdot L_D. \tag{2.37}$$

The Fowler-Nordheim regime holds $\xi > q\phi_0$ and with x_1 defined by $q\phi - qEx_1 = \xi$ the transmission coefficient

$$T(\xi) = \exp\left(-\frac{2}{\hbar}\int_0^{x_1}\sqrt{2m(q\phi - qEx - \xi)}dx\right) \tag{2.38}$$

results in

$$T(\xi) = \exp\left(-4\frac{\sqrt{2m}}{3\hbar qE}\left((q\phi-\xi)^{3/2}\right)\right). \tag{2.39}$$

UNIVERSITAT ROVIRA I VIRGILI
TWO-DIMENSIONAL ANALYTICAL PREDICTIVE MODELING OF SCHOTTKY BARRIER SOI AND MULTI-GATE MOSFETS
Mike Schwarz
Dipòsit Legal: T.456-2013

The Gundlach Method

The Gundlach Method [107, 126, 140] is able to solve Schrödinger's equation analytically for linear barriers. Schrödinger's equation evolves into Airy differential equation

$$\frac{\partial^2}{\partial \mathrm{u}^2}\psi(\mathrm{u}(\mathrm{x})) - (\mathrm{u}(\mathrm{x}))\psi(\mathrm{u}(\mathrm{x})) = 0. \tag{2.40}$$

The solutions of this differential equation are the Airy functions $\mathrm{Ai}(\mathrm{u}(\mathrm{x}))$ and $\mathrm{Bi}(\mathrm{u}(\mathrm{x}))$. The wave functions consists of linear superposition's of the Airy functions [126]

$$\psi(\mathrm{x}) = \mathrm{A}\mathrm{Ai}(\mathrm{u}(\mathrm{x})) + \mathrm{B}\mathrm{Bi}(\mathrm{u}(\mathrm{x})) \tag{2.41}$$

where the function $\mathrm{u}(\mathrm{x})$ is given as

$$\mathrm{u}(\mathrm{x}) = -\left(\frac{2\mathrm{m}}{\hbar^2}\right)^{1/3}\left(\frac{\mathrm{x}_1 - \mathrm{x}_0}{\mathrm{V}_1 - \mathrm{V}_0}\right)^{2/3}(\xi - \mathrm{V}(\mathrm{x})) \tag{2.42}$$

with $\mathrm{V}_1 = \mathrm{V}(\mathrm{x}_1)$ and $\mathrm{V}_0 = \mathrm{V}(\mathrm{x}_0)$. Assuming constant electron mass, Gundlach derives an expression for the transmission coefficient

$$\mathrm{T}(\xi) = \frac{\mathrm{k_n}}{\mathrm{k}_1}\frac{4}{\pi^2}\left(\left(\frac{\mathrm{z}'}{\mathrm{k}_1}\mathrm{A} + \frac{\mathrm{k_n}}{\mathrm{z}'}\mathrm{B}\right)^2 + \left(\frac{\mathrm{k_n}}{\mathrm{k}_1}\mathrm{C} + \mathrm{D}\right)^2\right)^{-1} \tag{2.43}$$

where

$$\begin{aligned}
\mathrm{A} &= \mathrm{Ai}'(\mathrm{z}_0)\,\mathrm{Bi}'(\mathrm{z_s}) - \mathrm{Ai}'(\mathrm{z_s})\,\mathrm{Bi}'(\mathrm{z}_0),\\
\mathrm{B} &= \mathrm{Ai}(\mathrm{z}_0)\,\mathrm{Bi}(\mathrm{z_s}) - \mathrm{Ai}(\mathrm{z_s})\,\mathrm{Bi}(\mathrm{z}_0),\\
\mathrm{C} &= \mathrm{Ai}(\mathrm{z_s})\,\mathrm{Bi}'(\mathrm{z}_0) - \mathrm{Ai}'(\mathrm{z}_0)\,\mathrm{Bi}(\mathrm{z_s}),\\
\mathrm{D} &= \mathrm{Ai}(\mathrm{z}_0)\,\mathrm{Bi}'(\mathrm{z_s}) - \mathrm{Ai}'(\mathrm{z_s})\,\mathrm{Bi}(\mathrm{z}_0)
\end{aligned} \tag{2.44}$$

with z_0, $\mathrm{z_s}$ and z' are

$$\begin{aligned}
\mathrm{z}_0 &= (\mathrm{q}\phi_0 - \xi)\left(\frac{\frac{2}{\hbar}\sqrt{2\mathrm{m}}\mathrm{L_D}}{2\mathrm{q}(\phi - \phi_0)}\right)^{2/3},\\
\mathrm{z_s} &= (\mathrm{q}\phi - \xi)\left(\frac{\frac{2}{\hbar}\sqrt{2\mathrm{m}}\mathrm{L_D}}{2\mathrm{q}(\phi - \phi_0)}\right)^{2/3},\\
\mathrm{z}' &= -\left(\frac{\left(\frac{2}{\hbar}\sqrt{2\mathrm{m}}\right)^2}{4}\frac{\mathrm{q}\phi - \mathrm{q}\phi_0}{\mathrm{L_D}}\right)^{1/3}.
\end{aligned} \tag{2.45}$$

UNIVERSITAT ROVIRA I VIRGILI
TWO-DIMENSIONAL ANALYTICAL PREDICTIVE MODELING OF SCHOTTKY BARRIER SOI AND MULTI-GATE MOSFETS
Mike Schwarz
Dipòsit Legal: T.456-2013

The Transfer-Matrix Method

The transfer-matrix (TM) is based on the work of Tsu and Esaki [105]. It is an approximation of an arbitrary barrier by a series of piecewise linear functions. Since the wave function in such barriers can be easily calculated, the total transfer-matrix can be calculated by a number of several matrix computations [126].

The transfer-matrix is divided into two parts, namely the piecewise constant potential and piecewise linear potential. Simulations using the transfer-matrix method were reported by several authors [161, 162] which compared the constant and linear approaches and recommended the constant potential method for device simulators [126]. Of course the accuracy of the linear potential approach is improved compared to the constant approach and a further advantage is that the linear potential approach accuracy does not depend on the resolution.

Quantum Transmitting Boundary Method

Alternatively, Schrödinger's equation can be solved by quantum transmitting boundary method (QTBM) which has been proposed by Frensley and Einspruch [163]. The method is based on the finite-difference approximation of the stationary one-dimensional Schrödinger equation on an equidistant grid [126]. Due to further relations and approximations, unknown values are eliminated and result in a fast and more robust method compared to the transfer-matrix method. A further advantage is the possibility of a two- or three dimensional extension while the transfer-matrix method is limited to one-dimensional problems [126].

Comparison

The analytical WKB approximation and Gundlach methods deliver similar results for the triangular barrier [126]. Both methods are limited and only can be used for single-layer junctions, like the gate-to-insulator junction in conventional MOSFET devices. If multiple stacked dielectrics are investigated, both methods are useless. The numerical WKB approximation, transfer-matrix, and QTBM methods deliver similar results while the WKB approximation method does not take into account oscillations in the transmission coefficient [126].

In this thesis the analytically method of the WKB approximation for triangular barriers is applied. Due to the modeling of the tunneling between the metal-semiconductor junctions at source and drain and the aim to receive a compact model for the tunneling current, the WKB approximation is sufficient enough to describe the tunneling mechanism. Furthermore, robustness and a fast solution are desired and recommended for an implementation in circuit simulation software.

2.4. Operation Principle of Schottky Barrier MOSFETs

In principle the operation behavior between the different device structures of Schottky barrier Single-Gate MOSFETs, Double-Gate and Multi-Gate MOSFETs is similar. The main difference between the various structures is the reduction of the short-channel effects [41]. As shown in literature, simulations and measurements show that the leakage current in Single-Gate MOSFET devices is increasing while the gate length is reduced. This effect is related to the reduced gate surface and the resulting reduced electric field which controls the channel underneath the insulating oxide. Further, the drain takes influence and weakens the gate control of the channel [41]. Therefore, new device types like Double-Gate or Multi-Gate MOSFETs are introduced to increase the channel control and reduce the short-channel effects [72, 150].

Schottky barrier Single-Gate MOSFETs, Double-Gate and Multi-Gate MOSFETs with metallic source/drain regions are biased with two Schottky diodes in reverse mode which inhibit current flow, as opposed to pn-diodes in conventional Single-Gate MOSFETs, Double-Gate and Multi-Gate MOSFETs. Applying a gate voltage, a band bending takes place at the semiconductor-gate interface while the source/drain Schottky barriers are modified. Therefore, the source to drain current is controlled by the gate terminals. Schottky barrier Single-Gate MOSFETs, Double-Gate and Multi-Gate MOSFETs are ambipolar, this means that two I-V characteristics are achievable with a single device. In the following the operation principle is described with the help of a Schottky barrier Double-Gate structure.

The basics of the energy-band diagram operating principles of a Schottky barrier Double-Gate MOSFET are shown in Fig. 2.15. The device structure is given at the top and the Schottky contacts are shown as red source/drain contacts. The orange line in the schematic drafts is the profile cut in the y-direction. The silicon channel is assumed undoped for simplification. Without external voltage the energy band is in thermal equilibrium and is constant throughout the channel, Fig. 2.15(a).

Decreasing the applied gate potential $\mathrm{V_g}$ the conduction and valence bands are raised up as shown in Fig. 2.15(b) and hole (majority carriers in this case) accumulate at the semiconductor-gate interface. This increases the degree of the band bending at the source and drain junctions while the barrier width decreases at each junction. If the barrier width is becoming smaller, the tunneling probability for the accumulated carriers increases. In accumulation mode and for relatively large Schottky barrier heights to holes (ϕ_{Bp}), tunneling current is the dominant current component.

By increasing the applied gate voltage $\mathrm{V_g}$ the conduction and valence bands are dropped down as shown in Fig. 2.15(c). In depletion mode a n-channel is formed at the semiconductor-gate interface. If the hole barrier height is large, then the inver-

sion mode electron barrier height (ϕ_{Bn}) is relatively small and thermionic emission of electrons over the Schottky barrier becomes the dominant current process.

The influence of applied drain-source potential V_{ds} forces electrons to pass the Schottky barrier by thermionic emission, if their energy is high enough to overcome the barrier. If the Schottky barrier width at the source contact is thin enough, the electrons are able to tunnel into the channel region. When the influence of V_{ds} reaches the point as shown in Fig. 2.15(d) an ambipolar behavior of the device is possible. This means that at the drain contact, the barrier width becomes thin enough that holes are able to pass the barrier by quantum mechanical tunneling. The current behavior of the device is different to a conventional Double-Gate MOSFET, the device exhibits an ambipolar behavior. This ambipolar behavior leads to a significant difference in the electrical performance compared to conventional Double-Gate MOSFETs.

Leakage, Drain-Induced Barrier Lowering (DIBL) and Drain-Induced Barrier Thinning (DIBT)

Considering gate leakage and defect/trap-induced leakage, the leakage process within a Schottky barrier Double-Gate MOSFET is different from that in a conventional MOSFET due to the existing Schottky diodes.

In a conventional MOSFET leakage results from generation current in the reverse biased diode. A further leakage process, especially in short-channel devices, results from drain-induced barrier lowering (DIBL) where the electric field from the drain decreases the thermal barrier height. Further leakage can be induced by gate-to-drain coupling at large drain voltages and a relatively low gate voltage where the magnitude of the surface near the drain is large enough to induce band-to-band tunneling. Such leakage is called gate-induced drain leakage (GIDL) [154].

Besides, the effects due to leakage and DIBL another phenomena is the so-called drain-induced barrier thinning (DIBT). Within shorter channel devices, the potential distribution along the channel is strongly affected by the source and drain. The depletion regions of the drain penetrate deeply into the channel region as V_{ds} increases and influence the control of the channel charge by the gate. In this case a Schottky barrier Double-Gate MOSFET device exhibits a larger subthreshold slope (SSlope). During the on-state, the drain voltage increases and a high electric field penetrates the channel, the Schottky barrier width is thinned, leading to an increased tunneling current.

For long-channel devices the drain bias has little effect on the Schottky barrier width. However, in a short-channel device the Schottky barrier width is strongly affected by V_{ds}.

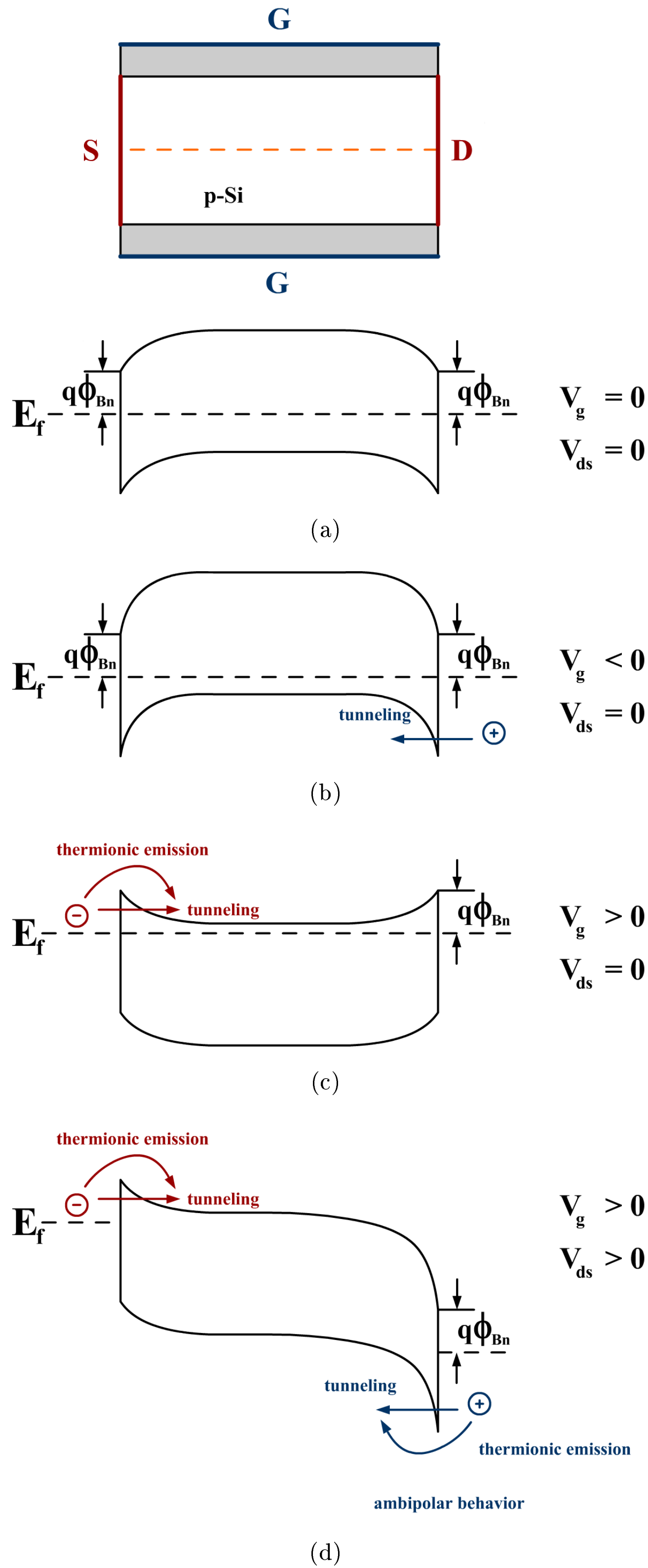

Figure 2.15.: Schematic energy-band diagram to demonstrate the operating principle of n-channel SB-DG-MOSFET.

Chapter 3.

Mathematical Basics

Generally, by the downscaling of the MOSFET structure or geometry the influence of multi-dimensional effects increase. These effects are caused by the inhomogeneous electric field within the device. The electrical field lines are more-dimensional. Modeling these effects and taking as many of them as possible into account it is necessary to calculate the electrostatic potential distribution within a MOSFET solving Poisson's equation. Furthermore, to obtain closed-from explicit equations the complex potential theory is used to solve the partial differential equations. In this chapter some methods to calculate the electrostatics with aid of the conformal mapping technique and its mathematical description are explained.

3.1. Poisson's and Laplace's Equation

The Poisson equation is a partial differential equation in electrostatics, mechanical engineering and theoretical physics. As part of boundary value problems Poisson's equation finds itself in many parts of physical applications and is part of Maxwell's equations which relate the charge density ρ along a gradient r to the electric field $\vec{\mathrm{E}}$

$$\nabla \cdot \vec{\mathrm{E}}(\mathrm{r}) = \frac{\rho(\mathrm{r})}{\epsilon} \tag{3.1}$$

where ϵ is the permittivity of the medium and is material dependent [137]. Thus for the inhomogeneous Poisson equation of the electrical field

$$-\nabla\vec{\mathrm{E}}(\mathrm{r}) = \Delta\Phi(\mathrm{r}) = -\frac{\rho(\mathrm{r})}{\epsilon_0\epsilon_{\mathrm{Si}}} \tag{3.2}$$

where the potential Φ and the charge ρ are three-dimensionally dependent. This circumstance is described by the Laplace operator Δ

$$\Delta = \frac{\partial^2}{\partial \mathrm{x}^2} + \frac{\partial^2}{\partial \mathrm{y}^2} + \frac{\partial^2}{\partial \mathrm{z}^2} \tag{3.3}$$

and results in

$$\Delta\Phi(\mathrm{x},\mathrm{y},\mathrm{z}) = -\frac{\rho(\mathrm{x},\mathrm{y},\mathrm{z})}{\epsilon}. \tag{3.4}$$

UNIVERSITAT ROVIRA I VIRGILI
TWO-DIMENSIONAL ANALYTICAL PREDICTIVE MODELING OF SCHOTTKY BARRIER SOI AND MULTI-GATE MOSFETS
Mike Schwarz
Dipòsit Legal: T.456-2013

If there is no charge $\rho(\mathrm{x,y,z}) = 0$, a homogeneous Laplace equation is obtained [137]

$$\Delta\Phi(\mathrm{x,y,z}) = 0. \tag{3.5}$$

Laplace's equation is a special case of Poisson's equation where solutions of the Laplacian are called harmonic functions. Harmonic functions fulfill the Laplace equation, if they are differentiable twice. Furthermore, the properties of harmonic functions help to solve potential problems with the complex potential theory. Harmonic functions hold the principle of superposition. A function Φ is unique which satisfies Laplace's equation, in an enclosed volume and satisfies one of the generally occurring boundary conditions on the enclosing boundary. Finally, Φ satisfies Laplace's equation by a surface bounded region, neither a maximum nor a minimum within the region can be attained. Extreme values can only occur at the surface [137].

The general boundary conditions are Dirichlet condition (value of the function is specified on the entire boundary), Neumann condition (value of the normal derivative, $\mathrm{n}\cdot\nabla\Phi$ is specified on the entire boundary) and mixed conditions of Dirichlet and Neumann (Φ is specified on part of the boundary and $\mathrm{n}\cdot\nabla\Phi$ on the rest) [137].

The electrostatics modeled in the thesis lead to a boundary value problem for Laplace's equation in two dimensions. One method to solve Laplace's equation in two dimensions is via the conformal mapping method which is valid for the transformation of a 2D system from one geometry to another. Therefore, the problem has to be 2D and the boundary conditions can only contain two variables. For the solution of these two-dimensional potential problems the complex potential theory constitutes itself which permits a compact description of the potential and field [137, 164].

3.2. Complex Potential Theory

If each complex value accept the variable z is assigned as value of a variable w with $\mathrm{w} = \mathrm{P(z)} = \mathrm{u(x,y)} + \mathrm{jv(x,y)}$ with $\mathrm{z} = \mathrm{x} + \mathrm{jy}$, then w is called a complex function of the complex variable z. A complex function maps all values within a region R of the z-plane to the values within a region R^* of the w-plane. P is regular, if R equals the definition set D(P) and partial derivatives are continuously to D(P) and the CauchyRiemann differential equations are valid [137, 165].

3.2.1. Differentiation

Assuming functions of complex variables as

$$\mathrm{w} = \mathrm{f(z)} = \mathrm{u(x,y)} + \mathrm{jv(x,y)}. \tag{3.6}$$

UNIVERSITAT ROVIRA I VIRGILI
TWO-DIMENSIONAL ANALYTICAL PREDICTIVE MODELING OF SCHOTTKY BARRIER SOI AND MULTI-GATE MOSFETS
Mike Schwarz
Dipòsit Legal: T.456-2013

The real and imaginary part are real functions from x and y. If z is changed continuously then the points z form a curve C_1 in the z-plane. In the w-plane w changes accordingly and it emerges a curve C_2. The allocation of C_1 and C_2 is unique, the change of w, e.g. Δw, must be uniquely assigned by a change Δz; generally this case is not given.

Building the derivative [137, 165]

$$\frac{df(z)}{dz} = \lim_{\Delta z \to 0} \frac{f(z_0 - \Delta z) - f(z_0)}{\Delta z} =$$

$$\lim_{\Delta x, \Delta y \to 0} \frac{u(x+\Delta x, y+\Delta y) - u(x,y)}{\Delta x + j\Delta y} + j\frac{v(x+\Delta x, y+\Delta y) - v(x,y)}{\Delta x + j\Delta y} =$$

$$\lim_{\Delta x, \Delta y \to 0} \frac{u(x,y) + \frac{\partial u}{\partial x}\Delta x + \frac{\partial u}{\partial y}\Delta y - u(x,y)}{\Delta x + j\Delta y} + j\frac{v(x,y) + \frac{\partial v}{\partial x}\Delta x + \frac{\partial v}{\partial y}\Delta y - v(x,y)}{\Delta x + j\Delta y} =$$

$$\lim_{\Delta x, \Delta y \to 0} \frac{(\frac{\partial u}{\partial x} + j\frac{\partial v}{\partial x})\Delta x + (-j\frac{\partial u}{\partial y} + \frac{\partial v}{\partial y})j\Delta y}{\Delta x + j\Delta y}, \tag{3.7}$$

it is only unique, if it is independent from the direction of Δz. Set $\Delta y = \alpha \Delta x$ then α identifies the direction of Δz. Insert in equation (3.7) results in the derivative

$$\frac{df(z)}{dz} = \lim_{\Delta x \to 0} \frac{(\frac{\partial u}{\partial x} + j\frac{\partial v}{\partial x}) + (-j\frac{\partial u}{\partial y} + \frac{\partial v}{\partial y})j\alpha}{1 + j\alpha},$$

which is only independent from α, if both bracketed terms within the numerator equal [166]

$$\frac{\partial u}{\partial x} + j\frac{\partial v}{\partial x} = -j\frac{\partial u}{\partial y} + \frac{\partial v}{\partial y}$$

or

$$\frac{\partial u}{\partial x} = \frac{\partial v}{\partial y}, \; \frac{\partial u}{\partial y} = -\frac{\partial v}{\partial x}. \tag{3.8}$$

These are the Cauchy–Riemann differential equations [167]. They are necessary and sufficient conditions for any complex function f(z) to be analytic at a point P(x, y) [137]. The function f(z) is called analytic or regular in a region where the Cauchy–Riemann conditions are valid. However, if the derivative is $df(z)/dz = 0$ or ∞ at so-called singularities, then f(z) is not analytic in these points. If f(z) is analytic, both real part u and imaginary part v fulfill Laplace's equation [137, 165]. If equation (3.8) is differentiated partially to x and y

$$\frac{\partial^2 u}{\partial x^2} = \frac{\partial^2 v}{\partial x \partial y}, \; \frac{\partial^2 u}{\partial y^2} = -\frac{\partial^2 v}{\partial x \partial y}$$

and the mixed derivatives are eliminated, it yields

$$\frac{\partial^2 u}{\partial x^2} + \frac{\partial^2 u}{\partial y^2} = 0 \tag{3.9}$$

and

$$\frac{\partial^2 \mathrm{v}}{\partial \mathrm{x}^2}+\frac{\partial^2 \mathrm{v}}{\partial \mathrm{y}^2}=0. \tag{3.10}$$

Both u and v can represent potentials of two-dimensionally electrostatic problems. If one of the two functions is the potential function, then the other function is the electric flow. The field follows from the complex of the function f(z), equation (3.6). The functions u and v are harmonic functions, because they archive the two-dimensional Laplace equation, as already mentioned before [137, 165].

3.2.2. Integration

It is desirable to assure integrability of the analytic function f(z) in the complex plane [137]. With equation (3.6) follows

$$\int \mathrm{f(z)dz}=\int(\mathrm{u}+\mathrm{jv})(\mathrm{dx}+\mathrm{jdy})=\int(\mathrm{udx}-\mathrm{vdy})+\mathrm{j}\int(\mathrm{udy}+\mathrm{vdx}). \tag{3.11}$$

For a closed regular path with no cross overs or discontinuities in the real z-plane, each of the line integrals can be transformed into a surface integral of the partial derivatives of u and v

$$\begin{aligned}\int(\mathrm{udx}-\mathrm{vdy}) &= -\int\int\left(\frac{\partial \mathrm{u}}{\partial \mathrm{y}}+\frac{\partial \mathrm{v}}{\partial \mathrm{x}}\right)\mathrm{dxdy}\\ \int(\mathrm{udy}+\mathrm{vdx}) &= +\int\int\left(\frac{\partial \mathrm{u}}{\partial \mathrm{x}}+\frac{\partial \mathrm{v}}{\partial \mathrm{y}}\right)\mathrm{dxdy}.\end{aligned} \tag{3.12}$$

However, for the analytic function, the Cauchy-Riemann equations (3.8) make the integrands on the right-hand side vanish at every regular point. Hence, any closed regular path within a regular region yields [137, 165]

$$\oint \mathrm{f(z)dz}=0. \tag{3.13}$$

Due to this circumstance the integral over any open path in a regular region cannot depend on the path itself, only on the end points (Cauchy's integral theorem). The integral will be an analytic function itself or either one of the limits, since its derivative is f(z) which has been assumed to be analytic. It follows that for analytic functions derivatives of any order exist and that they are all analytic functions [137, 165].

3.2.3. Complex Potential Theory of Electrostatics

In the complex potential theory of electrostatics the real part of the complex harmonic function P(z) is specified as electric potential $\Phi(\mathrm{x},\mathrm{y})$. The vector field of the electric field strength follows as a gradient in the real z-plane

$$\vec{\mathrm{E}}=\vec{\mathrm{e}}_{\mathrm{x}}\mathrm{E}_{\mathrm{x}}+\vec{\mathrm{e}}_{\mathrm{y}}\mathrm{E}_{\mathrm{y}} \tag{3.14}$$

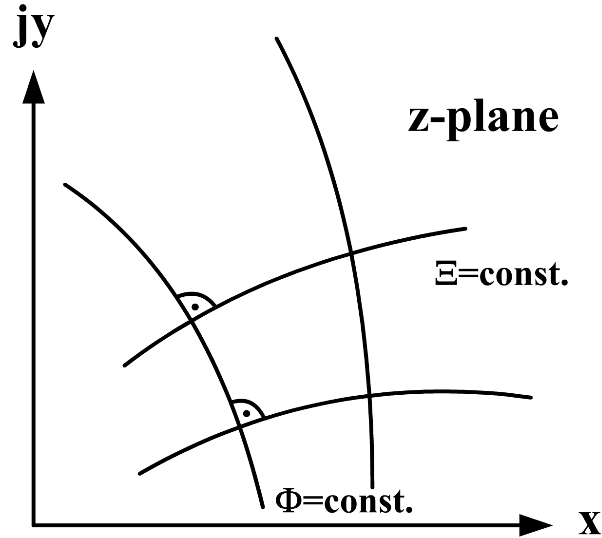

Figure 3.1.: Curves of a complex potential function $P(z) = \Phi(x, y) + j\Xi(x, y)$ in the z-plane for constant real part Φ and imaginary part Ξ, respectively.

with

$$E_x = -\frac{\partial u}{\partial x} \quad E_y = -\frac{\partial v}{\partial y} \tag{3.15}$$

follows the complex expression of equations (3.8) and (3.15)

$$E = E_x + jE_y = -\frac{\partial u}{\partial x} + j\frac{\partial v}{\partial x} = -\overline{\left(\frac{dP}{dz}\right)}. \tag{3.16}$$

The dielectric flow between two points 1 and 2 is calculated with the complex potential theory

$$\int_1^2 (D_x dy - D_y dx) = \epsilon(\Xi_1 - \Xi_2) \tag{3.17}$$

where D_x and D_y describe the components of the dielectric flow.

The potential function $\Phi(x, y)$ is identified with the real part $u(x, y)$ of the complex function $w(z)$. To find the potential solution Φ a complex potential solution can be constructed as

$$P = \Phi(x, y) + j\Xi(x, y). \tag{3.18}$$

It's called a complex potential function, whereby the curve family $\Phi(x, y) = \text{const.}$ represents the equipotential lines while the curve family $\Xi(x, y) = \text{const.}$ describes the field line in Fig. 3.1.

3.3. Conformal Mapping

The conformal mapping technique is a transformation that preserves local angles. Analytic functions are conformal at any point where they have a non-zero derivative. Due to this circumstance any conformal mapping of a complex variable which has continuous partial derivatives, is analytic and holomorphic.

3.3.1. Transformation of a Potential

A function $z = f(w) = x(u,v) + jy(u,v)$, is regular with $w = u + jv$ and $f'(w) \neq 0$ is valid for every D(f), then the function is called conformal and the angles of intersection of the curves in the complex w-plane are invariant in size and direction of rotation.

If a complex potential function according to equation (3.18) is accomplished with the help of bi-unique conformal mapping a coordinate transformation of the z-plane into w-plane, the function

$$\widetilde{P} = \widetilde{\Phi}(u,v) + j\widetilde{\Xi}(u,v) \tag{3.19}$$

is obtained. In each regular point the Laplace differential equation is invariant with respect to bi-unique conformal mapping. Therefore, $\widetilde{\Phi}(u,v)$ and $\widetilde{\Xi}(u,v)$ are harmonic functions and solutions of a scalar potential problem. The absolute value of the field strength is scaled by the geometry ratio in every point

$$|E|_{(z)} = |E|_{(w)} \left| \frac{dw}{dz} \right|. \tag{3.20}$$

In case of Poisson's equation with the space charge $\rho(z) \neq 0$ a scaling factor is needed due to [137]

$$\rho(w) = \frac{\rho(z)}{\left|\frac{dw}{dz}\right|^2}. \tag{3.21}$$

3.3.2. Points of Non-conformality of Mapping

As described in section 3.2, conformality is maintained only at regular points of the mapping function f(z) at which its derivative does not vanish $df(z)/dz \neq 0$, otherwise these points are singularities and f(z) is not analytic in these very points [137, 165].

If one assumes f(z) to be analytic in every point of a region R of the z-plane around a point z_0, then $f(z)/(z - z_0)$ will also be analytic in these points even very close to $z = z_0$, except directly at $z = z_0$ where the derivative does not exist; one might exclude this point z_0 by a small circle $\overline{C}$, Fig. 3.2 [137, 165].

The integral of $f(\overline{z})$ over any closed curve Γ around z_0 and with points $\overline{z}$ residing within R vanishes due to Cauchy's integral theorem (3.13). Now the integral of $f(\overline{z})/(\overline{z} - z_0)$ over

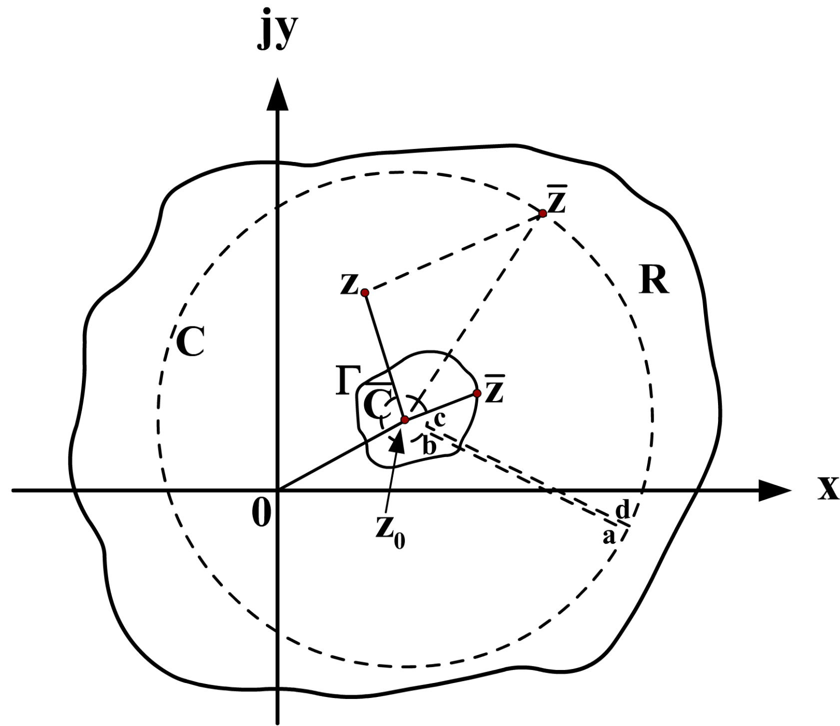

Figure 3.2.: Series expansion of analytic functions [137].

the same closed curve Γ will not vanish, but due to equation (3.13) it can be contracted into the small circle $\overline{\mathrm{C}}$ along which can be parametrized as

$$\begin{aligned}(\overline{\mathrm{z}} - \mathrm{z}_0) &= \mathrm{r}\exp(\mathrm{j}\varsigma),\\ \mathrm{d}\overline{\mathrm{z}} &= \mathrm{jr}\exp(\mathrm{j}\varsigma)\mathrm{d}\varsigma,\\ \overline{\mathrm{z}} &= \mathrm{z}_0 + \mathrm{r}\exp(\mathrm{j}\varsigma).\end{aligned} \tag{3.22}$$

This gives

$$\int_{\overline{\mathrm{C}}} \frac{\mathrm{f}(\overline{\mathrm{z}})\mathrm{d}\overline{\mathrm{z}}}{\overline{\mathrm{z}} - \mathrm{z}_0} = \mathrm{j}\int_{\varsigma=0}^{2\pi} \mathrm{f}(\mathrm{z}_0 + \mathrm{r}\exp(\mathrm{j}\varsigma)\mathrm{d}\varsigma \approx 2\pi\mathrm{j}\mathrm{f}(\mathrm{z}_0) \tag{3.23}$$

where r can be made very small that $\mathrm{f}(\overline{\mathrm{z}}) \to \mathrm{f}(\mathrm{z}_0)$. Relation (3.23) leads to Cauchy's integral

$$\mathrm{f}(\mathrm{z}_0) = \frac{1}{2\pi\mathrm{j}} \oint \frac{\mathrm{f}(\overline{\mathrm{z}})\mathrm{d}\overline{\mathrm{z}}}{\overline{\mathrm{z}} - \mathrm{z}_0}, \tag{3.24}$$

which states that the value of an analytic function at any point z_0 in a regular region R can always be expressed in terms of the known values along a regular closed curve within R surrounding that point [137, 165].

However, several mechanisms in the complex function theory exist to handle and identify singularities or isolated points, e.g. Taylor series expansion, Laurent series and Residuum. The aim of the conformal mapping is that within a finite regular region

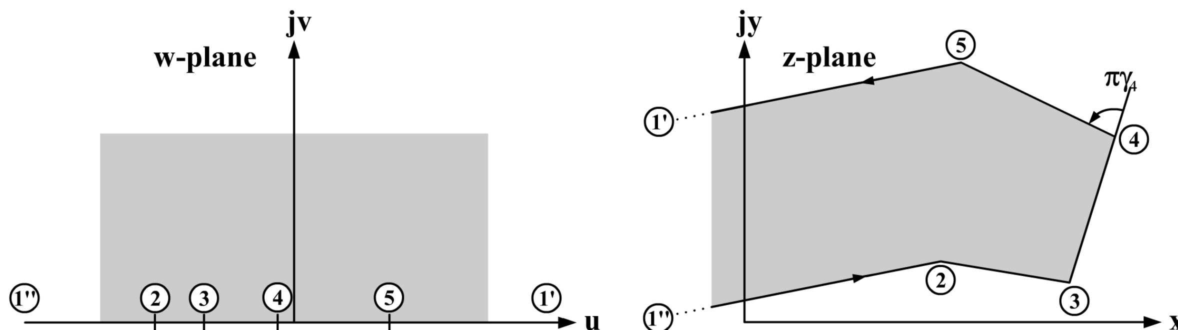

Figure 3.3.: Schwarz-Christoffel transformation allows the construction of a function which maps the inner region of a polygon in the z-plane upon the upper half plane of a w-plane.

isolated points or singularities can be excluded during integration by extremely small circles around each of them, and therefore a non-vanishing solution of the integration results [137, 165].

3.3.3. Mapping of the Inside of Closed Polygons

If the delimitation of the area in the z-plane corresponds to a polygon, in which a potential solution is going to be revealed, the Schwarz-Christoffel transformation [137] maps the problem upon the upper half plane of a w-plane (Fig. 3.3). The delimitations of the region thereby coincides with the real axis.

The Schwarz-Christoffel transformation allows the calculation of the bi-unique function $\mathrm{z = f(w)}$ which maps the upper w-half plane bi-uniquely and conformally into the considered area in the z-plane. The differential dz/dw of this function is calculated by [137, 165]

$$\frac{\mathrm{dz}}{\mathrm{dw}} = \mathrm{C}(\mathrm{w}-\mathrm{w}_1)^{-\gamma_1}(\mathrm{w}-\mathrm{w}_2)^{-\gamma_2}...(\mathrm{w}-\mathrm{w}_\nu)^{-\gamma_\nu} = \mathrm{C}\prod_{(\alpha)}(\mathrm{w}-\mathrm{w}_\alpha)^{-\gamma_\alpha}. \tag{3.25}$$

The vertices of the polygon are given by $\mathrm{z}_\alpha = \mathrm{f}(\mathrm{w}_\alpha)$ and $\pi\gamma_\alpha$ corresponds to the respective angle change of the polygon and is measured with the closed region lying to the left. The point in the z-plane which results from the mapping of the point $\mathrm{w} = \pm\infty$, is not considered. The investigated conformal mapping is received by integration of

$$\mathrm{f(w)} = \mathrm{C}\int\prod_{(\alpha)}(\mathrm{w}-\mathrm{w}_\alpha)^{-\gamma_\alpha}\mathrm{dw} + \mathrm{D} \tag{3.26}$$

where the constant D represents the origin of the z-plane. For calculation of the remaining parameters of the conformal mapping additional relations given by the geometry in

UNIVERSITAT ROVIRA I VIRGILI
TWO-DIMENSIONAL ANALYTICAL PREDICTIVE MODELING OF SCHOTTKY BARRIER SOI AND MULTI-GATE MOSFETS
Mike Schwarz
Dipòsit Legal: T.456-2013

the z-plane have to be taken into account. If $\gamma_\nu = +1$, then $z_\nu = \infty$ results and the corresponding lines of the polygons are parallel. The distance of the parallel lines are given by

$$z''_\nu - z'_\nu = -j\pi C \prod_{(\alpha \neq \nu)} (w - w_\alpha)^{-\gamma_\alpha}. \tag{3.27}$$

Additionally, if $w_\nu = \pm\infty$ is fulfilled as it is the case in Fig. 3.3 for point 1, then the distance is calculated by

$$z''_\nu - z'_\nu = j\pi C. \tag{3.28}$$

If N is the number of vertices of the polygon, then together with the integration constants C and D and with the points w_α there are N+2 unknown parameters of which maximum three can be arbitrarily chosen. The remaining $N - 1$ constants have to be solved with equations (3.27), (3.28) or further geometrical relations.

3.4. Potential Solutions for Boundary Conditions of First Kind

Generally, mixed boundary conditions emerge for solutions of the potential equation in the MOS transistor. Here, the development of the model structure takes place in the way where Dirichlet boundary conditions are sufficient for the description of the potential problem. With the aid of superposition a solution for arbitrary potential problems for the potential solution is possible.

3.4.1. Potential Solution Single Vertex

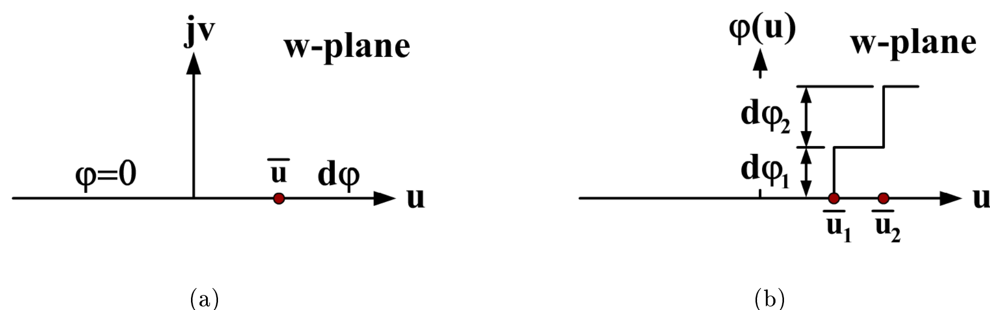

Figure 3.4.: For two electrodes along the real axis u with infinitesimal gap $\overline{u}$ the potential solution is well known. This is used by superposition of two electrode arrangements according to (a) with different position $\overline{u}$ and potential difference $d\varphi$ for the computation of a potential problem with boundary conditions according to (b).

The closed solution of a potential problem within the z-plane via a transformation into the upper w-half plane with the help of conformal mapping due to subsection 3.3.3 presupposes that those potential problems are calculated in closed-form in the w-plane. The solution of the complex potential in the upper w-half plane in Fig. 3.4 shows two electrodes along the u-axis with the potential difference $\mathrm{d}\varphi$ which has the infinitesimal gap $\mathrm{w} = \bar{\mathrm{u}}$, known as Single Vertex approach [137]

$$\mathrm{P} = \Phi + \mathrm{j}\Xi = \mathrm{d}\varphi + \mathrm{j}\frac{\mathrm{d}\varphi}{\pi}\ln(\mathrm{w} - \bar{\mathrm{u}}). \tag{3.29}$$

Due to subsection 3.3.2 the vertex itself will never be conformal. A very small circle excluding $\mathrm{w} = \bar{\mathrm{u}}$ suffices to relieve this difficulty [137].

3.4.2. Solution for Arbitrary Boundary Conditions

Boundary Integral

By the use of the Cauchy–Riemann differential equations (3.8) the normal component of the electric field along two electrodes with the potential difference $\mathrm{d}\varphi$ (Figure 3.4(a)) can be calculated using

$$\mathrm{dE}_{\perp(\mathrm{w})} = -\frac{\partial\Phi}{\partial \mathrm{v}} = \frac{\partial\Xi}{\partial \mathrm{u}} = \frac{\partial}{\partial \mathrm{u}}\frac{\mathrm{d}\varphi}{\pi}\ln(\mathrm{u} - \bar{\mathrm{u}}) = \frac{\mathrm{d}\varphi}{\pi}\frac{1}{\mathrm{u} - \bar{\mathrm{u}}}. \tag{3.30}$$

If the electric field strength within a z-plane is searched which results from the conformal mapping of the upper w-half plane with a function $\mathrm{z} = \mathrm{f(w)}$, then a scaling with the differential of the mapping function must be accomplished [168]

$$\mathrm{dE}_{\perp} = \mathrm{dE}_{\perp(\mathrm{z})} = \left|\frac{\mathrm{dw}}{\mathrm{dz}}\right|\frac{\mathrm{d}\varphi}{\pi}\frac{1}{\mathrm{u} - \bar{\mathrm{u}}}. \tag{3.31}$$

If several boundary conditions due to Fig. 3.4(a) are superposed with a different position of the infinitesimal gap $\bar{\mathrm{u}}$ between the electrodes and several potential differences $\mathrm{d}\varphi$, then a potential in the form of steps results along the u-axis, Fig. 3.4(b). If the gaps between the electrodes have the infinitesimal distance $\mathrm{d}\bar{\mathrm{u}}$ and the potential difference is given by [168]

$$\mathrm{d}\varphi = \left.\frac{\partial\varphi(\mathrm{u})}{\partial \mathrm{u}}\right|_{\bar{\mathrm{u}}}\mathrm{d}\bar{\mathrm{u}}, \tag{3.32}$$

then the superposition gives all electrodes $\varphi(\mathrm{u})$ as boundary conditions of the first order along the u-axis. With (3.31) the normal component of the electric field strength in the z-plane leads to [168]

$$\mathrm{E}_{\perp}(\mathrm{u}) = \mathrm{E}_{\perp(\mathrm{z})}(\mathrm{u}) = \int_{-\infty}^{+\infty}\mathrm{dE}_{\perp(\mathrm{z})} = \frac{1}{\pi}\left|\frac{\mathrm{dw}}{\mathrm{dz}}\right|\int_{-\infty}^{+\infty}\frac{1}{\mathrm{u} - \bar{\mathrm{u}}}\left.\frac{\partial\varphi(\mathrm{u})}{\partial \mathrm{u}}\right|_{\bar{\mathrm{u}}}\mathrm{d}\bar{\mathrm{u}}. \tag{3.33}$$

Figure 3.5.: Solution of first boundary value problem on unit circle [137].

General Laplacian Problems and Conformal Mapping

The potential solution of any first kind boundary value problem of any simply interior connected region bounded by regular curves can be mapped upon the interior of the unit circle in a one-to-one conformal manner by Riemann's fundamental theorem [137]. It is possible to solve any potential problem for the unit circle with Poisson's integral if the boundary value problem of the first kind is given and the function $z = r\exp(j\phi)$ is assumed

$$\Phi = \frac{1}{2\pi}\int_0^{2\pi} \frac{1-r^2}{1-2r\cos(\phi-\overline{\phi})+r^2}\Phi(\overline{\phi})d\overline{\phi} \tag{3.34}$$

where (r,ϕ) define a point P within the unit circle, and $\overline{\phi}$ a point on the unit circle as shown in Fig. 3.5.

With the complex potential function of Schwarz follows

$$P = \frac{1}{2\pi}\int_0^{2\pi} \frac{\exp(j\overline{\phi})+z}{\exp(j\overline{\phi})-z}\Phi(\overline{\phi})d\overline{\phi} \equiv \Phi + j\Xi \tag{3.35}$$

where the real part is based on equation (3.34) [137].

The most mapping problems are easier if they are mapped upon the upper half w-plane, rather than upon a unit circle. With the function

$$w = j\frac{1-z}{1+z}, \tag{3.36}$$

UNIVERSITAT ROVIRA I VIRGILI
TWO-DIMENSIONAL ANALYTICAL PREDICTIVE MODELING OF SCHOTTKY BARRIER SOI AND MULTI-GATE MOSFETS
Mike Schwarz
Dipòsit Legal: T.456-2013

the unit circle can be mapped from the z-plane upon the upper half w-plane by the Schwarz-Christoffel transformation with

$$\mathrm{z} = -\frac{\mathrm{w}-\mathrm{j}}{\mathrm{w}+\mathrm{j}},\ \exp(\mathrm{j}\overline{\phi}) = -\frac{\overline{\mathrm{u}}-\mathrm{j}}{\overline{\mathrm{u}}+\mathrm{j}},\ \mathrm{d}\phi' = \frac{2\mathrm{d}\overline{\mathrm{u}}}{1+\overline{\mathrm{u}}^2} \tag{3.37}$$

into

$$\mathrm{P} = \frac{\mathrm{j}}{\pi}\int_{-\infty}^{+\infty}\frac{1+\overline{\mathrm{u}}\mathrm{w}}{(1+\overline{\mathrm{u}}^2)(\mathrm{w}-\overline{\mathrm{u}})}\Phi(\overline{\mathrm{u}})\mathrm{d}\overline{\mathrm{u}} = \Phi + \mathrm{j}\Xi, \tag{3.38}$$

which results in a general solution of the first boundary value problem. In equation (3.38), $\overline{\mathrm{u}}$ is the integration variable along the real u-axis and w is the arbitrary point where the potential P exists. The real part of equation (3.38) leads to the Poisson's integral on the unit circle [137]

$$\Phi(\mathrm{u},\mathrm{v}) = \frac{1}{\pi}\int_{-\infty}^{+\infty}\frac{\mathrm{v}}{(\mathrm{u}-\overline{\mathrm{u}})^2+\mathrm{v}^2}\Phi(\overline{\mathrm{u}})\mathrm{d}\overline{\mathrm{u}}. \tag{3.39}$$

Here, $\Phi(\overline{\mathrm{u}})$ represents the conformally mapped boundary condition along the regarded area

$$\Phi(\overline{\mathrm{u}}) = \Phi(\mathrm{f}^{-1}(\overline{\mathrm{z}})). \tag{3.40}$$

Chapter 4.

General Modeling Simplifications

The aim of this work is to develop a compact model for Schottky barrier Double-Gate MOSFET devices in closed-form. As mentioned in the introductory part, receiving a compact model is depends on the applied simplifications to describe the behavior of the device. Therefore, compact modeling is always a trade-off between accuracy and the simplifications which in the end, results in a fast model described by only few equations.

The developed model in this thesis has some general limitations. It should be noted that effects of fringing fields are not taken into account. Therefore, the gate oxides are assumed to be thin enough that fringing fields have a negligible influence. One method to include those fringing fields is presented by Ernst et al. in [169, 170]. Furthermore, this model excludes quantum confinement (QC) effects which would be very significant for diameters below 10 nm [171].

4.1. Area Definition

The basic idea in this thesis is to describe the Schottky barrier Double-Gate MOSFET by a simple structure, neglecting influences which result from fabrication processes. Therefore, the model is defined by a rectangular area from the source to drain region wherein Poisson's equation is to be solved in 2D. The area includes the oxide as shown by an orange rectangle in Fig. 4.1(a). In Fig. 4.1(b) the corresponding coordinates of the area is shown.

The origin of the device is set to the bottom left-hand corner. In x-direction we have the distance l_{ch} on the bottom right-hand corner while in y-direction the oxide is represented by the grey region with thickness t_{ox}. Then the channel begins with thickness t_{ox} and ends at distance $t_{ox}+t_{ch}$. With the oxide on top we receive the distance $2\cdot t_{ox}+t_{ch}$ for the upper left-hand corner. An arbitrary point within the channel region is described via the coordinates of Δt_{ch} and Δl_{ch} [172, 173, 174].

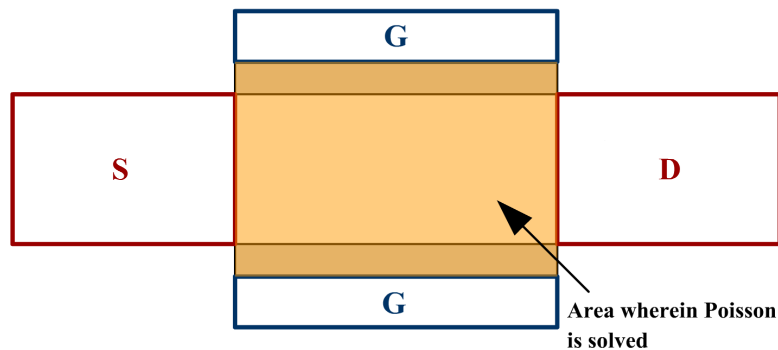

(a)

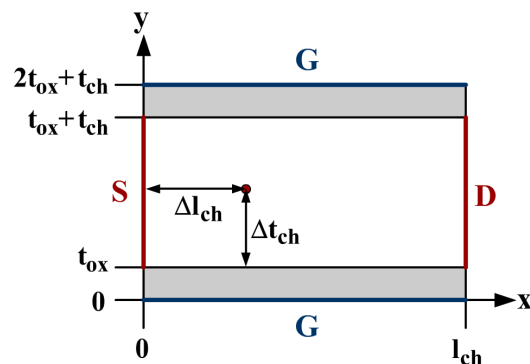

(b)

Figure 4.1.: In (a) a region is shown, wherein 2D Poisson is solved while in (b) the definition of the corresponding geometry represented by the orange rectangular is given.

4.2. Simplifications

4.2.1. Poisson's Equation

At first some initial conditions must be met to keep mathematics as simple as possible. The first simplification leads to Laplace's equation [174]. In general, the electrostatic problem for a Schottky barrier Double-Gate MOSFET can be described by Poisson's equation for the potential ϕ where the Poisson equation in the channel region with space charge ρ reads

$$\Delta\phi_{2D} = -\frac{\rho}{\epsilon} = -\frac{Q_{inv} + Q_{dep}}{\epsilon}. \tag{4.1}$$

Considering a non or lightly doped device results in a negligible depletion charge ($Q_{dep} \approx 0$). Furthermore, Poisson's equation within the subthreshold region of the device is calculated and therefore the inversion charge within the channel region can be neglected

UNIVERSITAT ROVIRA I VIRGILI
TWO-DIMENSIONAL ANALYTICAL PREDICTIVE MODELING OF SCHOTTKY BARRIER SOI AND MULTI-GATE MOSFETS
Mike Schwarz
Dipòsit Legal: T.456-2013

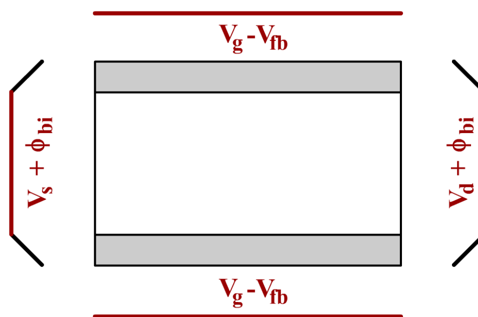

Figure 4.2.: Applied basic boundary conditions of the model.

($Q_{inv} \approx 0$). These assumptions lead to the simplification of Poisson's equation to a Laplacian equation

$$\Delta\phi_{2D} = 0. \tag{4.2}$$

4.2.2. Oxide Transformation

The second simplification which was made, is related to the discontinuity of the electric field caused by the different permeabilities of the gate oxide and the silicon at the silicon-to-oxide interface. In order to keep the conformal mapping technique as simple as possible the aim is to neglect this discontinuity by a scaling of the oxide according to the relationship of the permeability of the SiO_2 and the Si. If the oxide is sufficiently small enough which is common in MOSFET structures, the electric field in the oxide is assumed to be homogeneous. The discontinuity of the normal component in the electric field at the $Si - SiO_2$ interface (E_0) has to be avoided, with

$$D_{ox} = \epsilon_0\epsilon_{Si} \cdot E_0 = \epsilon_0\epsilon_{ox} \cdot E_{ox} = \epsilon_0\epsilon_{ox} \cdot \frac{V_{ox}}{t_{ox}}. \tag{4.3}$$

D_{ox} is the dielectric displacement, V_{ox} is the voltage drop across the oxide, E_{ox} is the electric field across the oxide, ϵ_{ox} denominates the dielectric permittivity of insulator/dielectric and ϵ_{Si} the dielectric permittivity of silicon. Scaling t_{ox} to

$$\tilde{t_{ox}} = \frac{\epsilon_{Si}}{\epsilon_{ox}} \cdot t_{ox} \tag{4.4}$$

the electric field E_0 is continuous at the interface

$$D_{ox} = \epsilon_0\epsilon_{Si} \cdot E_0 = \epsilon_0\epsilon_{Si} \cdot \frac{V_{ox}}{\tilde{t_{ox}}} \tag{4.5}$$

due to the unchanged voltage drop across the oxide [174].

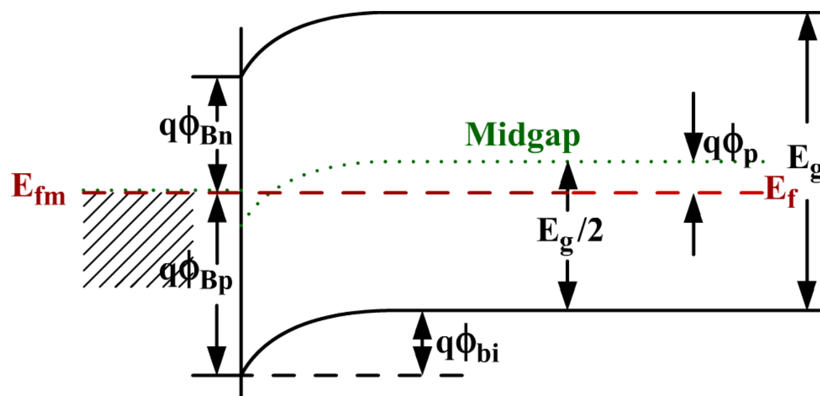

Figure 4.3.: Built-in potential ϕ_{bi} of a p-type Schottky contact [150].

4.3. Boundary Conditions

The basic applied boundary conditions are illustrated in Fig. 4.2. $\mathrm{V_g}$ represents the gate potential, $\mathrm{V_{fb}}$ the flat band voltage. $\mathrm{V_s}$ and $\mathrm{V_d}$ describe the source and drain potentials, respectively. At the source electrode $\mathrm{V_s} + \phi_{\mathrm{bi}}$ is used as condition while for the drain electrode $\mathrm{V_d}+\phi_{\mathrm{bi}}$ applies. At both gate electrodes the condition $\mathrm{V_g}-\mathrm{V_{fb}}$ is applied. The built-in potential at the source and drain contacts is represented by ϕ_{bi} and developed due to the approach made in Fig. 4.3 for a p-type Schottky contact. Therefore,

$$\phi_{\mathrm{p}} = \mathrm{V_t} \cdot \ln\left(\frac{\mathrm{N_A}}{\mathrm{n_i}}\right) = \frac{\mathrm{kT}}{\mathrm{q}} \cdot \ln\left(\frac{\mathrm{N_A}}{\mathrm{n_i}}\right) \tag{4.6}$$

$$\phi_{\mathrm{bi}} = \phi_{\mathrm{Bp}} - \left(\frac{\mathrm{E_g}}{2} - \phi_{\mathrm{p}}\right) \tag{4.7}$$

$$\phi_{\mathrm{bi}} = (\mathrm{E_g} - \phi_{\mathrm{Bn}}) - \left(\frac{\mathrm{E_g}}{2} - \phi_{\mathrm{p}}\right) \tag{4.8}$$

where the relationship $\mathrm{E_g} = \phi_{\mathrm{Bn}} + \phi_{\mathrm{Bp}}$ is valid [150]. $\mathrm{V_t}$ is the thermal voltage which consists of the Boltzmann constant k, temperature T and elementary charge q. $\mathrm{N_A}$ describes the acceptor impurity concentration for a p-type semiconductor. If a n-type semiconductor is used, $\mathrm{N_A}$ is replaced by $\mathrm{N_D}$ which describes the donor impurity concentration. The intrinsic carrier concentration is represented by $\mathrm{n_i}$. ϕ_{Bp} describes the barrier height for holes and ϕ_{Bn} for electrons while $\mathrm{E_g}$ represents the distance between the valence and conduction band [174].

4.4. Decomposition Strategy

The decomposition strategy is a further simplification which is very valuable. Generally, a Schottky barrier Double-Gate MOSFET is described by a 4-corner structure. Solving

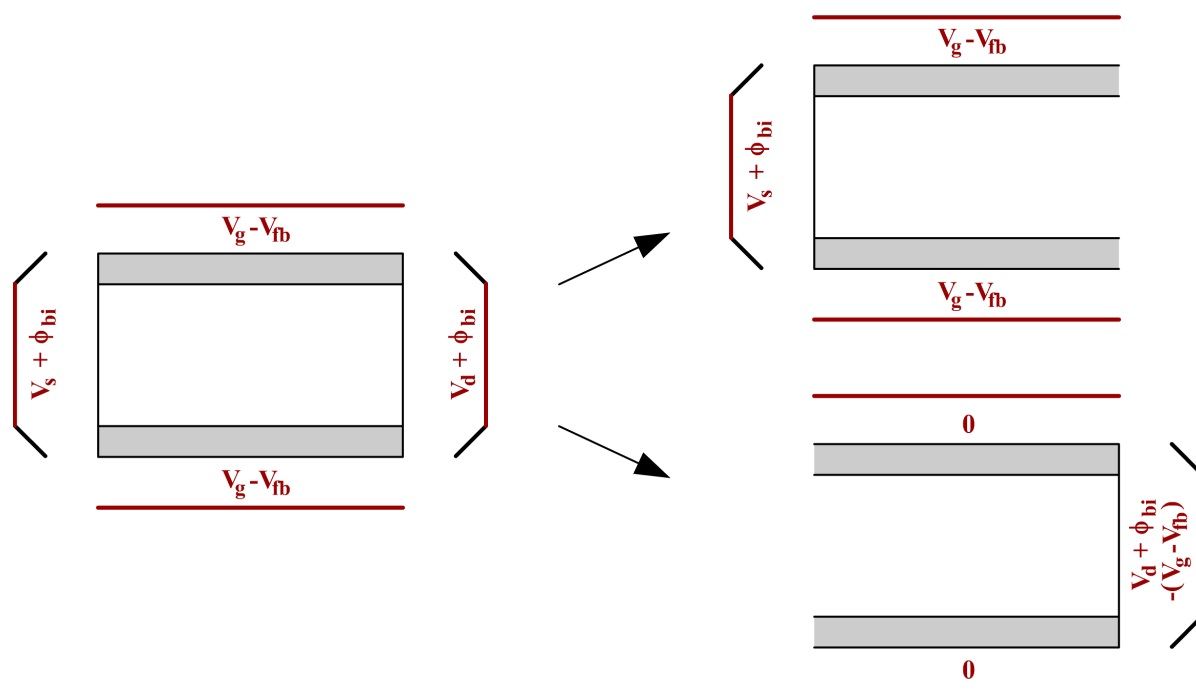

Figure 4.4.: Decomposition of the boundary conditions of a 4-corner problem into two 2-corner problems.

the potential problems in a 4-corner structure requires a lot of mathematical effort and often no closed-form solutions are found. Due to this circumstance a decomposition of the 4-corner problem into two 2-corner problems (Fig. 4.4) is made to keep the mathematics simple [174].

The approximation is reasonable if the relationship $l_{ch} > t_{ch}$ is valid which is usually the case in Double-Gate MOSFETs [175]. One obtains two 2-corner problems, one each for the source and drain influence the so called source and drain related cases. The boundary conditions are modified as presented in Fig. 4.4 to calculate the influence for the source and drain related case. One 2-corner problem shows the source influence, the second one the drain influence. Both 2-corner problems can be solved by the conformal mapping technique and their solutions, superposition. Short-channel effects are considered by this approach, e.g. the drain related case also includes the drain influence on the source end of the channel and vice versa [174].

UNIVERSITAT ROVIRA I VIRGILI
TWO-DIMENSIONAL ANALYTICAL PREDICTIVE MODELING OF SCHOTTKY BARRIER SOI AND MULTI-GATE MOSFETS
Mike Schwarz
Dipòsit Legal: T.456-2013

Chapter 5.

Modeling Approaches for the Electrostatics

After the discussion of the simplifications in chapter 4, this chapter deals with the modeling approaches for the electrostatics. Various approaches for the electrostatic potential and the electric field are presented and discussed. They have been modeled with the help of the conformal mapping technique. Therefore, the introduced 2-corner structures are mapped from z-plane into w-plane.

5.1. Boundary Conditions

In general the boundary conditions for the source and drain related cases which have to be applied result from the decomposition strategy from section 4.4 as shown in Fig. 4.4. Due to these circumstances the definition for both cases which describe the behavior of the Schottky barrier Double-Gate MOSFET is necessary. Therefore, several important points along the boundary are defined. They will represent the integration boundaries for the closed-form solutions which are presented in the following section. The important points represent the piecewise parts of the device, as shown in Fig. 5.1. Additionally, the y-component of the electric field within the oxide at the boundaries (refer to Fig. 5.2(a)) is assumed to be $E_y = \text{const}$ while we approximate the voltage drop within the oxide as a linear function.

From Fig. 5.2(a), e.g. the source related case, result the following boundary conditions. Between ①'' and ② a constant boundary with the bias condition $V_g - V_{fb}$ prevails. From ② to ③ a linear boundary is applied. Between ③ and ④ one has again a constant boundary with the bias condition $V_s + \phi_{bi}$. As for ② to ③ also a linear boundary exists between ④ and ⑤. The last boundary is applied from ② to ①'; a constant boundary with the bias condition $V_g - V_{fb}$.

Afterwards, all components have to be superposed to calculate the overall influence of the source related case. The calculation for the drain related case is done analogously, only the changed boundary conditions have to be considered and also the structure for

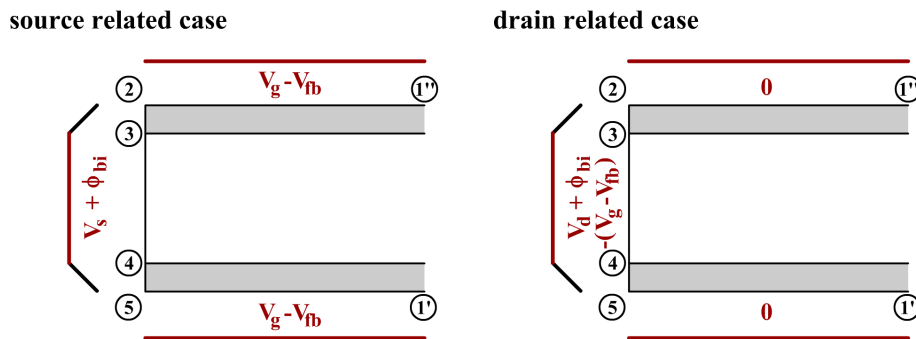

Figure 5.1.: Definition of the boundaries and integration borders for the source and drain related case of a SB-DG-MOSFET.

the drain related case is mirrored. The resulting transformed boundary conditions in the w-plane, are content of Fig. 5.2(b) [174, 176, 177].

5.1.1. Special Case: Boundary Condition Single Vertex

For the special case of the single vertex approach for the electrostatic potential it can be observed from Fig. 5.2(a) that between ② → ③ and ⑤ → ④ for both cases the voltage drop along the oxide is approximated by a linear function. In order to the approach of the single vertex shown in Fig. 3.4 for both the source and drain related cases the boundaries are decomposed with respect to equation (3.29).

Due to these circumstances the boundary conditions for the source and drain related cases are obtained, see Fig. 5.3(a) and Fig. 5.3(b). Within the oxide the voltage drop is realized by a linear function, refer to Fig. 5.4(a). This linear function is approximated by a step function, see Fig. 5.4(b), with superposition of electrode functions with different $\overline{\mathrm{y}}$ and $\mathrm{d}\varphi$. Therefore, it follows

$$\mathrm{d}\varphi = \phi_2 - \phi_1,$$

$$\widetilde{\mathrm{d}}\varphi = \frac{\mathrm{d}\varphi}{\mathrm{n}},$$

$$\Delta\widetilde{\mathrm{t}}_{\mathrm{ox}} = \frac{\widetilde{\mathrm{t}}_{\mathrm{ox}}}{\mathrm{n}+1},$$

$$\overline{\mathrm{y}_{\mathrm{i}}} = \mathrm{y}_0 + \mathrm{i}\cdot\Delta\widetilde{\mathrm{t}}_{\mathrm{ox}}; \mathrm{i} = 1...\mathrm{n}. \tag{5.1}$$

Each part of the step function within the oxide is superposed and leads to the solutions for the source and drain related 2-corner problems [174].

UNIVERSITAT ROVIRA I VIRGILI
TWO-DIMENSIONAL ANALYTICAL PREDICTIVE MODELING OF SCHOTTKY BARRIER SOI AND MULTI-GATE MOSFETS
Mike Schwarz
Dipòsit Legal: T.456-2013

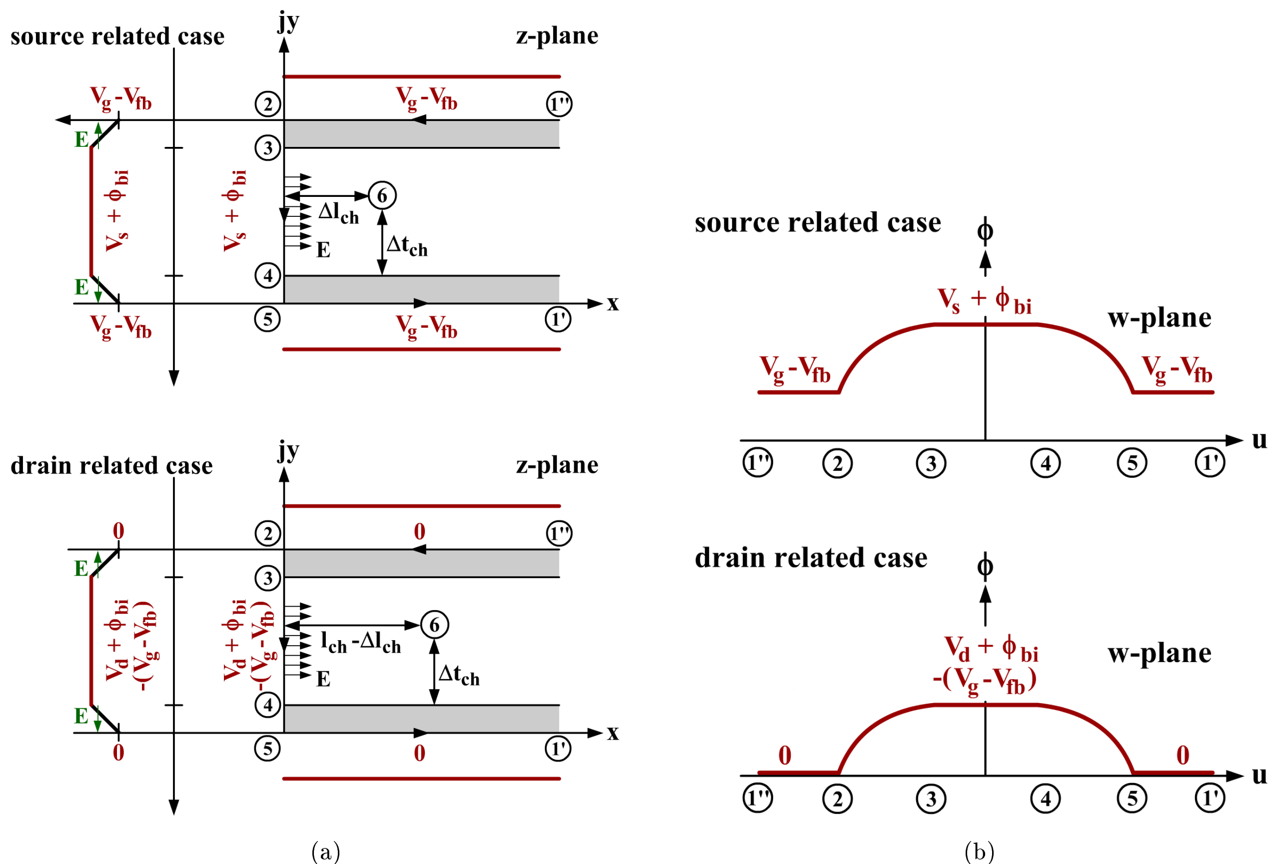

Figure 5.2.: Coordinates and boundary conditions for the calculation of the electrostatics for the source related case and for the drain related case (a) in the z-plane and (b) the resulting transformed boundary conditions in w-plane.

5.2. Conformal Mapping of the Structure

The Schwarz-Christoffel transformation in equation (3.25) is the applied method to map the inside of the closed polygon, shown in Fig. 4.1, 4.2 and 4.4, in the complex z-plane upon the upper half plane of a complex w-plane. Table 5.1 shows the relationship between a point in the z-plane and w-plane as well as the change of angle at the vertices of the polygon.

With the use of equation (3.25) the differential of the conformal mapping is

$$\frac{\mathrm{dz}}{\mathrm{dw}} = \frac{\mathrm{C}}{\sqrt{\mathrm{w}-1}\cdot\sqrt{\mathrm{w}+1}}, \tag{5.2}$$

after integration it becomes

$$\mathrm{z} = \mathrm{f(w)} = 2\mathrm{C}\cdot\ln(\sqrt{\mathrm{w}-1}\cdot\sqrt{\mathrm{w}+1}) + \mathrm{D}. \tag{5.3}$$

UNIVERSITAT ROVIRA I VIRGILI
TWO-DIMENSIONAL ANALYTICAL PREDICTIVE MODELING OF SCHOTTKY BARRIER SOI AND MULTI-GATE MOSFETS
Mike Schwarz
Dipòsit Legal: T.456-2013

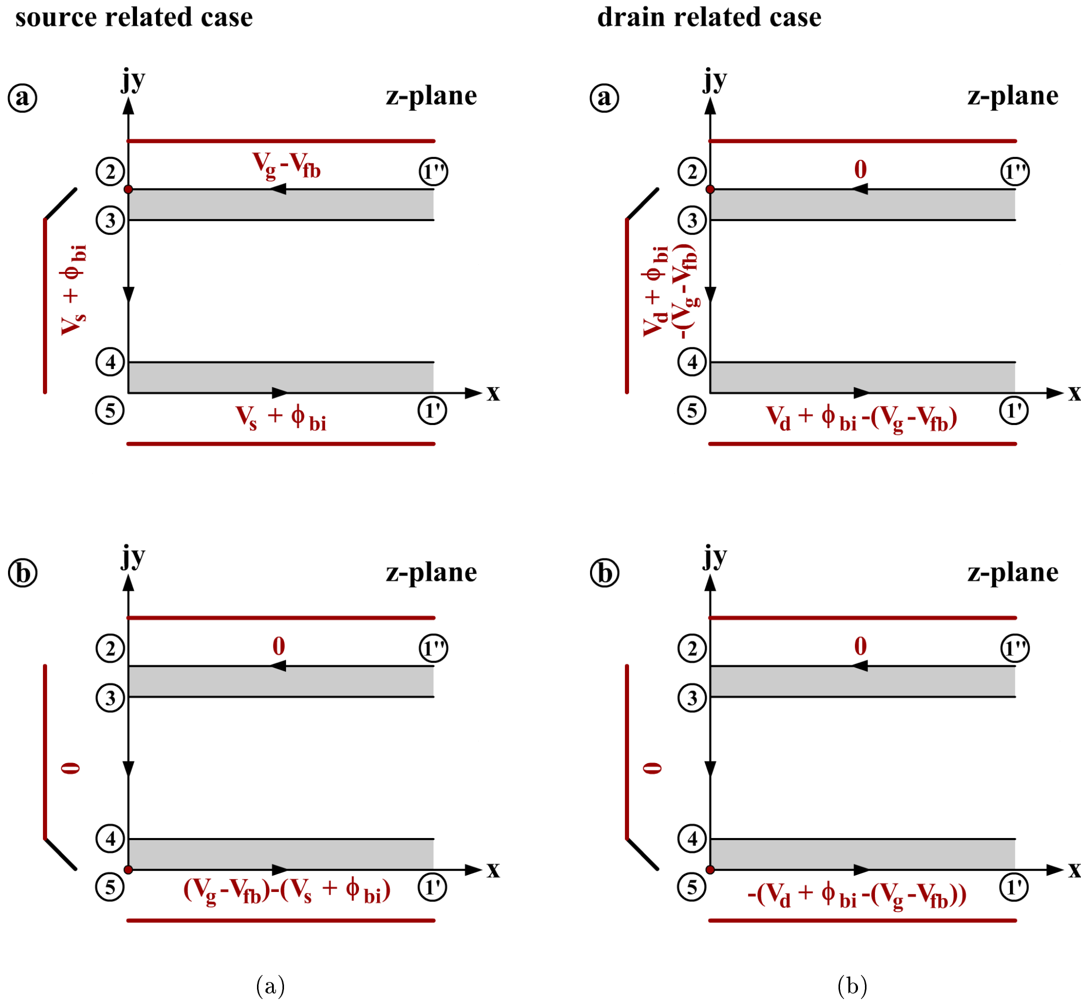

Figure 5.3.: Decomposition of the source and drain related 2-corner boundary conditions for the single vertex case.

The integration constant is D = 0, because the absolute coordinates are not relevant. The constant C can be calculated by equation (3.28)

$$z_1'' - z_1' = j\Delta y = j\pi C \quad \Rightarrow \quad C = \frac{\Delta y}{\pi}. \tag{5.4}$$

Now all parameters of the conformal mapping are solved.

With the mapping of the boundary condition from the z-plane into w-plane and the re-transformation into the original geometry of the computed solution for the inverse transformation, it is necessary to know the mapping of any point along the electrodes in both complex planes while the mapping is valid for every point within the polygon.

The mapping from the w-plane to z-plane results from equation (5.3). The function $z = f(w) = 2\frac{\Delta y}{\pi} \cdot \ln(\sqrt{w-1} \cdot \sqrt{w+1})$ maps a point w from the upper half of complex

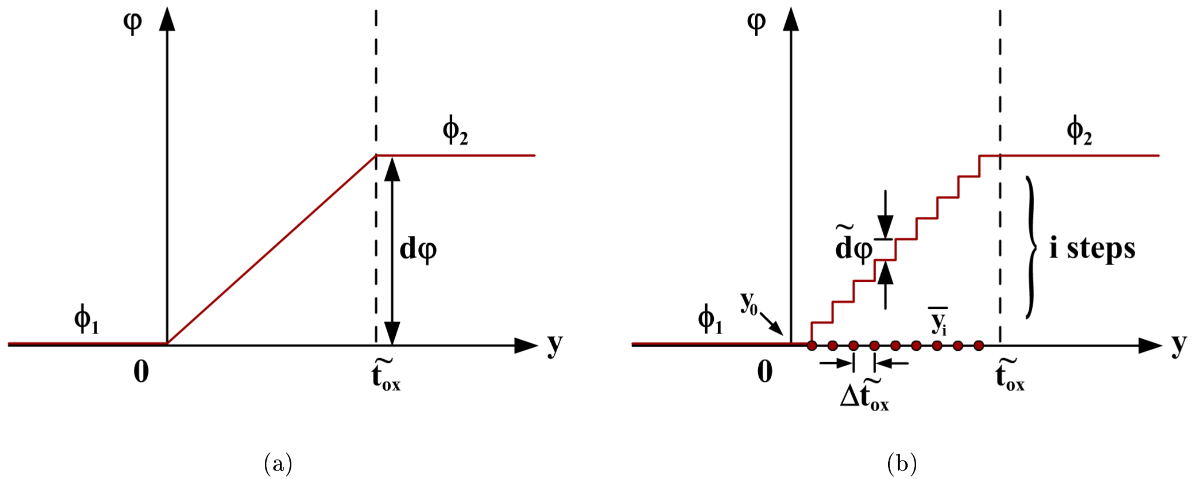

Figure 5.4.: In (a) the approximation of the voltage drop within the oxide by a linear function is shown and in (b) the approximated solution of the linear function ($i \rightarrow \infty$) by a step function with superposition of electrode formations with different $\bar{y}$ and $\widetilde{d\varphi}$.

Table 5.1.: Definition of basic elements.

ν	w_ν	z_ν	$\pi\gamma_\nu$	γ_ν
1	$\pm\infty$	$+\infty$	$+\pi$	$+1$
2	-1	z_2	$+\frac{\pi}{2}$	$+\frac{1}{2}$
3	$+1$	z_3	$+\frac{\pi}{2}$	$+\frac{1}{2}$

w-plane upon its representation at point z within a 2-corner structure in complex z-plane [137,178]. Thus the inverse function of $z = f(w)$ maps the point from plane z upon plane w

$$w = f^{-1}(z) = u + jv = \cosh\left(\frac{\pi z}{\Delta y}\right) = \cosh\left(\frac{\pi(x + jy)}{\Delta y}\right) \tag{5.5}$$

where $\Delta y = 2\tilde{t}_{ox} + t_{ch}$, resulting from the device geometry. With the help of this relation one can solve the structure in w-plane while it is given in z-plane. As described in the following section, for the solution of the electric field, the complex conjugate of w is needed in (5.51) [176].

As already explained, several important points along the boundary, see Fig. 5.5, are marked which define the applied boundary conditions. ①" represents the end of the device in x-direction for the top gate. It lies in the infinite region due to the conformal mapping technique [137]. ② is the end of the device in y-direction, and point ③ is the end of the upper oxide or the end of the channel. The end of the lower oxide and start of the channel is described by ④ while ⑤ is the origin within the z-plane. ①' represents

also a point in infinite region as already described for ⓵” [137]. An arbitrary point within the channel region which represents the point on which the potential, or electric field takes influence is represented by ⑥. By applying conformal mapping technique everything is transformed into w-plane whereby all point are now located on the real axis u in w-plane, except the arbitrary point within the channel region which is located upon the upper half of w-plane (Fig 5.5) [174, 176, 177].

As described the points ①” and ①’ lie in the infinite region. Considering the infinite for both points in the implementation, the distance in x-direction is set three times higher than the end of the device, indicated with l_{ch}. This is considered in the following calculations for the important points ①” and ①’.

$$
\begin{aligned}
\bar{u}_{①”} &= \cosh\left(\frac{\pi\left(3l_{ch} + j\left(2\tilde{t}_{ox} + t_{ch}\right)\right)}{\Delta y}\right) \\
\bar{u}_{②} &= \cosh\left(\frac{\pi\left(0 + j\left(2\tilde{t}_{ox} + t_{ch}\right)\right)}{\Delta y}\right) \\
\bar{u}_{③} &= \cosh\left(\frac{\pi\left(0 + j\left(\tilde{t}_{ox} + t_{ch}\right)\right)}{\Delta y}\right) \\
\bar{u}_{④} &= \cosh\left(\frac{\pi\left(0 + j\tilde{t}_{ox}\right)}{\Delta y}\right) \\
\bar{u}_{⑤} &= \cosh\left(\frac{\pi\left(0 + j0\right)}{\Delta y}\right) \\
\bar{u}_{①’} &= \cosh\left(\frac{\pi\left(3l_{ch} + j0\right)}{\Delta y}\right)
\end{aligned}
\tag{5.6}
$$

The arbitrary point which represents the point on which the potential, or electric field takes influence, is calculated for the source related case by

$$
w_{⑥,sce} = \cosh\left(\frac{\pi\left(\Delta l_{ch} + j\left(\tilde{t}_{ox} + \Delta t_{ch}\right)\right)}{\Delta y}\right), \tag{5.7}
$$

while it is calculated for the drain related case by

$$
w_{⑥,drn} = \cosh\left(\frac{\pi\left(l_{ch} - \Delta l_{ch} + j\left(\tilde{t}_{ox} + \Delta t_{ch}\right)\right)}{\Delta y}\right). \tag{5.8}
$$

5.2.1. Special Case: Conformal Mapping Single Vertex

The special case of the single vertex approach for the electrostatic potential with the Schwarz-Christoffel approach for the defined important points along the boundary the

UNIVERSITAT ROVIRA I VIRGILI
TWO-DIMENSIONAL ANALYTICAL PREDICTIVE MODELING OF SCHOTTKY BARRIER SOI AND MULTI-GATE MOSFETS
Mike Schwarz
Dipòsit Legal: T.456-2013

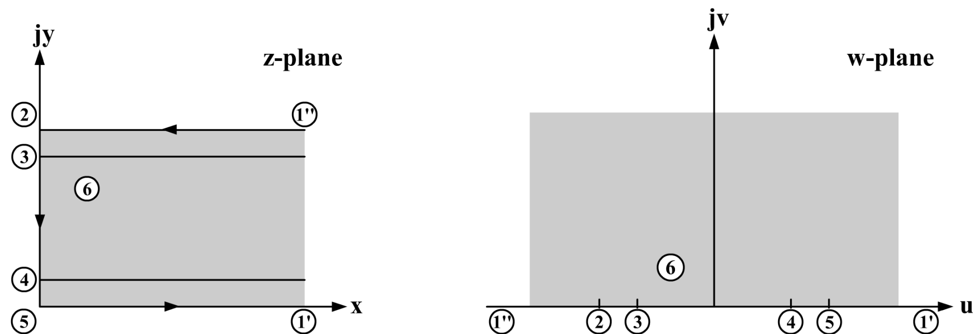

Figure 5.5.: Several important points are marked along the boundary and an arbitrary point ⑥ is mapped by using Schwarz-Christoffel upon the upper half of w-plane.

solutions for w and $\overline{u}$ is defined as follows. Several parts are calculated by the approach of a staircase-shaped potential as shown in Fig. 5.4 for the special case of the single vertex approach from section 5.1.1. This is considered by the marking of $\overline{y}$ for the points ② → ③ and ⑤ → ④ where $\overline{y}$ represents the moving coordinates of the single vertex within the oxide

$$\overline{u}_{i,②\rightarrow③} = \cosh\left(\frac{\pi\big(0 + j(\overline{y}_{i,top} + t_{ch})\big)}{2\tilde{t}_{ox} + t_{ch}}\right), \tag{5.9}$$

$$\overline{u}_{i,⑤\rightarrow④} = \cosh\left(\frac{\pi\big(0 + j\overline{y}_{i,bottom}\big)}{2\tilde{t}_{ox} + t_{ch}}\right) \tag{5.10}$$

with $\overline{y}_{i,top} = 2\tilde{t}_{ox}...\tilde{t}_{ox}$ and $\overline{y}_{i,bottom} = 0...\tilde{t}_{ox}$ with i steps [174].

5.3. Electrostatic Potential

Taking into account the introduced preliminaries, the electrostatic potential can be solved with the help of the Schwarz-Christoffel transformation in the complex w-plane. Within the following sections two kind of approaches for the potential are presented. Finally, a comparison of both is presented. The first approach is developed with the potential solution of a single vertex, already presented in section 3.4.1. The second approach is developed from the Poisson's integral in section 3.4.2.

5.3.1. Single Vertex Approach

The single vertex approach from equation (3.29) is used to model the electrostatic potential within the channel region of the device. With the decomposition of the 4-corner problem into two 2-corner problems the boundary conditions are adapted according to

Fig. 4.4. Afterwards, the device geometry is mapped into the w-plane and with the help of the single vertex approach the solution of the potential problem can be approximated. Finally, a superposition of all calculated results leads to the complete potential solution.

Potential Solution

Due to Fig. 5.3(a) and 5.3(b) the potentials are solved with equation (3.29) with the staircase-shaped potential (moving Single Vertex) for the source and drain related cases [174].

For the source related case follows due the conditions shown in Fig. 5.3(a) and from equation (3.29), the source influence part a with $\phi_1 = V_g - V_{fb}$ and $\phi_2 = V_s + \phi_{bi}$

$$\varphi_{sce,a}(x,y) = \sum_{i=1}^{n} \left[\frac{(V_s + \phi_{bi})}{n} + j\frac{(V_s + \phi_{bi}) - (V_g - V_{fb})}{\pi \cdot n} \cdot \ln(w_{⑥,sce} - \bar{u}_i) \right]. \tag{5.11}$$

The source related case influence part b is then calculated in the same manner with $\phi_1 = 0$ and $\phi_2 = (V_g - V_{fb}) - (V_s + \phi_{bi})$

$$\varphi_{sce,b}(x,y) = \sum_{i=1}^{n} \left[\frac{\big((V_g - V_{fb}) - (V_s + \phi_{bi})\big)}{n} + j\frac{\big((V_g - V_{fb}) - (V_s + \phi_{bi})\big) - 0}{\pi \cdot n} \cdot \ln(w_{⑥,sce} - \bar{u}_i) \right]. \tag{5.12}$$

Superposing both parts

$$\varphi_{sce}(x,y) = \varphi_{sce,a}(x,y) + \varphi_{sce,b}(x,y) \tag{5.13}$$

results in the source influence on the potential in point ⑥.

By applying $\phi_1 = 0$ and $\phi_2 = V_d + \phi_{bi} - (V_g - V_{fb})$ the drain related case influence part a (Fig. 5.3(b)) is calculated as

$$\varphi_{drn,a}(x,y) = \sum_{i=1}^{n} \left[\frac{\big(V_d + \phi_{bi} - (V_g - V_{fb})\big)}{n} + j\frac{\big(V_d + \phi_{bi} - (V_g - V_{fb})\big) - 0}{\pi \cdot n} \cdot \ln(w_{⑥,drn} - \bar{u}_i) \right]. \tag{5.14}$$

The drain related case influence part b is then calculated in the same manner with $\phi_1 = 0$ and $\phi_2 = -((V_g - V_{fb}) - (V_d + \phi_{bi}))$

$$\varphi_{drn,b}(x,y) = \sum_{i=1}^{n} \left[\frac{-\big((V_g - V_{fb}) - (V_d + V_{bi})\big)}{n} + j\frac{-\big((V_g - V_{fb}) - (V_d + V_{bi})\big) - 0}{\pi \cdot n} \cdot \ln(w_{⑥,drn} - \bar{u}_i) \right]. \tag{5.15}$$

Superposing both parts

$$\varphi_{\mathrm{drn}}(\mathrm{x},\mathrm{y}) = \varphi_{\mathrm{drn,a}}(\mathrm{x},\mathrm{y}) + \varphi_{\mathrm{drn,b}}(\mathrm{x},\mathrm{y}) \tag{5.16}$$

results in the drain influence on the potential in point ⑥. From equations (5.13) and (5.16) the superposed 4-corner potential is

$$\varphi(\mathrm{x},\mathrm{y}) = \varphi_{\mathrm{sce}}(\mathrm{x},\mathrm{y}) + \varphi_{\mathrm{drn}}(\mathrm{x},\mathrm{y}). \tag{5.17}$$

Using this result one can calculate the potential φ for each position (x,y) within the channel region of a Double-Gate MOSFET as well as Schottky barrier DG MOSFETs.

5.3.2. Square Root Approximation Approach

The square root approximation approach is based on Poisson's integral from equation (3.39) and is used to model the electrostatic potential within the channel region of the device. Also for this approach the decomposition of the 4-corner problem into two 2-corner problems is applied and the boundary conditions are modified according to Fig. 4.4. In a last step the potential solutions obtained from the separately calculated parts are superposed in order to get the complete potential solution. [177, 179].

Closed-form Solution Electrostatic Potential

The closed-form solution of a potential problem within the z-plane via a transformation in the upper w-halfplane with the help of conformal mapping technique presupposes that those potential problems are calculated in closed-form in the w-plane.

The potential solution of any boundary value problem of first order on plane z is solved after mapping into a w-plane with the help of equation (3.39), the Poisson integral [137]

$$\varphi(\mathrm{u},\mathrm{v}) = \frac{1}{\pi}\int_{-\infty}^{+\infty} \frac{\mathrm{v}}{(\mathrm{u}-\overline{\mathrm{u}})^2+\mathrm{v}^2}\cdot\varphi(\overline{\mathrm{u}})\cdot \mathrm{d}\overline{\mathrm{u}} \tag{5.18}$$

where $\varphi(\overline{\mathrm{u}})$ is the conformally mapped boundary condition along the regarded area.

For the calculation of the potential solution of one arbitrary point within the channel region in z-plane, it is necessary to transform the linear constant boundaries of z to boundaries depending on w. Therefore, the inverse transformation of equation (5.5) is used, it follows

$$\mathrm{z} = \mathrm{f}^{-1}(\mathrm{w}) = \frac{\Delta\mathrm{y}}{\pi}\,\mathrm{arcosh}(\mathrm{w}), \tag{5.19}$$

while for the special case along the boundaries one is able to write

$$\overline{\mathrm{z}} = \mathrm{f}^{-1}(\overline{\mathrm{u}}) = \frac{\Delta\mathrm{y}}{\pi}\,\mathrm{arcosh}(\overline{\mathrm{u}}) \tag{5.20}$$

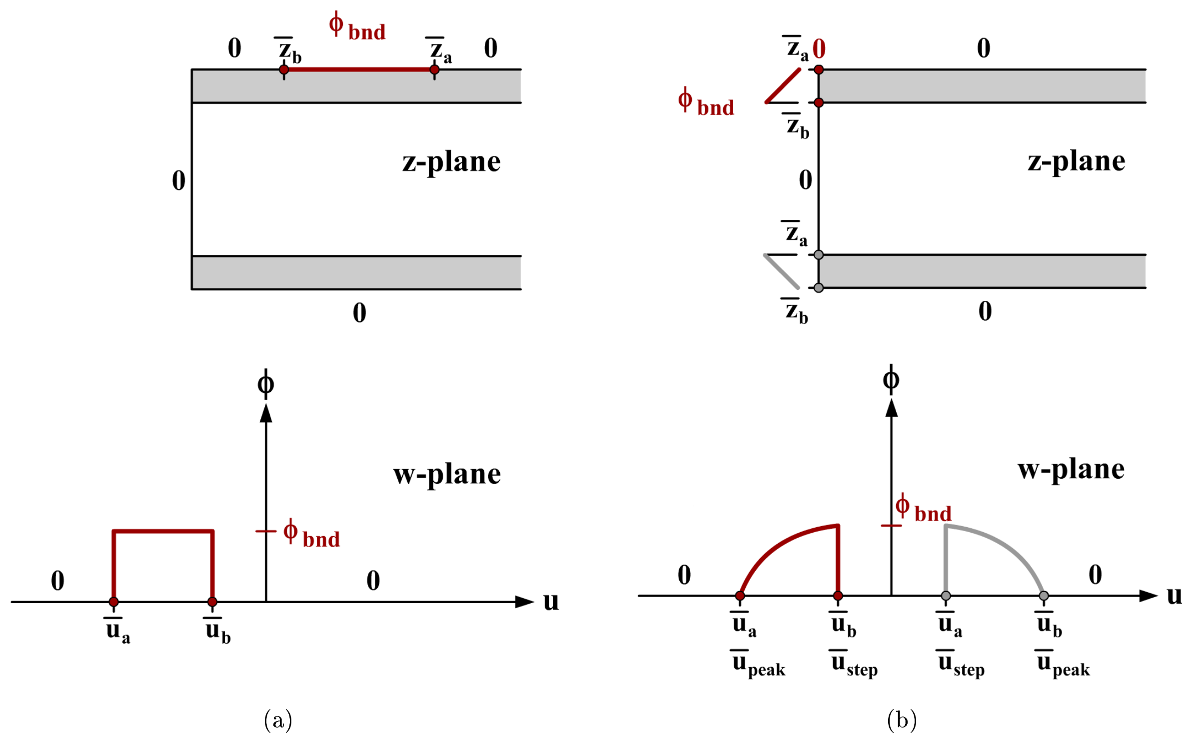

Figure 5.6.: In (a) a constant piecewise boundary in the z-plane mapped to the w-plane and in (b) a linear piecewise boundary in the z-plane mapped to the w-plane is presented, respectively.

where the boundary conditions which are represented by the term $\varphi(\overline{u})$, are depending on z with $\overline{u} = f(\overline{z})$.

If the boundary conditions are constant, see Fig. 5.6(a), it follows

$$\varphi(z) = \frac{1}{\pi} \int_{-\infty}^{+\infty} \frac{v}{(u - \overline{u})^2 + v^2} \cdot \phi_{bnd} \cdot d\overline{u}. \tag{5.21}$$

For linear constant boundaries, see Fig. 5.6(b), one receives the following equation

$$\varphi(z) = \frac{1}{\pi} \int_{-\infty}^{+\infty} \frac{v}{(u - \overline{u})^2 + v^2} \cdot E \cdot \frac{\Delta y}{\pi} \operatorname{arcosh}(\overline{u}) \cdot d\overline{u} \tag{5.22}$$

where the term $\varphi(\overline{u}) = E \cdot \frac{\Delta y}{\pi} \operatorname{arcosh}(\overline{u})$ results from the transformed linear boundary $\varphi(z) = E \cdot x$, and E is the electric field along the boundary.

Both integrals in equation (5.21) and equation (5.22) have to be solved. For the integral in equation (5.21) one is able to find a closed-form solution. It follows the solution for the piecewise constant boundary between $\overline{u}_a$ and $\overline{u}_b$ [177, 179]

$$\varphi_{const}(z, \phi_{bnd}, \overline{u}_a, \overline{u}_b) = -\left. \frac{\phi_{bnd} \cdot \arctan\left(\frac{u - \overline{u}}{v}\right)}{\pi} \right|_{\overline{u}_a}^{\overline{u}_b}. \tag{5.23}$$

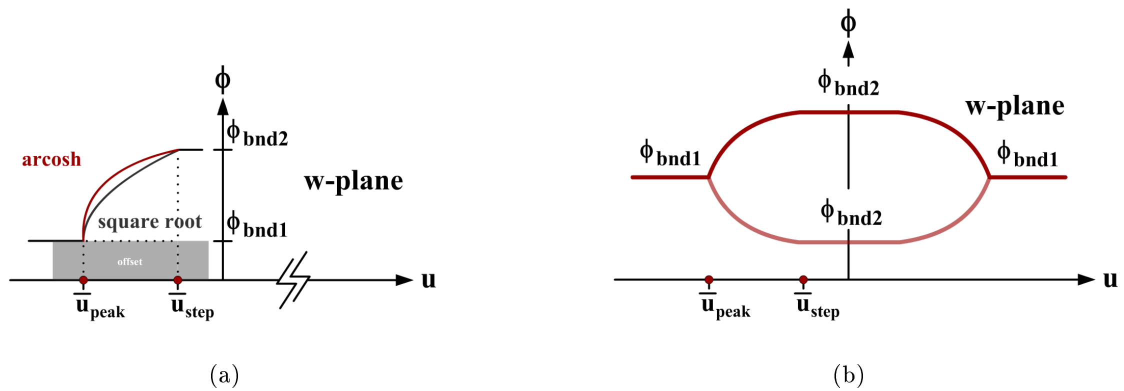

Figure 5.7.: In (a) a square root approximation is used for the arcosh term in the w-plane. In (b) the $\pm$ of equation (5.25) depends on the applied bias conditions of ϕ_{bnd2} and ϕ_{bnd1}.

For the integral in equation (5.22) no primitive was found, therefore the term $\mathrm{E} \cdot \frac{\Delta \mathrm{y}}{\pi} \operatorname{arcosh}(\bar{\mathrm{u}})$ is approximated by a square root function which is similar to an area hyperbolic cosine function

$$\varphi(\mathrm{z}) = \frac{1}{\pi} \int_{-\infty}^{+\infty} \frac{\mathrm{v}}{(\mathrm{u}-\bar{\mathrm{u}})^2 + \mathrm{v}^2} \cdot \pm \sqrt{\frac{\bar{\mathrm{u}} - \mathrm{b}}{\mathrm{a}}} \cdot \mathrm{d}\bar{\mathrm{u}}, \tag{5.24}$$

replacing the area hyperbolic cosine with the square root the following closed-form solution results. It follows the solution for the piecewise linear boundary between $\bar{\mathrm{u}}_{\mathrm{a}}$ and $\bar{\mathrm{u}}_{\mathrm{b}}$ [177, 179]

$$\varphi_{\mathrm{lin}}(\mathrm{z}, \mathrm{a}, \mathrm{b}, \phi_{\mathrm{bnd}}, \bar{\mathrm{u}}_{\mathrm{a}}, \bar{\mathrm{u}}_{\mathrm{b}}) = \pm \frac{\mathrm{j} \arctan\left[\frac{1}{\sigma_4}\left(\mathrm{a} \cdot \mathrm{u} \cdot \sigma_1 \cdot \sigma_3 - \mathrm{a} \cdot \mathrm{b} \cdot \sigma_1 \cdot \sigma_3 + \mathrm{j} \cdot \mathrm{a} \cdot \mathrm{v} \cdot \sigma_1 \cdot \sigma_3\right)\right] \sigma_3}{\pi} + \left. \frac{\mathrm{j} \arctan\left[\frac{1}{\sigma_4}\left(\mathrm{a} \cdot \mathrm{b} \cdot \sigma_1 \cdot \sigma_2 - \mathrm{a} \cdot \mathrm{u} \cdot \sigma_1 \cdot \sigma_2 + \mathrm{j} \cdot \mathrm{a} \cdot \mathrm{v} \cdot \sigma_1 \cdot \sigma_2\right)\right] \sigma_2}{\pi} \right|_{\bar{\mathrm{u}}_{\mathrm{a}}}^{\bar{\mathrm{u}}_{\mathrm{b}}} \tag{5.25}$$

with

$$\sigma_1 = \sqrt{-\frac{\mathrm{b} - \bar{\mathrm{u}}}{\mathrm{a}}}, \quad \sigma_2 = \sqrt{-\frac{\mathrm{u} - \mathrm{b} + \mathrm{j} \cdot \mathrm{v}}{\mathrm{a}}}$$

$$\sigma_3 = \sqrt{\frac{\mathrm{b} - \mathrm{u} + \mathrm{j} \cdot \mathrm{v}}{\mathrm{a}}}, \quad \sigma_4 = \mathrm{b}^2 - 2 \cdot \mathrm{b} \cdot \mathrm{u} + \mathrm{u}^2 + \mathrm{v}^2$$

where the point of interest z is linked to the coordinates u and v in w-plane by equation (5.5). It should be noticed that for the square roots angles of $-\frac{\pi}{2}$ to $\frac{\pi}{2}$ for the complex results are assumed.

UNIVERSITAT ROVIRA I VIRGILI
TWO-DIMENSIONAL ANALYTICAL PREDICTIVE MODELING OF SCHOTTKY BARRIER SOI AND MULTI-GATE MOSFETS
Mike Schwarz
Dipòsit Legal: T.456-2013

From Fig. 5.7(b) the relations are shown, when the closed-form solution of the integral with the square root approximation in equation (5.25) has to be positive for $\phi_{\text{bnd2}} \geq \phi_{\text{bnd1}}$ and negative for $\phi_{\text{bnd2}} < \phi_{\text{bnd1}}$.

Here, $\phi_{\text{bnd}} = \phi_{\text{bnd2}} - \phi_{\text{bnd1}}$ is included in equation (5.25) in the parameter a from the square root approximation.

Square Root Approximation

As described in section 5.3.2 a square root approximation is used for the arcosh term in the Poisson integral in w-plane. A closer view on the approximation and its parameters a and b of equation (5.25) is necessary.

Therefore, a detailed view on the approximation in w-plane is made, because as explained before a linear boundary in the z-plane is represented by an area hyperbolic cosine boundary in the w-plane as shown in Fig. 5.7(a).

From Fig. 5.7(a) a square root approximation is observed, it follows

$$\sqrt{\frac{\bar{\text{u}} - \text{b}}{\text{a}}} \tag{5.26}$$

with a and b as mapped values in the w-plane of the approximated square root function which describe the linear boundary in the z-plane. The parameter b in the square root describes the shift along the u-axis in w-plane. Furthermore, b indicates the peak of the square root, it follows [177]

$$\text{b} = \bar{\text{u}}_{\text{peak}}. \tag{5.27}$$

The parameter a describes the opening coefficient of the square root of the ϕ-axis. In w-plane the parameter is indicated with $\bar{\text{u}}_{\text{step}}$. The calculation of the parameter a for the red case and/or grey case of Fig. 5.6(b) is made with 5.7(a), it follows [177]

$$\phi_{\text{bnd2}} - \phi_{\text{bnd1}} = \pm\sqrt{\frac{\bar{\text{u}}_{\text{step}} - \text{b}}{\text{a}_{\text{red|grey}}}} \tag{5.28}$$

where $\pm$ depends on the applied bias conditions as depicted in Fig. 5.7(b).

Solving with respect to $\text{a}_{\text{red|grey}}$ follows [177]

$$\text{a}_{\text{red|grey}} = \frac{\bar{\text{u}}_{\text{step}} - \text{b}}{(\phi_{\text{bnd2}} - \phi_{\text{bnd1}})^2} \tag{5.29}$$

where $\text{a}_{\text{red}} > 0$ and $\text{a}_{\text{grey}} < 0$.

Electrostatic Potential Solution

After mapping the defined important points, the solutions for each piece can be applied. In equation (5.23), equation (5.25) function values for the variable z are defined which

describe the point of interest. They are inserted as transformed values w calculated from equation (5.5) where $\Delta \mathrm{y} = 2\tilde{\mathrm{t}}_{\mathrm{ox}} + \mathrm{t}_{\mathrm{ch}}$.

Potential piecewise solution source related case

$\underline{ⓘ'' \rightarrow ②}$:

$$\varphi_{\mathrm{const,sce}}\left(\mathrm{w}_{⑥,\mathrm{sce}}, \mathrm{V_g} - \mathrm{V_{fb}}, \overline{\mathrm{u}}_{1''}, \overline{\mathrm{u}}_{2}\right) \tag{5.30}$$

$\underline{② \rightarrow ③}$:

$$\begin{aligned}&\varphi_{\mathrm{const,sce}}\left(\mathrm{w}_{6,\mathrm{sce}}, \mathrm{V_g} - \mathrm{V_{fb}}, \overline{\mathrm{u}}_{2}, \overline{\mathrm{u}}_{3}\right) + \\ &\varphi_{\mathrm{lin,sce}}\left(\mathrm{w}_{6,\mathrm{sce}}, \mathrm{a_{red}}, \mathrm{b}, \mathrm{V_s} + \phi_{\mathrm{bi}} - \mathrm{V_g} + \mathrm{V_{fb}}, \overline{\mathrm{u}}_{2}, \overline{\mathrm{u}}_{3}\right)\end{aligned} \tag{5.31}$$

with

$$\mathrm{a_{red}} = \frac{\overline{\mathrm{u}}_{3} - \mathrm{b}}{\left(\mathrm{V_s} + \phi_{\mathrm{bi}} - \mathrm{V_g} + \mathrm{V_{fb}}\right)^2}$$

and

$$\mathrm{b} = \overline{\mathrm{u}}_{2}$$

where equation (5.25) has to be positive for $\mathrm{V_s} + \phi_{\mathrm{bi}} \geq \mathrm{V_g} - \mathrm{V_{fb}}$ and negative for $\mathrm{V_s} + \phi_{\mathrm{bi}} < \mathrm{V_g} - \mathrm{V_{fb}}$.

$\underline{③ \rightarrow ④}$:

$$\varphi_{\mathrm{const,sce}}\left(\mathrm{w}_{6,\mathrm{sce}}, \mathrm{V_s} + \phi_{\mathrm{bi}}, \overline{\mathrm{u}}_{3}, \overline{\mathrm{u}}_{4}\right) \tag{5.32}$$

$\underline{④ \rightarrow ⑤}$:

$$\begin{aligned}&\varphi_{\mathrm{const,sce}}\left(\mathrm{w}_{6,\mathrm{sce}}, \mathrm{V_g} - \mathrm{V_{fb}}, \overline{\mathrm{u}}_{4}, \overline{\mathrm{u}}_{5}\right) + \\ &\varphi_{\mathrm{lin,sce}}\left(\mathrm{w}_{6,\mathrm{sce}}, \mathrm{a_{grey}}, \mathrm{b}, \mathrm{V_s} + \phi_{\mathrm{bi}} - \mathrm{V_g} + \mathrm{V_{fb}}, \overline{\mathrm{u}}_{4}, \overline{\mathrm{u}}_{5}\right)\end{aligned} \tag{5.33}$$

with

$$\mathrm{a_{grey}} = \frac{\overline{\mathrm{u}}_{4} - \mathrm{b}}{\left(\mathrm{V_s} + \phi_{\mathrm{bi}} - \mathrm{V_g} + \mathrm{V_{fb}}\right)^2}$$

and

$$\mathrm{b} = \overline{\mathrm{u}}_{5}$$

where equation (5.25) has to be positive for $\mathrm{V_s} + \phi_{\mathrm{bi}} \geq \mathrm{V_g} - \mathrm{V_{fb}}$ and negative for $\mathrm{V_s} + \phi_{\mathrm{bi}} < \mathrm{V_g} - \mathrm{V_{fb}}$.

$\underline{⑤ \rightarrow ①'}$:

$$\varphi_{\mathrm{const,sce}}\left(\mathrm{w}_{6,\mathrm{sce}}, \mathrm{V_g} - \mathrm{V_{fb}}, \overline{\mathrm{u}}_{5}, \overline{\mathrm{u}}_{1'}\right) \tag{5.34}$$

Potential piecewise solution drain related case

$\underline{(1") \rightarrow (2)}$:

$$\varphi_{\mathrm{const,drn}}\left(\mathrm{w}_{(6),\mathrm{drn}}, 0, \bar{\mathrm{u}}_{(1")}, \bar{\mathrm{u}}_{(2)}\right) \tag{5.35}$$

$\underline{(2) \rightarrow (3)}$:

$$\begin{aligned}&\varphi_{\mathrm{const,drn}}\left(\mathrm{w}_{(6),\mathrm{drn}}, 0, \bar{\mathrm{u}}_{(2)}, \bar{\mathrm{u}}_{(3)}\right) + \\ &\varphi_{\mathrm{lin,drn}}\left(\mathrm{w}_{(6),\mathrm{drn}}, \mathrm{a}_{\mathrm{red}}, \mathrm{b}, \mathrm{V_d} + \phi_{\mathrm{bi}} - \mathrm{V_g} + \mathrm{V_{fb}}, \bar{\mathrm{u}}_{(2)}, \bar{\mathrm{u}}_{(3)}\right)\end{aligned} \tag{5.36}$$

with

$$\mathrm{a}_{\mathrm{red}} = \frac{\bar{\mathrm{u}}_{(3)} - \mathrm{b}}{\left(\mathrm{V_d} + \phi_{\mathrm{bi}} - \mathrm{V_g} + \mathrm{V_{fb}}\right)^2}$$

and

$$\mathrm{b} = \bar{\mathrm{u}}_{(2)}$$

where equation (5.25) has to be positive for $\mathrm{V_d} + \phi_{\mathrm{bi}} - \mathrm{V_g} + \mathrm{V_{fb}} \geq 0$ and negative for $\mathrm{V_d} + \phi_{\mathrm{bi}} - \mathrm{V_g} + \mathrm{V_{fb}} < 0$.

$\underline{(3) \rightarrow (4)}$:

$$\varphi_{\mathrm{const,drn}}\left(\mathrm{w}_{(6),\mathrm{drn}}, \mathrm{V_d} + \phi_{\mathrm{bi}} - \mathrm{V_g} + \mathrm{V_{fb}}, \bar{\mathrm{u}}_{(3)}, \bar{\mathrm{u}}_{(4)}\right) \tag{5.37}$$

$\underline{(4) \rightarrow (5)}$:

$$\begin{aligned}&\varphi_{\mathrm{const,drn}}\left(\mathrm{w}_{(6),\mathrm{drn}}, 0, \bar{\mathrm{u}}_{(4)}, \bar{\mathrm{u}}_{(5)}\right) + \\ &\varphi_{\mathrm{lin,drn}}\left(\mathrm{w}_{(6),\mathrm{drn}}, \mathrm{a}_{\mathrm{grey}}, \mathrm{b}, \mathrm{V_d} + \phi_{\mathrm{bi}} - \mathrm{V_g} + \mathrm{V_{fb}}, \bar{\mathrm{u}}_{(4)}, \bar{\mathrm{u}}_{(5)}\right)\end{aligned} \tag{5.38}$$

with

$$\mathrm{a}_{\mathrm{grey}} = \frac{\bar{\mathrm{u}}_{(4)} - \mathrm{b}}{\left(\mathrm{V_d} + \phi_{\mathrm{bi}} - \mathrm{V_g} + \mathrm{V_{fb}}\right)^2}$$

and

$$\mathrm{b} = \bar{\mathrm{u}}_{(5)}$$

where equation (5.25) has to be positive for $\mathrm{V_d} + \phi_{\mathrm{bi}} - \mathrm{V_g} + \mathrm{V_{fb}} \geq 0$ and negative for $\mathrm{V_d} + \phi_{\mathrm{bi}} - \mathrm{V_g} + \mathrm{V_{fb}} < 0$.

$\underline{(5) \rightarrow (1')}$:

$$\varphi_{\mathrm{const,drn}}\left(\mathrm{w}_{(6),\mathrm{drn}}, 0, \bar{\mathrm{u}}_{(5)}, \bar{\mathrm{u}}_{(1')}\right) \tag{5.39}$$

From the boundary conditions of the above described parts for the drain related case follows the simplification that the constant solutions of (1")→(2), (2)→(3), (4)→(5) and (5)→(1') $\varphi_{\mathrm{const,drn}} = 0$.

After the calculation of the piecewise solutions a simple superposition of all components is necessary to predict the overall influence on one specific point in the entire

Table 5.2.: Parameter settings of the simulated TCAD device.

l_{ch}	22	[nm]	channel length
t_{ch}	10	[nm]	channel thickness
t_{ox}	2	[nm]	oxide thickness
ϕ_{Bn}	0.28, 0.1	[eV]	SBH electrons
N_B	10^{15}	[cm^{-3}]	substrate doping
ϵ_{ox}	7	[-]	permittivity oxide

channel region of the device. An interior point (x, y) from the complex z-plane is transformed with the help of equation (5.7) and equation (5.8) on the upper half of the complex w-plane. Afterwards, the point $w_{⑥}$, a point (u, v) is used to calculate the influence of the piecewise solutions on the electrostatic potential at the corresponding point (x, y). It follows [177]

$$\begin{aligned}\varphi_{sce}(x,y) =& \varphi_{const,sce,①''\to②+②\to③+③\to④+④\to⑤+⑤\to①'}(x,y)+\\ & \varphi_{lin,sce,②\to③+④\to⑤}(x,y) \end{aligned} \tag{5.40}$$

$$\begin{aligned}\varphi_{drn}(x,y) =& \varphi_{const,drn,③\to④}(x,y)+\\ & \varphi_{lin,drn,②\to③+④\to⑤}(x,y) \end{aligned} \tag{5.41}$$

$$\varphi(x,y) = \varphi_{sce}(x,y) + \varphi_{drn}(x,y). \tag{5.42}$$

5.3.3. Electrostatic Potential Results

Two kind of approaches have been discussed in the above sections. Both approaches, the single vertex from section 3.4.1 and the one solved with Poisson's integral from section 3.4.2, differ slightly and in general the same results are received. However, different approximations for the approaches result in several results for various bias conditions. The solutions of both approaches are compared with numerical device simulations of TCAD Sentaurus [64] with the parameters shown in Table 5.2. The estimated threshold voltages from the numerical device simulations of TCAD Sentaurus [64] for the investigated devices are shown in Table 5.3 [177].

In Fig. 5.8(a) the comparison of the electrostatic potential between the two approaches within a SB-DG-MOSFET for a slice at the middle of the channel is shown. As we can observe for the device with a Schottky barrier height ϕ_{Bn}=0.28 eV, the difference between the approach of the single vertex solution (blue lines) and the approach of the square root approximation solution (red lines) is likely to be non existing. No essential difference between both solutions can be observed, especially if one has a more detailed view on Fig. 5.8(b) where the source section is zoomed. Furthermore, the comparison

Table 5.3.: Estimated threshold voltages for the investigated devices from TCAD Sentaurus.

SBH electrons device parameter	V_{th}
$\phi_{Bn} = 0.28\,eV$	$\approx 0.744\,V$
$\phi_{Bn} = 0.1\,eV$	$\approx 0.457\,V$

to the simulated data (black symbols), shows a very good agreement for the several bias conditions [177].

From Fig. 5.8(a) it is easy to recognize that for V_g=1 V inversion region starts to be reached and additional charge carriers influence the results. Therefore, the accuracy of the model decreases. Also this influence can be observed for Fig. 5.9(a) for a cut underneath the silicon-to-oxide interface along the channel. Comparing both cuts due to the emerging inversion charge carriers (electrons) which shield the influence of the gate, it is clear that near the silicon-to-oxide interface the influence is lower. It should be stated out that this behavior is to be observed in the middle of the device for a cross section from gate to gate. Also an inaccuracy for a V_g=−0.2 V due to the emerging accumulation charge carriers (holes) is observed. The identical behavior as for the emerging inversion charge carriers results [177].

However, the observed higher inaccuracy close to the device junctions as in Fig. 5.9(a) presented, is a product of the made approximation within the oxide region in the potential solution. Normally, a non linear voltage drop in the oxide has to be assumed. If a parabolic voltage drop is used, no closed-form solutions can be developed. Therefore, a linear voltage drop was applied as explained before. From this approximation especially the inaccuracies closed to the junctions result for the slices underneath the silicon-to-oxide interface while at the middle of the device the influence is less [177].

Furthermore, the difference is negligible for a cut at the silicon-to-oxide interface, see Fig. 5.9(a), between the compared approaches at the source and drain junction is observed. The detailed figure from the source section, see Fig. 5.9(b), shows that the difference results in a few mV [177].

3D plots of the absolute deviation $\sigma(x, y)$ between the single vertex approach which is set as reference, and the square root approximation approach are given in Fig. 5.10(a) and 5.10(b) for two different bias conditions. From both plots it can be observed that this difference is about a few mV only over the channel region of a SB-DG-MOSFET [177].

Furthermore, a similar behavior for both approaches can be observed for a device with a Schottky barrier height ϕ_{Bn}=0.1 eV. The identical behavior due to the emerging charges as well as for the approach comparison could be observed. For a slice at the middle of the channel, see Fig. 5.11(a) and 5.11(b), the difference between both approaches is of minor importance and can be neglected. At the silicon-to-oxide interface, again

Table 5.4.: MatLab computation time and memory consumption for the potential.

Resolution $(\Delta l_{ch}, \Delta t_{ch})$	Approach	Computation time	Memory
1 nm	SingleVertex (n=50)	0.044 s	1 MB
	SingleVertex (n=10)	0.010 s	0.15 MB
	SquareRoot	0.008 s	0.3 MB
0.1 nm	SingleVertex (n=50)	1.574 s	21.5 MB
	SingleVertex (n=10)	0.353 s	2 MB
	SquareRoot	0.250 s	3.8 MB
0.01 nm	SingleVertex (n=50)	110.258 s	2.61 GB
	SingleVertex (n=10)	13.798 s	0.43 GB
	SquareRoot	9.965 s	0.47 GB

one is able to observe a difference at the source and drain regions which is negligible, Fig. 5.12(a) and 5.12(b). Over the entire channel region the difference amounts a few mV. This is shown in the 3D plots of the absolute deviation $\sigma(x, y)$, see Fig. 5.13(a) and 5.13(b) [177].

Both approaches calculate the electrostatic potential very well compared to the numerical device simulations of TCAD Sentaurus. The difference of both predictions is very low, nearly the same results are calculated by both approaches. However, the approach of the square root approximation has several advantages. The solution is closed-form while for the single vertex approach still sums are needed. Due to this reason, the computation time (average), estimated with the MatLab profiler, of the square root approximation solution is up to ten times lower compared to the single vertex solution for an arbitrary bias condition for a device with l_{ch}=22 nm and t_{ch}=10 nm, if the resolution $(\Delta l_{ch}, \Delta t_{ch})$=0.01 nm (channel region resolution) and n=50 (step number), Table 5.4. All given plots were estimated with a channel resolution of $(\Delta l_{ch}, \Delta t_{ch})$=0.1 nm. This resolution is sufficient enough and need only a fractional amount of the calculation time compared to numerical simulation tools like TCAD [177].

Furthermore, in this case the memory consumption is less for the square root approximation. With decreasing n=10, the single vertex approach is comparable with the square root approximation, but looses accuracy. Beside the advantages the square root approximation includes one disadvantage which results from the approximation of the inverse hyperbolic cosine. With increasing length of the linear piecewise the approximation looses its accuracy [177]. A verification is given in the Appendix C.

Due to the made comparison of both approaches in terms of accuracy, computation time and memory consumption the approach of the square root approximation is chosen to calculate the current contributions in the next chapter for reasonable device structures.

UNIVERSITAT ROVIRA I VIRGILI
TWO-DIMENSIONAL ANALYTICAL PREDICTIVE MODELING OF SCHOTTKY BARRIER SOI AND MULTI-GATE MOSFETS
Mike Schwarz
Dipòsit Legal: T.456-2013

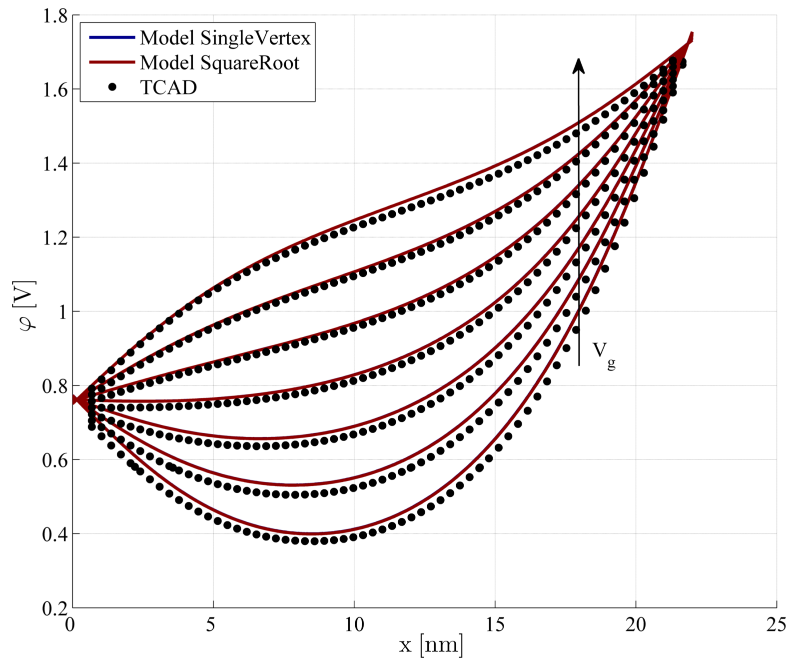

(a)

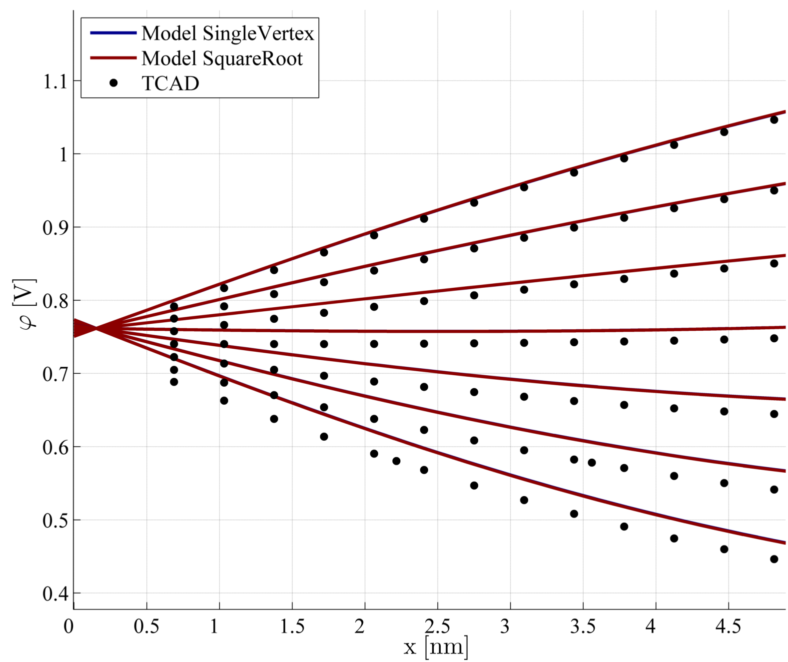

(b)

Figure 5.8.: Electrostatic potential φ (a) at the middle of the channel, (b) at the middle of the channel source section for a SB-DG-MOSFET. Results for ϕ_{Bn}=0.28 eV. Device geometry: l_{ch}=22 nm, t_{ch}=10 nm, t_{ox}=2 nm. Bias conditions: V_{ds}=1 V, V_g=−0.2 V to 1 V with 0.2 V stepping.

UNIVERSITAT ROVIRA I VIRGILI
TWO-DIMENSIONAL ANALYTICAL PREDICTIVE MODELING OF SCHOTTKY BARRIER SOI AND MULTI-GATE MOSFETS
Mike Schwarz
Dipòsit Legal: T.456-2013

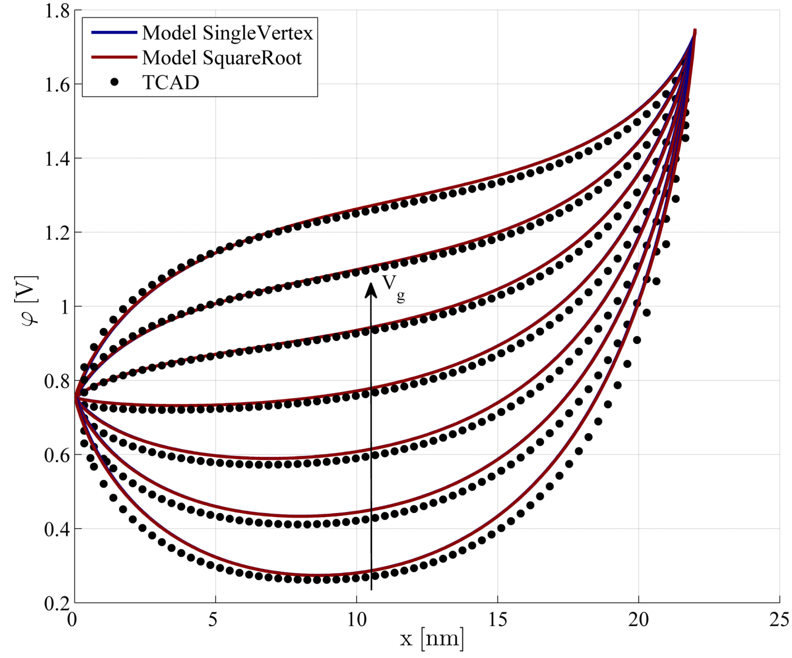

(a)

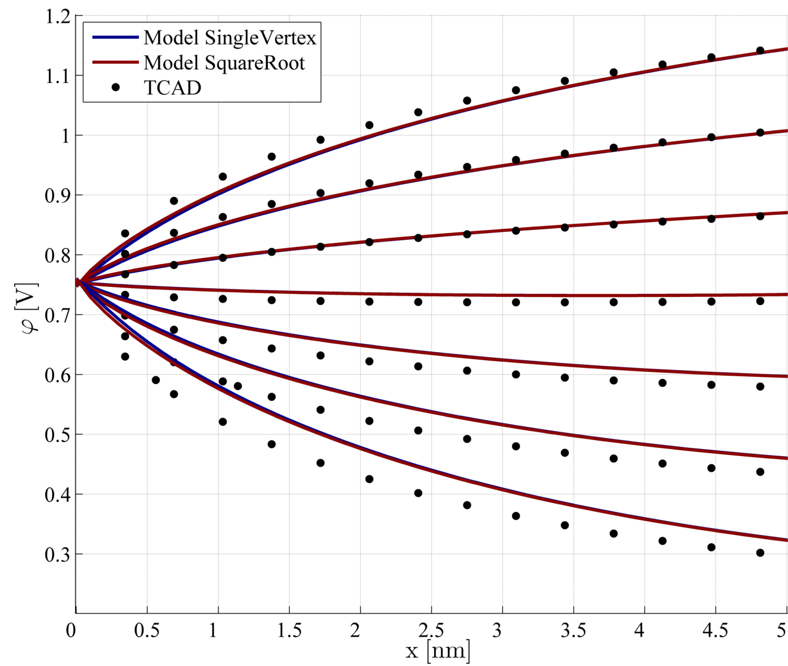

(b)

Figure 5.9.: Electrostatic potential φ (a) at the silicon-to-oxide interface, (b) at the silicon-to-oxide interface source section for a SB-DG-MOSFET. Results for ϕ_{Bn}=0.28 eV. Device geometry: l_{ch}=22 nm, t_{ch}=10 nm, t_{ox}=2 nm. Bias conditions: V_{ds}=1 V, V_g=−0.2 V to 1 V with 0.2 V stepping.

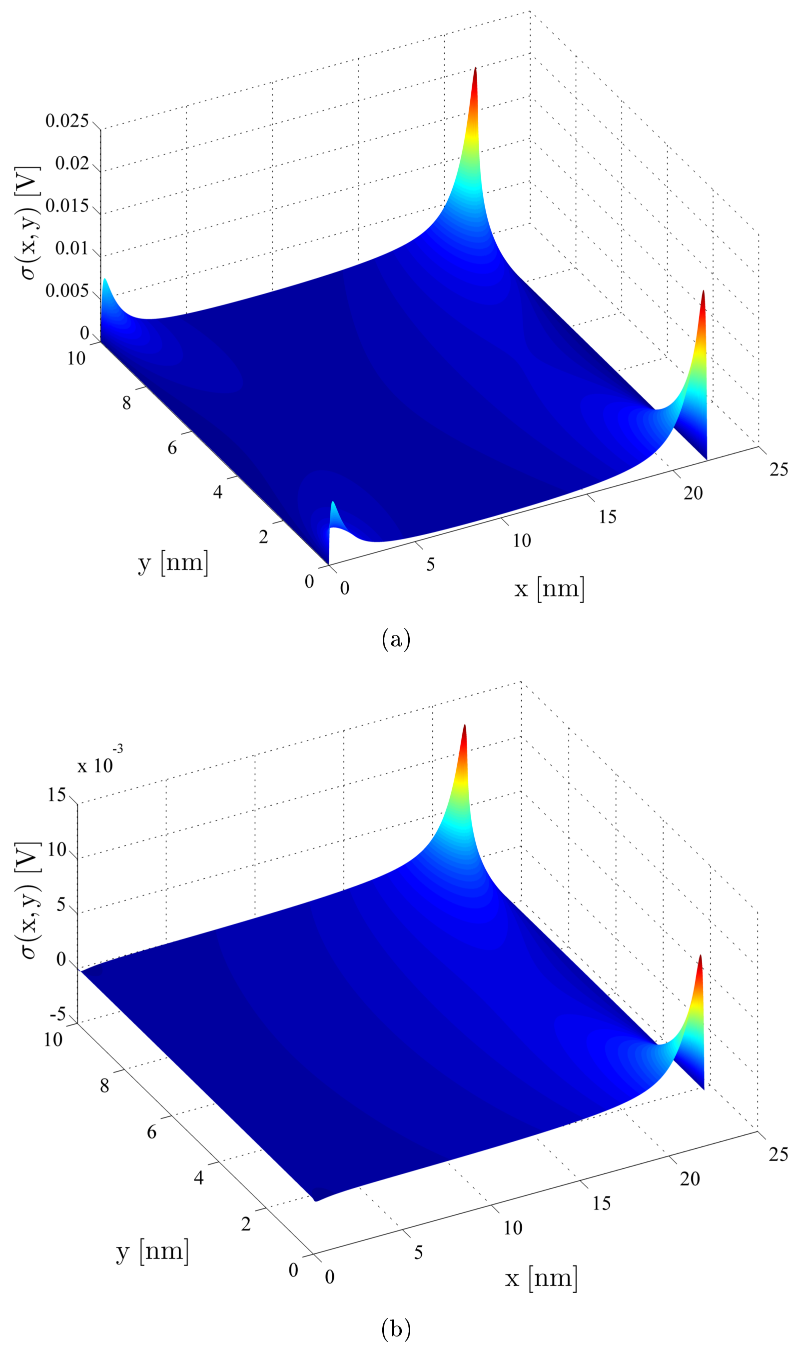

Figure 5.10.: 3D plot of absolute deviation $\sigma(x, y)$ between the single vertex approach (reference) and the square root approximation approach. Results for ϕ_{Bn}=0.28 eV. Device geometry: l_{ch}=22 nm, t_{ch}=10 nm, t_{ox}=2 nm. Bias conditions: (a) V_{ds}=1 V, V_g=−0.3 V, (b) V_{ds}=1 V, V_g=0.3 V.

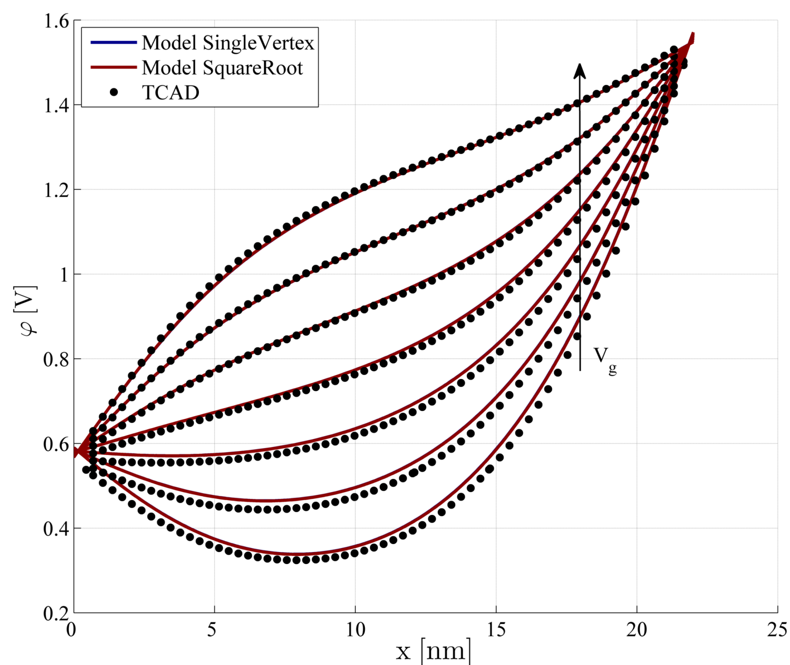

(a)

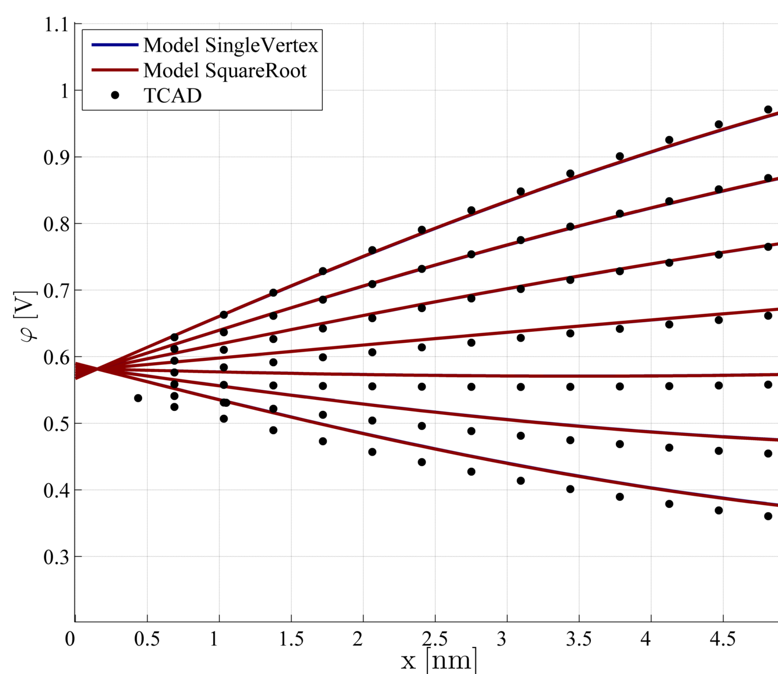

(b)

Figure 5.11.: Electrostatic potential φ (a) at the middle of the channel, (b) at the middle of the channel source section for a SB-DG-MOSFET. Results for ϕ_{Bn}=0.1 eV. Device geometry: l_{ch}=22 nm, t_{ch}=10 nm, t_{ox}=2 nm. Bias conditions: V_{ds}=1 V, V_g=−0.2 V to 1 V with 0.2 V stepping.

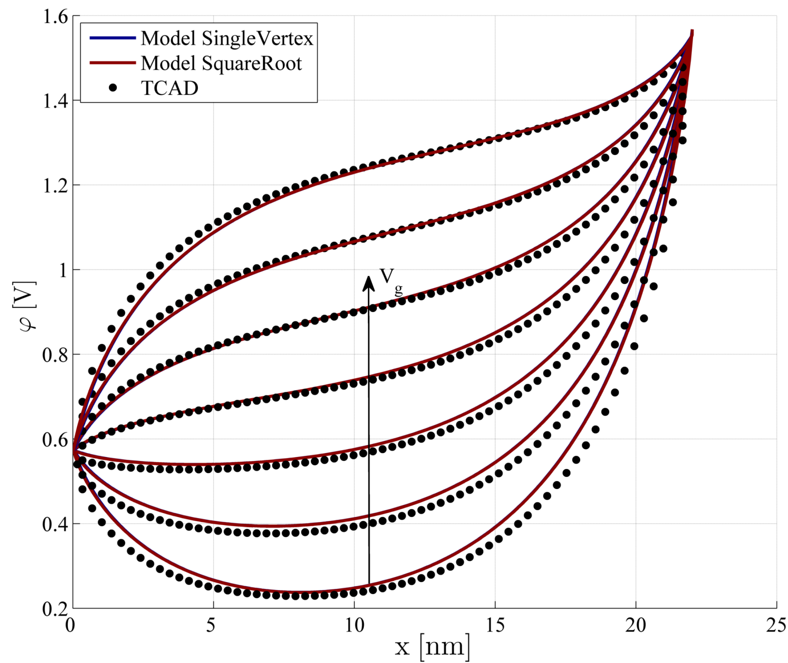

(a)

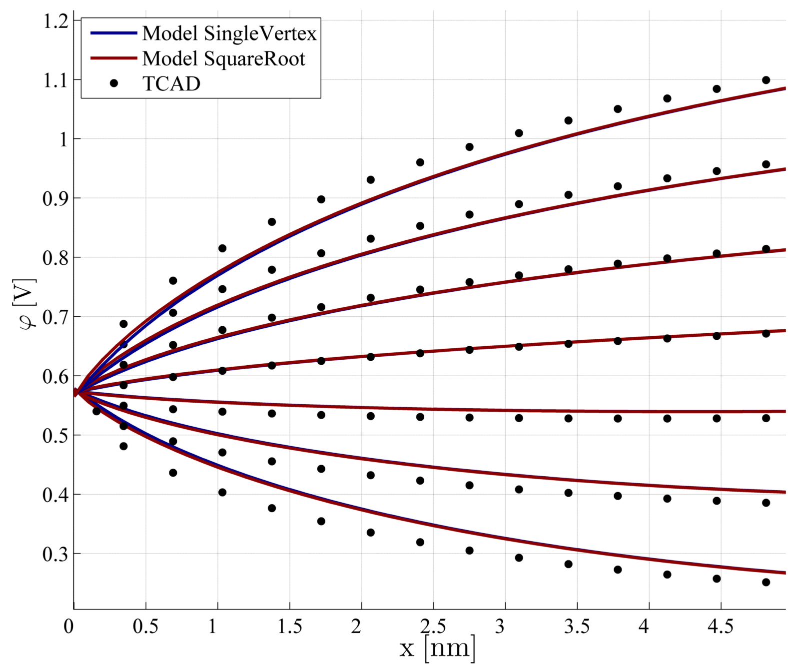

(b)

Figure 5.12.: Electrostatic potential φ (a) at the silicon-to-oxide interface, (b) at the silicon-to-oxide interface source section for a SB-DG-MOSFET. Results for ϕ_{Bn}=0.1 eV. Device geometry: l_{ch}=22 nm, t_{ch}=10 nm, t_{ox}=2 nm. Bias conditions: V_{ds}=1 V, V_g=−0.2 V to 1 V with 0.2 V stepping.

UNIVERSITAT ROVIRA I VIRGILI
TWO-DIMENSIONAL ANALYTICAL PREDICTIVE MODELING OF SCHOTTKY BARRIER SOI AND MULTI-GATE MOSFETS
Mike Schwarz
Dipòsit Legal: T.456-2013

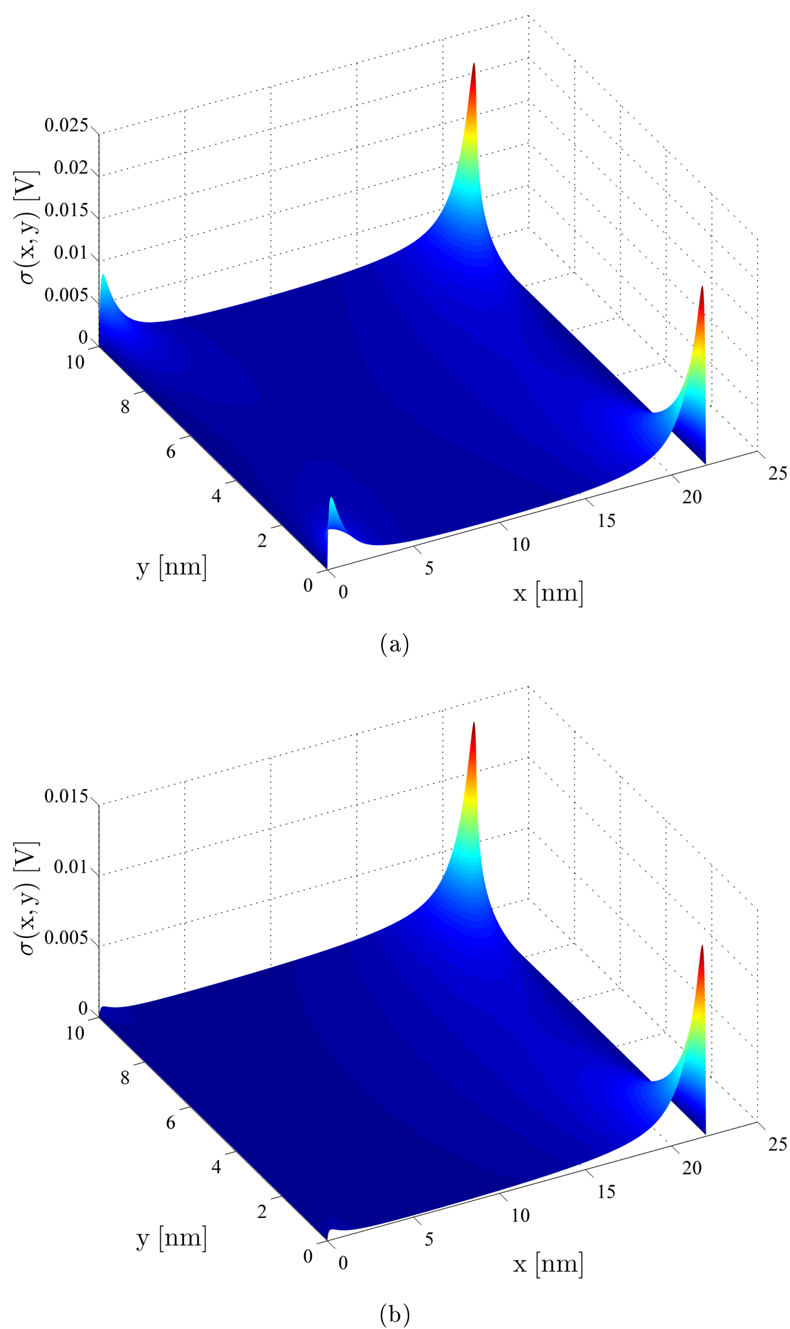

Figure 5.13.: 3D plot of absolute deviation $\sigma(x, y)$ between the single vertex approach (reference) and the square root approximation approach. Results for ϕ_{Bn}=0.1 eV. Device geometry: l_{ch}=22 nm, t_{ch}=10 nm, $t_{ox}4$=2 nm. Bias conditions: (a) V_{ds}=1 V, V_g=−0.2 V, (b) V_{ds}=1 V, V_g=0.4 V.

5.4. Electric Field

As for the electrostatic potential in section 5.3 also the preliminaries for the electric field are necessary. Then the electric field can be solved by the Schwarz-Christoffel transformation. The closed-form solution of the electric field is based on the single vertex approach from section 3.4.1. With the help of some further approximations an explicit equation is derived.

Before developing the solution for the electric field, again the several important points along the boundary from Fig. 5.5 have to be marked. They will define later as already for the electrostatic potential the applied boundary conditions. With the conformal mapping technique everything is transformed into w-plane and all points lay on the real axis, except the arbitrary point within the channel region which is located upon the upper half of w-plane, see Fig 5.5.

5.4.1. Single Vertex Approach

The single vertex approach from equation (3.29) was chosen to solve the electric field problem in the upper half of w-plane. Figure 3.4 contains the structure which shows an infinitesimal gap at position $\overline{\mathrm{u}}$ for two electrodes along the real axis u and equation (3.29) follows [137,178].

$$\mathrm{P} = \Phi + \mathrm{j}\Xi = \mathrm{d}\varphi + \mathrm{j}\frac{\mathrm{d}\varphi}{\pi}\ln(\mathrm{w} - \overline{\mathrm{u}}). \tag{5.43}$$

Applying the Cauchy Riemann differential equations [137] the electric field in the w-plane for the two coplanar electrodes in Fig. 3.4 with the potential difference $\mathrm{d}\varphi$ can be calculated in the following way [176,180,181].

The electric field in w-plane is expressed as

$$\mathrm{d}\underline{\mathrm{E}}_{(\mathrm{w})} = -\frac{\partial\Phi}{\partial\mathrm{w}}, \tag{5.44}$$

and one is able to write for

$$-\frac{\partial\Phi}{\partial\mathrm{w}} = -\frac{\partial\Phi}{\partial\mathrm{u}} + \mathrm{j}\frac{\partial\Phi}{\partial\mathrm{v}}. \tag{5.45}$$

Now applying the Cauchy Riemann differential equations to (5.45) one receives

$$-\frac{\partial\Phi}{\partial\mathrm{w}} = \left(-\frac{\partial\Xi}{\partial\mathrm{v}} + \mathrm{j}\frac{\partial\Xi}{\partial\mathrm{u}}\right). \tag{5.46}$$

UNIVERSITAT ROVIRA I VIRGILI
TWO-DIMENSIONAL ANALYTICAL PREDICTIVE MODELING OF SCHOTTKY BARRIER SOI AND MULTI-GATE MOSFETS
Mike Schwarz
Dipòsit Legal: T.456-2013

From the imaginary part Ξ of equation (3.29) it follows

$$\begin{aligned}\Xi(\mathrm{u},\mathrm{v}) &= \mathrm{Im}\left\{\mathrm{d}\varphi + \mathrm{j}\frac{\mathrm{d}\varphi}{\pi}\ln(\mathrm{w}-\overline{\mathrm{u}})\right\}\\ &= \mathrm{Re}\left\{\frac{\mathrm{d}\varphi}{\pi}\ln(\mathrm{w}-\overline{\mathrm{u}})\right\}\\ &= \frac{\mathrm{d}\varphi}{\pi}\ln\sqrt{(\mathrm{u}-\overline{\mathrm{u}})^2+\mathrm{v}^2},\end{aligned} \tag{5.47}$$

and with equation (5.46) one is able to write for

$$-\frac{\partial\Phi}{\partial\mathrm{w}} = \left(-\frac{\partial}{\partial\mathrm{v}} + \mathrm{j}\frac{\partial}{\partial\mathrm{u}}\right)\frac{\mathrm{d}\varphi}{\pi}\ln\sqrt{(\mathrm{u}-\overline{\mathrm{u}})^2+\mathrm{v}^2}. \tag{5.48}$$

In equation (5.48) one differentiates with respect to u and v and receive

$$\begin{aligned}-\frac{\partial\Phi}{\partial\mathrm{w}} &= -\frac{\mathrm{d}\varphi}{\pi}\frac{\mathrm{v}}{\sqrt{(\mathrm{u}-\overline{\mathrm{u}})^2+\mathrm{v}^2}\sqrt{(\mathrm{u}-\overline{\mathrm{u}})^2+\mathrm{v}^2}} + \frac{\mathrm{d}\varphi}{\pi}\frac{(\mathrm{u}-\overline{\mathrm{u}})}{\sqrt{(\mathrm{u}-\overline{\mathrm{u}})^2+\mathrm{v}^2}\sqrt{(\mathrm{u}-\overline{\mathrm{u}})^2+\mathrm{v}^2}}\\ &= -\mathrm{j}\frac{\mathrm{d}\varphi}{\pi}\frac{\mathrm{v}-\mathrm{j}(\mathrm{u}-\overline{\mathrm{u}})}{(\mathrm{u}-\overline{\mathrm{u}})^2+\mathrm{v}^2} = \mathrm{j}\frac{\mathrm{d}\varphi}{\pi}\frac{(\mathrm{u}-\overline{\mathrm{u}})+\mathrm{j}\mathrm{v}}{(\mathrm{u}-\overline{\mathrm{u}})^2+\mathrm{v}^2}.\end{aligned} \tag{5.49}$$

With a complex conjugate of equation (5.49) it follows

$$\begin{aligned}-\frac{\partial\Phi}{\partial\mathrm{w}} &= \mathrm{j}\frac{\mathrm{d}\varphi}{\pi}\frac{(\mathrm{u}-\overline{\mathrm{u}})+\mathrm{j}\mathrm{v}}{[(\mathrm{u}-\overline{\mathrm{u}})+\mathrm{j}\mathrm{v}]\,[(\mathrm{u}-\overline{\mathrm{u}})-\mathrm{j}\mathrm{v}]}\\ &= \mathrm{j}\frac{\mathrm{d}\varphi}{\pi}\frac{1}{(\mathrm{u}-\overline{\mathrm{u}})-\mathrm{j}\mathrm{v}} = \mathrm{j}\frac{\mathrm{d}\varphi}{\pi}\frac{1}{\mathrm{w}^*-\overline{\mathrm{u}}}.\end{aligned} \tag{5.50}$$

Therefore, the electric field in the w-plane is

$$\mathrm{d}\underline{\mathrm{E}}_{(\mathrm{w})} = \mathrm{j}\frac{\mathrm{d}\varphi}{\pi}\frac{1}{\mathrm{w}^*-\overline{\mathrm{u}}}. \tag{5.51}$$

Closed-form Solution Electric Field

For the calculation of the electrical field strength at a corresponding point in the complex z-plane, it is necessary to scale equation (5.51) by the derivative $\left|\frac{\mathrm{dw}}{\mathrm{dz}}\right|$ of the mapping function [137]

$$\mathrm{d}\underline{\mathrm{E}} = \mathrm{d}\underline{\mathrm{E}}_{(\mathrm{z})} = \left|\frac{\mathrm{dw}}{\mathrm{dz}}\right|\frac{\mathrm{d}\varphi}{\pi}\frac{1}{\mathrm{w}^*-\overline{\mathrm{u}}}. \tag{5.52}$$

The derivative $\left|\frac{\mathrm{dw}}{\mathrm{dz}}\right|$ is calculated with

$$\left|\frac{\mathrm{dw}}{\mathrm{dz}}\right| = \frac{1}{\left|\frac{\mathrm{dz}}{\mathrm{dw}}\right|} \tag{5.53}$$

where $\left|\frac{\mathrm{dz}}{\mathrm{dw}}\right|$ is expressed with equation (5.2) by

$$\left|\frac{\mathrm{dz}}{\mathrm{dw}}\right| = \frac{\mathrm{C}}{\sqrt{\mathrm{w}-1}\sqrt{\mathrm{w}+1}}. \tag{5.54}$$

Here, w is received from the conformal mapping and $\mathrm{C} = \left(2 \cdot \tilde{\mathrm{t}}_{\mathrm{ox}} + \mathrm{t}_{\mathrm{ch}}\right)/\pi$.

If one superpose several boundary conditions, each with a different position of the infinitesimal gap $\overline{\mathrm{u}}$ between the electrodes and several potential differences $\mathrm{d}\varphi$, then a step-like potential results along the u-axis or rather a linear potential drop. For infinitesimal gaps $\mathrm{d}\overline{\mathrm{u}}$ between the electrodes the potential difference is given by

$$\mathrm{d}\varphi = \left.\frac{\partial\varphi(\mathrm{u})}{\partial \mathrm{u}}\right|_{\overline{\mathrm{u}}} \mathrm{d}\overline{\mathrm{u}}, \tag{5.55}$$

then the superposition obtains $\varphi(\mathrm{u})$ as boundary condition of the first order along the u-axis. With equation (5.52) the electric field strength in the complex z-plane becomes

$$\begin{aligned} \underline{\mathrm{E}}_{(\mathrm{z})} &= \left|\frac{\mathrm{dw}}{\mathrm{dz}}\right| \int_{-\infty}^{+\infty} \mathrm{d}\underline{\mathrm{E}}_{(\mathrm{w})} \\ &= \frac{1}{\pi}\left|\frac{\mathrm{dw}}{\mathrm{dz}}\right| \int_{-\infty}^{+\infty} \frac{1}{\mathrm{w}^* - \overline{\mathrm{u}}} \left.\frac{\partial\varphi(\mathrm{u})}{\partial \mathrm{u}}\right|_{\overline{\mathrm{u}}} \mathrm{d}\overline{\mathrm{u}}. \end{aligned} \tag{5.56}$$

This approach for the electric field is applied to the model. If the integration takes place along the boundaries only contributions of the electric field with non-zero value have to be considered, because for those the integral will result in a non-zero value. This is the case for the oxide regions where a linear voltage drop is assumed, all other parts have constant boundary conditions with an electric field of zero. The corresponding relations between the complex w-plane and complex z-plane are used and the expression $\left.\frac{\partial\varphi(\mathrm{u})}{\partial \mathrm{u}}\right|_{\overline{\mathrm{u}}} \mathrm{d}\overline{\mathrm{u}}$ from equation (5.56) is substituted with

$$\left.\frac{\partial\varphi(\mathrm{u})}{\partial \mathrm{u}}\right|_{\overline{\mathrm{u}}} \mathrm{d}\overline{\mathrm{u}} = \frac{\partial \mathrm{y}}{\partial \overline{\mathrm{u}}}\frac{\partial \varphi}{\partial \mathrm{y}} \mathrm{d}\overline{\mathrm{u}}. \tag{5.57}$$

Furthermore, one replaces the expression $\frac{\partial \mathrm{y}}{\partial \overline{\mathrm{u}}} = 1/\sqrt{1-\overline{\mathrm{u}}^2} \cdot \Delta \mathrm{y}/\pi$ from the conformal mapping function and $\frac{\partial \varphi}{\partial \mathrm{y}} = \mathrm{E_y} = \mathrm{const}$ in equation (5.57), see Fig. 5.2(a). Here, $\mathrm{E_y} = \mathrm{const}$ due to the linear voltage drop approximation within the oxide. $\Delta \mathrm{y}$ results from the geometry of the device. The solution of the integral in equation (5.56) with equation (5.57) is

$$\begin{aligned} \underline{\mathrm{E}}_{(\mathrm{z})} &= \frac{1}{\pi}\left|\frac{\mathrm{dw}}{\mathrm{dz}}\right| \mathrm{E_y} \int_{\overline{\mathrm{u}}_\mathrm{a}}^{\overline{\mathrm{u}}_\mathrm{b}} \frac{1}{\mathrm{w}^* - \overline{\mathrm{u}}} \frac{1}{\sqrt{1-\overline{\mathrm{u}}^2}} \frac{\Delta \mathrm{y}}{\pi} \mathrm{d}\overline{\mathrm{u}} \\ &= \frac{1}{\pi}\left|\frac{\mathrm{dw}}{\mathrm{dz}}\right| \mathrm{E_y} \left[-\frac{\Delta \mathrm{y}}{\pi} \frac{\sigma}{\sqrt{1-\mathrm{w}^{*2}}}\right]_{\overline{\mathrm{u}}_\mathrm{a}}^{\overline{\mathrm{u}}_\mathrm{b}} \end{aligned} \tag{5.58}$$

with

$$\sigma = \ln\left(\frac{\sqrt{\overline{\mathrm{u}}^2 - 1} + (\overline{\mathrm{u}} \cdot \mathrm{w}^* - 1)\sqrt{\frac{1}{\mathrm{w}^{*2}-1}}}{\overline{\mathrm{u}} - \mathrm{w}^*}\right)$$

where w^* describes the conjugate complex point of point w where the electric field is calculated.

Electric Field Solution

After mapping the defined important points, the solutions for each piece can be applied. In equation (5.58) function values for the variable z are defined which describe the point of interest. Furthermore, the equation has been developed from the structure in Fig. 5.5. Nevertheless, the equation can be applied orthogonal to the structure from Fig. 5.5. Therefore, $\mathrm{E_y}$ from equation (5.58), in general, can be replaced by $\mathrm{E_{x|y}}$. It follows

$$\underline{\mathrm{E}}(\mathrm{z}, \mathrm{E_{x|y}}, \bar{\mathrm{u}}_\mathrm{a}, \bar{\mathrm{u}}_\mathrm{b}) = \frac{1}{\pi}\left|\frac{\mathrm{dw}}{\mathrm{dz}}\right| \mathrm{E_{x|y}} \left[-\frac{\Delta \mathrm{y}}{\pi} \frac{\sigma}{\sqrt{1-\mathrm{w}^{*2}}} \right] \Bigg|_{\bar{\mathrm{u}}_\mathrm{a}}^{\bar{\mathrm{u}}_\mathrm{b}} \tag{5.59}$$

The defined important points are insert as transformed values w calculated from equation (5.5) where $\Delta\mathrm{y} = 2\tilde{\mathrm{t}}_\mathrm{ox} + \mathrm{t_{ch}}$.

From the boundary conditions of the above described parts for the drain related case follows the simplification that the constant solutions of ①"→②, ②→③, ④→⑤ and ⑤→①' $\varphi_{\mathrm{const,drn}} = 0$.

Electric field piecewise solution source related case

<u>② → ③</u> :

$$\underline{\mathrm{E}}_\mathrm{sce}\left(\mathrm{w}_{⑥,\mathrm{sce}}, \mathrm{E_y}, \bar{\mathrm{u}}_{②}, \bar{\mathrm{u}}_{③}\right) \tag{5.60}$$

with

$$\mathrm{E_y} = \frac{\mathrm{V_g} - \mathrm{V_{fb}} - (\mathrm{V_s} + \phi_\mathrm{bi})}{\tilde{\mathrm{t}}_\mathrm{ox}}.$$

<u>④ → ⑤</u> :

$$\underline{\mathrm{E}}_\mathrm{sce}\left(\mathrm{w}_{⑥,\mathrm{sce}}, \mathrm{E_y}, \bar{\mathrm{u}}_{④}, \bar{\mathrm{u}}_{⑤}\right) \tag{5.61}$$

with

$$\mathrm{E_y} = -\frac{\mathrm{V_g} - \mathrm{V_{fb}} - (\mathrm{V_s} + \phi_\mathrm{bi})}{\tilde{\mathrm{t}}_\mathrm{ox}}.$$

Electric field piecewise solution drain related case

<u>② → ③</u> :

$$\underline{\mathrm{E}}_\mathrm{drn}\left(\mathrm{w}_{⑥,\mathrm{drn}}, \mathrm{E_y}, \bar{\mathrm{u}}_{②}, \bar{\mathrm{u}}_{③}\right) \tag{5.62}$$

with

$$\mathrm{E_y} = -\frac{-\mathrm{V_g} + \mathrm{V_{fb}} + (\mathrm{V_d} + \phi_\mathrm{bi})}{\tilde{\mathrm{t}}_\mathrm{ox}}.$$

<u>④ → ⑤</u> :

$$\underline{\mathrm{E}}_\mathrm{drn}\left(\mathrm{w}_{⑥,\mathrm{drn}}, \mathrm{E_y}, \bar{\mathrm{u}}_{④}, \bar{\mathrm{u}}_{⑤}\right) \tag{5.63}$$

with

$$E_y = \frac{-V_g + V_{fb} + (V_d + \phi_{bi})}{\tilde{t}_{ox}}.$$

Finally, after the calculation of the piecewise parts a superposition takes place to predict the overall influence on one specific point in the entire channel region of the device. An interior point (x, y) from the complex z-plane is transformed with the help of equation (5.7) and equation (5.8) on the upper half of the complex w-plane. Afterwards, the point $w_{⑥}$, a point (u, v) is used to calculate the influence of the piecewise solutions on the electric field at the corresponding point (x, y). It follows [176, 180, 181]

$$\underline{E}_{sce}(x, y) = \underline{E}_{sce,②\to③}(x, y) + \underline{E}_{sce,④\to⑤}(x, y) \quad (5.64)$$

$$\underline{E}_{drn}(x, y) = \underline{E}_{drn,②\to③}(x, y) + \underline{E}_{drn,④\to⑤}(x, y) \quad (5.65)$$

$$\underline{E}(x, y) = \underline{E}_{sce}(x, y) + \underline{E}_{drn}(x, y). \quad (5.66)$$

5.4.2. Electric Field Results

The developed approach for the electric field is based on the single vertex from section 3.4.1 as already described. The closed-form solution and the following presented results are calculated with identical parameters (refer to Table 5.2 and 5.3), and compared with numerical device simulations of TCAD Sentaurus [64].

Fig. 5.14(a) to 5.15(b) show the electric field for a SB-DG-MOSFET device with a Schottky barrier height of ϕ_{Bn}=0.28 eV and ϕ_{Bn}=0.1 eV for slices at the middle of the channel and the silicon-to-oxide interface along the channel [176, 182].

As one can observe from Fig. 5.14(a) for a Schottky barrier height ϕ_{Bn}=0.28 eV with V_{ds} =1 V, the model (red lines) returns good results compared to the simulated data (black symbols) for several V_g. Taking a closer look onto the behavior of the electric field shows that the electric field for a cut at the middle of the channel for several V_g and V_{ds}=1 V is accurate, Fig. 5.14(a). A very good match between the model and the simulated curves from TCAD Sentaurus can be recognized. Furthermore, the inaccuracy due to the emerging charge carriers from accumulation and inversion can be noticed. Also it can be observed, the higher V_g becomes, the closer the potential minimum ($|E| = 0$) moves to the source contact. Moreover, the model predicts the intersection point in the middle of the device (l_{ch}=11 nm) very well [176, 182].

If one moves from the middle of the channel to the silicon-to-oxide interface as displayed in Fig. 5.14(b), a good agreement expect the region between 5 nm and 15 nm is observed. The deeper one moves from the metal-semiconductor source and drain contact into the channel, the higher the inaccuracy becomes. The same behavior is observed for a barrier height of ϕ_{Bn}=0.1 eV. However, this effect results from the made decomposition, but might be negligible on the device tunneling current behavior [176, 182].

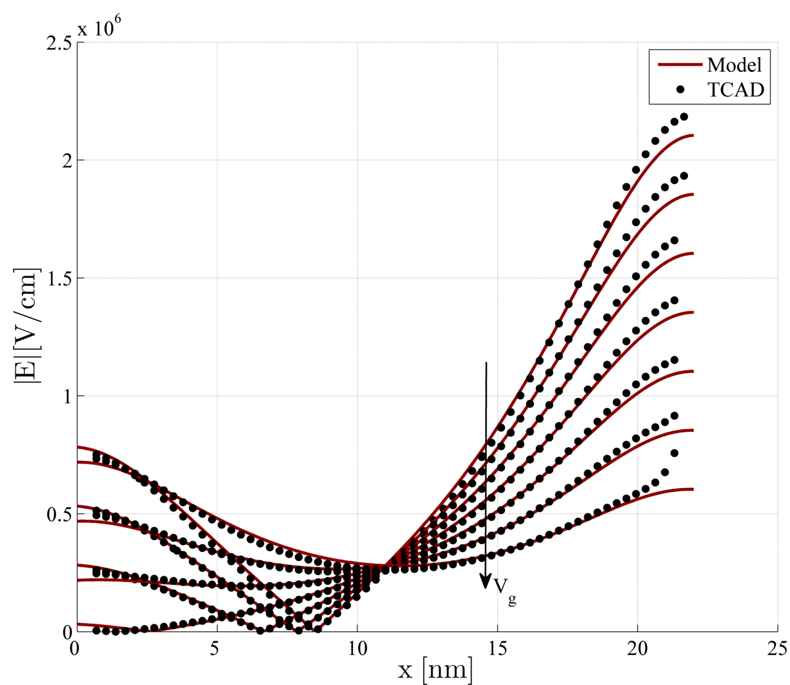

(a)

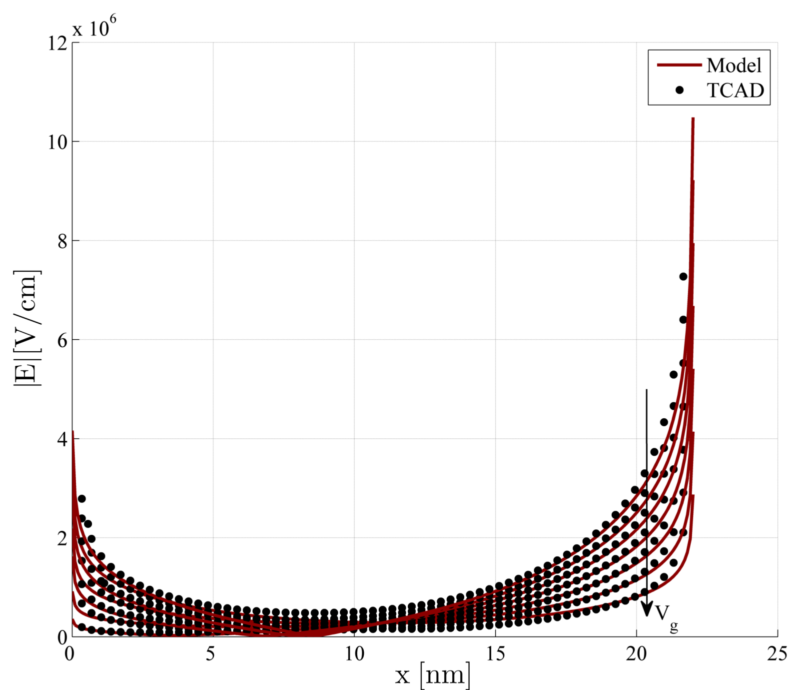

(b)

Figure 5.14.: Electric field |E| (a) at the middle of the channel, (b) at the silicon-to-oxide interface for a SB-DG-MOSFET. Results for ϕ_{Bn}=0.28 eV. Device geometry: l_{ch}=22 nm, t_{ch}=10 nm, t_{ox}=2 nm. Bias conditions: V_{ds}=1 V, V_g=−0.2 V to 1 V with 0.2 V stepping.

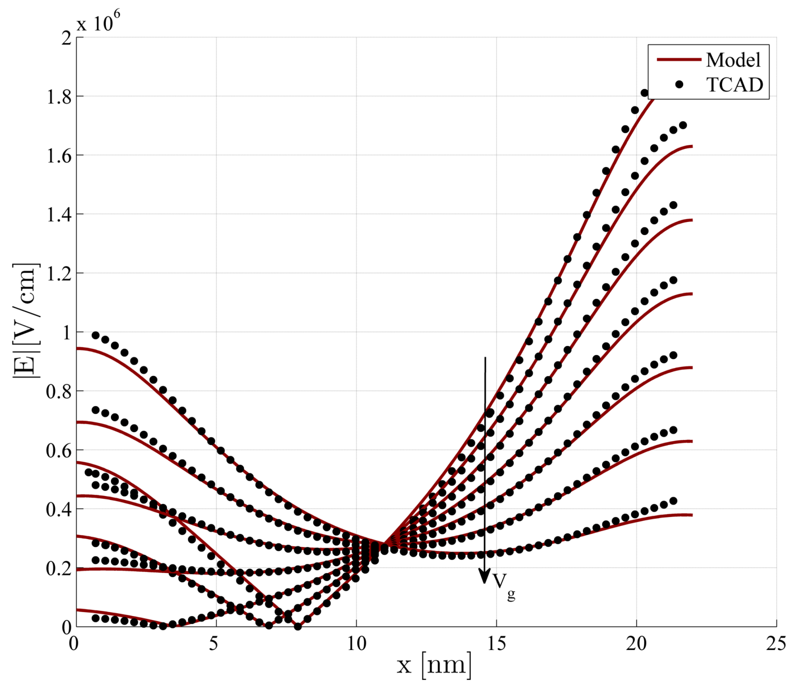

(a)

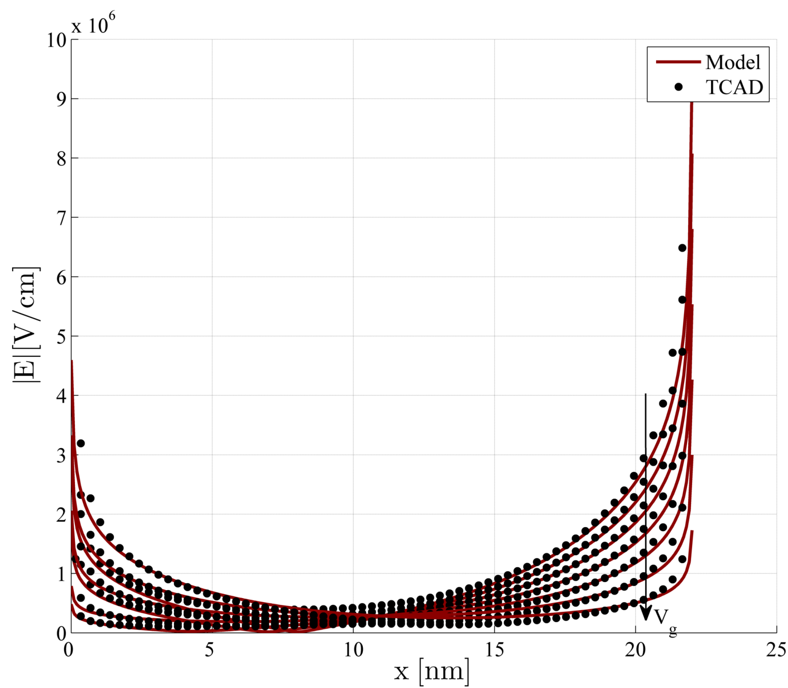

(b)

Figure 5.15.: Electric field |E| (a) at the middle of the channel, (b) at the silicon-to-oxide interface for a SB-DG-MOSFET. Results for ϕ_{Bn}=0.1 eV. Device geometry: l_{ch}=22 nm, t_{ch}=10 nm, t_{ox}=2 nm. Bias conditions: V_{ds}=1 V, V_g=−0.2 V to 1 V with 0.2 V stepping.

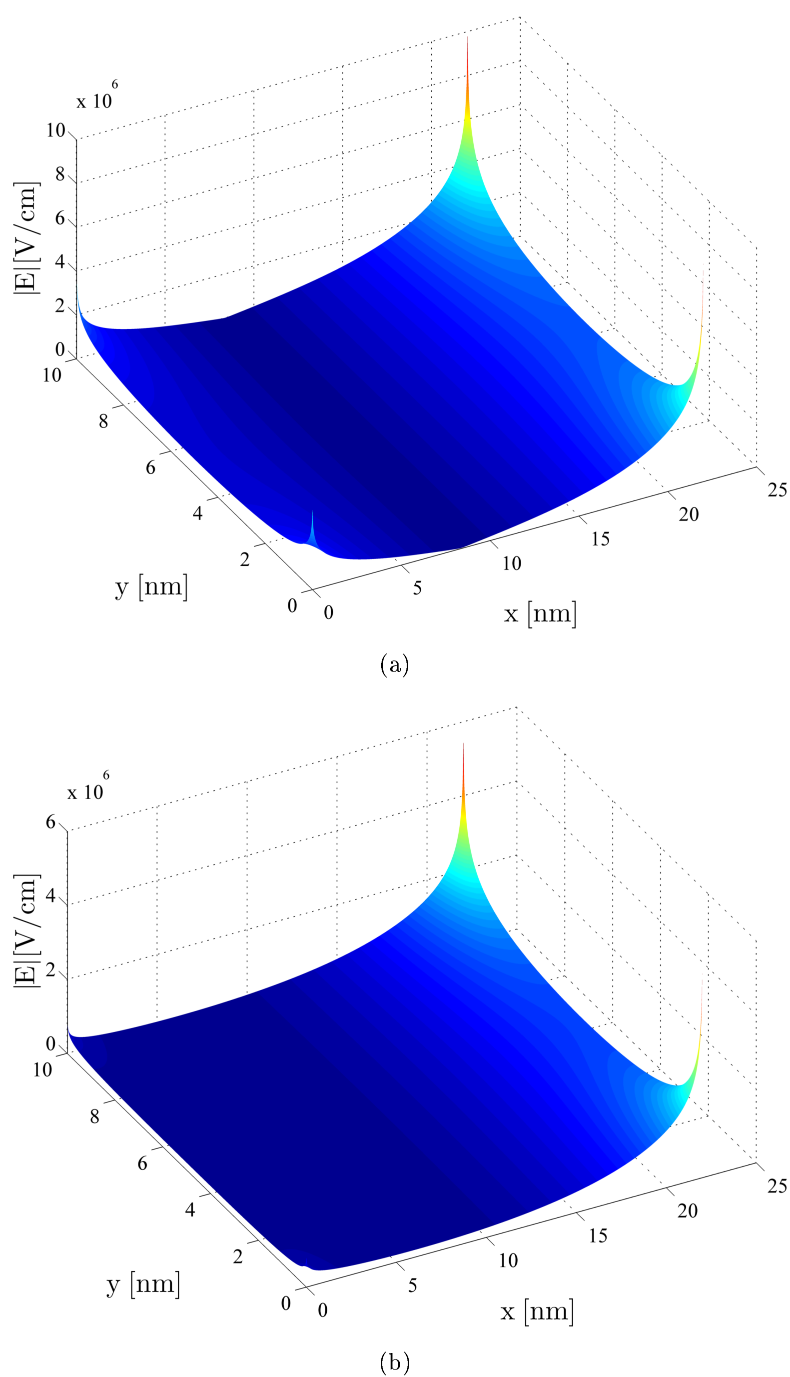

Figure 5.16.: 3D plot of the electric field |E| for a SB-DG-MOSFET. Results for ϕ_{Bn}=0.28 eV. Device geometry: l_{ch}=22 nm, t_{ch}=10 nm, t_{ox}=2 nm. Bias conditions: V_{ds}=1 V, (a) V_g=−0.3 V, (b) V_g=0.4 V.

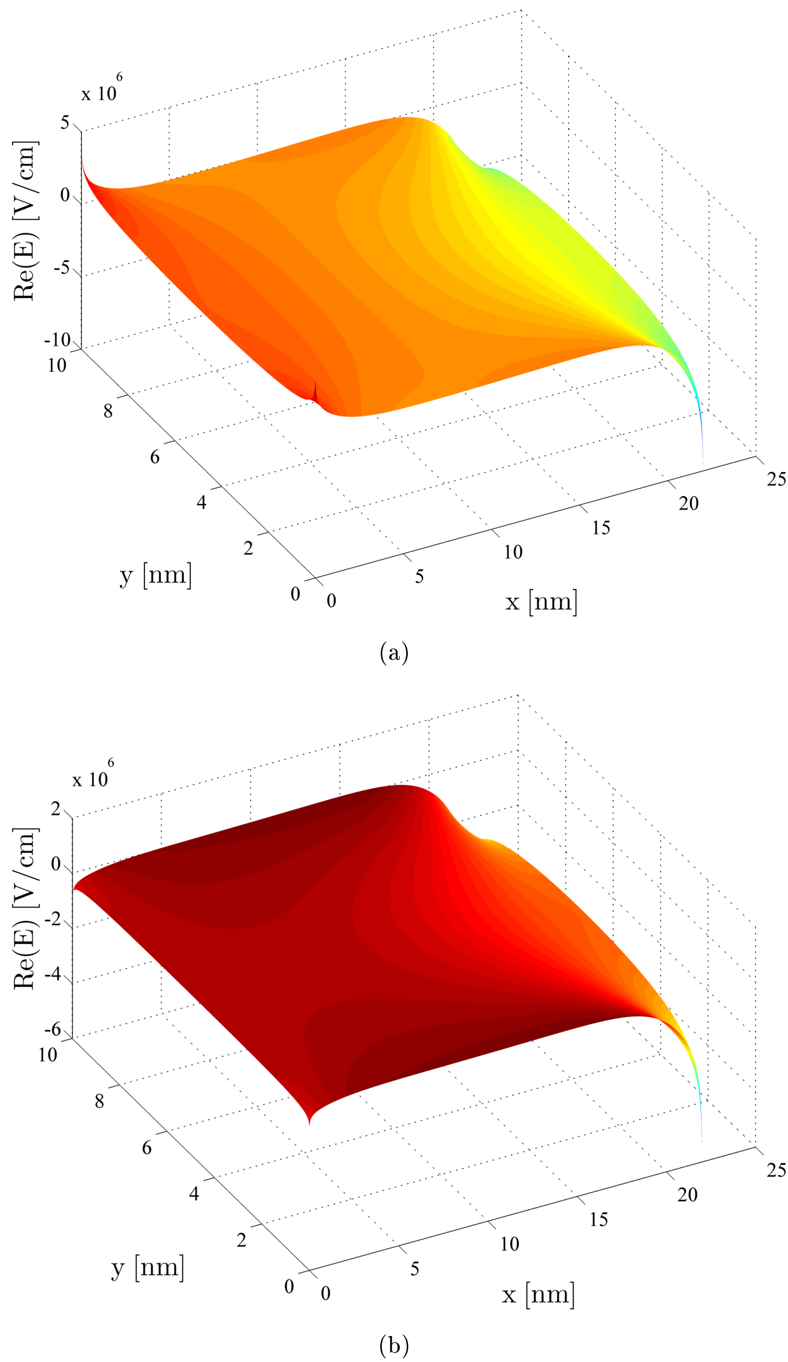

Figure 5.17.: 3D plot of the real part of the electric field Re(E) for a SB-DG-MOSFET. Results for ϕ_{Bn}=0.28 eV. Device geometry: l_{ch}=22 nm, t_{ch}=10 nm, t_{ox}=2 nm. Bias conditions: V_{ds}=1 V, (a) V_g=−0.3 V, (b) V_g=0.4 V.

UNIVERSITAT ROVIRA I VIRGILI
TWO-DIMENSIONAL ANALYTICAL PREDICTIVE MODELING OF SCHOTTKY BARRIER SOI AND MULTI-GATE MOSFETS
Mike Schwarz
Dipòsit Legal: T.456-2013

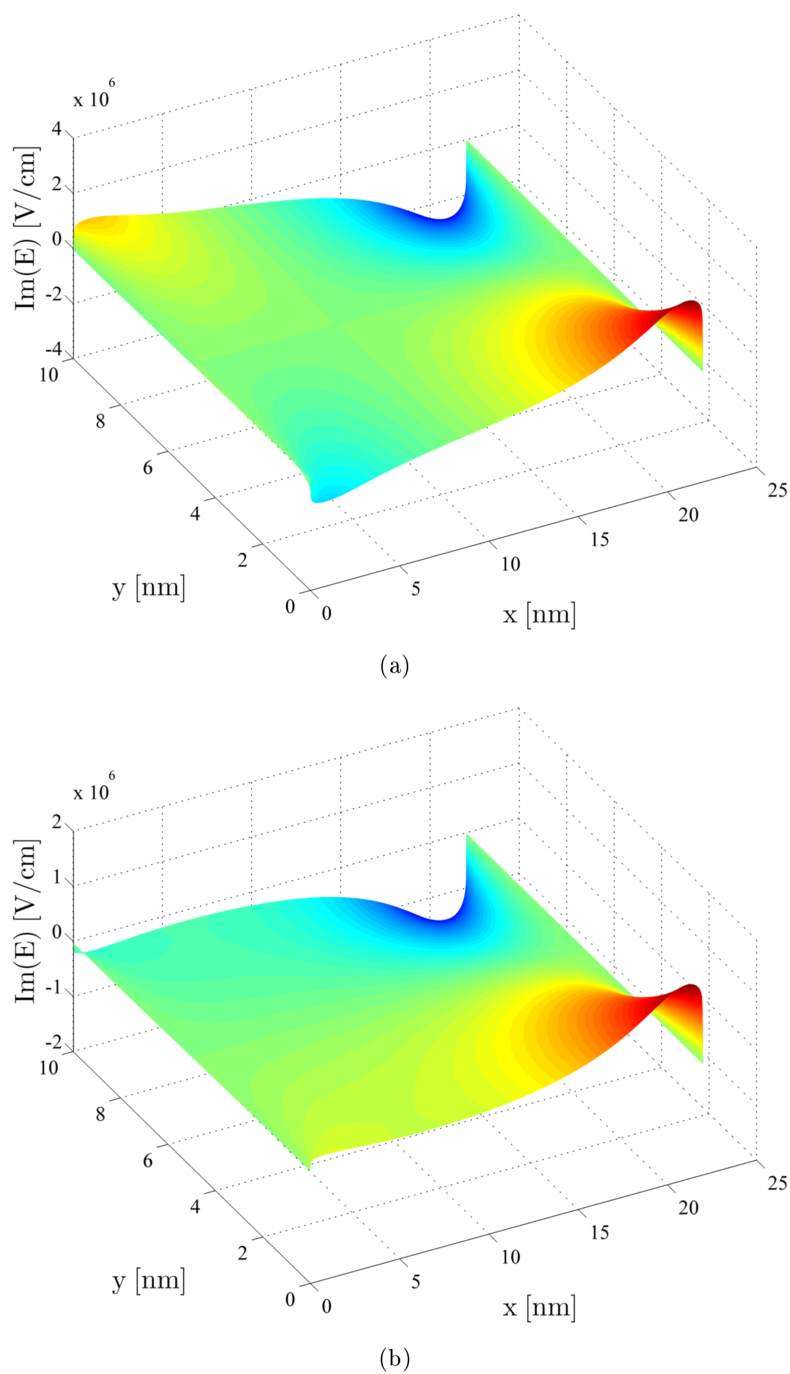

Figure 5.18.: 3D plot of the imaginary part of the electric field Im(E) for a SB-DG-MOSFET. Results for ϕ_{Bn}=0.28 eV. Device geometry: l_{ch}=22 nm, t_{ch}=10 nm, t_{ox}=2 nm. Bias conditions: V_{ds}=1 V, (a) V_g=−0.3 V, (b) V_g=0.4 V.

UNIVERSITAT ROVIRA I VIRGILI
TWO-DIMENSIONAL ANALYTICAL PREDICTIVE MODELING OF SCHOTTKY BARRIER SOI AND MULTI-GATE MOSFETS
Mike Schwarz
Dipòsit Legal: T.456-2013

Fig. 5.16(a) shows a 3D plot of the absolute value of the electric field in the channel region for the bias conditions $V_g = -0.3\,V$ and $V_{ds} = 1\,V$. As one can observe the behavior is as expected, e.g. at the potential minimum where a zero electric field ($|E| = 0$) can be observed. The Fig. 5.17(a) and 5.18(a) show the real and imaginary part of the before presented electric field, see Fig. 5.16(a). In Fig. 5.17(a) the real component is shown and the behavior is as expected. Near the source contact we observe a positive electric field due to the negative gradient of the potential in accumulation. The deeper one moves into the channel towards the drain contact, the electric field decreases as expected. Close to the drain contact the gradient of the potential is positive, therefore the electric field itself becomes negative. Fig. 5.18(a) shows the corresponding imaginary part, estimated with the analytical solution. As expected one observes a positive and negative symmetric gradient for the imaginary components. Furthermore, a complete solution in the entire channel region is presented [176, 182].

Fig. 5.18(b) shows again a 3D plot of the electric field and the components of the electric field in the channel region. Now for the bias conditions $V_g = 0.4\,V$ and $V_{ds} = 1\,V$. As discussed before, a similar behavior is observed with changed bias conditions. Both components from Fig. 5.17(b) and 5.18(b) behave as expected. From both parts the resulting absolute electric field is presented in Fig. 5.16(b) [176, 182].

5.5. Conclusion

Within this chapter two analytical approaches to calculate the 2D electrostatic potential and electric field in SB-DG-MOSFETs have been presented. They are valid for the subthreshold operation region and they do not introduce any fitting parameters. All parameters depend on geometry and boundary conditions. The 2D Poisson's equation has been solved using the conformal mapping technique.

The electrostatic potential with two kind of approaches has been studied and both have been compared to each other in terms of accuracy, computation time and memory consumption. Finally, the square root approximation approach from section 5.3.2 exhibits a good trade off between accuracy and hardware consumption for reasonable devices and results in a fully 2D analytical closed-form model.

The electric field with a fully 2D analytical closed-form model was derived without an approximation from the single vertex approach, presented in section 5.4.1.

Both approaches, the selected one for the electrostatic potential and the electric field show a good agreement for a comparison with TCAD simulation data down to channel lengths of 22 nm. From the results it can be observed that the electrostatics are predicted very well for a large range of device biasing, for several barrier heights and geometries.

UNIVERSITAT ROVIRA I VIRGILI
TWO-DIMENSIONAL ANALYTICAL PREDICTIVE MODELING OF SCHOTTKY BARRIER SOI AND MULTI-GATE MOSFETS
Mike Schwarz
Dipòsit Legal: T.456-2013

Nevertheless, some inaccuracies still exist in the model, e.g. the neglected mobile charges, fringing fields and transformed oxide thickness which lead to the inaccuracies observed in the results. In both models there is space for improvements.

However, by using the developed framework for the approaches it is easy to include 2D effects by calculating the electrostatics of (Schottky barrier) Double-Gate MOSFET devices. Furthermore, they are calculated in a very efficient way without the need of numerical simulations which in a result might be a useful contribution of a compact model for circuit simulators.

UNIVERSITAT ROVIRA I VIRGILI
TWO-DIMENSIONAL ANALYTICAL PREDICTIVE MODELING OF SCHOTTKY BARRIER SOI AND MULTI-GATE MOSFETS
Mike Schwarz
Dipòsit Legal: T.456-2013

Chapter 6.

Analytical Numerical Modeling Approach (ANMA) for the Currents

The models of the electrostatic potential and the electric field of chapter 5 are now used to model the current components in the device. Before presenting and discussing these components, further simplifications and definitions have to be introduced. Therefore, in the following sections the main contributions of the device are discussed and afterwards the approaches to model these are presented.

6.1. Simplification & Definition

As discussed in sections 2.2.2 and 2.3.1, several current transport processes and tunneling mechanisms exist in Schottky barrier devices. Furthermore, a variety of current contributions as in common MOSFET technology take influence on the device behavior [53].

In the subthreshold operation region, leakage current is typically dominated by the three components (not including gate insulator leakage) gate-induced drain-leakage current (GIDL), junction leakage current and source/drain thermal-emission leakage current [53]. Furthermore, current contributions from the source to drain tunneling mechanism have to be taken into account for the subthreshold behavior if the channel length is below 10 nm [183].

In the on-state operation region, depending on the charge carriers and applied bias, contributions from tunneling current, thermionic emission current and drift-diffusion current are the typical components. One can limit each other, therefore all contributions have to be kept in mind for the overall current calculation.

In this work leakage currents from the gates are neglected. Furthermore, this work concentrates on the modeling of the main current contributions from tunneling, thermionic emission and drift-diffusion mechanisms. The currents which flow from the metal junctions into the semiconductor, are used to model the characteristics of the device. The aim should be to analyze these components and find explicit solutions.

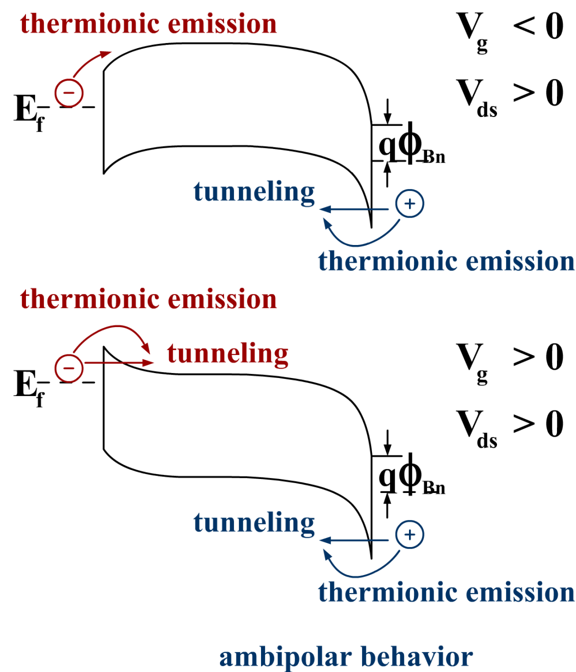

Figure 6.1.: Current contribution in accumulation and inversion.

Therefore, the main contributions of the current in the model result from electrons at the source electrode and holes at the drain electrode, depending on the bias condition. In Fig. 6.1 the contributions for the cases of accumulation and inversion are shown, it follows [176, 184]

$$I_{TTE} = I_{tun} + I_{therm}. \tag{6.1}$$

All other components are neglected. Fig. 6.1 shows that by accumulation at the source electrode electrons are able to contribute to the current by thermionic emission. At the drain electrode holes are able to contribute by tunneling and thermionic emission. In inversion a similar behavior can be observed, except for the source electrode where additionally electrons are able to contribute to the current by tunneling.

Fermi-Dirac Distribution

In equation (2.31) for the tunneling current density calculation the Fermi-Dirac distribution is needed. In equilibrium the distribution function of electrons and holes is given by

$$f(\xi) = \frac{1}{\exp\left(\frac{\xi - E_f}{kT}\right) + 1}, \tag{6.2}$$

which can be derived from statistical thermodynamics [126, 185].

UNIVERSITAT ROVIRA I VIRGILI
TWO-DIMENSIONAL ANALYTICAL PREDICTIVE MODELING OF SCHOTTKY BARRIER SOI AND MULTI-GATE MOSFETS
Mike Schwarz
Dipòsit Legal: T.456-2013

The modeling approach of the tunneling current follows with the equation (6.2)

$$\mathrm{f_s}(\xi) = \frac{1}{\exp\left(\frac{\xi - \mathrm{E_{fs}}}{\mathrm{kT}}\right) + 1},$$
$$\mathrm{f_m}(\xi) = \frac{1}{\exp\left(\frac{\xi - \mathrm{E_{fm}}}{\mathrm{kT}}\right) + 1} \tag{6.3}$$

where $\mathrm{E_{fs}}$ and $\mathrm{E_{fm}}$ describe the Fermi energies in the semiconductor and metal, respectively. ξ describes the carrier energy, k represents the Boltzmann constant and T the temperature in Kelvin.

In the approach some further simplification or assumptions are made. First, the Fermi level in close vicinity of the tunneling barrier, i.e. where carriers are generated by tunneling, is assumed to be constant for each of the source and drain related case while for the drain related case the drain to source voltage $\mathrm{V_{ds}}$ is also considered and $\mathrm{E_f}$ in equations (6.3) is replaced by $\mathrm{E_{fs}} + \mathrm{V_{ds}}$ for the semiconductor and $\mathrm{E_{fm}} + \mathrm{V_{ds}}$ for the metal, respectively. An additional approximation is made with the fact that the Fermi level of the metal is equal to the one of the semiconductor as reported in [154]

$$\mathrm{f_m}(\xi) \approx \mathrm{f_s}(\xi). \tag{6.4}$$

We further define the Fermi level in the metal at the source as reference in the energy space. Due to this definition follows

$$\mathrm{E_{fm,sce}} = 0\mathrm{eV}. \tag{6.5}$$

6.2. Tunneling Current

As discussed in section 2.2.2 several components contribute to the tunneling current. Generally, the calculation of the tunneling current is made by integration of the current equation with respect to the energy [126, 133, 150, 154]. Here, the tunneling current is solved with respect to the coordinates which results in an improvement of the estimated tunneling current, Fig. 6.2.

Due to these circumstances, in the following it is aimed to define the necessary contributions from the Fermi-Dirac distributions, the tunneling probability as well as the integration of the current density with respect to the coordinates to predict the tunneling current of the device quite accurately [184, 186, 187, 188].

6.2.1. Tunneling Probability Estimation

The tunneling probability is estimated with the WKB approximation from equation (2.39) in section 2.3.2. Neglecting the Schottky barrier lowering effect due to section

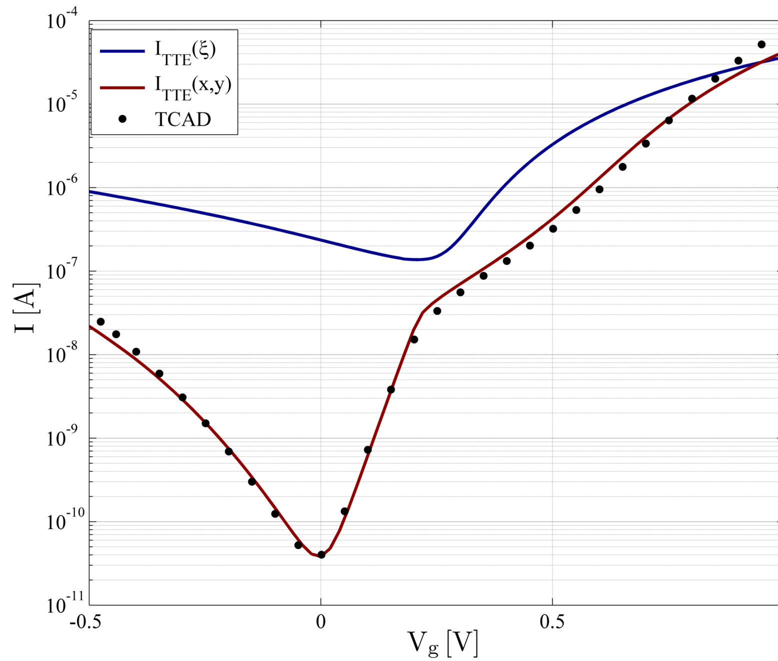

Figure 6.2.: Current I_{TTE} solved with respect to the energy (ξ) and with respect to the coordinates (x, y) for a SB-DG-MOSFET with a channel length $l_{ch} = 65nm$ compared to TCAD Sentaurus simulations.

2.2.1 follows for the tunneling probability and assuming a triangular shape of the barrier (Fig. 6.3)

$$T(E, x, y) = \exp\left(\frac{-4\sqrt{2m \cdot m_0}\left(|E(x, y)| \cdot x\right)^{3/2}}{3q\hbar|E(x, y)|}\right). \tag{6.6}$$

Here, m describes the effective mass, m_0 the electron or hole rest mass, q the elementary charge, $\hbar$ the reduced Planck constant and E the electric field at the point of interest [110] defined by the position x (distance from the barrier) and y (Fig. 6.4). The electric field results from the 2D analytical solution via the conformal mapping technique presented in chapter 5 [176, 186, 189] which is obtained by a 2D analysis below threshold.

6.2.2. Tunneling Current Density

As already explained the tunneling current density is calculated with respect to the coordinates. Referring to the made approximations and by assuming only current flux from metal to semiconductor $J_{tun,m\to s} \approx J_{tun}$, as indicated in Fig. 6.1 follows for equation (2.31) for one slice as shown in Fig. 6.4 and the several current contributions due to Fig. 6.5

$$J_{tun}(y) = \frac{A^*T}{k}\int_0^{l_{ch}} T(E, x, y) f_m(\xi(x))\left[1 - f_s(\xi(x))\right]\frac{\partial \xi}{\partial x}dx. \tag{6.7}$$

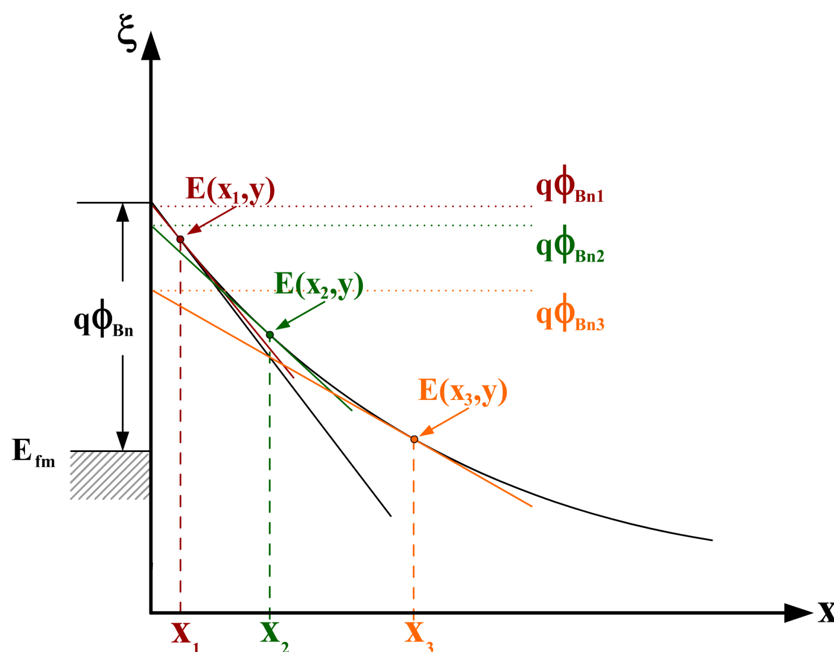

Figure 6.3.: Applying the WKB approximation from equation (6.6), several triangular shapes depending on the coordinate result for the estimation of the tunneling probability. Each triangular shape results in an individual effective height of the potential barrier.

Here, integration with respect to coordinate x along the channel takes place, $\mathrm{T(E, x, y)}$ is the tunneling probability from equation (6.6) for the carriers and $\frac{\partial \xi}{\partial \mathrm{x}}$ refers to the electric field E for one slice which links the energy space to the coordinate space [176,189]. Here, the absolute value of the electric field from equation (5.58) is used, because tunneling occurs in the direction of the electric field vector.

The Fermi-Dirac distributions at the metal/semiconductor contacts are described by $\mathrm{f_m}(\xi(\mathrm{x}))$ and $\mathrm{f_s}(\xi(\mathrm{x}))$ where $\xi(\mathrm{x})$ is the charge carrier energy. With equation (6.3) follows

$$\mathrm{f_s}(\xi(\mathrm{x})) = \frac{1}{\exp\left(\frac{\xi(\mathrm{x})-\mathrm{E_{fs}}}{\mathrm{kT}}\right)+1},$$
$$\mathrm{f_m}(\xi(\mathrm{x})) = \frac{1}{\exp\left(\frac{\xi(\mathrm{x})-\mathrm{E_{fm}}}{\mathrm{kT}}\right)+1} \tag{6.8}$$

whereby the charge carrier energy $\xi(\mathrm{x})$ is solved with the electrostatics from chapter 5.

Furthermore, an enhancement in equation (6.7) is made by including drift-diffusion effects. Carriers which are being injected from a barrier by thermionic emission or tunneling, will encounter scattering on their way through the channel. The effect of a drift-diffusion limited current will have an increasing influence if a strong electric field

UNIVERSITAT ROVIRA I VIRGILI
TWO-DIMENSIONAL ANALYTICAL PREDICTIVE MODELING OF SCHOTTKY BARRIER SOI AND MULTI-GATE MOSFETS
Mike Schwarz
Dipòsit Legal: T.456-2013

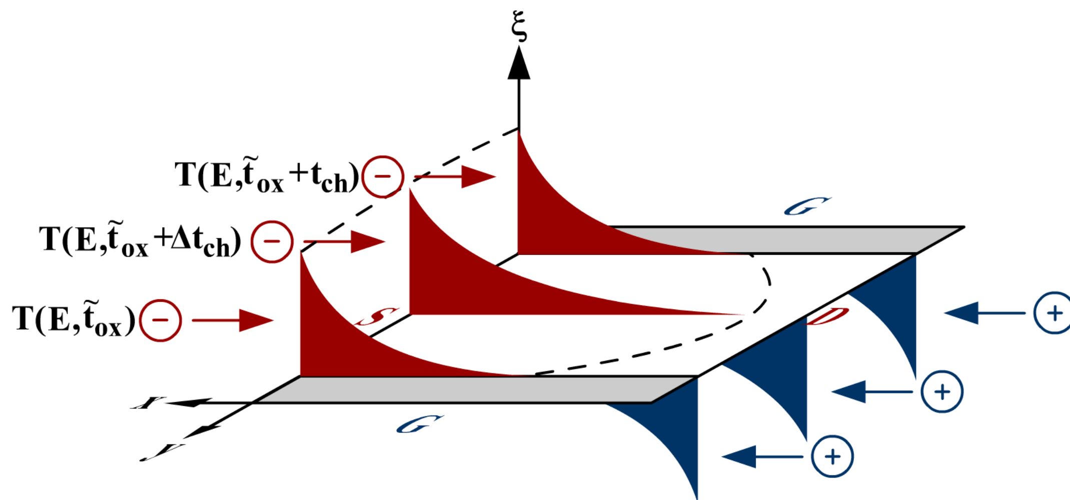

Figure 6.4.: The schematic tunneling probability and current density for inversion mode is calculated depending on the position y.

is in the channel near the barrier which is the case for higher gate biases. The barrier is thinned and tunneling dominates the current.

According to the diffusion theory of section 2.2.2 in the emission current density the Richardson constant A^* can be rewritten in terms of the carrier mobility μ, the effective density of states in the valence band N_V or conduction band N_C, and the electric field at the barrier $E(x = 0, y)$. This way the thermionic emission current becomes bias dependent.

This theory is to be applied to the tunneling current density. Therefore, it is assumed that a carrier which is generated by tunneling within the valence band or conduction band of the channel in distance x to the barrier, will encounter a similar drift-diffusion effect as the carriers considered in thermionic emission theory, but with the individual electric field at the position of generation, instead of the electric field at the barrier.

Here, one obtains the tunneling generation rate at position (x, y) [189, 190]

$$\mathrm{TGR}(x,y) = \frac{\mu N_{C,V}|E(x,y)|}{kT} \cdot T(E,x,y) \cdot f_m(\xi(x))[1 - f_s(\xi(x))]\frac{\partial \xi}{\partial x}. \tag{6.9}$$

Therefore, equation (6.7) for the tunneling current density can be rewritten with

$$A^* = \frac{q\mu N_{C,V}|E(x,y)|}{T^2}, \tag{6.10}$$

as

$$J_{tun}(y) = \frac{q\mu N_{C,V}}{kT}\int_0^{l_{ch}} |E(x,y)| \cdot T(E,x,y) \cdot f_m(\xi(x))[1 - f_s(\xi(x))]\frac{\partial \xi}{\partial x}dx. \tag{6.11}$$

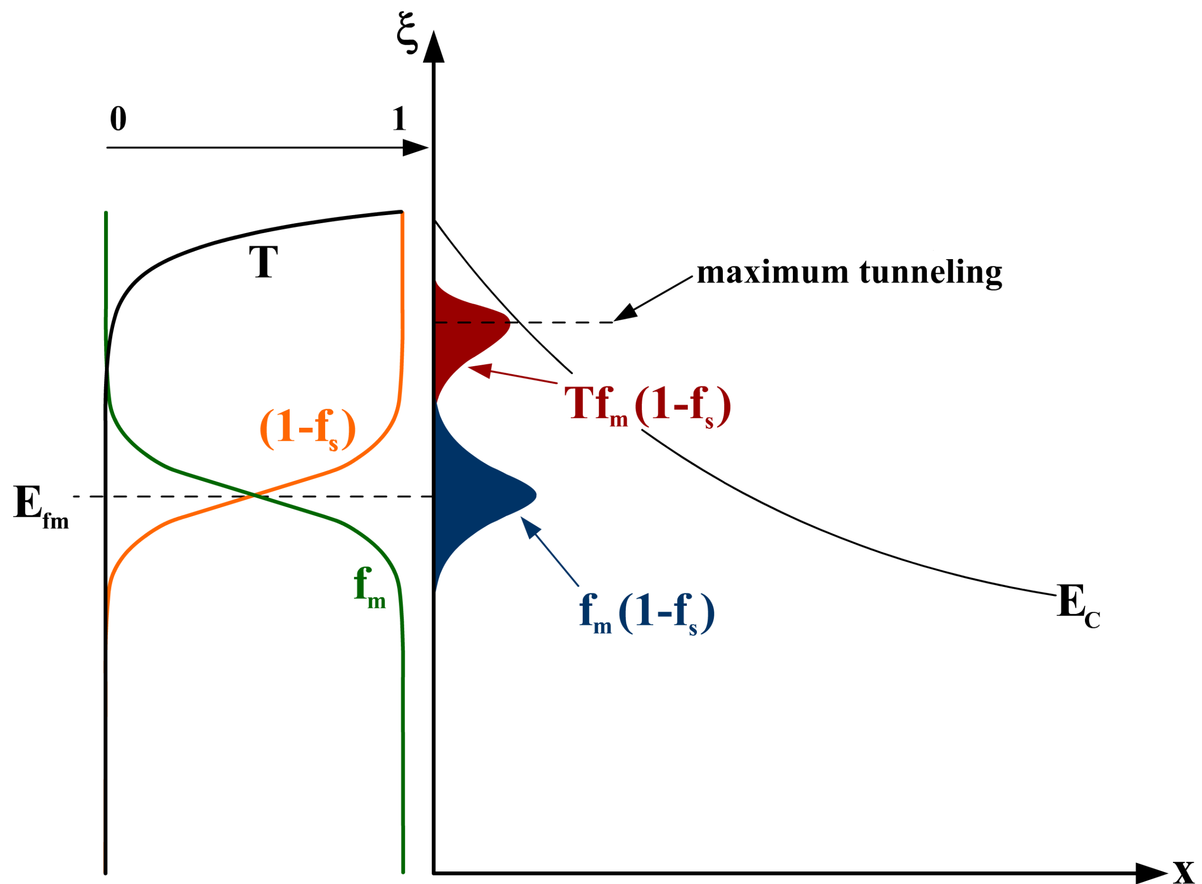

Figure 6.5.: Contributions to the tunneling current density for one slice.

6.2.3. Tunneling Current Calculation

The tunneling current results from

$$I_{tun} = \int_{0}^{w_{ch}} \int_{t_{ox}}^{t_{ox}+t_{ch}} J_{tun}(y) \cdot dy \cdot dz. \tag{6.12}$$

Here, the integration along the boundary for the channel thickness t_{ch} and the channel width w_{ch} of the device is made. With this equation the tunneling current I_{tun} is estimated in an analytical numerical way with the above defined assumptions and solutions from the conformal mapping technique. Due to the numerical integration the accuracy depends on the refinement of the coordinates in the device. The results for the tunneling currents are accurately for a mesh with a refinement of approximately 0.1 nm. This is sufficient enough and in terms of computation time for the numerical approach an acceptable trade off [176, 189, 190].

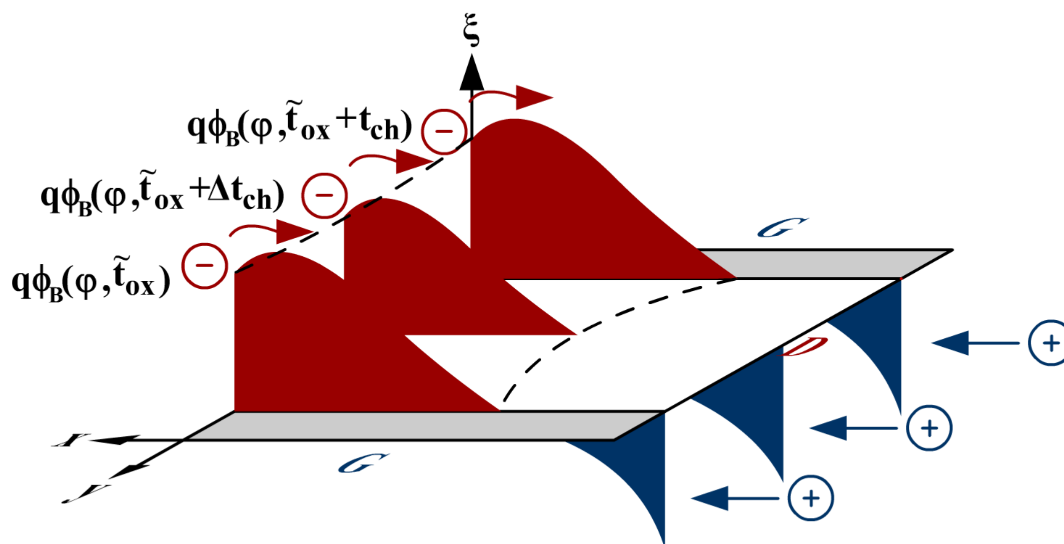

Figure 6.6.: The schematic thermionic emission current density for accumulation mode is calculated depending on the position y.

6.3. Thermionic Current

In section 2.2.2 the thermionic emission diffusion current is explained with its contribution. Literature already presents an explicit equation to predict the thermionic current for a list of assumptions [150]. However, in most cases the calculation is quite accurate. Due to this circumstance, in the model approach the one-dimensional solution from literature is applied.

6.3.1. Thermionic Current Density

As explained, the thermionic current density is calculated using equation (2.27). Again referring to the defined approximations and by assuming only a current flux from metal to semiconductor $J_{therm,m\rightarrow s} \approx J_{therm}$, as indicated in Fig. 6.1. Therefore, it follows for one slice as shown in Fig. 6.6

$$J_{therm}(y) = A^{*}T^{2}\exp\left(-\frac{q\phi_{B}(y)}{kT}\right)\left[1-\exp\left(\frac{-qV_{ds}}{kT}\right)\right]. \tag{6.13}$$

Here, A^{*} represents again the Richardson constant, $\phi_B(y)$ describes the barrier height or maximum barrier which the charge carriers have to surmount in the slice at position y. For the case of accumulation $\phi_B(y)$ is represented by the minimum of the electrostatic potential in the channel region. In inversion $\phi_B(y)$ is obtained by the Schottky barrier height itself, if the Schottky barrier lowering effect is neglected [176, 189, 190].

UNIVERSITAT ROVIRA I VIRGILI
TWO-DIMENSIONAL ANALYTICAL PREDICTIVE MODELING OF SCHOTTKY BARRIER SOI AND MULTI-GATE MOSFETS
Mike Schwarz
Dipòsit Legal: T.456-2013

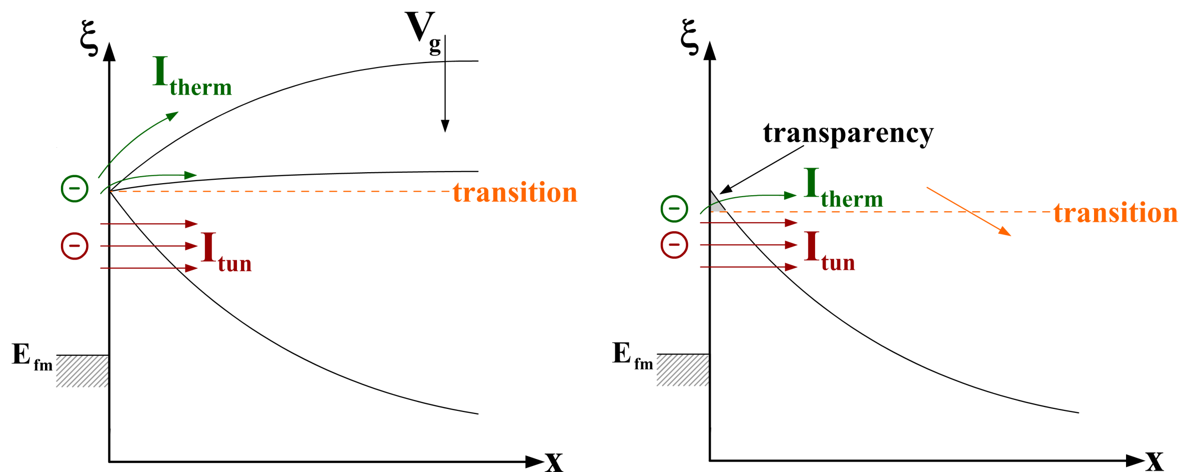

Figure 6.7.: When the tunneling mechanism starts to influence the device and charge carriers are able to tunnel, thermionic emission for the higher energies close to the top of the barrier influences the current.

6.3.2. Thermionic Current Calculation

The thermionic current results from

$$I_{therm} = \int_{0}^{w_{ch}} \int_{t_{ox}}^{t_{ox}+t_{ch}} J_{therm}(y) \cdot dy \cdot dz \tag{6.14}$$

with channel thickness t_{ch} and width w_{ch}. With this equation the analytical numerical thermionic current I_{therm} is calculated with the above defined assumptions and solutions from the conformal mapping technique. Also the accuracy of the thermionic current depends on the refinement of the device. The influence on the mesh in x-direction is less due to the explicit equation.

If the barrier height for the electrons at the source junction is low enough, the thermionic emission current is mainly described by the electrons from the source. The thermionic emission current resulting from the holes at the drain junction is negligible due to the huge barrier height at the junction. This is a reasonable behavior for state of the art devices.

6.4. Transition; Thermionic to Tunneling Current

From equation (6.1) it is clear that both components are combined by summarizing those. As in sections explained above, the tunneling current starts to influence the device, when the bands are flat and thermionic emission is saturated due to the barrier height. Fig. 6.7 illustrates this behavior and from the figure it is clear that if the bands are flat, a

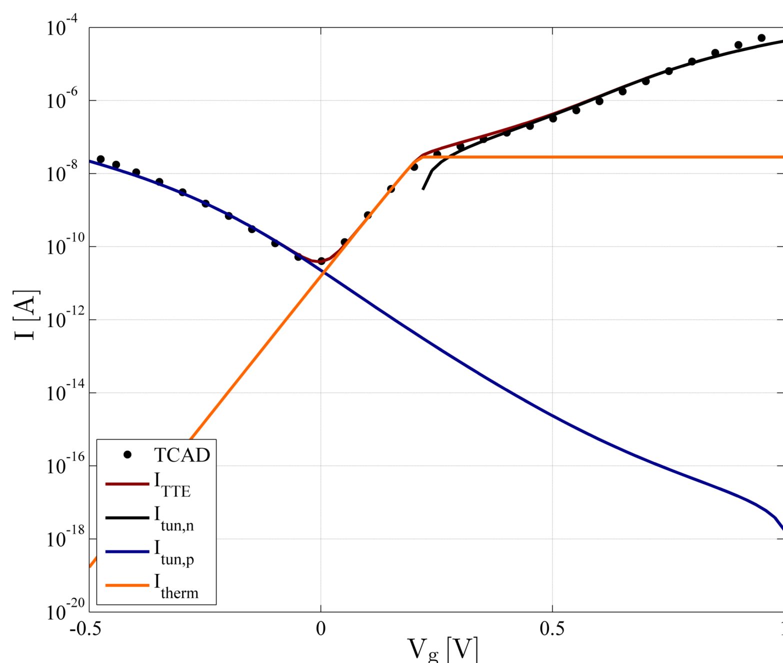

Figure 6.8.: Superposed $\mathrm{I_d - V_g}$ current components $\mathrm{I_{tun,n}}$, $\mathrm{I_{tun,p}}$, $\mathrm{I_{therm}}$ result in the model current $\mathrm{I_{TTE}}$, compared to the simulated TCAD Sentaurus current.

discontinuity results. In real devices, a transition area between both mechanisms exists. When the tunneling mechanism starts to influence the device and charge carriers are able to tunnel, thermionic emission for the higher energies close to the top of the barrier can still take place. This is possible due to the fact that the top of the barrier is thin enough, nearly transparent. By taking this into account, a smooth continuous transition between the thermionic emission and the tunneling current range is guaranteed. In the model implementation this transparency has been considered within the transition area. Therefore, in the following results the transition area has been smoothed.

6.5. Results $\mathrm{I_d - V_g}$

In this section the results of the transfer characteristics $\mathrm{I_d - V_g}$ for the analytical numerical modeling approach with various device parameters and biases in comparison with the corresponding numerical device simulations from TCAD Sentaurus [64] are presented. The parameters of electron mass $\mathrm{m_n}$, hole mass $\mathrm{m_p}$, electron mobility μ_n, hole mobility μ_p, and Richardson constant $\mathrm{A^*}$ have been adjusted in the model, refer to Tables 6.1 to 6.3.

In Fig. 6.8 the several current components of the current model are shown while in the figure the tunneling currents are predicted with equation (6.7). As observed from the illustration, for the lower gate potentials $\mathrm{V_g}$, the hole current $\mathrm{I_{tun,p}}$ due to the tunneling

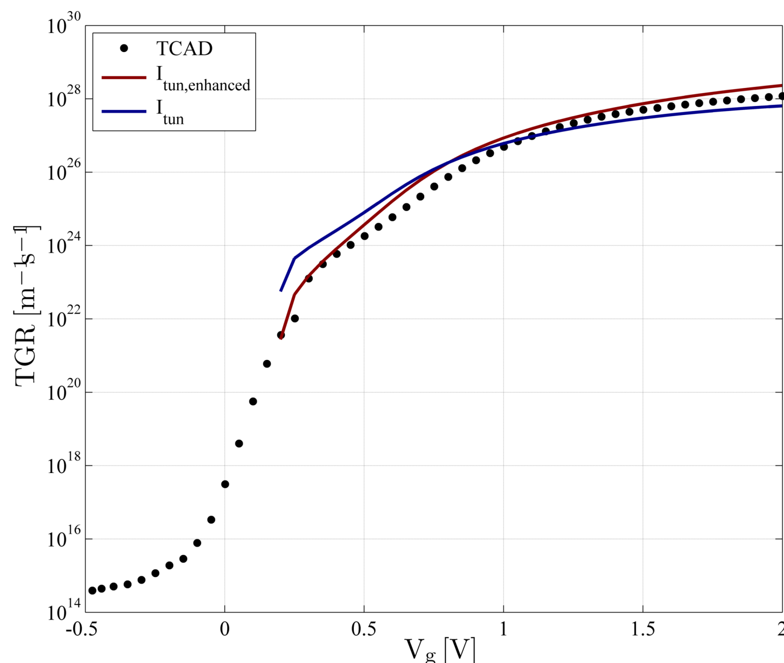

Figure 6.9.: Comparison of the Tunneling Generation Rate (TGR) TCAD vs. TGR of I_{tun} (equation 6.7) and the enhancement of the Richardson constant in $I_{tun,enhanced}$ (equation 6.11) of the electrons in a SB-DG-MOSFET with a channel length of l_{ch}=45 nm.

mechanism at the highly bent bands at the drain electrode dominates compared to the thermionic emission current I_{therm} [176, 189]. The thermionic emission current is approximated by $I_{therm,n} \approx I_{therm}$ for reasonable barrier heights devices, because the amount of $I_{therm,p}$ is negligible for high Schottky barrier heights ϕ_{Bp} for holes.

At approximately V_g=0 V the thermionic emission current I_{therm} becomes more significant by the fact that at the drain junction the barrier is modulated by the gate potential V_g. The barrier becomes thicker and the hole current decreases while at the same time the bands close to the source junction are bent downwards, and the barrier for the electrons on the source side is decreasing. Therefore, the thermionic emission current I_{therm} due to the electrons is increased [176, 189].

If the gate potential reaches V_g=0.25 V, the bands are flat and the electron tunneling mechanism at the source junction starts to dominate. An electron current $I_{tun,n}$ can be observed which increases with the gate potential V_g, because the barrier at the source side is modulated and thinned. Therefore, the tunneling probability increases which at least results in a higher tunneling electron current $I_{tun,n}$. At a certain gate potential $V_g \approx$ 1V additionally drift-diffusion effects take influence [176, 189].

This behavior is more or less the same for every Schottky barrier Double-Gate MOSFET device. Several parameters, e.g. Schottky barrier height ϕ_{Bn} and/or geometry can

Table 6.1.: Adjusted device model parameters for a channel length l_{ch}=100 nm & 65 nm.

Structural	l_{ch}	100 | 65	[nm]	channel length
	t_{ch}	20	[nm]	channel thickness
	t_{ox}	2	[nm]	oxide thickness
Misc	N_B	10^{15}	[cm^{-3}]	substrate doping
	V_{fb}	0	[V]	flatband voltage
	ϕ_{bi}	0.56	[V]	built-in potential s/d
	ϕ_{Bn}	0.4 | 0.28	[eV]	SBH electrons
	A_n^*	112	[A/cm^2K^2]	elec. Richardson constant
	A_p^*	32	[A/cm^2K^2]	hole Richardson constant
	m_n	0.26	[-]	elec. effect. mass
	m_p	0.36	[-]	hole effect. mass

influence the several gate potentials V_g where the various mechanisms start to influence, but in general the behavior is similar. Of course, additional short-channel effects tend to influence the device behavior the shorter the channel length becomes [176, 189].

In Fig. 6.9 a comparison between equation (6.7) and equation (6.11) for the Tunneling Generation Rate (TGR) of the electrons at the source junction is shown. Including the drift-diffusion effects an improvement of the Tunneling Generation Rate for the electrons for the higher gate potentials V_g is observed [176, 189].

The results in Fig. 6.10 and Fig. 6.11 have been predicted with equation (6.7) and adjusted as indicated in Table 6.1. As for the 100 nm and 65 nm devices it can be observed that the results slightly differ from the simulated data, especially in the accumulation and inversion regime. In the accumulation and inversion regions this occurs, because additional charge carriers begin to influence the current, and also neglected drift-diffusion transport which dominates in the very strong inversion regime. Therefore, the model from equation (6.7) is not expected to work at high V_g. In addition, no essential difference between the TCAD Sentaurus curves of both devices, see Fig. 6.10(a), 6.10(b) and Fig. 6.11(a), 6.11(b) is observed, due to the longer channels and the minor influence on the potentials and electric fields at the electrodes [176, 189]. Furthermore, approximations made in the derivation of the analytical model for the potential, e.g. linear boundary conditions in the oxide (refer to [174, 176, 189]), and the neglect of mobile charges contribute to the deviation between model and TCAD results.

Additionally, the assumption of constant Fermi levels is obviously not sufficient for the case of accumulation and strong inversion.

UNIVERSITAT ROVIRA I VIRGILI
TWO-DIMENSIONAL ANALYTICAL PREDICTIVE MODELING OF SCHOTTKY BARRIER SOI AND MULTI-GATE MOSFETS
Mike Schwarz
Dipòsit Legal: T.456-2013

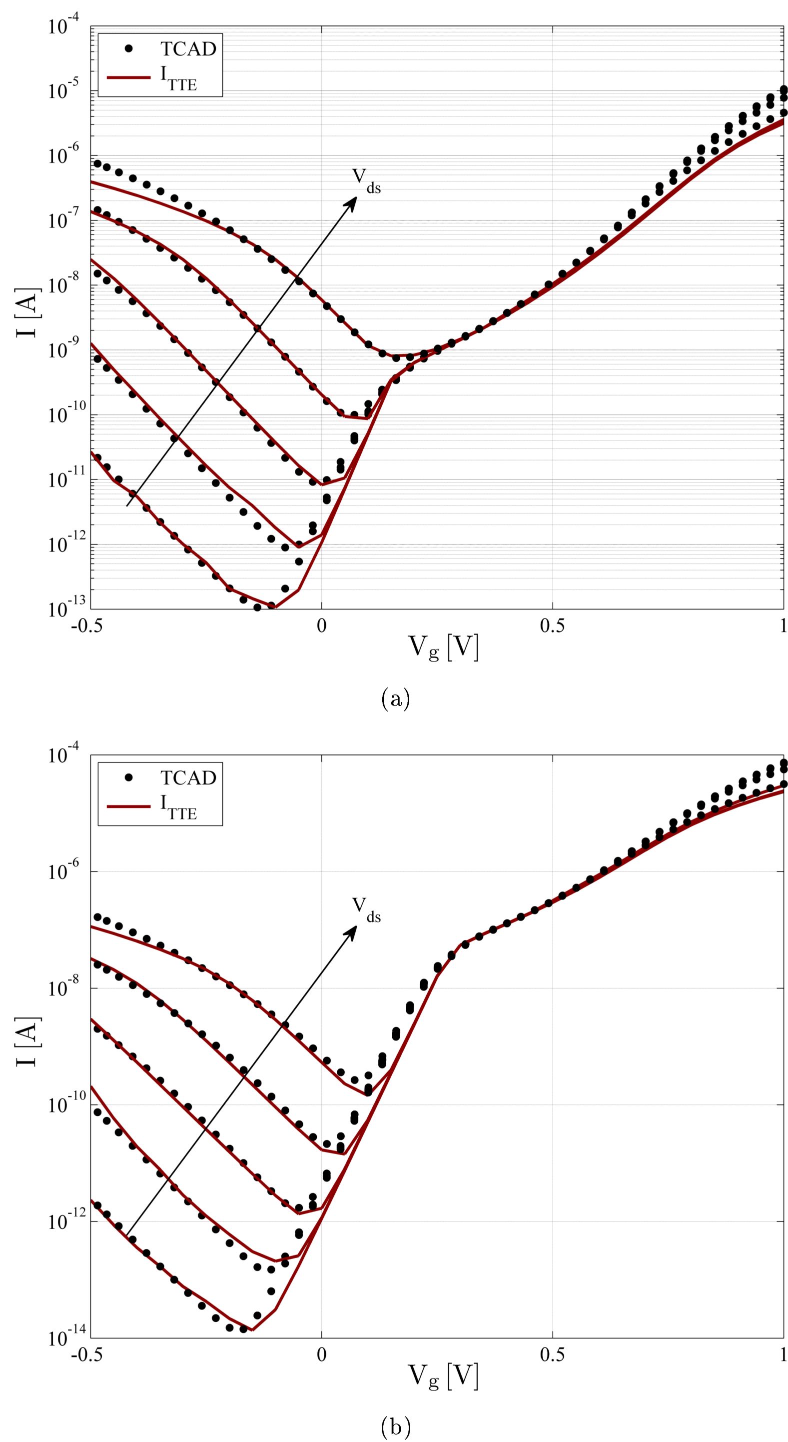

Figure 6.10.: $I_d - V_g$ characteristics of current I_{TTE} vs. TCAD for a SB-DG-MOSFET with (a) ϕ_{Bn}=0.4 eV, (b) ϕ_{Bn}=0.28 eV. Device geometry: l_{ch}=100 nm, t_{ch}=20 nm, t_{ox}=2 nm, w_{ch}=1 µm. Bias conditions: V_{ds}=0.2 V to 1 V with 0.2 V stepping, V_g=−0.5 V to 1 V with 0.01 V stepping.

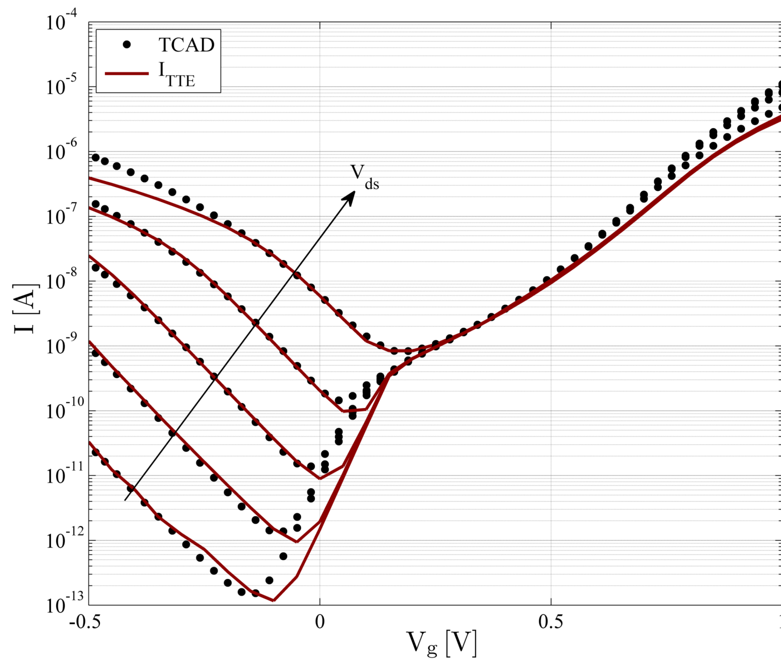

(a)

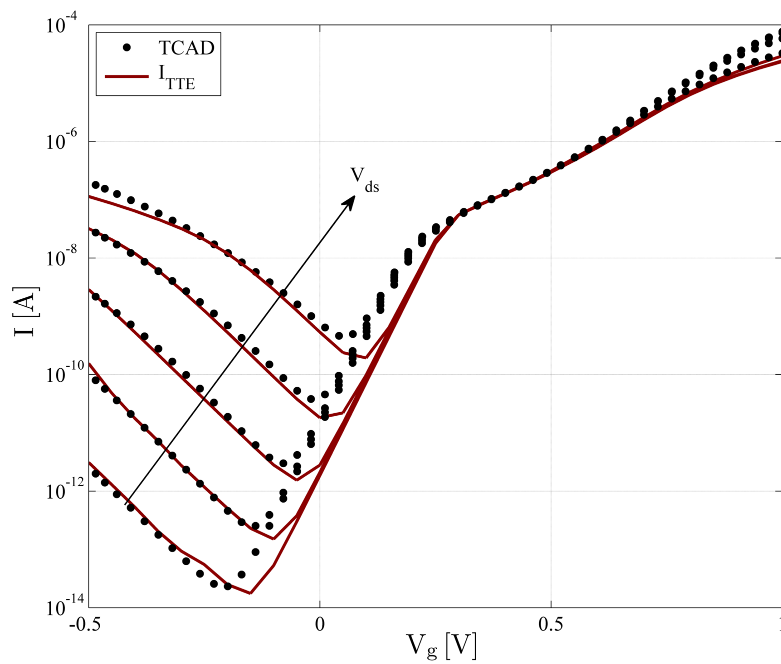

(b)

Figure 6.11.: $I_d - V_g$ characteristics of current I_{TTE} vs. TCAD for a SB-DG-MOSFET with (a) ϕ_{Bn}=0.4 eV, (b) ϕ_{Bn}=0.28 eV. Device geometry: l_{ch}=65 nm, t_{ch}=20 nm, t_{ox}=2 nm, w_{ch}=1 µm. Bias conditions: V_{ds}=0.2 V to 1 V with 0.2 V stepping, V_g=−0.5 V to 1 V with 0.01 V stepping.

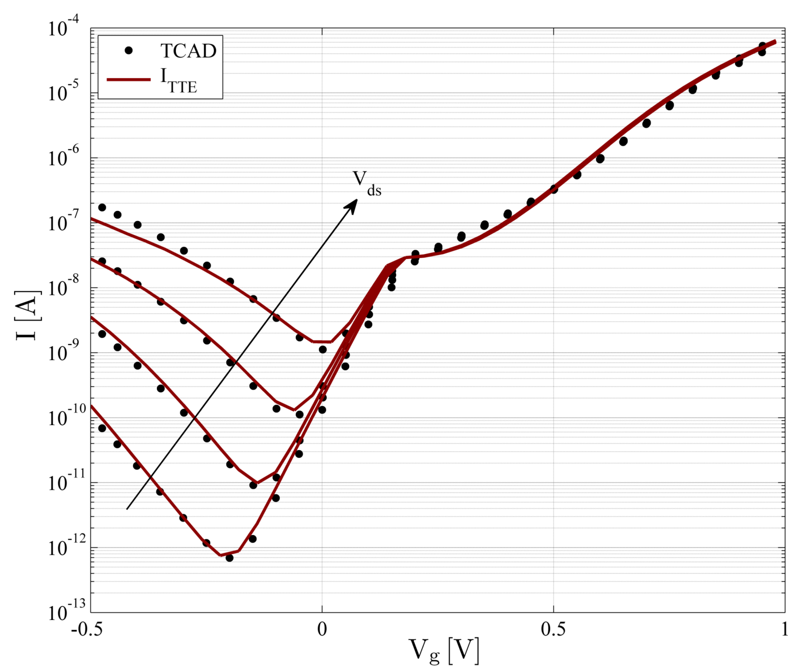

(a)

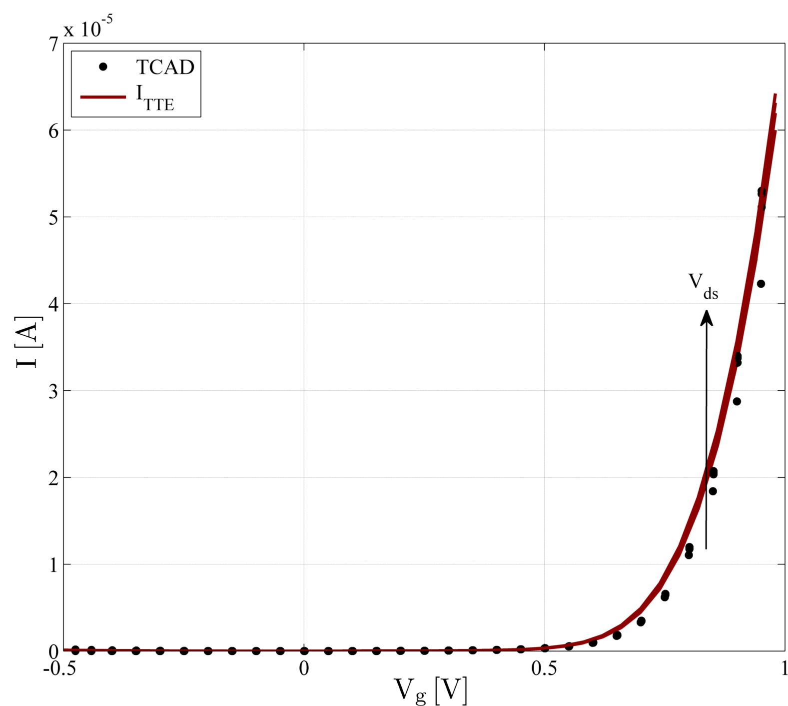

(b)

Figure 6.12.: $I_d - V_g$ characteristics of current I_{TTE} vs. TCAD for a SB-DG-MOSFET in (a) log-scale, (b) lin-scale for ϕ_{Bn}=0.28 eV. Device geometry: l_{ch}=45 nm, t_{ch}=20 nm, t_{ox}=2 nm, w_{ch}=1 µm. Bias conditions: V_{ds}=0.4 V to 1 V with 0.2 V stepping, V_g=−0.5 V to 1 V with 0.01 V stepping.

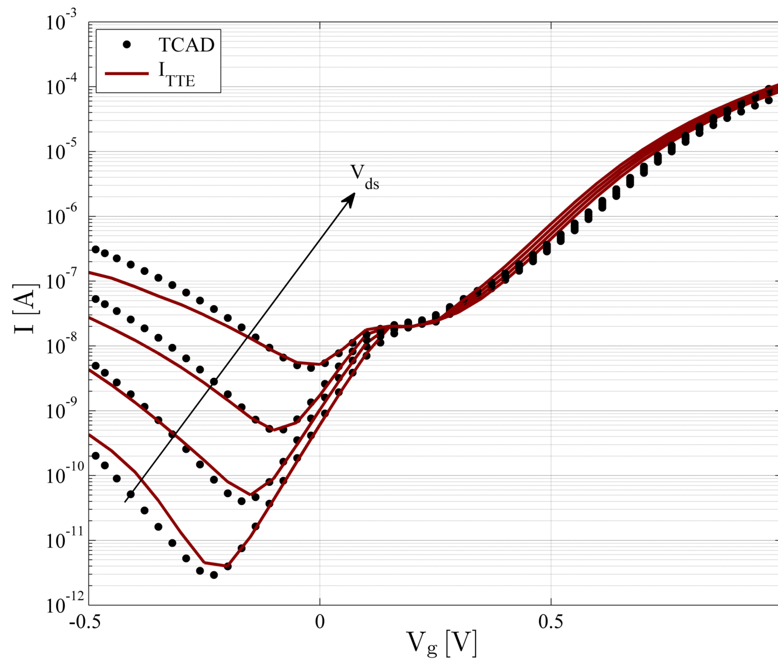

(a)

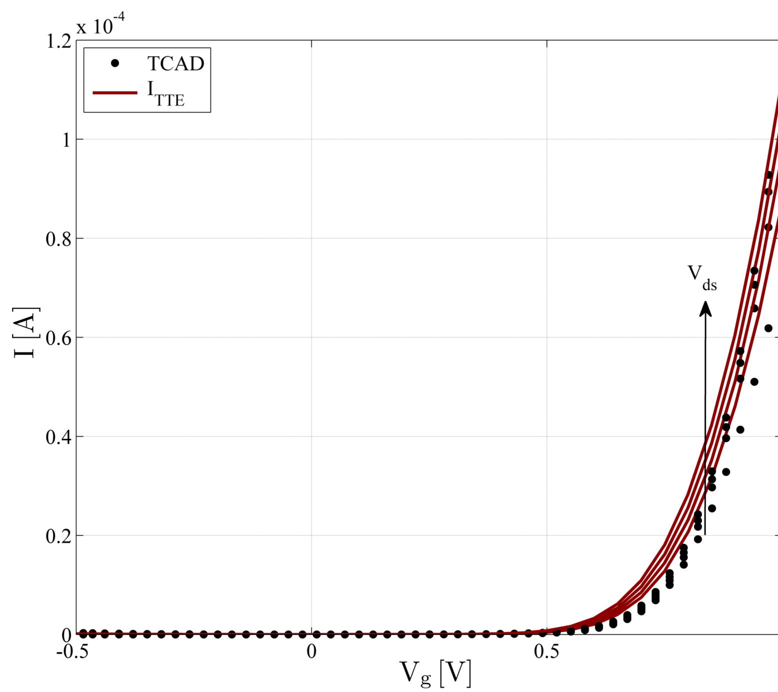

(b)

Figure 6.13.: $I_d - V_g$ characteristics of current I_{TTE} vs. TCAD for a SB-DG-MOSFET in (a) log-scale, (b) lin-scale for ϕ_{Bn}=0.28 eV. Device geometry: l_{ch}=22 nm, t_{ch}=10 nm, t_{ox}=2 nm, w_{ch}=1 µm. Bias conditions: V_{ds}=0.4 V to 1 V with 0.2 V stepping, V_g=−0.5 V to 1 V with 0.01 V stepping.

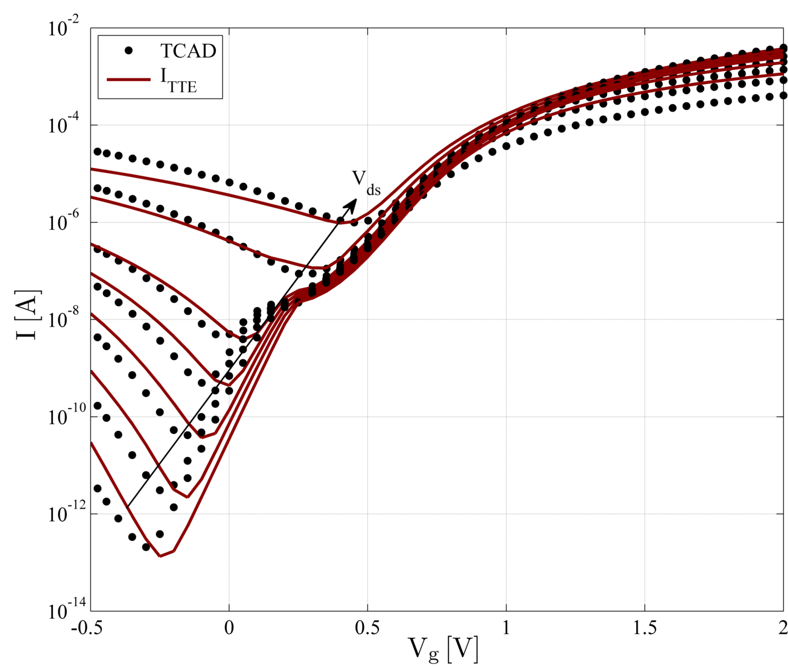

(a)

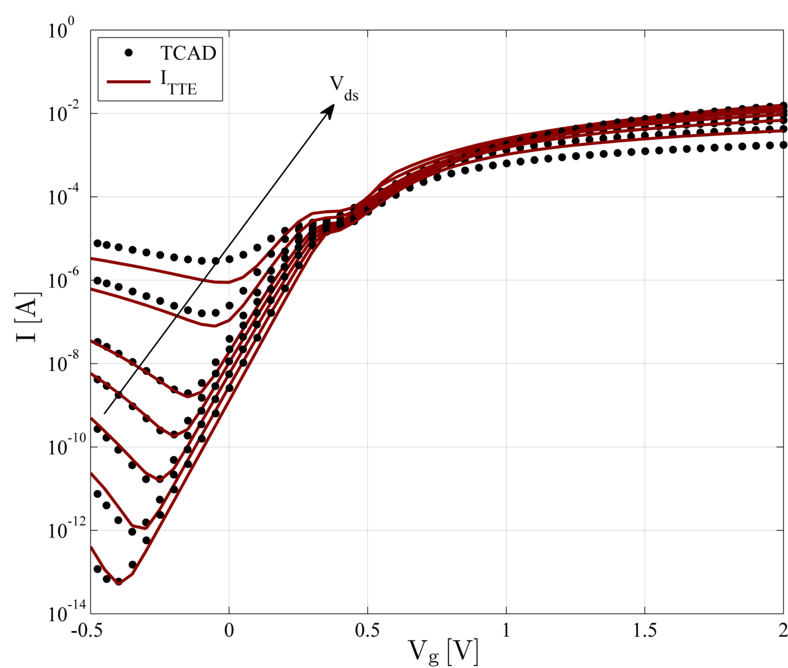

(b)

Figure 6.14.: $I_d - V_g$ characteristics of current I_{TTE} vs. TCAD for a SB-DG-MOSFET with (a) ϕ_{Bn}=0.28 eV, (b) ϕ_{Bn}=0.1 eV. Device geometry: l_{ch}=22 nm, t_{ch}=10 nm, t_{ox}=2 nm, w_{ch}=1 µm. Bias conditions: V_{ds}=0.2 V to 2 V with 0.2/0.5 V stepping, V_g=−0.5 V to 2 V with 0.01 V stepping.

Table 6.2.: Adjusted device model parameters for a channel length l_{ch}=45 nm.

Structural	l_{ch}	45	[nm]	channel length
	t_{ch}	20	[nm]	channel thickness
	t_{ox}	2	[nm]	oxide thickness
Mobility	μ_n	1.8	[cm^2/Vs]	elec. tunneling mobility
	μ_p	1.5	[cm^2/Vs]	hole tunneling mobility
Misc	N_B	10^{15}	[cm^{-3}]	substrate doping
	V_{fb}	-0.1	[V]	flatband voltage
	ϕ_{bi}	0.56	[V]	built-in potential s/d
	ϕ_{Bn}	0.28	[eV]	SBH electrons
	A_n^*	82	[A/cm^2K^2]	elec. Richardson constant
	A_p^*	32	[A/cm^2K^2]	hole Richardson constant
	m_n	0.22	[-]	elec. effect. mass
	m_p	0.16	[-]	hole effect. mass

From the source into the channel, the Fermi level is expected to considerably decrease due to the increasing current in strong inversion. Therefore, for an electron tunneling from the source into the channel, one receives an increased probability for finding a hole, i.e. a free state in the conduction band of the channel. The identical behavior is valid for the case of accumulation [176, 189].

Nevertheless, the behavior of the model is close to the results from TCAD Sentaurus in the subthreshold regime where tunneling/thermionic transport effects dominate. Of course, due to the simplifications described above some inaccuracies occur, but the shape of the several curves show a very good agreement. According to [135] in deep subthreshold region, thermionic emission is dominant, whereas in the subthreshold region tunneling limits the device current. Above the threshold voltage the drift-diffusion effects have an increasing influence [176, 189].

Furthermore, the model predicts the tunneling and thermionic current accurately for several barrier heights and channel lengths, e.g. Fig. 6.10(a) to 6.11(b). The presented model estimates the current for several contact materials, indicated by the parameter ϕ_{Bn} very well. As it can be seen from the Fig. 6.11(a) and 6.11(b) the electron barrier height varies with ϕ_{Bn}=0.4 eV and 0.28 eV. Both results are predicted accurately, e.g. the increased current for the electrons due to the lower barrier height in Fig. 6.11(b). This behavior indicates that lower barrier heights for electrons are desired to avoid the ambipolar behavior.

Furthermore, for the lower barrier height the shift to the left due to the increased thermionic emission current is calculated correctly. By using optimized parameters it is possible to predict the thermionic emission more correctly. One solution is an adjusted

Table 6.3.: Adjusted device model parameters for a channel length l_{ch}=22 nm.

Structural	l_{ch}	22	[nm]	channel length
	t_{ch}	10	[nm]	channel thickness
	t_{ox}	2	[nm]	oxide thickness
Mobility	μ_n	2.7	[cm^2/Vs]	elec. tunneling mobility
	μ_p	1.6	[cm^2/Vs]	hole tunneling mobility
Misc	N_B	10^{15}	[cm^{-3}]	substrate doping
	V_{fb}	-0.1	[V]	flatband voltage
	ϕ_{bi}	0.56	[V]	built-in potential s/d
	ϕ_{Bn}	0.28 | 0.1	[eV]	SBH electrons
	A_n^*	62	[A/cm^{2}K^2]	elec. Richardson constant
	A_p^*	32	[A/cm^{2}K^2]	hole Richardson constant
	m_n	0.18	[-]	elec. effect. mass
	m_p	0.20	[-]	hole effect. mass

flat band voltage V_{fb}. However, the masses and the Richardson constant have to be modified as well.

Beside this, also the influence of the device geometry is included in the model. For l_{ch}=100 nm and l_{ch}=65 nm one observes only minor influence of the channel length. The limiting factors are thermionic emission and tunneling current. Therefore, the influence of SCEs and DIBL are low, as Fig. 6.10(a) to 6.11(b) show. Finally, the slope from the model compared to the simulated results from TCAD shows promising results, due to the similarity between the two [176, 189].

Additional results, predicted with the enhanced equation (6.11) are given in Fig. 6.12 to 6.14 and adjusted as indicated in Tables 6.2 and 6.3. In Fig. 6.12(a) the transfer characteristic in log-scale for a 45 nm device at different drain biases are presented. Especially in log-scale one is able to observe the dependency of the hole current from the drain bias V_{ds}. With increasing V_{ds} the hole current increases due to the thinned barrier at the drain junction and the therefore increased probability of the hole charge carriers to tunnel. Furthermore, a good prediction of the slope to inversion can be observed. In Fig. 6.12(b) the corresponding lin-scale plot is shown which is predicted quite very well [189].

As already explained, the behavior is more or less identical, this is observed in Fig. 6.13(a) and 6.13(b) where the transfer characteristics are shown for a 22 nm device. The identical dependency of the hole current from the drain bias V_{ds} can be observed. A good agreement can be noticed, especially in the thermionic emission and tunneling regions [189].

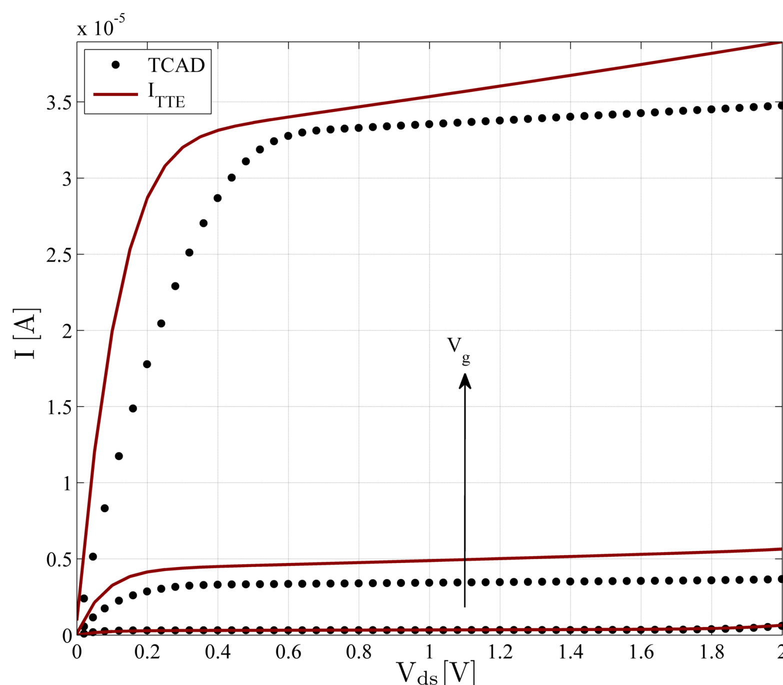

Figure 6.15.: $I_d - V_{ds}$ characteristics of current I_{TTE} vs. TCAD with ϕ_{Bn}=0.28 eV. Device geometry: l_{ch}=45 nm, t_{ch}=20 nm, t_{ox}=2 nm, w_{ch}=1 µm. Bias conditions: V_{ds}=0 V to 2 V with 0.01 V stepping, V_g=0.5 V to 0.9 V with 0.2 V stepping.

Finally, in Fig. 6.14 a comparison of the transfer characteristics for 22 nm devices with two barrier heights ϕ_{Bn} are shown. Both characteristics are calculated over a large range. The gate potential V_g is biased from −0.5 V to 2 V and the drain to source voltage V_{ds} from −0.2 V to 2 V. As expected the device for the lower barrier height shows an increased electron current, Fig. 6.14(b). Furthermore, in both devices the slopes are predicted very accurately, as well as the hole and electron tunneling currents while the fitting parameters between both devices slightly differ [189].

From the presented results for the ANMA it is easy to observe that the modeling approaches work well. Of course, approximations have been made which were necessary, to calculate the current contributions with the aim to built a compact model. However, from the curves a very good agreement over a wide range can be seen and by including more effects with additional models, a further improvement has to be expected.

6.6. Results $I_d - V_{ds}$

The results of the output characteristics $I_d - V_{ds}$ for the analytical numerical modeling approach have been simulated and calculated with the identical parameters as for the $I_d - V_g$ curves from Tables **??** to 6.3. Furthermore, the identical parameters for the

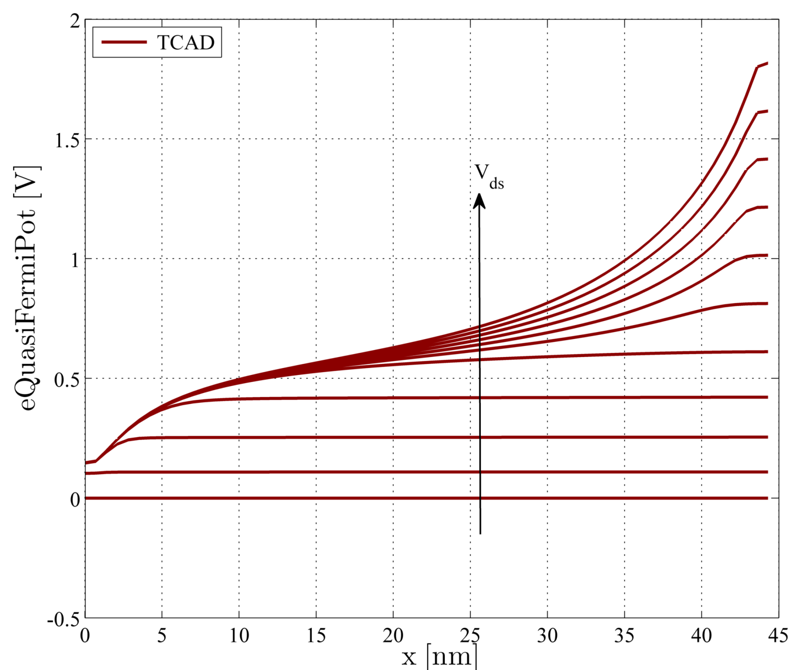

Figure 6.16.: TCAD eQuasiFermiPotential at the silicon-to-oxide interface. Results for ϕ_{Bn}=0.28 eV. Device geometry: l_{ch}=45 nm, t_{ch}=20 nm, t_{ox}=2 nm. Bias conditions: V_{ds}=0 V to 2 V with 0.2 V stepping, V_g=1 V. A behavior of two parts can be observed, one voltage drop at the junctions and one in the channel region.

carrier masses, mobilities, and Richardson constants are used in the model, depending on the presented result and the used equation for the estimation of the tunneling current.

In Fig. 6.15 the $I_d - V_{ds}$ curves in lin-scale are presented and compared with TCAD Sentaurus device simulation. As one can observe from the figure the device is biased for V_{ds} from 0 V to 2 V and for V_g from 0.5 V to 0.9 V with 0.2 V stepping. The output characteristic for the lower gate bias is predicted quite accurately while for an increased gate potential an inaccuracy can be observed. The current for the lower V_{ds} saturates too fast. Literature until today holds no publications known which deal with this resulting problem of modeling approaches for Schottky barrier devices. If $I_d - V_{ds}$ curves are presented, as in [133], they are in log-scale. Here, the influence of the too early saturated current is of minor interest [189, 190].

6.6.1. Analyses

To predict the $I_d - V_{ds}$ curve correctly, it is necessary to analyze the device behavior and understand how, why and where the inaccuracy results from. Therefore, an analyses of several components with the TCAD Sentaurus device simulator is made [189, 190].

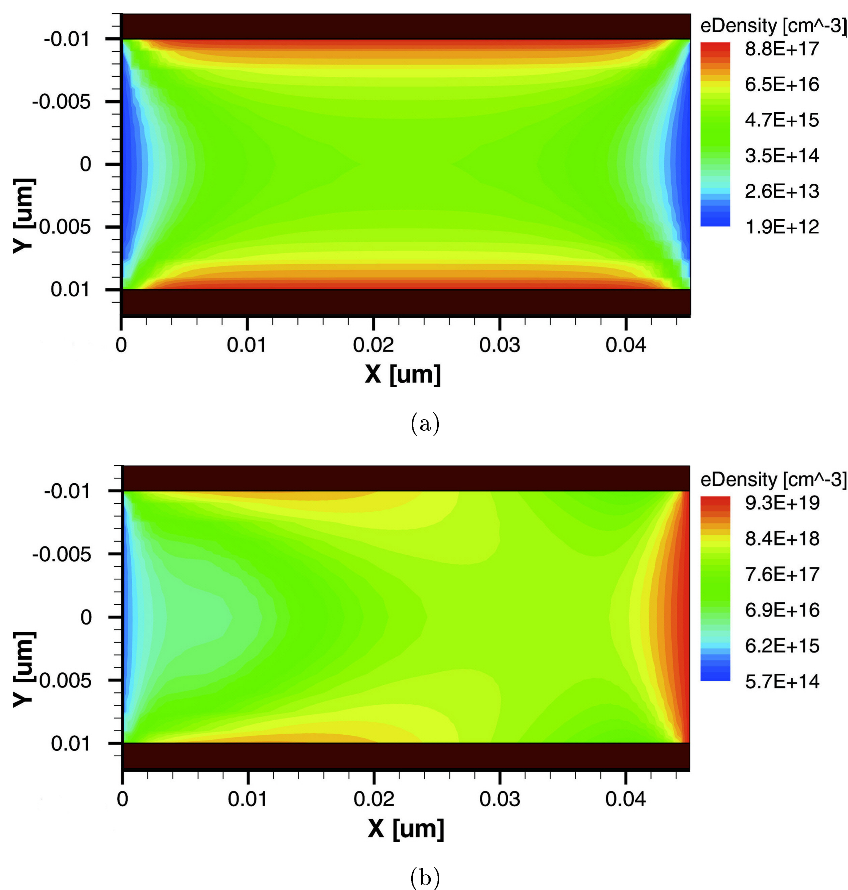

Figure 6.17.: TCAD eCurrentDensity at the silicon-to-oxide interface with (a) V_g=0 V and (b) V_g=1 V. Results for ϕ_{Bn}=0.28 eV. Device geometry: l_{ch}=45 nm, t_{ch}=20 nm, t_{ox}=2 nm. Bias conditions: V_{ds}=1 V. The device operates in the linear mode.

In a first step, the electron quasi Fermi potential is analyzed, as illustrated in Fig. 6.16. The following behavior on the device is observed. For a gate bias of V_g=1 V and various V_{ds} one is able to see an increasing influence on the device. The lower the V_{ds}, the main voltage drop results at the Schottky barrier junctions. While the V_{ds} rises to 1 V, an increasing influence onto the channel is to be observed. Here, also a voltage drop for higher V_{ds} can be seen [189, 190].

Due to these circumstances, the Schottky barrier Double-Gate MOSFET can be split into two parts. One can assume that the Schottky barrier Double-Gate MOSFET consists of two devices. The first device is a SBJ-DG-MOSFET (Schottky barrier junction DG-MOSFET) excluding drift-diffusion effects in the channel, of which the model describes the influence of two-dimensional effects on the currents at the Schottky barrier junctions. Second, a CH-DG-MOSFET (Channel DG-MOSFET) predicting the drift-diffusion current behavior in the channel region [189, 190].

UNIVERSITAT ROVIRA I VIRGILI
TWO-DIMENSIONAL ANALYTICAL PREDICTIVE MODELING OF SCHOTTKY BARRIER SOI AND MULTI-GATE MOSFETS
Mike Schwarz
Dipòsit Legal: T.456-2013

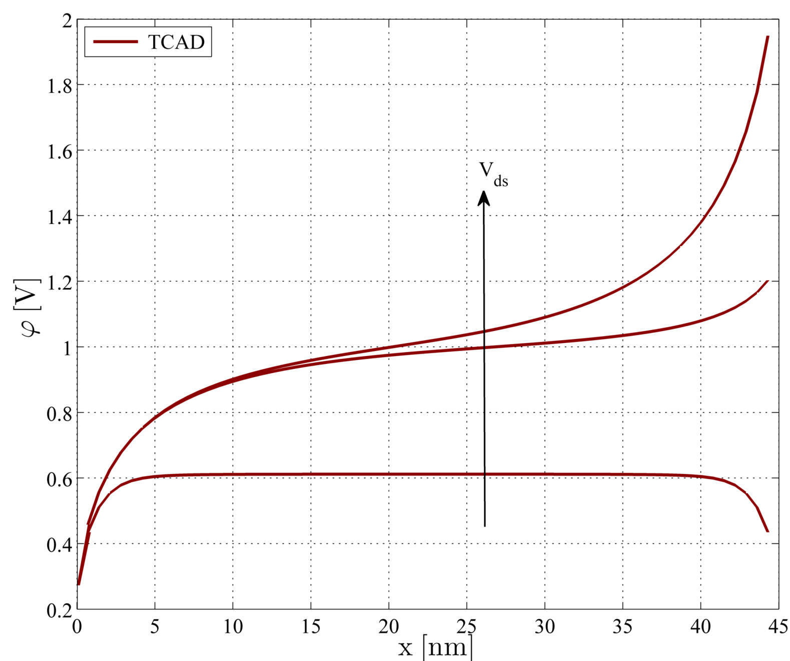

Figure 6.18.: TCAD electrostatic potential φ at the silicon-to-oxide interface. Results for ϕ_{Bn}=0.28 eV. Device geometry: l_{ch}=45 nm, t_{ch}=20 nm, t_{ox}=2 nm. Bias conditions: V_{ds}=0 V to 2 V with 0.01 V stepping, V_g=1 V.

Some further investigations show that the second device, the CH-DG-MOSFET which predicts the drift-diffusion effects, operates in the linear mode. This is to be observed from the Fig. 6.17(a) and 6.17(b) where the electron density is shown. From both plots it can be seen that underneath the oxide the main concentration results which operates in the linear region [189, 190].

If one observes the corresponding potential distributions, as in Fig. 6.18, it is clear that the observed behavior confirms the before made observations. The main voltage drop results at the ideal Schottky barrier junctions, and with increasing the V_{ds} an additional voltage drop within the channel results. This voltage drop is still in the linear operation region which results in a current limitation by the Schottky barrier junctions. The current is mainly limited by the Schottky barrier junction device [189, 190].

6.6.2. Macro Model Approach

With the knowledge won from the analyses, the following approach is applied to consider the drift-diffusion effects in the channel. From the assumption that the Schottky barrier Double-Gate MOSFET consists of two devices, a SBJ-DG-MOSFET and a CH-DG-MOSFET, a macro model is introduced to take account for the effects described above, as shown in Fig. 6.19 [189, 190].

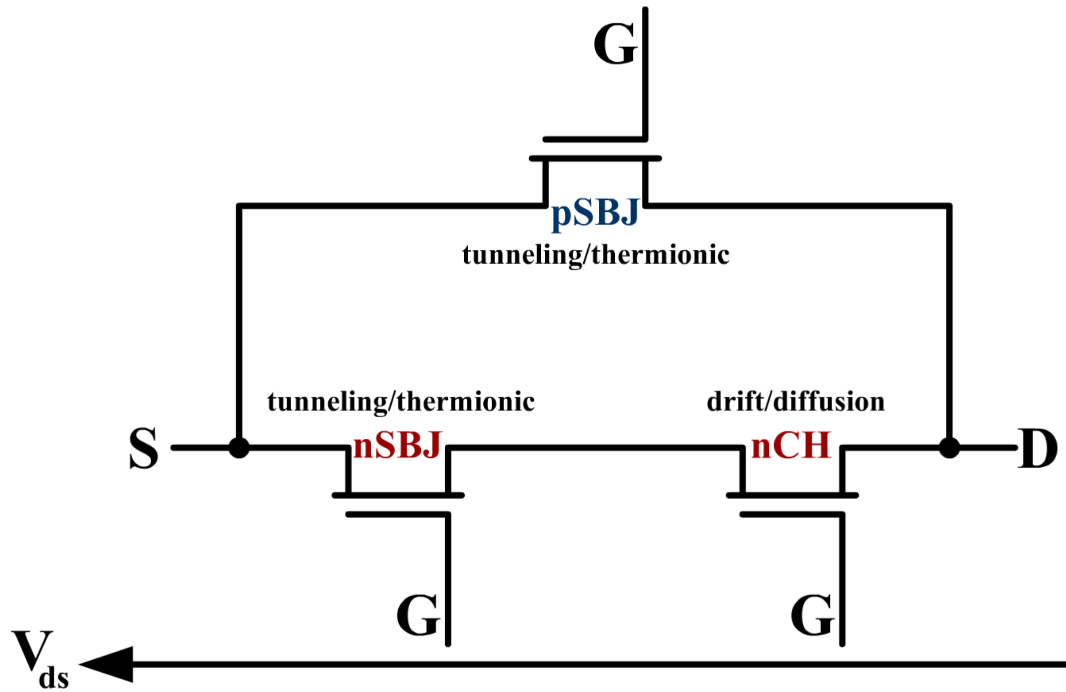

Figure 6.19.: A macro model is introduced to take account for the effects of drift-diffusion.

By neglecting the drift-diffusion effect for the holes, because for the $I_d - V_{ds}$ curve they are of minor interest, the following macro model is developed. A nSBJ-DG-MOSFET and a nCH-DG-MOSFET in series describes the behavior for the electrons. In parallel a pSBJ-DG-MOSFET for the holes is applied. By combining all transistors, the pSBJ-DG-MOSFET, the nSBJ-DG-MOSFET and the nCH-DG-MOSFET in a macro model, the $I_d - V_{ds}$ characteristic is calculated [189, 190].

For the nSBJ-DG-MOSFET and pSBJ-DG-MOSFET the ANMA approach for the electrons and holes as described in the previous sections are applied. The nCH-DG-MOSFET can be calculated by the following simple equation of a standard Double-Gate MOSFET in the linear operation regime. It follows

$$I_{DD} = \mu C'_{ox} \frac{2W}{L} \left(V_g - V_{th} - \frac{V_{ds}}{2} \right) V_{ds}. \tag{6.15}$$

The standard Double-Gate MOSFET equation is applied from the fact that the description should be sufficient enough.

6.6.3. Results

The approach of the macro model [189, 190] is applied in Fig. 6.20. For the $I_d - V_{ds}$ curves the voltage drop at the CH-DG-MOSFET due to equation (6.15) is calculated at the given current and additively considered in the voltage axis.

UNIVERSITAT ROVIRA I VIRGILI
TWO-DIMENSIONAL ANALYTICAL PREDICTIVE MODELING OF SCHOTTKY BARRIER SOI AND MULTI-GATE MOSFETS
Mike Schwarz
Dipòsit Legal: T.456-2013

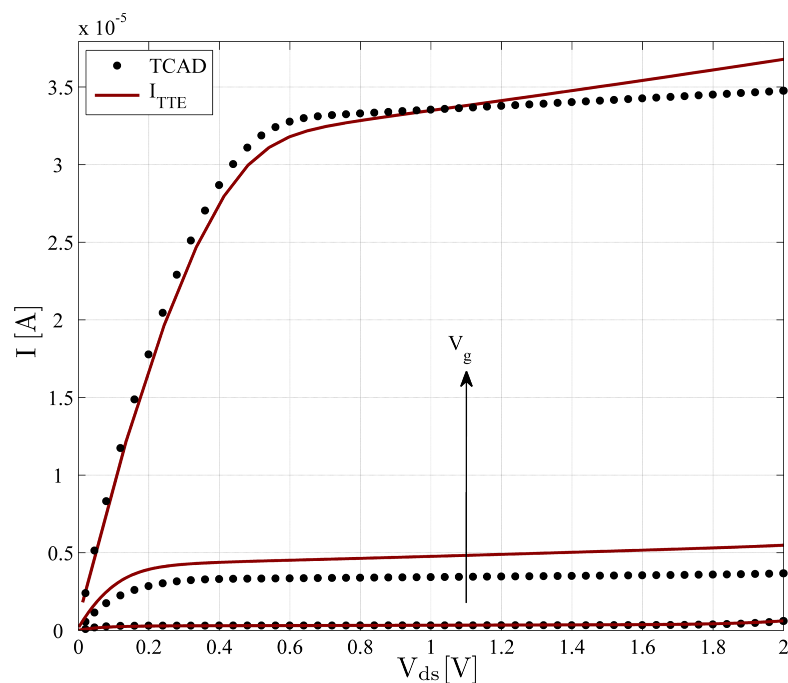

Figure 6.20.: $I_d - V_{ds}$ characteristics of current I_{TTE} vs. TCAD with ϕ_{Bn}=0.28 eV. Device geometry: l_{ch}=45 nm, t_{ch}=20 nm, t_{ox}=2 nm, w_{ch}=1 µm. Bias conditions: V_{ds}=0 V to 2 V with 0.01 V stepping, V_g=0.5 V to 0.9 V with 0.2 V stepping.

In Fig. 6.20 one is able to observe an improvement in the output characteristics, especially, when a comparison is made with Fig. 6.15. Now the currents for the higher gate potentials are predicted more accurately as without the approach of a macro model which takes into account the drift-diffusion effects in the channel region. Nevertheless, some inaccuracies are still in the output characteristics. The currents for the higher gate potentials are increasing with higher V_{ds}. This effect results from the overestimated drain induced barrier thinning (DIBT) effect. Additional charges influence and shield the source junction and therefore the tunneling current increases much lower, if the DIBT is included due to the lower tunneling probability [189, 190].

In Fig. 6.21 the $I_d - V_{ds}$ curves for a channel length of l_{ch}=22 nm are presented. As one can observe the device is biased for V_{ds} from 0 V to 1 V and for V_g from 0.5 V to 1 V with 0.1 V stepping. Similar effects are observed. Furthermore, a large inaccuracy for V_g=1 V is observed where the current for the gate potential is much lower than that from the simulation result. Here, it might be that the applied simple equation for the standard Double-Gate MOSFET in the model is not accurate enough. However, an approach has been presented which is able to correct the influence in the channel region and predict the overall current in the $I_d - V_{ds}$ curves more accurately [189, 190].

UNIVERSITAT ROVIRA I VIRGILI
TWO-DIMENSIONAL ANALYTICAL PREDICTIVE MODELING OF SCHOTTKY BARRIER SOI AND MULTI-GATE MOSFETS
Mike Schwarz
Dipòsit Legal: T.456-2013

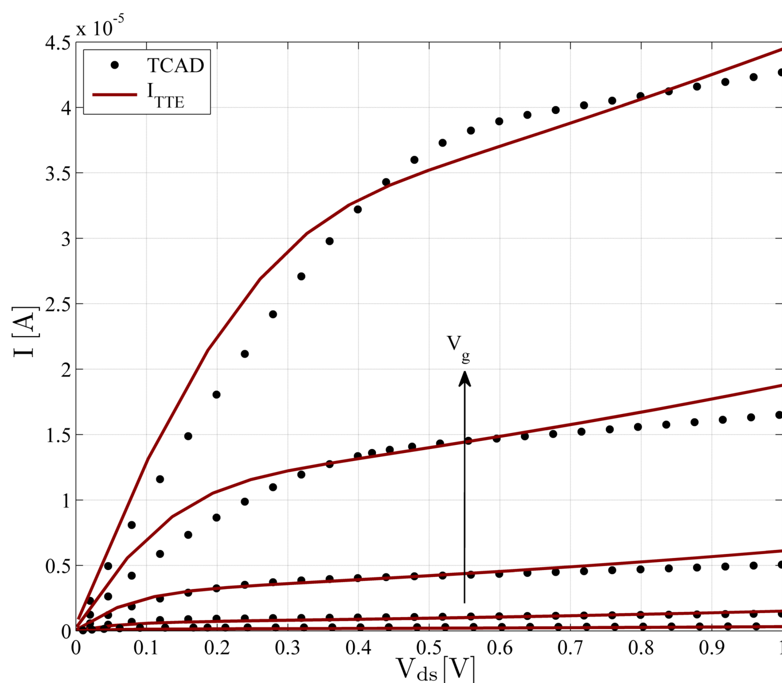

Figure 6.21.: $I_d - V_{ds}$ characteristics of current I_{TTE} vs. TCAD with ϕ_{Bn}=0.28 eV. Device geometry: l_{ch}=22 nm, t_{ch}=10 nm, t_{ox}=2 nm, w_{ch}=1 µm. Bias conditions: V_{ds}=0 V to 1 V with 0.01 V stepping, V_g=0.5 V to 1 V with 0.1 V stepping.

6.7. Investigation of the Scaling Behavior of Schottky Barrier Double-Gate MOSFETs

In this section the analytical numerical modeling approach for the currents in SB-DG-MOSFETs has been used to investigate the scaling behavior. The model parameters like charge carrier masses, Richardson constants and tunneling mobilities have been adjusted on to a channel length l_{ch}=22 nm to fit the simulation data (Fig. 6.24) of TCAD Sentaurus (Table 6.3). The following analyses starts with the analytical numerical modeling approach whereby all model parameters are kept constant. Here, the qualitative prediction of the device scaling behavior is crucial instead of a quantitative reproducibility of the device current. Therefore, quantum mechanical effects are not considered in the analyses.

In Fig. 6.23 the schematic of the I_{on}/I_{off} ratio, the SSlope (subthreshold slope) and DIBL are shown. In our scaling study I_{off} is defined as the minimum current achievable, when the MOSFET is turned off, and the maximum drain to source bias of 1 V is applied. One estimates the current I_{on}, when the device is turned on with a gate voltage increase of 1 V with respect to the off state. This is a reasonable procedure e.g. for an inverter.

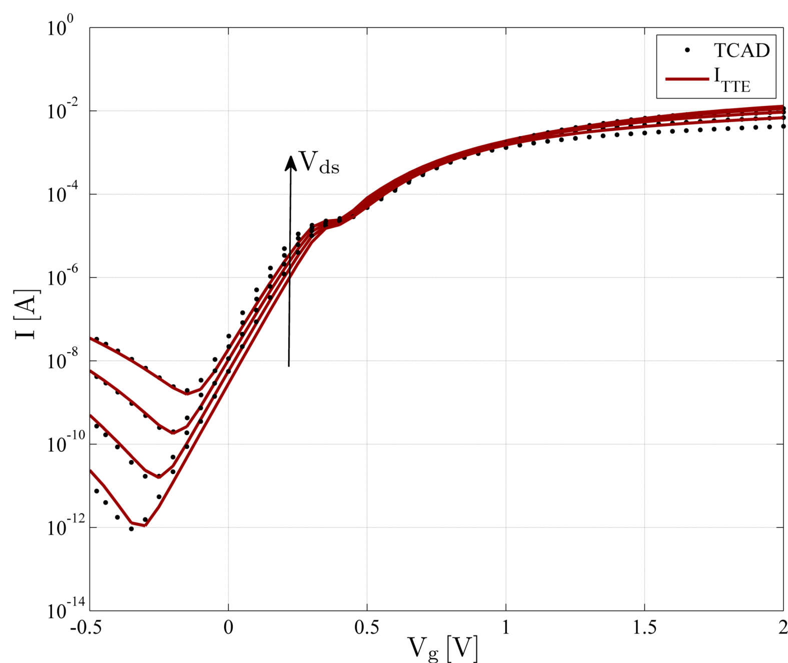

Figure 6.22.: $I_d - V_g$ characteristics of current I_{TTE} vs. TCAD for a SB-DG-MOSFET with ϕ_{Bn}=0.1 eV. Device geometry: l_{ch}=22 nm, t_{ch}=10 nm, t_{ox}=2 nm, w_{ch}=1 µm. Bias conditions: V_{ds}=0.4 V to 1 V with 0.2 V stepping, V_g=−0.5 V to 2 V with 0.01 Vstepping.

Fig. 6.24 ratio shows the I_{on}/I_{off} vs. Schottky barrier height ϕ_{Bn} for various device geometries. First, one observes the curves for a channel thickness of t_{ch}=10 nm. Generally, a low barrier height ϕ_{Bn} results in a better I_{on}/I_{off} ratio. This behavior results from a lower ambipolar behavior, caused by the holes which influence the I_{off}. Furthermore, a higher range of decades in the $I_d - V_g$ curves result. As expected, the higher the channel length the better the I_{on}/I_{off} ratio due to the better electrostatic control. This behavior matches with the results of Najari [191] for Schottky barrier carbon nanotube transistors where the I_{on} vs. Schottky barrier height ϕ_{Bn} is analyzed.

If one observes a reduced channel thickness of t_{ch}=5 nm whereby quantum effects are neglected, the behavior for the short-channel is as expected. The I_{on}/I_{off} ratio is improved by the increased gate control. For the long-channel device a non expected behavior results in a degradation of the I_{on}/I_{off} ratio. A higher leakage current due to the ambipolar behavior at the drain end of the channel is responsible. In the case of long-channel devices this influence is higher than for the short-channel devices, because in the latter additional 2D effects from the source take influence on to the drain, and at least on the resulting hole current. Therefore, as a result, it is very important to analyze the device scaling behavior in conjunction with the height of the Schottky barrier to find the optimal combination of parameters providing the best device performance.

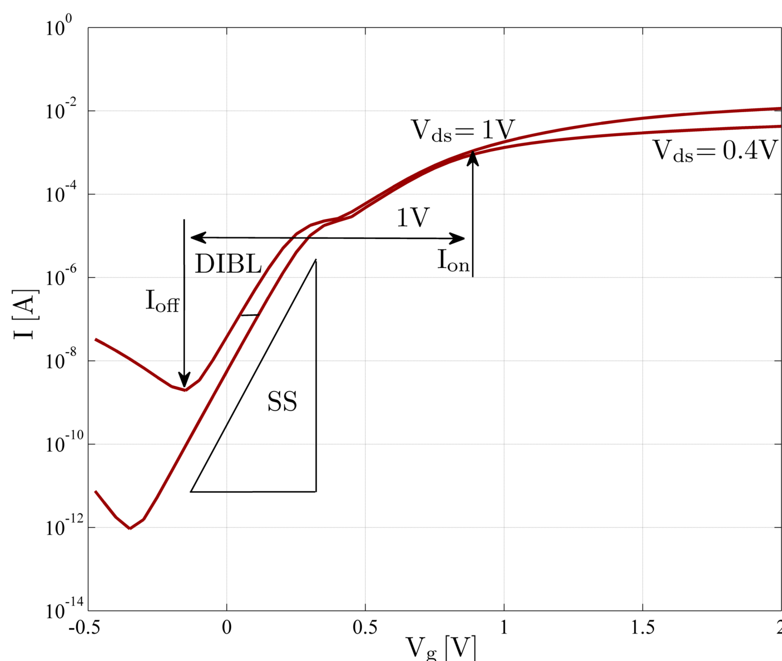

Figure 6.23.: The schematic of the estimation for the I_{on}/I_{off} ratio. The current I_{off} is extracted, when the device is turned off with a gate voltage resulting in a minimal leakage current. Current I_{on} is estimated, when the device is turned on with a gate voltage increase of 1V with respect to the off state.

The I_{on}/I_{off} ratio vs. SSlope is illustrated for various ϕ_{Bn} and $V_{ds} = 1V$ with a channel thickness t_{ch}=10 nm in Fig. 6.25(a). The degradation of the slopes for the long-channel devices is lower compared to the short-channel devices, as expected. In general the slopes of shorter channels are degraded, because the ambipolar behavior is increased which results in a higher degradation. For that two rules can be formulated. The lower the ϕ_{Bn}, the higher the I_{on}/I_{off} ratio. The lower the ϕ_{Bn}, the lower the SSlope.

As for the analysis in Fig. 6.24 here also for the I_{on}/I_{off} ratio vs. SSlope the channel thickness is reduced. A channel thickness t_{ch}=5 nm as shown in Fig. 6.25(b) might lead to a degradation. In general the behavior is similar to Fig. 6.25(a), except the decreased I_{on}/I_{off} ratio for the long-channel device. This behavior was expected from the analysis already made in Fig. 6.24. Again a higher leakage current due to the ambipolar behavior at the drain end of the channel is responsible for the degraded I_{on}/I_{off} ratio. Furthermore, an improvement of the I_{on}/I_{off} ratio for the short-channel device is observed due to the better electrostatic control for t_{ch}=5 nm. Still the above introduced rules are valid. However, sometimes a possible improvement can result in a degradation as presented in the analyses.

In Fig. 6.26(a) the SSlope vs. the channel length l_{ch} for channel thickness t_{ch}=10 nm is shown. As in the figure illustrated the behavior is similar to a conventional Double-Gate

UNIVERSITAT ROVIRA I VIRGILI
TWO-DIMENSIONAL ANALYTICAL PREDICTIVE MODELING OF SCHOTTKY BARRIER SOI AND MULTI-GATE MOSFETS
Mike Schwarz
Dipòsit Legal: T.456-2013

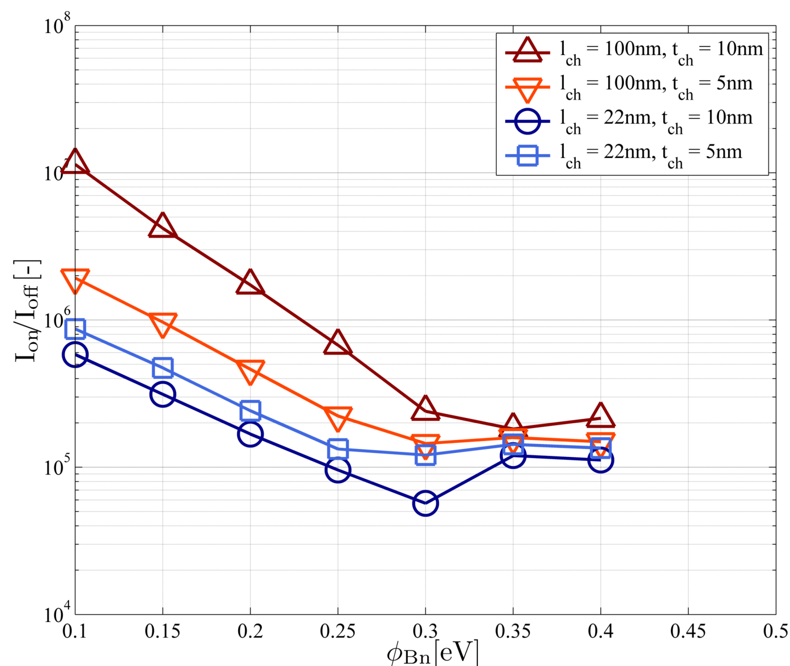

Figure 6.24.: Impact of I_{on}/I_{off} vs. ϕ_{Bn} for various geometries.

MOSFET. By decreasing the channel length a degradation of the SSlope is observed. In contrast to the conventional devices, here also the Schottky barrier height ϕ_{Bn} has an enormous influence, as already observed for the above made analyses. Due to the ambipolar behavior at the drain end of the channel the resulting leakage current from the holes influence the slope, especially for high V_{ds}. In this case due to the band bending at the drain junction and the low barrier height ϕ_{Bp} for the holes, a higher tunneling probability results and therefore a higher leakage current.

If one reduces the channel thickness again from t_{ch}=10 nm to t_{ch}=5 nm, a behavior as shown in Fig. 6.26(b) is observed. In general the SSlope vs. the channel length l_{ch} is improved, except the case for a ϕ_{Bn}=0.3 eV with a V_{ds}=1 V. Here, the SSlope for all channel lengths up to 100 nm is worse compared to the rest of the results. Of course for the shorter channel lengths also an improvement is observed, but for the longer channel devices a degradation of the SSlope results from the missing additional 2D effects.

Finally, an analysis of the DIBL vs. ϕ_{Bn} for a channel thickness of t_{ch}=10 nm is made (Fig. 6.27). If one observes the long-channel device, an improvement in DIBL for lower ϕ_{Bn} is observed which again results from the less ambipolar behavior. For the short-channel device a minor influence on the DIBL takes place. The effect of the barrier height reduction is less, because the DIBL is mainly dominated by the electrostatic influence from the drain than from the ambipolar behavior. Here, the DIBL is primarily influenced as in conventional MOS devices.

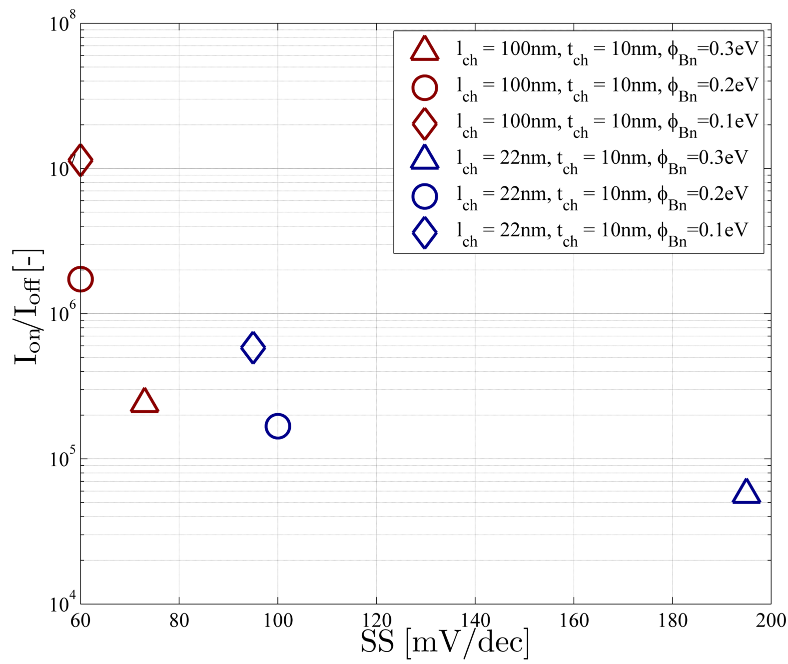

(a)

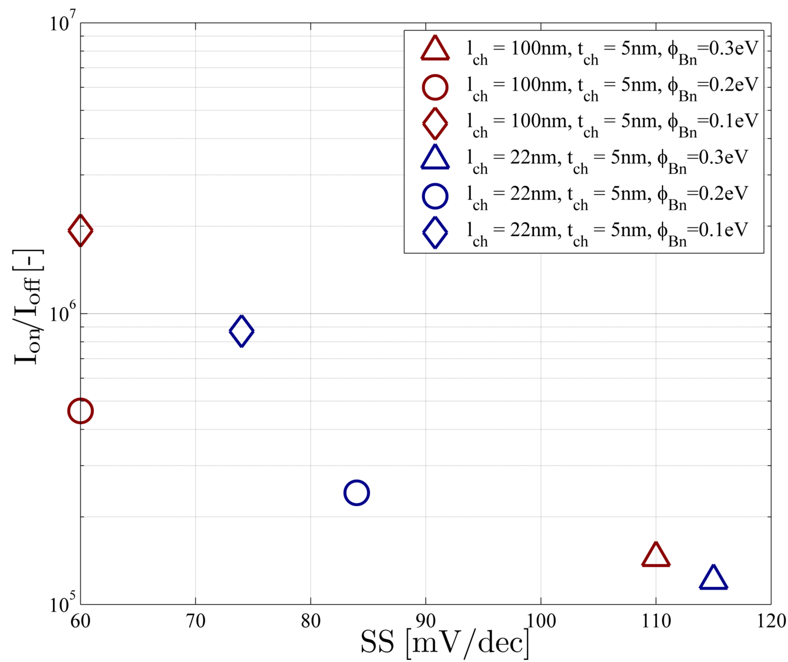

(b)

Figure 6.25.: Impact of I_{on}/I_{off} vs. SSlope for various ϕ_{Bn} and V_{ds}=1 V, with (a) t_{ch}=10 nm and (b) t_{ch}=5 nm.

UNIVERSITAT ROVIRA I VIRGILI
TWO-DIMENSIONAL ANALYTICAL PREDICTIVE MODELING OF SCHOTTKY BARRIER SOI AND MULTI-GATE MOSFETS
Mike Schwarz
Dipòsit Legal: T.456-2013

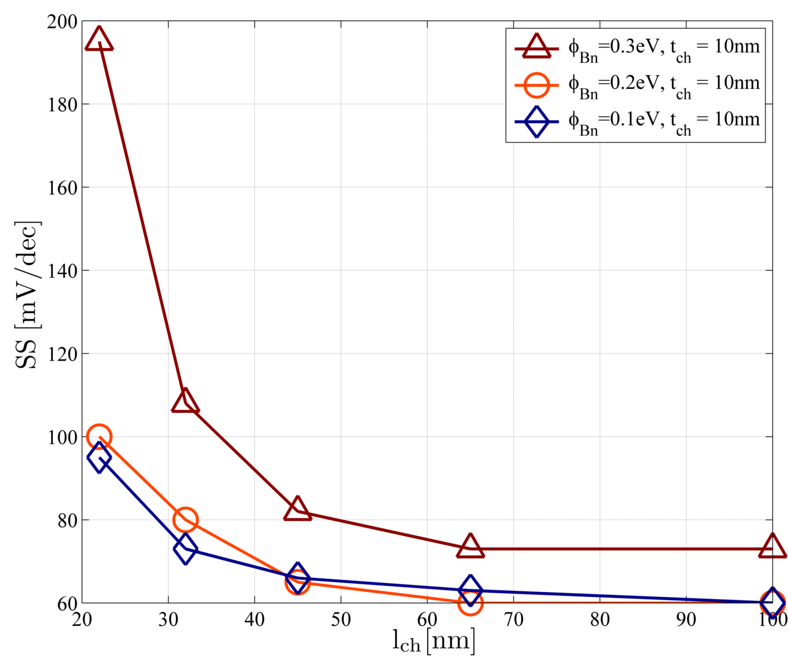

(a)

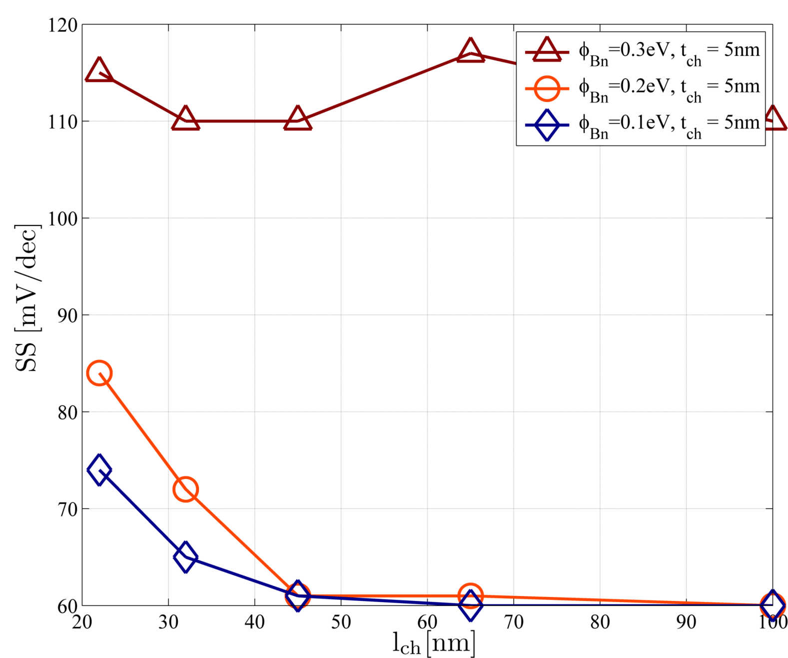

(b)

Figure 6.26.: Impact of SSlope vs. l_{ch} for V_{ds}=1 V, with (a) t_{ch}=10 nm and (b) t_{ch}=5 nm.

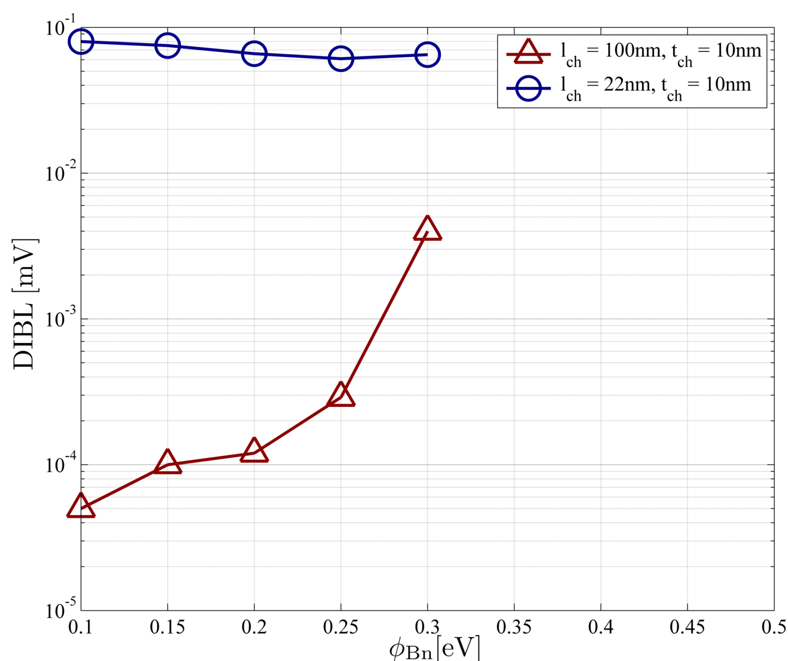

Figure 6.27.: Impact of DIBL vs. ϕ_{Bn} with l_{ch}=100 nm and l_{ch}=22 nm. For long-channel devices, an improvement in DIBL for lower ϕ_{Bn} is observed while for the short-channel devices a minor influence on the DIBL takes place.

The work presented here is very important from a circuit designer's point of view. Various parameter combinations are analyzed by using the analytical model which cost a fractional amount of time compared to state of the art device simulators like TCAD Sentaurus. Furthermore, more complex analyses can be done to fulfill the ITRS roadmap [3]. As example, for an I_{on}/I_{off} ratio of 10^6 it is necessary to lower the barrier height ϕ_{Bn}. But from Fig. 6.24 it can be observed that for a given gate length of 22 nm this is not achievable. An improvement of the leakage current and/or SSlope is necessary to fulfill the ITRS roadmap requirement.

6.8. Conclusion

Within this chapter an analytical numerical modeling approach for the currents in SB-DG-MOSFETs has been presented. Based on the models for the electrostatics of chapter 5 the tunneling and thermionic current mechanisms have been calculated and described in a quasi 2D approach.

The tunneling mechanism was estimated by the WKB approximation which was used for the tunneling probability of the charge carriers. The probability as well as the carrier distributions are calculated with the model of the electrostatics with respect to

UNIVERSITAT ROVIRA I VIRGILI
TWO-DIMENSIONAL ANALYTICAL PREDICTIVE MODELING OF SCHOTTKY BARRIER SOI AND MULTI-GATE MOSFETS
Mike Schwarz
Dipòsit Legal: T.456-2013

the coordinates. Additionally, in an enhanced approach also diffusion effects are included in the tunneling current calculation.

Furthermore, the thermionic emission mechanism is modeled with a given explicit equation from literature by the use of the electrostatics of chapter 5. In each slice of the quasi 2D approach the maximum barrier the charge carrier have to surmount is used to predict the thermionic emission current.

The analytical current calculations of the $I_d - V_g$ curves show a very good agreement for a comparison with TCAD simulation data down to channel lengths of 22 nm for reasonable device geometries. The results illustrate that the current components are predicted accurate for a large bias range, several barrier heights and geometries.

Nevertheless due to several approximations some inaccuracies exist in the model. These approximations are e.g. the neglected drift-diffusion effects for the deep inversion. They have to be included by additional models which take into account for the effects.

Furthermore, the analytical current calculations of the $I_d - V_{ds}$ curves have been improved by the introduction of a macro model which take into account for drift-diffusion effects. Considering the drift-diffusion effects in the $I_d - V_{ds}$ curves, a good agreement for a comparison with TCAD simulation data down to channel lengths of 22 nm can be observed.

Also, inaccuracies exist in the approach of a macro model due to the simplified CH-DG-MOSFET equation which was applied and has to be improved. Therefore, in a further work additional investigations are necessary. Also a model which reduces the overestimated DIBT effect is needed, to predict the $I_d - V_{ds}$ curves more precisely.

However, the model is able to predict the current with ambipolar behavior well for several barrier heights and geometries up to a relatively high gate bias while the approach in particular inherently includes 2D effects on the device current.

Furthermore, the analytical numerical modeling approach can be used to investigate the scaling behavior of SB-DG-MOSFETs which is very important from a circuit designer's point of view. Various parameter combinations have been analyzed in a fractional amount of time in a qualitative prediction. The presented results have shown that sometimes an expected improvement results in a degradation, or vice versa.

UNIVERSITAT ROVIRA I VIRGILI
TWO-DIMENSIONAL ANALYTICAL PREDICTIVE MODELING OF SCHOTTKY BARRIER SOI AND MULTI-GATE MOSFETS
Mike Schwarz
Dipòsit Legal: T.456-2013

Chapter 7.

2D Analyses of the Current Components

The solution for the currents in a Schottky barrier device, presented in the previous section, is based on an analytical numerical modeling approach (ANMA). However, for the definition of a compact model explicit equations have to be found which predict and describe the behavior of the device in a numerically efficient way.

To find explicit equations for the integrals in the analytical numerical modeling approach (ANMA), analyses with the state-of-the-art device simulator Synopsys TCAD Sentaurus are made in this section. Herewith, the main contributions to the tunneling current are investigated. Concentrating onto these primary effects, simplified analytical equations will be derived which predict the contributions well and can be solved in closed-from. Due to these circumstances the following chapter deals with the analysis of the current components. First, the Tunneling Generation Rate of TCAD is analyzed afterwards, the current contributions from the analytical numerical modeling approach (ANMA) are investigated and visualized. Finally, a comparison between the ANMA TGR and the TCAD Tunneling Generation Rate is made including an analysis of the model current densities.

7.1. Analyses of the TCAD Tunneling Generation Rate

The TCAD Tunneling Generation Rate is comparable to equation (6.9), the product of the carrier distributions, and the tunneling probability. A Schottky barrier Double-Gate device with a channel length l_{ch}=22 nm and a channel thickness t_{ch}=10 nm was simulated to illustrate the spatial distribution of the generated tunneling carriers. Various Schottky barrier heights, ϕ_{Bn}=0.1 eV, 0.28 eV, 0.4 eV with bias conditions for V_{ds}=1 V and V_g=−0.5 V, 0 V, 1 V have been investigated.

In Fig. 7.1 and 7.2 the Tunneling Generation Rate for ϕ_{Bn}=0.4eV is shown. In Fig. 7.1(a), 7.1(b), and 7.1(c) the hole Tunneling Generation Rate and in Fig. 7.2(a), 7.2(b), and 7.2(c) the electron Tunneling Generation Rate for the various gate potentials V_g=−0.5 V, 0 V, 1 V are illustrated.

UNIVERSITAT ROVIRA I VIRGILI
TWO-DIMENSIONAL ANALYTICAL PREDICTIVE MODELING OF SCHOTTKY BARRIER SOI AND MULTI-GATE MOSFETS
Mike Schwarz
Dipòsit Legal: T.456-2013

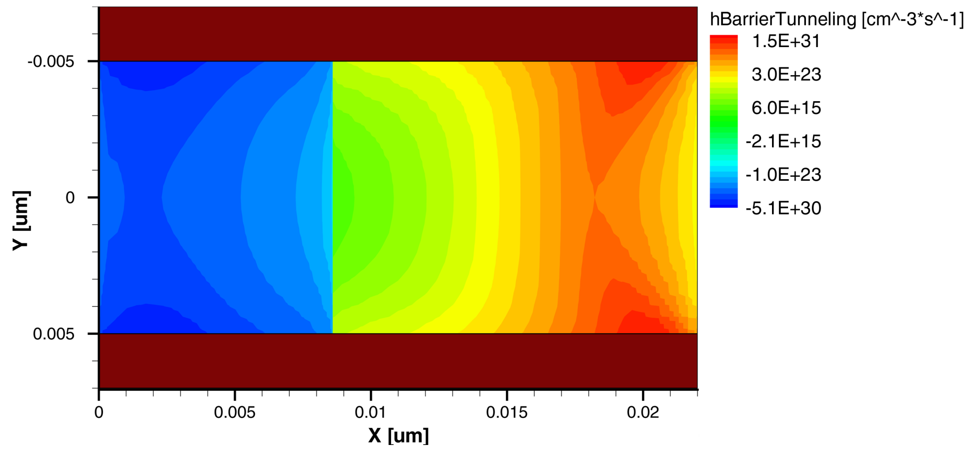

(a)

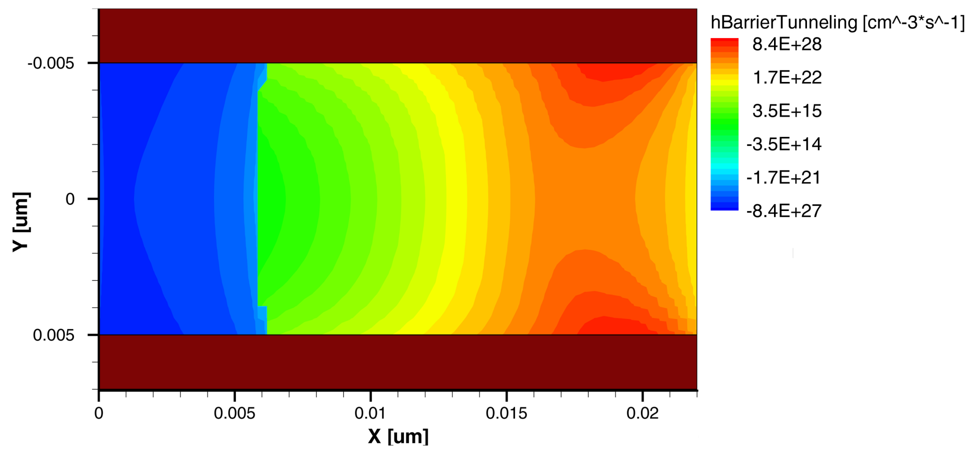

(b)

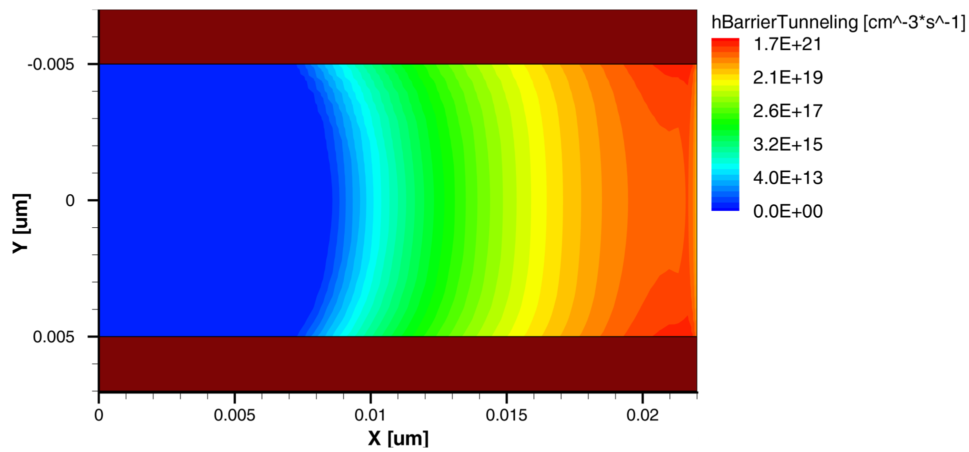

(c)

Figure 7.1.: TCAD Tunneling Generation Rate for ϕ_{Bn}=0.4 eV in (a) for holes at V_g=−0.5 V, (b) for holes at V_g=0 V, (c) for holes at V_g=1 V. Device geometry: l_{ch}=22 nm, t_{ch}=10 nm, t_{ox}=2 nm. Bias conditions: V_{ds}=1 V.

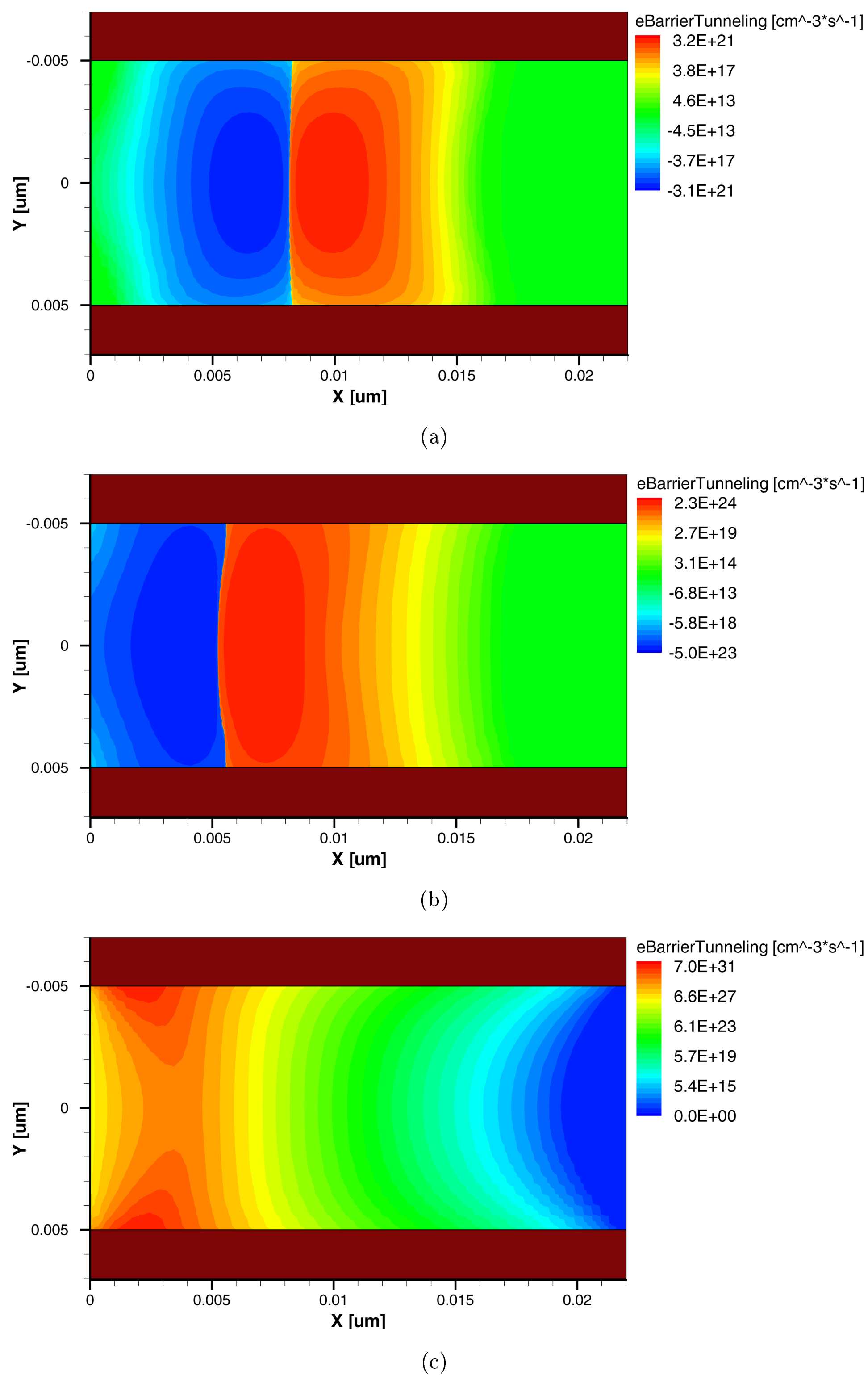

Figure 7.2.: TCAD Tunneling Generation Rate for ϕ_{Bn}=0.4 eV in (a) for electrons at V_g=−0.5 V, (b) for electrons at V_g=0 V, (c) for electrons at V_g=1 V. Device geometry: l_{ch}=22 nm, t_{ch}=10 nm, t_{ox}=2 nm. Bias conditions: V_{ds}=1 V.

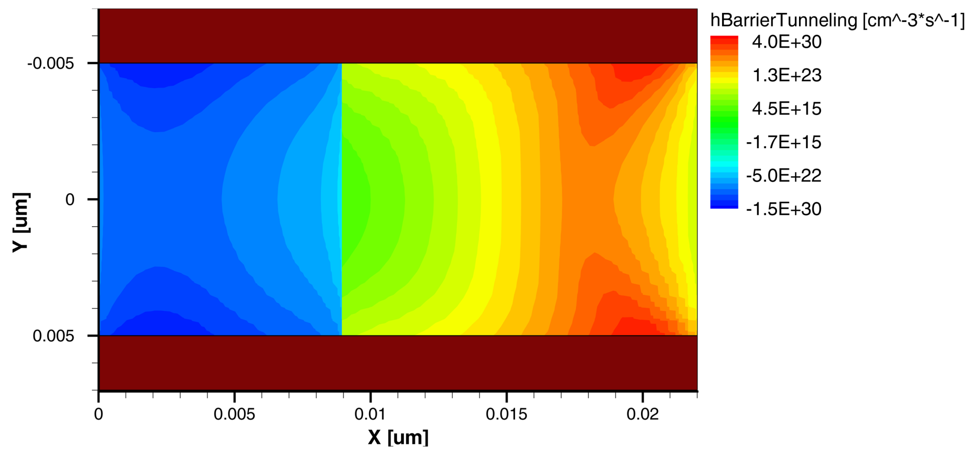

(a)

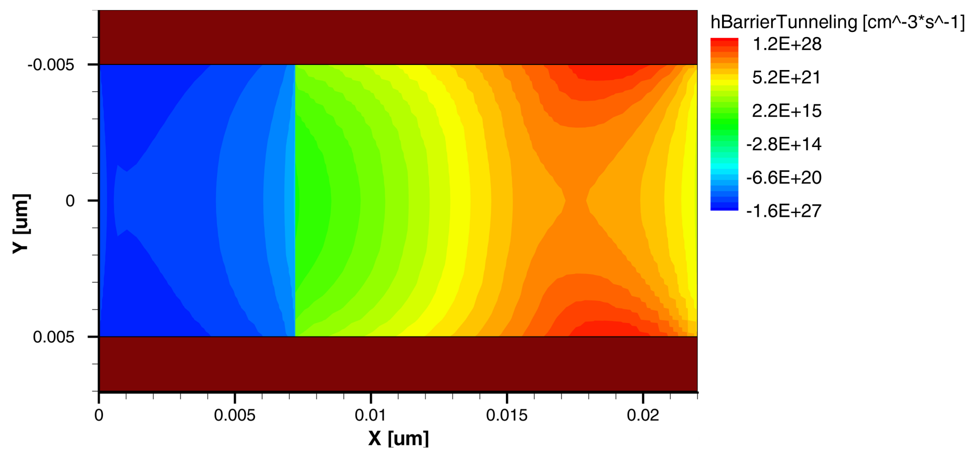

(b)

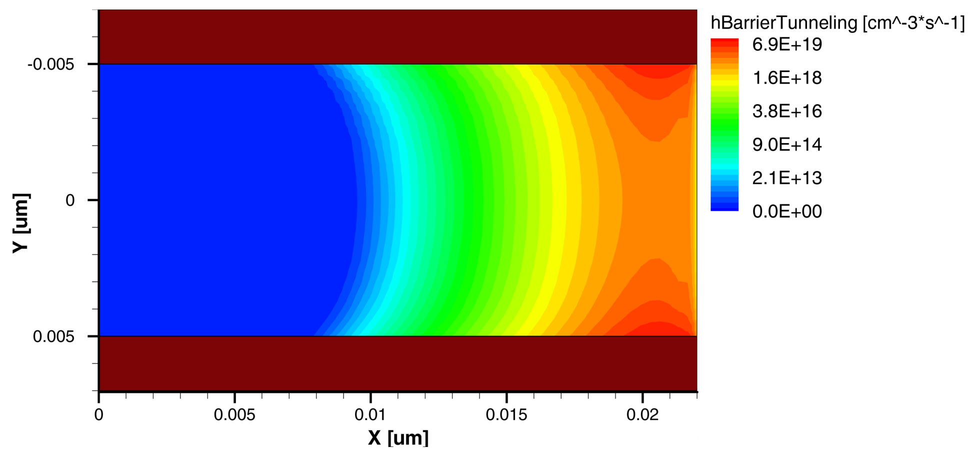

(c)

Figure 7.3.: TCAD Tunneling Generation Rate for ϕ_{Bn}=0.28 eV in (a) for holes at V_g=−0.5 V, (b) for holes at V_g=0 V, (c) for holes at V_g=1 V. Device geometry: l_{ch}=22 nm, t_{ch}=10 nm, t_{ox}=2 nm. Bias conditions: V_{ds}=1 V.

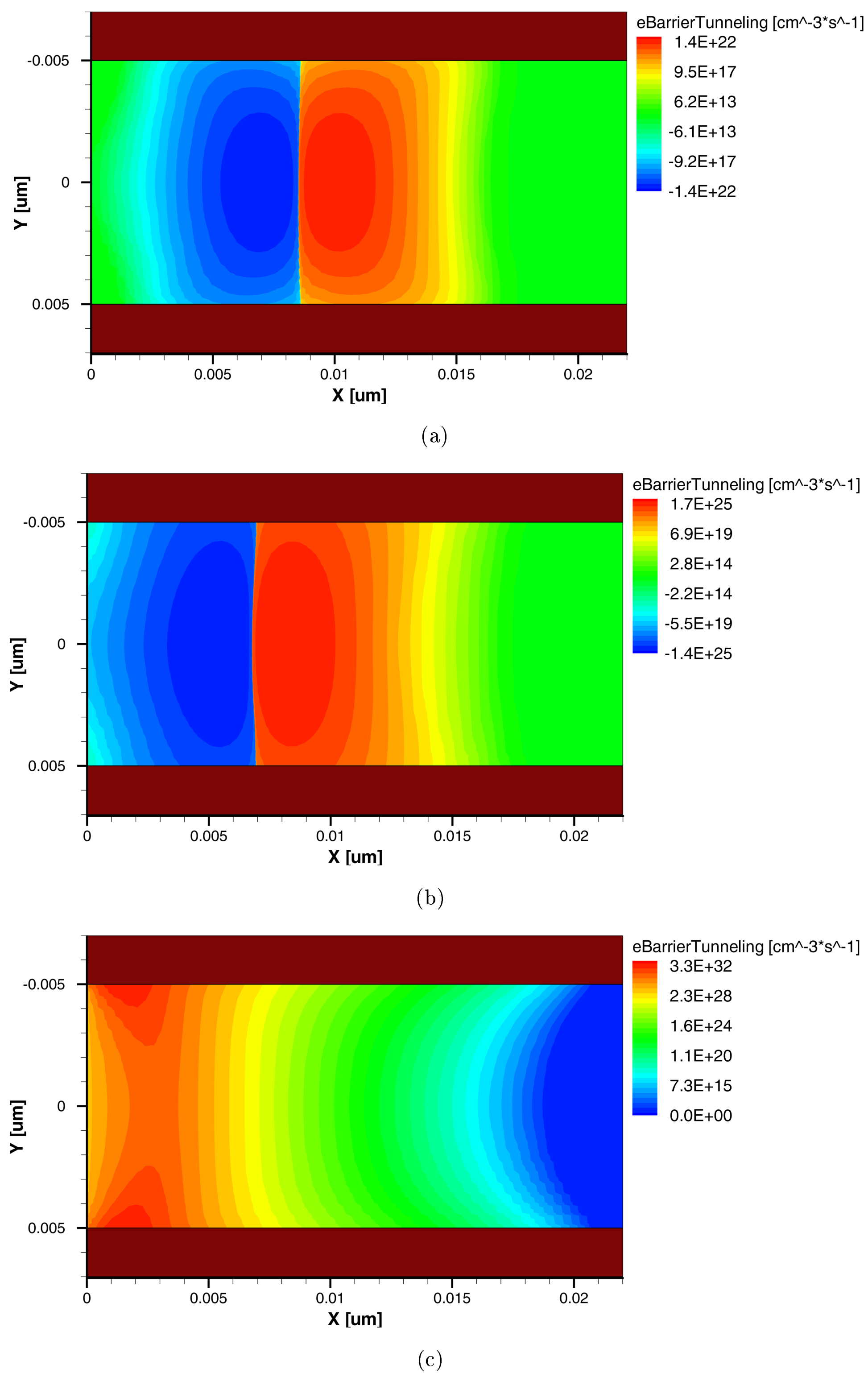

Figure 7.4.: TCAD Tunneling Generation Rate for ϕ_{Bn}=0.28 eV in (a) for electrons at V_g=−0.5 V, (b) for electrons at V_g=0 V, (c) for electrons at V_g=1 V. Device geometry: l_{ch}=22 nm, t_{ch}=10 nm, t_{ox}=2 nm. Bias conditions: V_{ds}=1 V.

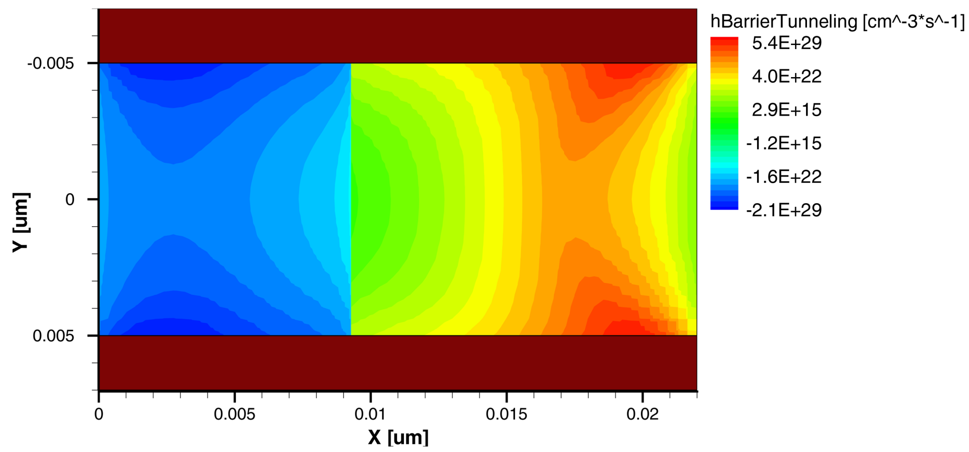

(a)

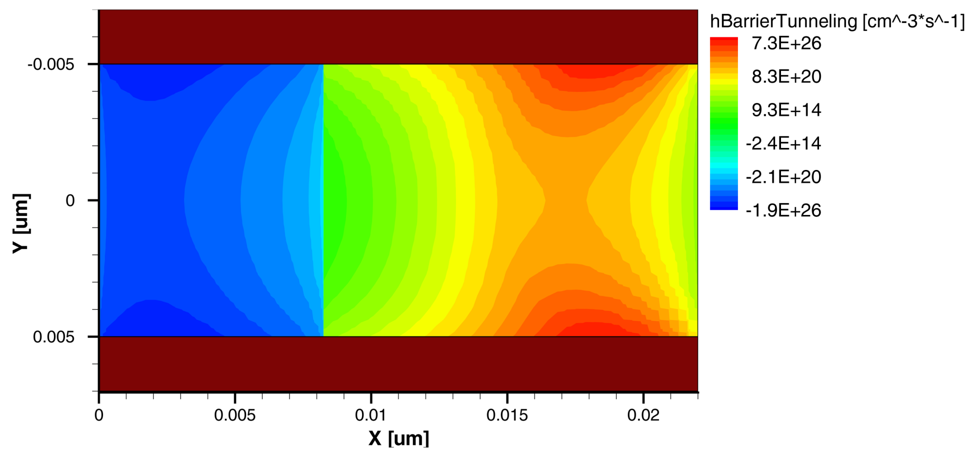

(b)

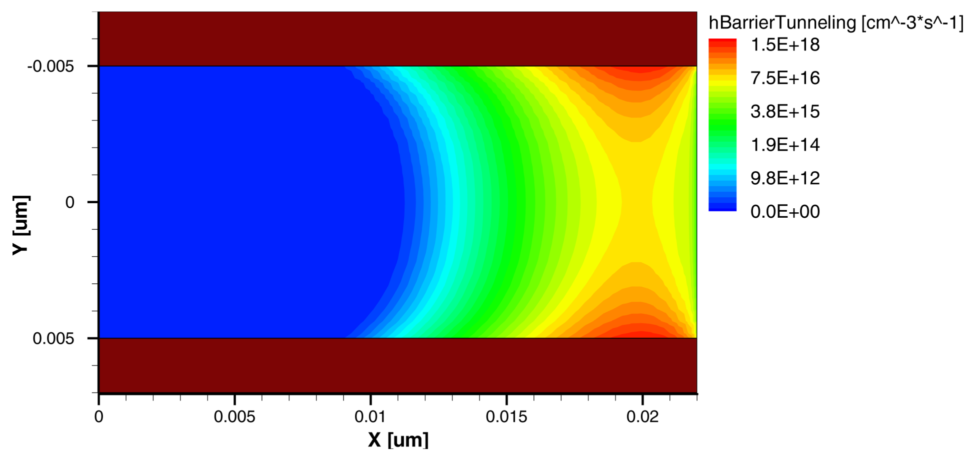

(c)

Figure 7.5.: TCAD Tunneling Generation Rate for ϕ_{Bn}=0.1 eV in (a) for holes at V_g=−0.5 V, (b) for holes at V_g=0 V, (c) for holes at V_g=1 V. Device geometry: l_{ch}=22 nm, t_{ch}=10 nm, t_{ox}=2 nm. Bias conditions: V_{ds}=1 V.

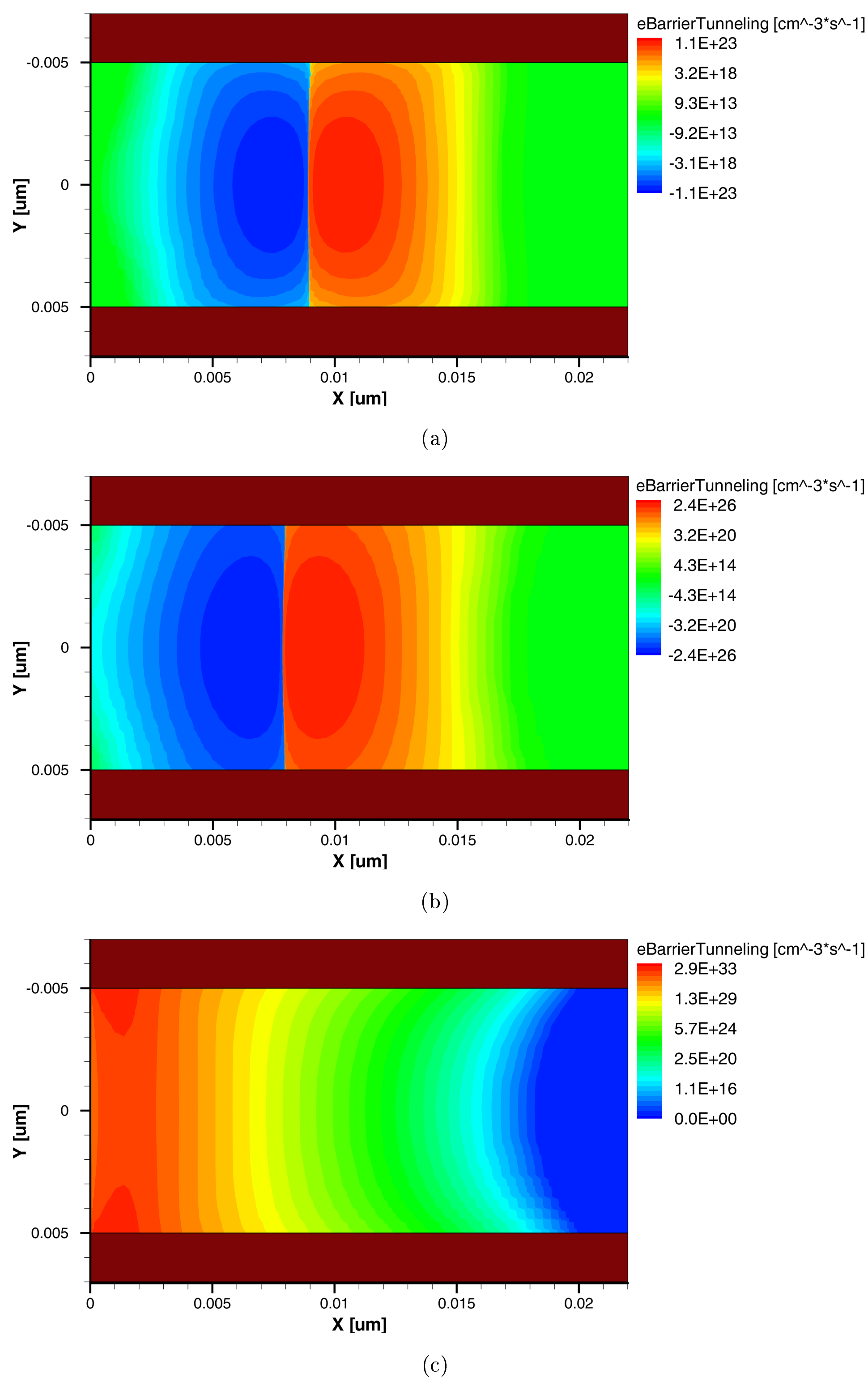

Figure 7.6.: TCAD Tunneling Generation Rate for ϕ_{Bn}=0.1 eV in (a) for electrons at V_g=−0.5 V, (b) for electrons at V_g=0 V, (c) for electrons at V_g=1 V. Device geometry: l_{ch}=22 nm, t_{ch}=10 nm, t_{ox}=2 nm. Bias conditions: V_{ds}=1 V.

UNIVERSITAT ROVIRA I VIRGILI
TWO-DIMENSIONAL ANALYTICAL PREDICTIVE MODELING OF SCHOTTKY BARRIER SOI AND MULTI-GATE MOSFETS
Mike Schwarz
Dipòsit Legal: T.456-2013

The following behavior can be observed for the several gate potentials V_g. If the device is in accumulation region as in Fig. 7.1(a) and 7.2(a) the main contribution results from the holes at the drain while the electron generation is nearly in balance. Furthermore, from Fig. 7.1(a) it can be observed that the concentration of the generated holes tend towards to the silicon-to-oxide interface and the corners of the device.

This behavior continues in Fig. 7.1(b) and 7.2(b) for the hole and electron Tunneling Generation Rate for V_g=0 V where the device operates still in weak accumulation. The distribution of the generated electrons starts slowly to influence the device and begins to move from the center to the source junction and tends towards to the silicon-to-oxide interface. However, their influence is still negligible while the distribution of the generated holes continues to move towards the silicon-to-oxide interface and the drain junction.

The amount of generated electrons for the case of inversion V_g=1 V is no longer negligible as observed in Fig. 7.2(c). Their behavior is similar to that of the generated holes in accumulation. Increasing the gate potential V_g the main concentration can be found at the source junction corners of the device. Also the hole Tunneling Generation Rate behaves as described before. In Fig. 7.1(c) the hole generation is spread along the drain junction. However, in inversion the amount and value of the generated holes are several orders of magnitude below the generated electrons and therefore negligible.

Similar is the behavior for the reduced ϕ_{Bn}=0.28 eV and ϕ_{Bn}=0.1 eV in Fig. 7.3, 7.4 and 7.5, 7.6. Here, the identical bias conditions are shown and the identical reaction as described before can be seen. Of course, the Tunneling Generation Rate of the holes and electrons are different due to the changed Schottky barrier heights, but in principle the same movement of the generated electrons and holes is observed. A concentration underneath the oxide and in the corners depending on the charge carriers results.

All these observations result in the reasonable assumption of section 6.1 that the main contributions of the current in the model result from electrons at the source electrode and holes at the drain electrode depending on the bias condition, as indicated in Fig. 6.1.

7.2. Analyses of the Model Tunneling Generation Rate

In equation (6.9) the Tunneling Generation Rate or in equation (6.11) the enhanced tunneling model consists of several components. In the following, these are analyzed to receive the main contributions and to understand the physical influence of the various equation parts in detail. Therefore, the ANMA is used to predict the components which are the tunneling probability $T(E, x, y)$ and the carrier distributions $f_s(\xi(x))$. The product of the carrier distributions from metal and semiconductor $f_m(\xi(x))\,[1 - f_s(\xi(x))]$

UNIVERSITAT ROVIRA I VIRGILI
TWO-DIMENSIONAL ANALYTICAL PREDICTIVE MODELING OF SCHOTTKY BARRIER SOI AND MULTI-GATE MOSFETS
Mike Schwarz
Dipòsit Legal: T.456-2013

and the product of the tunneling probability and the carrier distributions $\mathrm{T(E,x,y)} \cdot \mathrm{f_m}(\xi(\mathrm{x}))\,[1-\mathrm{f_s}(\xi(\mathrm{x}))]$ are estimated also with the ANMA.

7.2.1. Tunneling Probability

The tunneling probability is estimated with equation (6.6) as already explained. Having a detailed view on the calculated tunneling probability, as in Fig. 7.7(a) and in Fig. 7.7(b) where the tunneling probabilities for electrons at the source and holes at the drain are presented for accumulation mode. Fig. 7.8(a) and 7.8(b) show the tunneling probabilities for electrons at the source and holes at the drain in inversion mode. It is easy to recognize a two-dimensional influence on the tunneling probability from the two gates on top and bottom [188].

This two-dimensional influence results in the following behavior for the electron and hole tunneling. From the ANMA follows that at the source electrode only electrons are able to tunnel and contribute to the current and at the drain electrode only holes can contribute to the tunneling current.

As one can observe for the case of accumulation, a behavior as expected is noticed. The main contribution results from holes as charge carriers as the probability distribution shows, because in accumulation the bands are bent upwards and if the barrier at the drain becomes thin enough, holes are able to tunnel and enter the channel region. Furthermore, for the case of the holes, it can be observed that the tunneling probability for the charge carriers in the middle of the device is increased compared to the silicon-to-oxide interfaces, as one can see in Fig. 7.7(b). This behavior can be easily explained from the circumstance that the influence from the two gate electrodes on the drain electrode in the middle of the device on to the electrostatic potential and electric field is less compared to the silicon-to-oxide interfaces. Therefore, in the middle of the device the gradient of the potential is higher than underneath the oxide and the barrier in the middle is much thinner. This results in an increased tunneling probability for the hole charge carriers [188].

If one now concentrates on the case of inversion, electrons are contributors to the tunneling current as well and a similar behavior as for the holes can be expected. The bands are bent downwards and the Schottky barrier at the source is modulated and thinned by the bias, such that electrons are able to enter the channel region by the effect of quantum mechanical tunneling. Furthermore, the plots show the influence on the tunneling probability due to the two gate electrodes at the top and bottom. As observed in Fig. 7.8(a) and 7.8(b), a similar behavior as in Fig. 7.7(b) for the holes in accumulation is noticed. The influences from the two gate electrodes on the source electrode and the drain electrode are less on to the middle of the device.

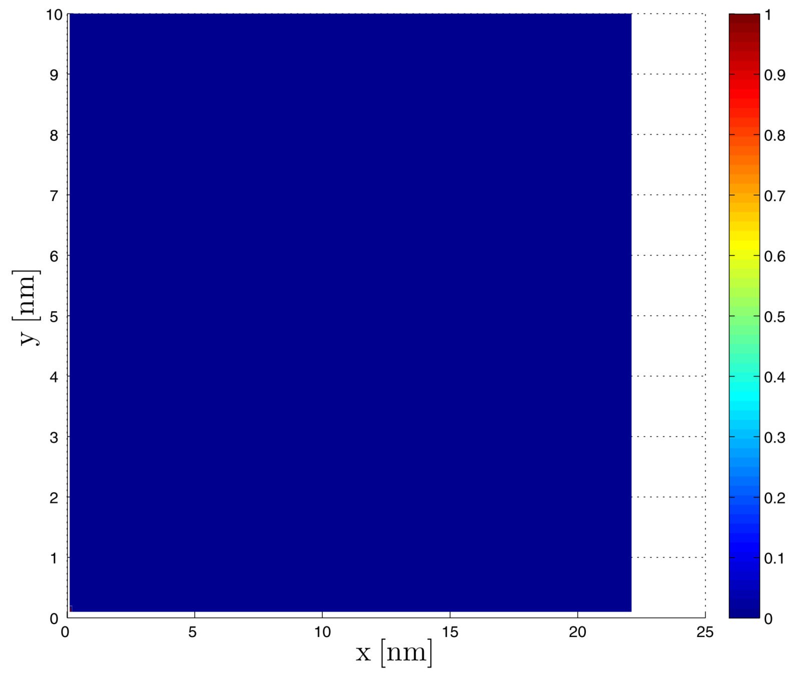

(a)

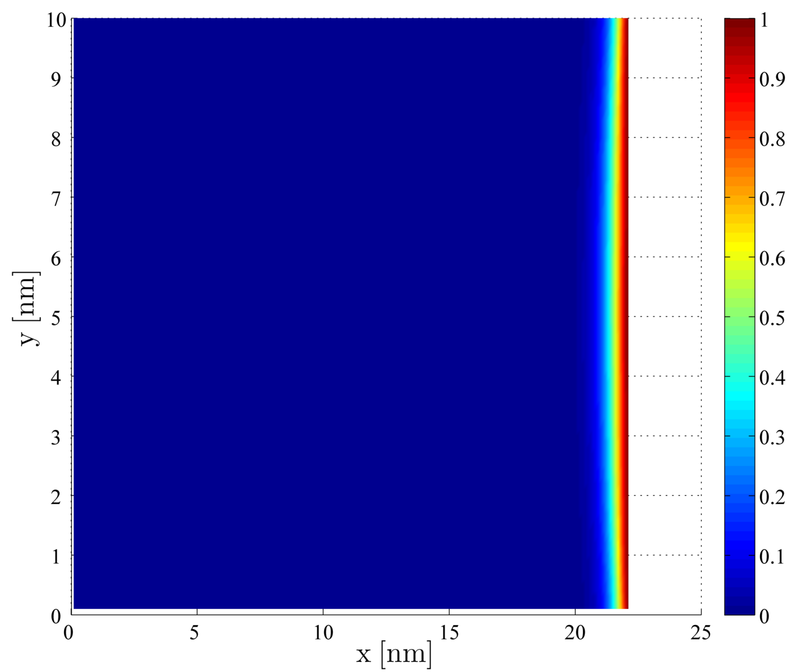

(b)

Figure 7.7.: Model tunneling probability $T(E, x, y)$ in (a) for electrons at the source electrode and in (b) for holes at the drain electrode in accumulation. Results for ϕ_{Bn}=0.1 eV. Device geometry: l_{ch}=22 nm, t_{ch}=10 nm, t_{ox}=2 nm. Bias conditions: V_{ds}=1 V, V_g=−0.5 V.

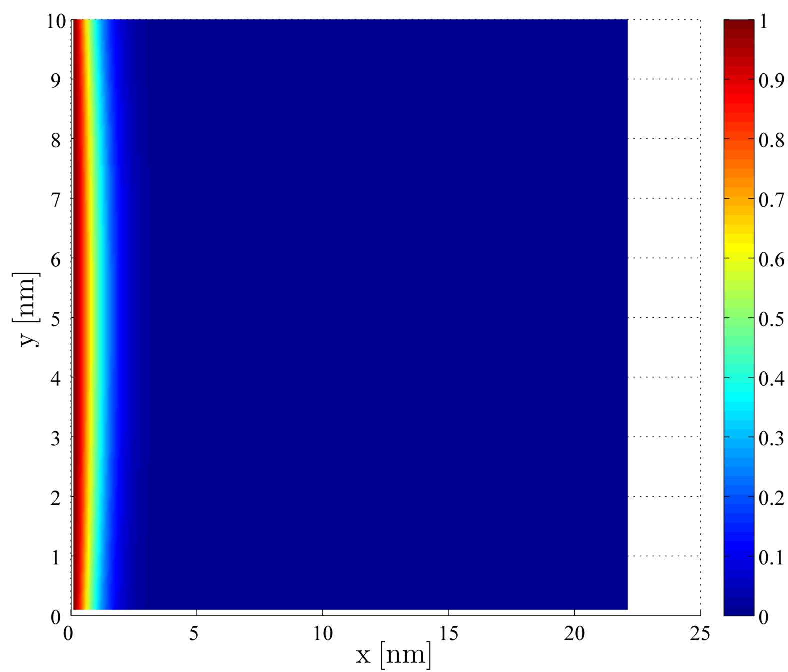

(a)

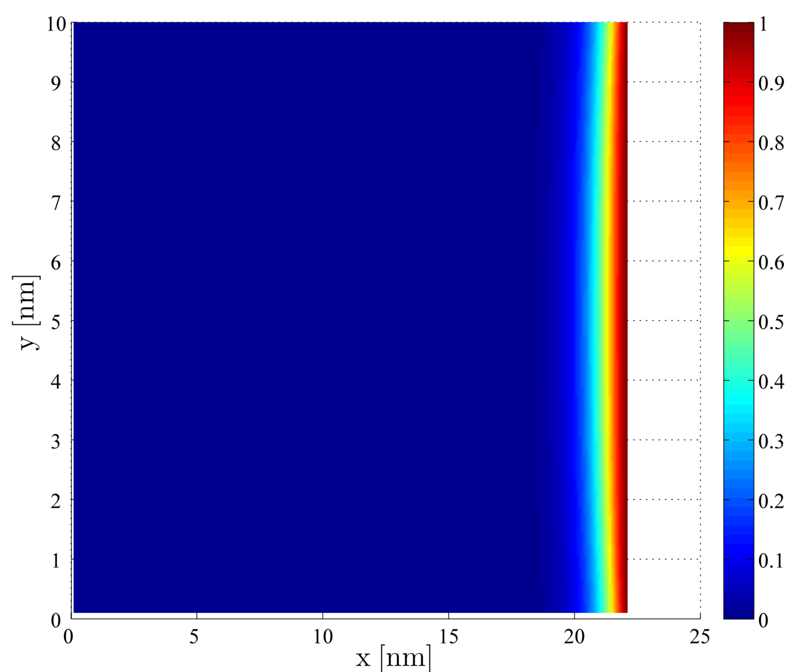

(b)

Figure 7.8.: Model tunneling probability T(E, x, y) in (a) for electrons at the source electrode and in (b) for holes at the drain electrode in accumulation. Results for ϕ_{Bn}=0.1 eV. Device geometry: l_{ch}=22 nm, t_{ch}=10 nm, t_{ox}=2 nm. Bias conditions: V_{ds}=1 V, V_g=1 V.

Due to this the electrostatics are less influenced compared to the electrostatics at the silicon-to-oxide interface. This results in an increased tunneling probability for the electrons at the source junctions and the holes at the drain junction. It is essential to consider this two-dimensional effect [188].

7.2.2. Carrier Distributions

The second important factor is that the carrier distributions and their product from equation (6.9) described in section 6.1 with the simplification from equation (**??**) have a remarkable influence on the results of the tunneling current density or the generation rate itself. In the following the influences of $f_s(\xi(x))$, $[1 - f_s(\xi(x))]$, and $f_m(\xi(x))\,[1 - f_s(\xi(x))]$ are analyzed, what they result in and how they effect the behavior.

In Fig. 7.9(a) and 7.9(b) the carrier distributions $f_s(\xi(x))$ in accumulation at the conduction band and the valence band are shown. The carrier distribution shown in Fig. 7.9(a) represents the value of the Fermi-Dirac distribution at the corresponding energy for electrons at the conduction band in the entire channel region which are the important charges to describe the electron tunneling current from the source while in Fig. 7.9(b) the corresponding available electrons at the valence band are given.

The charges of the valence band for the electrons in accumulation are not considered in the calculation of the electron tunneling due to the circumstance of a large band gap which results in a negligible tunneling probability. Electrons from the valence band are not considered in calculating the tunneling current of the electrons, but they are responsible for the prediction of the hole tunneling current from the drain due to equation (6.11).

From both figures in Fig. 7.9(a) and 7.9(b) one observes a two-dimensional influence on the carrier distributions. The behavior is similar to the one of the tunneling probability explained above. The influences from the two gate electrodes on the junctions are less at the middle of the device. Due to this the electrostatics are less influenced compared to the electrostatics at the silicon-to-oxide interface which is used to estimate the carrier distributions. This results in an increased carrier distribution in the middle of the device.

The Fig. 7.10(a) and 7.10(b) show the corresponding carrier distributions in inversion. Here, again a two-dimensional effect can be observed as expected. Now the shape changed and the highest concentration or probability to find an electron is given in the corner of the device close to the source junction.

The corresponding $[1 - f_s(\xi(x))]$ carrier distributions for the holes at the conduction band and the valence band are presented in Fig. 7.11(a) and 7.11(b) for the case of accumulation while the ones of inversion are given in Fig. 7.12(a) and 7.12(b). They show

UNIVERSITAT ROVIRA I VIRGILI
TWO-DIMENSIONAL ANALYTICAL PREDICTIVE MODELING OF SCHOTTKY BARRIER SOI AND MULTI-GATE MOSFETS
Mike Schwarz
Dipòsit Legal: T.456-2013

the available empty states in the device and behave as expected inversely to the electrons, because the calculation is made with the carrier distributions from the electrons.

Investigating the product of both probabilities $f_m(\xi(x))\,[1 - f_s(\xi(x))]$ in accumulation and inversion mode the following behavior for the carrier distributions at the conduction and valence band can be observed.

From Fig. 7.13(a) and 7.13(b) for the accumulation mode one is able to observe the highest probability to find a charge carrier close to the drain electrode. Furthermore, the possibility to find those carriers at the drain junction is higher underneath the oxide than in the middle of the device. This is an important result for the generation rate itself, as one can see in the following section.

However, the behavior for the inversion mode is similar. In Fig. 7.14(a) and 7.14(b) the available charges are illustrated and it can be seen that the highest probability is close to the source electrode. Also underneath the oxide the highest possibility to find carriers occurs, compared to the middle of the device. This behavior combined with the one of the corresponding tunneling probability results in the generation rate as already explained and has a significant influence on the device behavior.

7.2.3. Tunneling Generation Rate

In the model the generation rate results from the product of $T(E, x, y)$ and $f_m(\xi(x)) \cdot [1 - f_s(\xi(x))]$ given in equation (6.9) or equation (6.11). In equation (6.11) the enhanced tunneling current density with the additional electric field $|E(x, y)|$ is given. In the following discussion the factor $|E(x, y)|$ is not considered which of course will influence the result. However, this has only a minor influence and will not change the following interpretation.

Fig. 7.15(a) and 7.15(b) show the Tunneling Generation Rate, as predicted by the ANMA in chapter 6, for the case of accumulation for the electrons and holes, respectively. The generation rate for the electrons in accumulation is zero, see Fig. 7.15(a) due to the fact that no charges are able to tunnel because the energy bands are bent upwards, and hence $T(E, x, y) = 0$. For the holes exists a tunneling probability and therefore a generation rate can be observed. Fig. 7.15(b) illustrates the charge generation which is mainly concentrated in the corners of the device. Due to this circumstance the biggest tunneling probability is concentrated close to the drain. Further, the carrier distribution is concentrated close to the drain junction, but with a different shape. The combination of both, tunneling probability and carrier distribution, results in a concentration underneath the oxide near the drain junction. This is clear, because the carrier distributions underneath the oxide are closer to the junction than in the middle of the device where the tunneling probability is less [189].

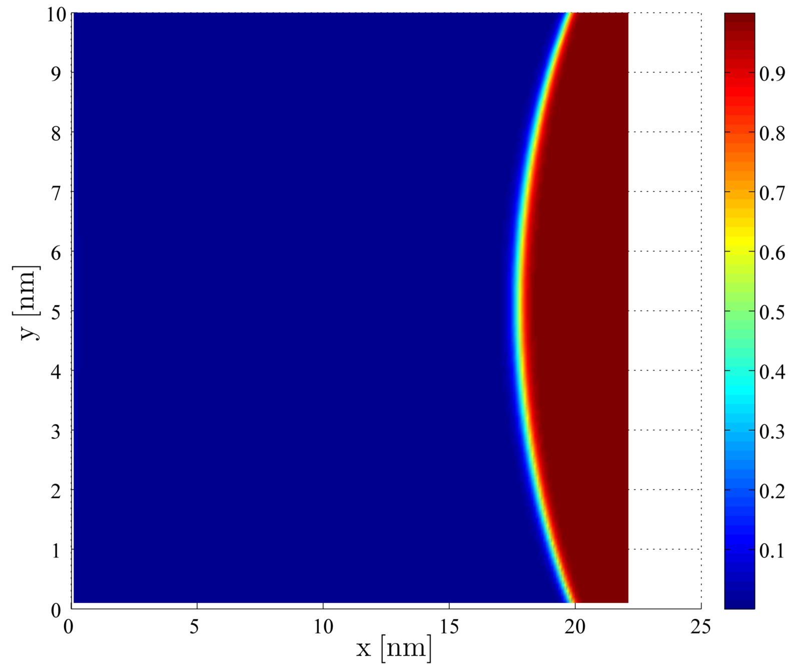

(a)

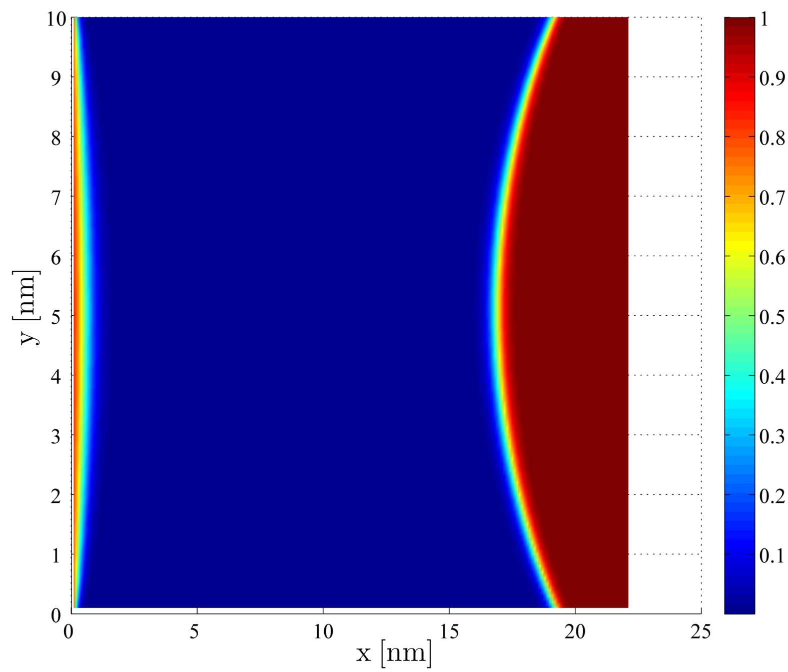

(b)

Figure 7.9.: Model carrier distribution $f_s(\xi(x))$ in (a) for electrons at the conduction band and in (b) for electrons at the valence band in accumulation. Results for ϕ_{Bn}=0.1 eV. Device geometry: l_{ch}=22 nm, t_{ch}=10 nm, t_{ox}=2 nm. Bias conditions: V_{ds}=1 V, V_g=−0.5 V.

UNIVERSITAT ROVIRA I VIRGILI
TWO-DIMENSIONAL ANALYTICAL PREDICTIVE MODELING OF SCHOTTKY BARRIER SOI AND MULTI-GATE MOSFETS
Mike Schwarz
Dipòsit Legal: T.456-2013

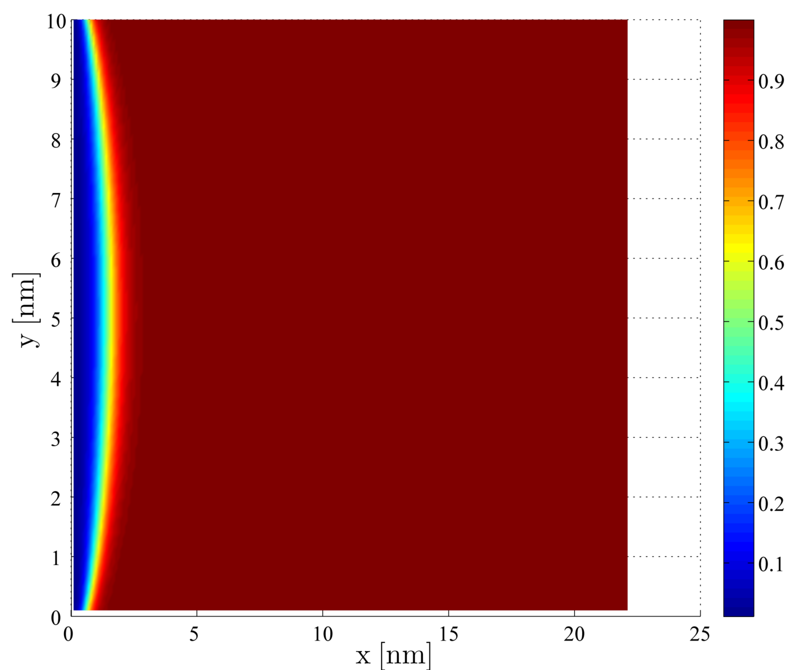

(a)

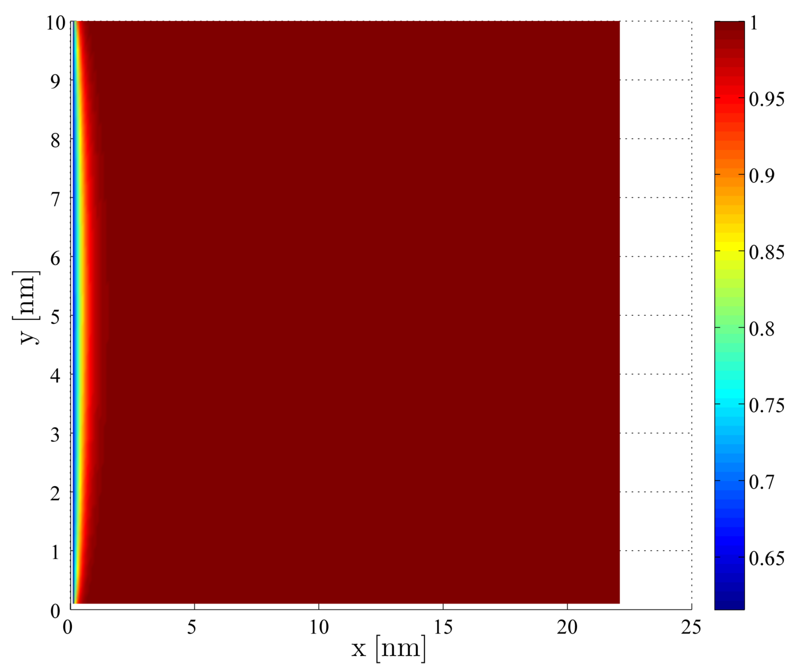

(b)

Figure 7.10.: Model carrier distribution $f_s(\xi(x))$ in (a) for electrons at the conduction band and in (b) for electrons at the valence band in inversion. Results for ϕ_{Bn}=0.1 eV. Device geometry: l_{ch}=22 nm, t_{ch}=10 nm, t_{ox}=2 nm. Bias conditions: V_{ds}=1 V, V_g=1 V.

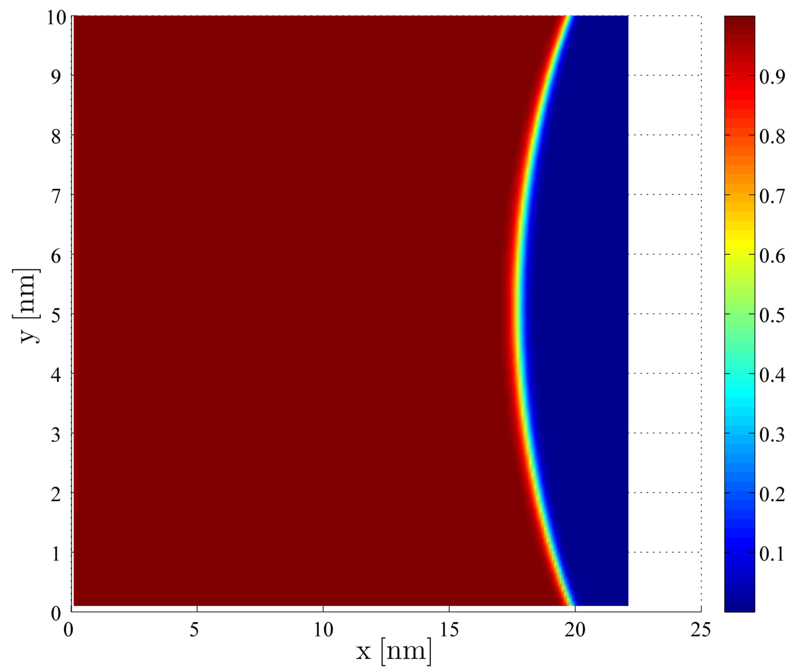

(a)

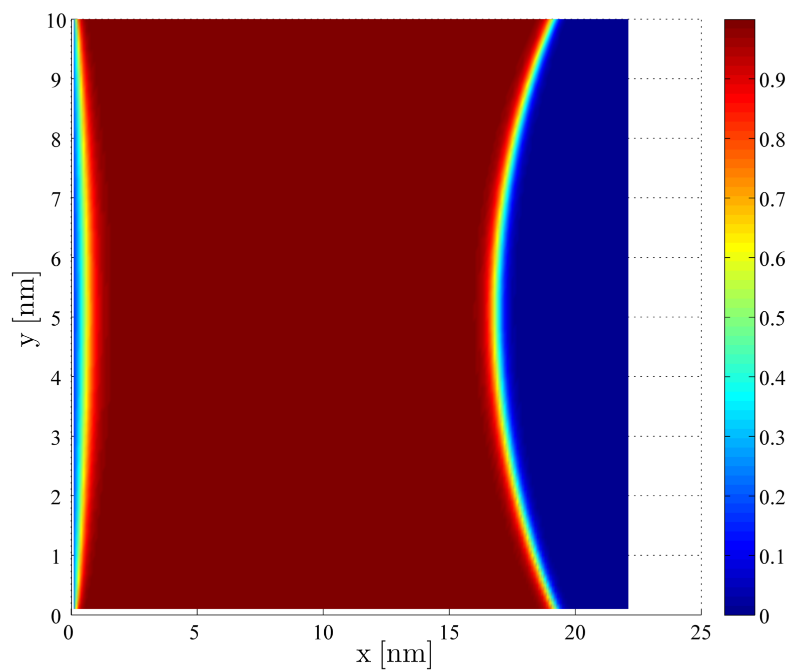

(b)

Figure 7.11.: Model carrier distribution $[1 - f_s(\xi(x))]$ in (a) for holes at the conduction band and in (b) for holes at the valence band in accumulation. Results for ϕ_{Bn}=0.1 eV. Device geometry: l_{ch}=22 nm, t_{ch}=10 nm, t_{ox}=2 nm. Bias conditions: V_{ds}=1 V, V_g=−0.5 V.

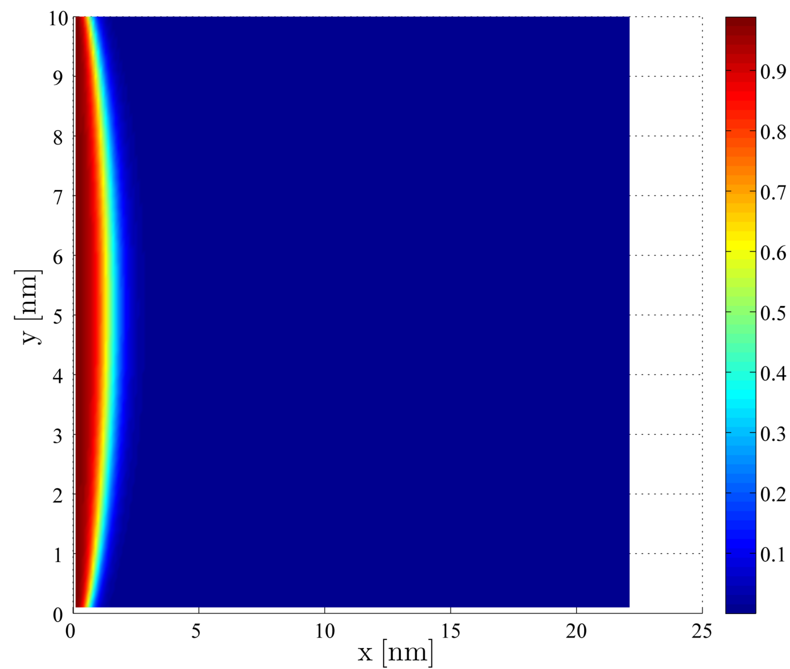

(a)

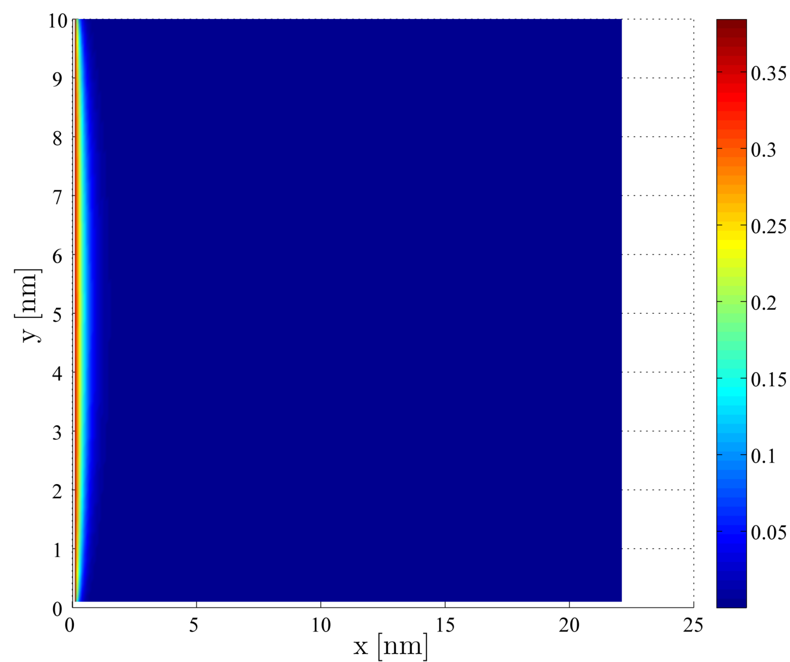

(b)

Figure 7.12.: Model carrier distribution $[1 - f_s(\xi(x))]$ in (a) for holes at the conduction band and in (b) for holes at the valence band in inversion. Results for ϕ_{Bn}=0.1 eV. Device geometry: l_{ch}=22 nm, t_{ch}=10 nm, t_{ox}=2 nm. Bias conditions: V_{ds}=1 V, V_g=1 V.

UNIVERSITAT ROVIRA I VIRGILI
TWO-DIMENSIONAL ANALYTICAL PREDICTIVE MODELING OF SCHOTTKY BARRIER SOI AND MULTI-GATE MOSFETS
Mike Schwarz
Dipòsit Legal: T.456-2013

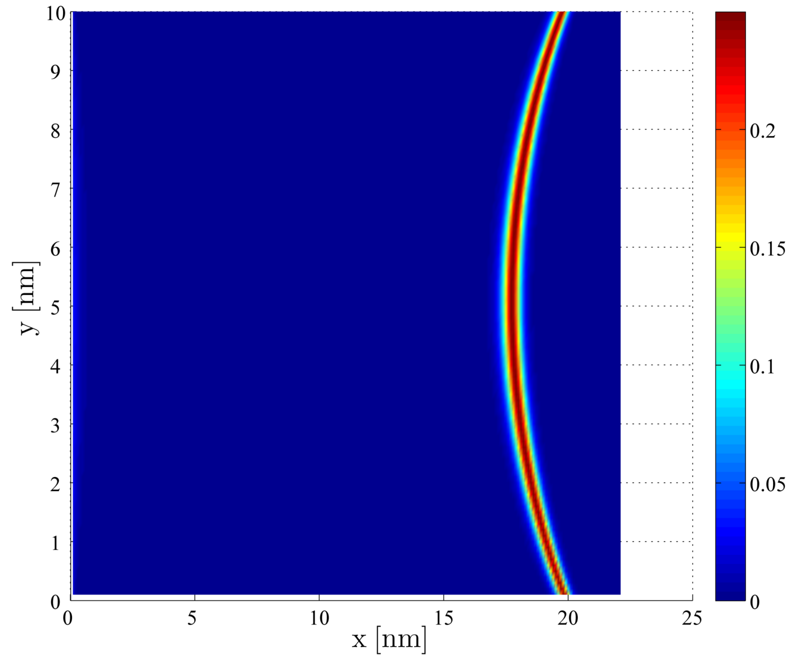

(a)

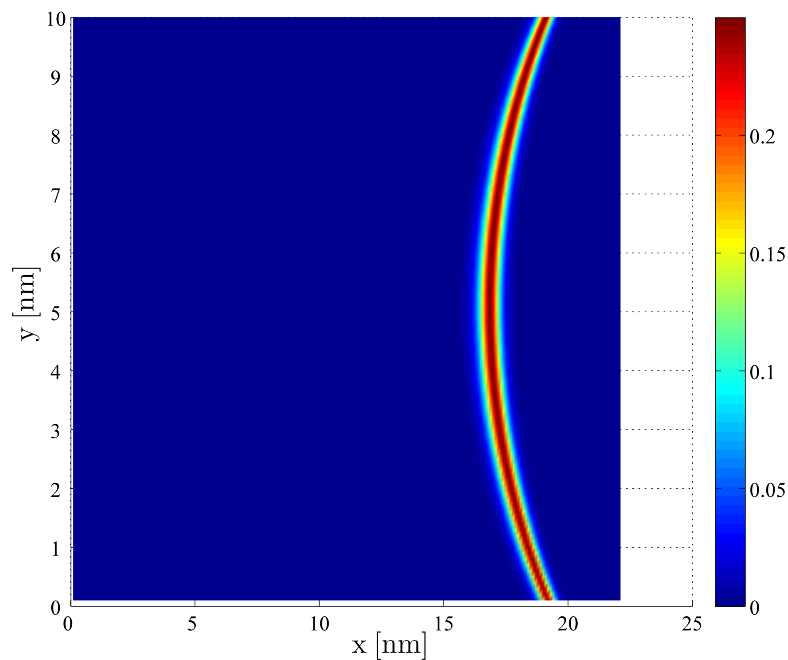

(b)

Figure 7.13.: Model carrier distribution product $f_m(\xi(x))\,[1 - f_s(\xi(x))]$ in (a) at the conduction band and in (b) at the valence band in accumulation. Results for ϕ_{Bn}=0.1 eV. Device geometry: l_{ch}=22 nm, t_{ch}=10 nm, t_{ox}=2 nm. Bias conditions: V_{ds}=1 V, V_g=−0.5 V.

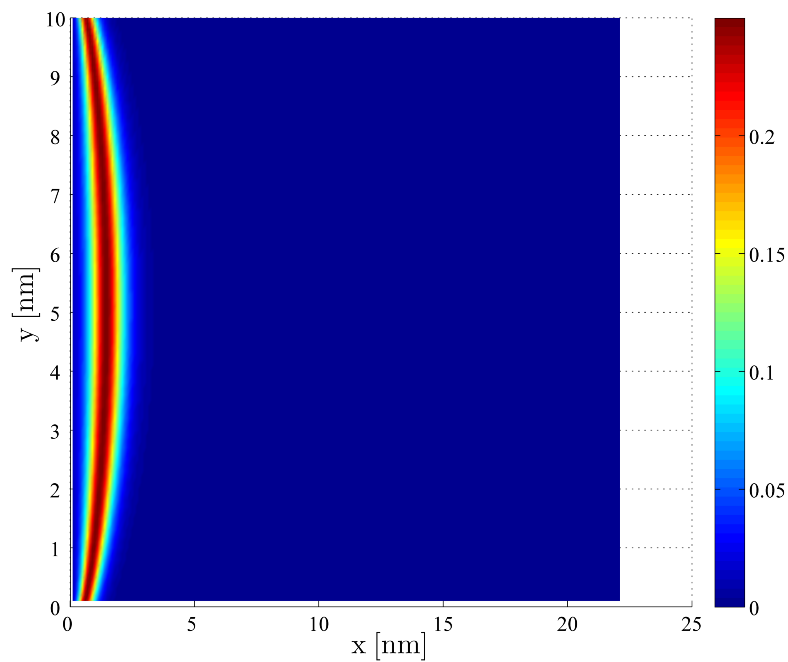

(a)

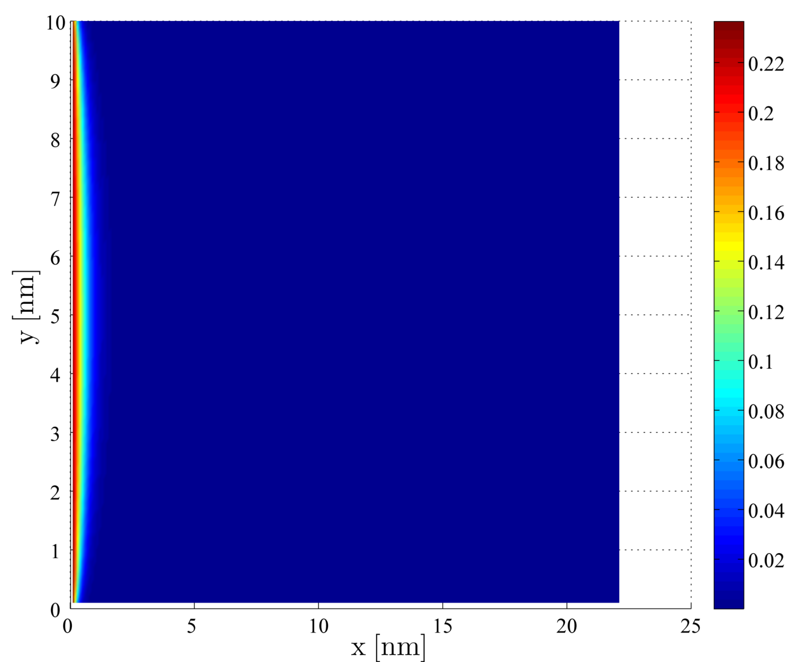

(b)

Figure 7.14.: Model carrier distribution product $\mathrm{f_m}(\xi(\mathrm{x}))\,[1-\mathrm{f_s}(\xi(\mathrm{x}))]$ in (a) at the conduction band and in (b) at the valence band in inversion. Results for ϕ_{Bn}=0.1 eV. Device geometry: $\mathrm{l_{ch}}$=22 nm, $\mathrm{t_{ch}}$=10 nm, $\mathrm{t_{ox}}$=2 nm. Bias conditions: $\mathrm{V_{ds}}$=1 V, $\mathrm{V_g}$=1 V.

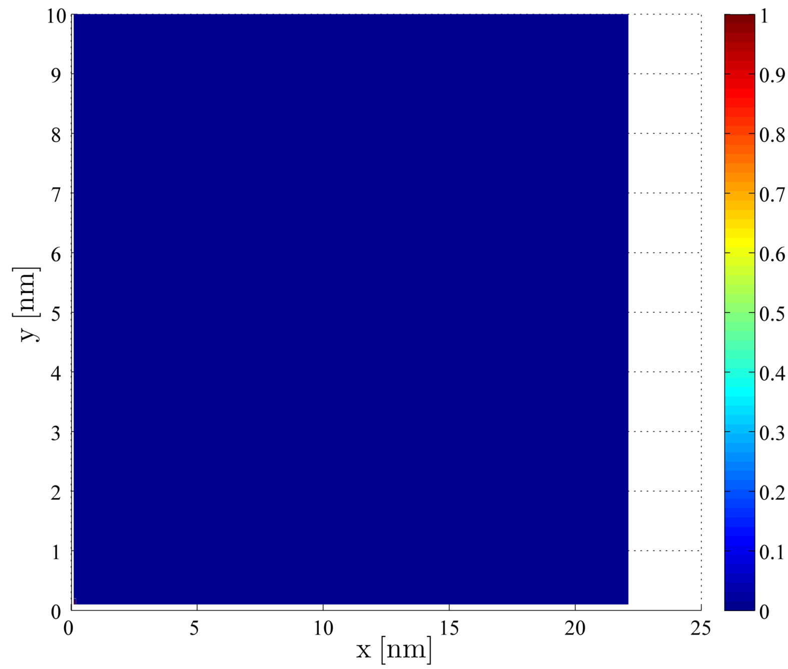

(a)

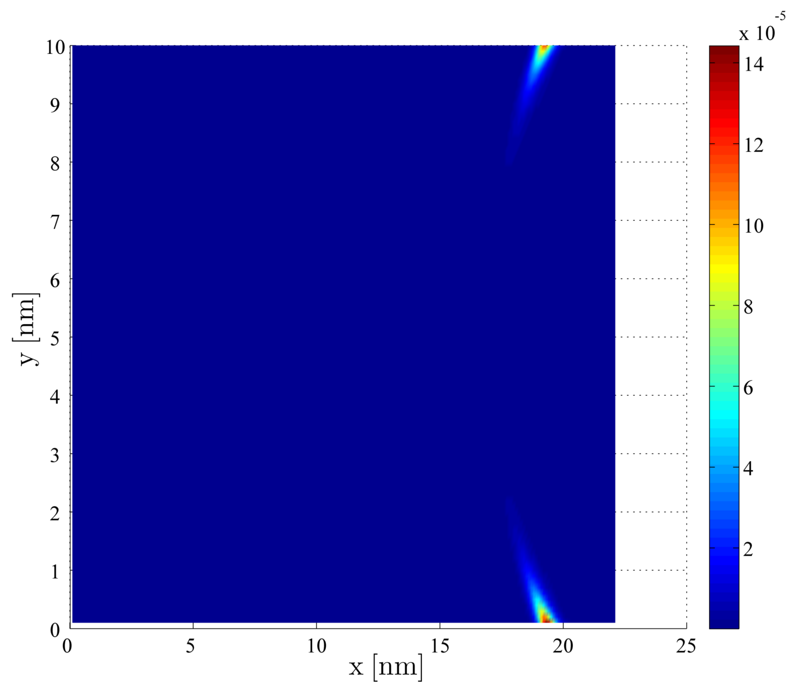

(b)

Figure 7.15.: Model Tunneling Generation Rate $\mathrm{T(E,x,y)} \cdot \mathrm{f_m}(\xi(\mathrm{x}))\,[1 - \mathrm{f_s}(\xi(\mathrm{x}))]$ in (a) at the conduction band and in (b) at the valence band in accumulation. Results for ϕ_{Bn}=0.1 eV. Device geometry: $\mathrm{l_{ch}}$=22 nm, $\mathrm{t_{ch}}$=10 nm, $\mathrm{t_{ox}}$=2 nm. Bias conditions: $\mathrm{V_{ds}}$=1 V, $\mathrm{V_g}$=−0.5 V.

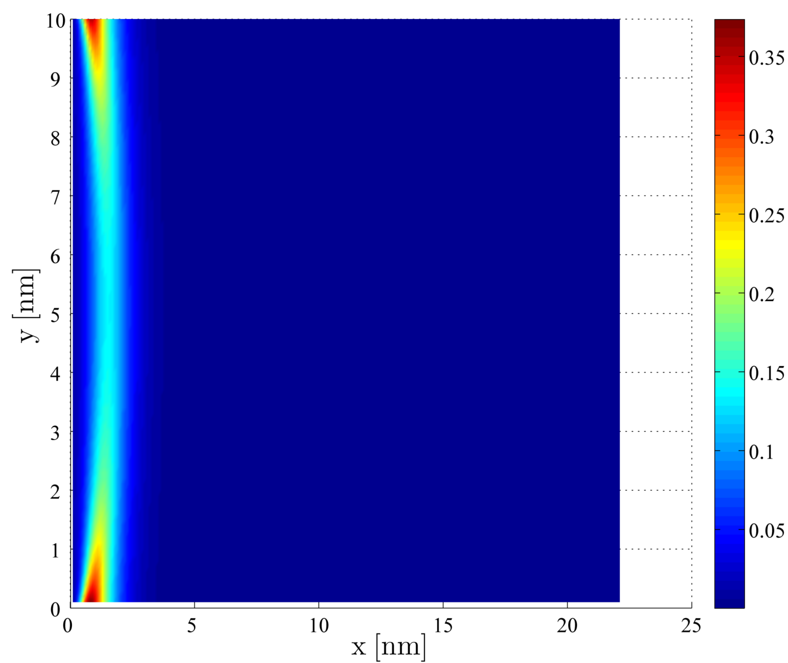

(a)

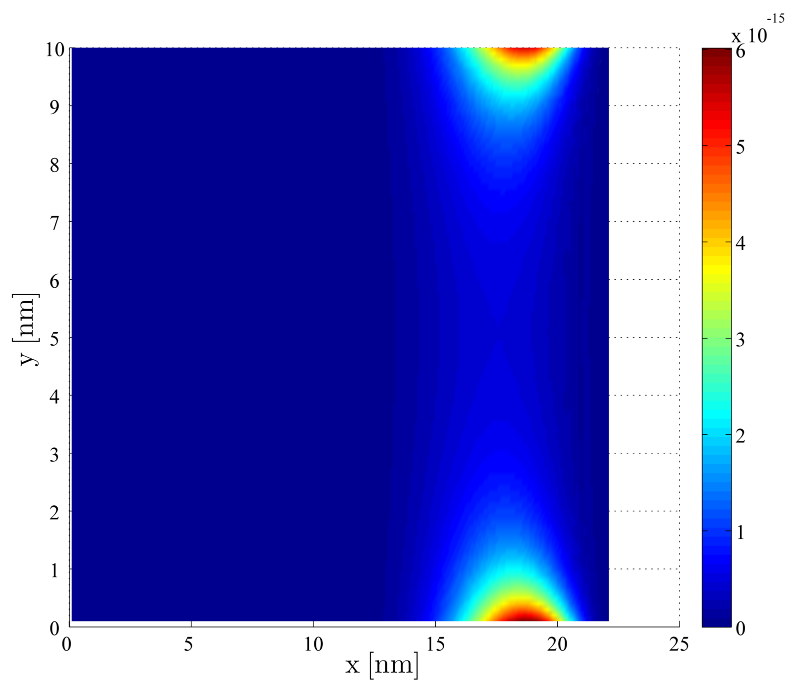

(b)

Figure 7.16.: Model Tunneling Generation Rate $\mathrm{T(E,x,y)} \cdot \mathrm{f_m}(\xi(\mathrm{x}))\,[1 - \mathrm{f_s}(\xi(\mathrm{x}))]$ in (a) at the conduction band and in (b) at the valence band in inversion. Results for ϕ_{Bn}=0.1 eV. Device geometry: $\mathrm{l_{ch}}$=22 nm, $\mathrm{t_{ch}}$=10 nm, $\mathrm{t_{ox}}$=2 nm. Bias conditions: $\mathrm{V_{ds}}$=1 V, $\mathrm{V_g}$=1 V.

UNIVERSITAT ROVIRA I VIRGILI
TWO-DIMENSIONAL ANALYTICAL PREDICTIVE MODELING OF SCHOTTKY BARRIER SOI AND MULTI-GATE MOSFETS
Mike Schwarz
Dipòsit Legal: T.456-2013

Similar is the behavior for the inversion mode. As can be seen in Fig. 7.16(a) and 7.16(b) the main generation results in the corners of the device for the electrons and holes. In Fig. 7.16(a) the distribution of the generated electrons is given. The main concentration is close to the source junction which is caused from the fact that here the tunneling probability for the electrons is biggest and the carrier distributions concentrate close underneath the oxide. At the drain junction the behavior for Fig. 7.16(b) can be described as follows. The tunneling probability is biggest at the drain electrode which was to be expected while the carrier distribution is concentrated at the source electrode. The main influence results also at the drain electrode due to the fact that the tunneling probability at the source is almost zero and the influence is minor. It can be observed that the amount of the holes is low compared to the one of the electrons [189].

If one now compares the behavior described above with the one from the TCAD Tunneling Generation Rate in section 7.1 a similar description of the physics and mechanisms is to be observed. This was to be expected for the ANMA, because the results already presented for device current are in very good agreement with the TCAD Sentaurus simulation data.

7.3. Analyses of the Model Current Densities

The tunneling current densities and thermionic current densities are predicted with equation (6.11) and equation (6.13), respectively. If the numerical integration from gate to gate takes place, as in the Fig. 7.17 and 7.18, it is obvious to observe a two-dimensional influence onto both estimated current densities [188].

This behavior was to be expected, if one analyses the Fig. 7.15(a) to 7.16(b) for the tunneling generation rate where the highest probability results underneath the oxides due to the two-dimensional influence of the electrostatics which are used to estimate the contributions [188].

From the plots in Fig. 7.17 and 7.18 it is clear that two-dimensional effects have to be considered for the calculation of Schottky barrier devices. Furthermore, if one analyzes the behavior two different two-dimensional influences can be observed [188].

The first is the result of the concentrated contribution from the corners as discussed before for the tunneling current density. Furthermore, if the tunneling current density is analyzed on the log-scale a parabolic shape from gate to gate at the boundary can be observed. This might be an important fact for the following simplification to a closed-form description of the tunneling current density [188].

The second behavior which is to be observed, is the one of the thermionic emission current density. If one has a detailed view onto the illustration in Fig. 7.17(a), one observes a higher concentration of the thermionic emission in the center of the device

UNIVERSITAT ROVIRA I VIRGILI
TWO-DIMENSIONAL ANALYTICAL PREDICTIVE MODELING OF SCHOTTKY BARRIER SOI AND MULTI-GATE MOSFETS
Mike Schwarz
Dipòsit Legal: T.456-2013

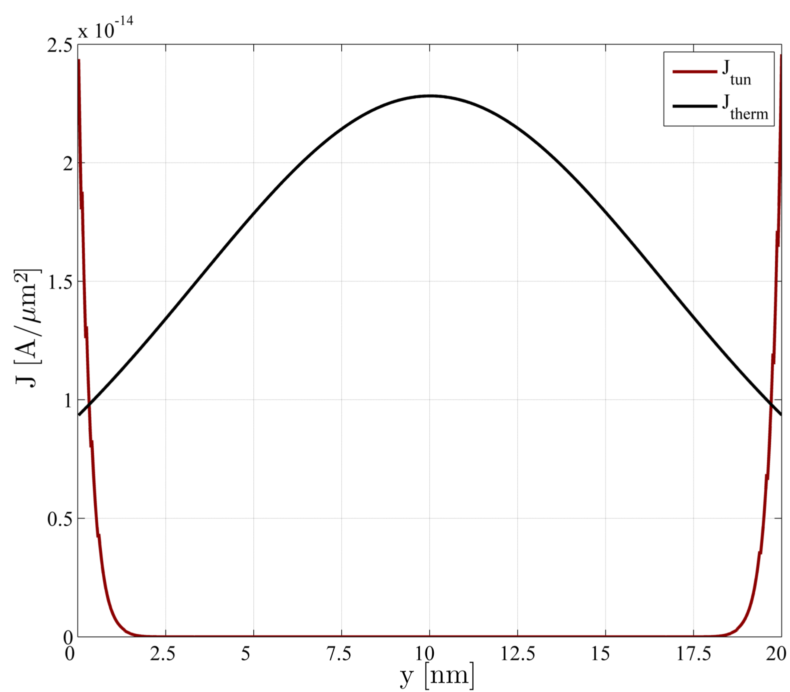

(a)

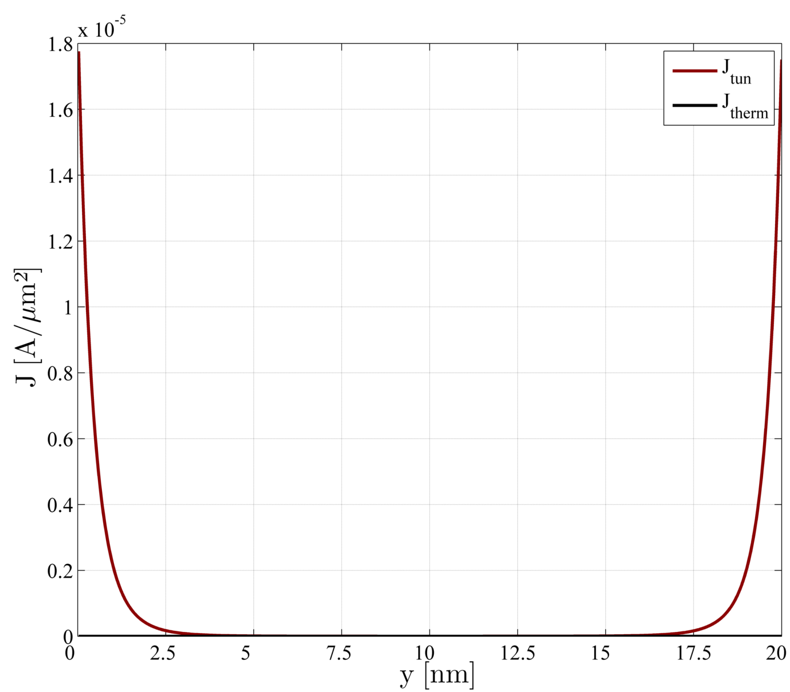

(b)

Figure 7.17.: Model current densities J_{tun} and J_{therm} in (a) along source electrode and in (b) along drain electrode in accumulation. Results for ϕ_{Bn}=0.4 eV. Device geometry: l_{ch}=65 nm, t_{ch}=20 nm, t_{ox}=2 nm. Bias conditions: V_{ds}=1 V, V_g=−0.2 V.

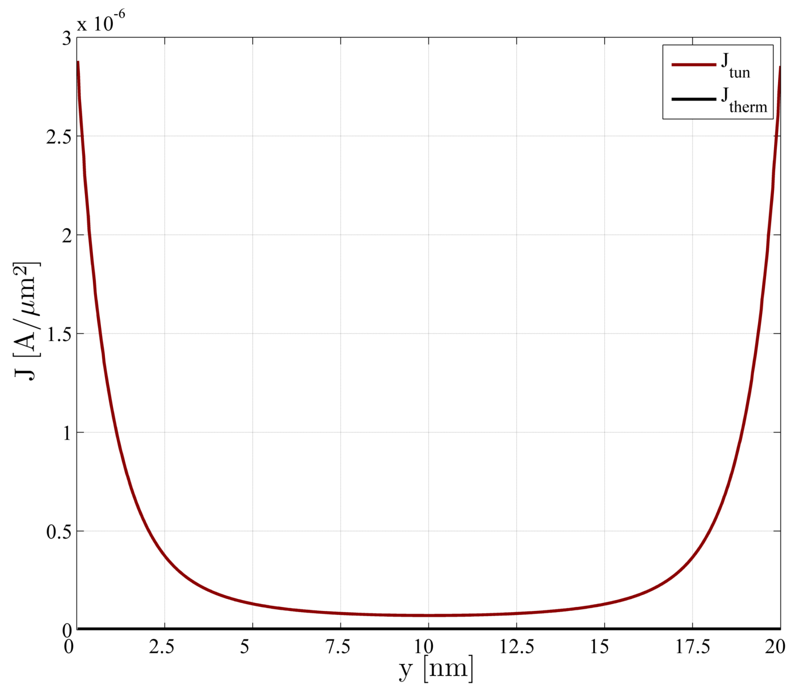

(a)

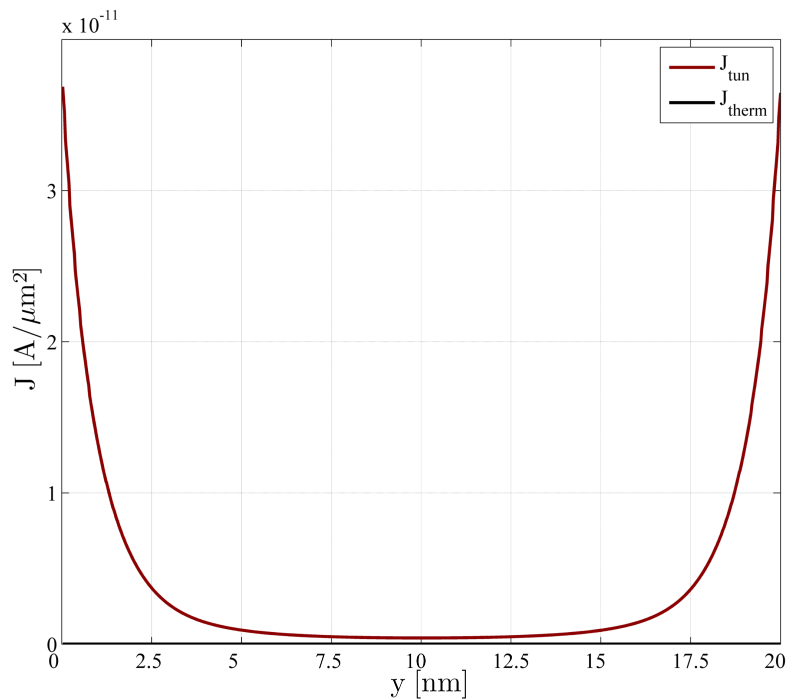

(b)

Figure 7.18.: Model current densities J_{tun} and J_{therm} in (a) along source electrode and in (b) along drain electrode in inversion. Results for ϕ_{Bn}=0.4 eV. Device geometry: l_{ch}=65 nm, t_{ch}=20 nm, t_{ox}=2 nm. Bias conditions: V_{ds}=1 V, V_g=0.6 V.

UNIVERSITAT ROVIRA I VIRGILI
TWO-DIMENSIONAL ANALYTICAL PREDICTIVE MODELING OF SCHOTTKY BARRIER SOI AND MULTI-GATE MOSFETS
Mike Schwarz
Dipòsit Legal: T.456-2013

for a slice from gate to gate. This effect results from the dependency of the barrier, the charge carrier has to surmount. As explained earlier, only charges with enough kinetic energy are allowed to contribute to the current. Then the charges which overcome the barrier are contributors due to the thermionic emission mechanism. Therefore, the barrier at the junction and the potential barrier within the device are the limiting factors [188].

In accumulation the potential barrier limits the current while the barrier itself is influenced not only from the source to drain voltage. Furthermore, the two gates influence the potential barrier and therefore a two-dimensional effect takes place. In the middle, if the device is in accumulation, the potential barrier is less, because of less influence from the gate. This results of course in an increased contribution for the slice at the middle of the device. In Fig. 7.17(a) the two-dimensional influence on thermionic emission can be observed due to the varying maximum barrier $\phi_{\mathrm{B}}(\mathrm{y})$ for the electrons in accumulation [188].

In inversion the behavior is similar to the one in accumulation, except the barrier for the charges. This one is now described by the Schottky barrier itself. If the Schottky barrier lowering effect is neglected, the barrier $\phi_{\mathrm{B}}(\mathrm{y})$ is described by the boundary condition which is assumed to be constant. Therefore, the thermionic emission is similar for each slice and no two-dimensional effect takes influence in inversion mode [188].

Besides the two-dimensional effects also the main contributions in accumulation and inversion are analyzed due to the already explained simplifications in section 6.1. In accumulation the hole tunneling current density dominates, compare Fig. 7.17(a) with 7.17(b) while in inversion the electron current density does, see Fig. 7.18(a) and 7.18(b). In inversion, see Fig. 7.18(a), a negligible constant emission current density for the electrons can be noticed. In Fig. 7.17(b) and 7.18(b) the thermionic emission current density for holes is presented. From both plots also a negligible constant emission current density can be observed [188].

7.4. Conclusion: Where are we? Where should we go?

The accurate results from section 6.5 and the 2D analyses of the TCAD Tunneling Generation Rate, the model Tunneling Generation Rate, and its several contributions as well as the analyzation of the model current densities have given an idea of the physical behavior and how to describe the primary contributions in a closed-form model. Furthermore, it has been shown that the description of the charge generation between TCAD and the model is in a good agreement which explains the accurate estimation of the results in section 6.5.

UNIVERSITAT ROVIRA I VIRGILI
TWO-DIMENSIONAL ANALYTICAL PREDICTIVE MODELING OF SCHOTTKY BARRIER SOI AND MULTI-GATE MOSFETS
Mike Schwarz
Dipòsit Legal: T.456-2013

Summarizing all this gained knowledge, the aim in the following should be to describe the model by analytical closed-form equations with the approximations made here.

It follows for the tunneling current a Gaussian-like shaped Tunneling Generation Rate a concentration in the device corners and a parabolic shape of the current density in log-scale. For the thermionic emission current follows in accumulation a concentration in the device middle, in inversion a constant concentration in the device, in accumulation a parabolic shape of the current density in log-scale and a negligible thermionic emission for holes.

With these assumptions a closed-form model for the tunneling and thermionic current is derived which may be able to predict the device current. For the thermionic emission mechanism an explicit equation already exists while for the tunneling mechanism an explicit expression has to be derived. Afterwards, closed-form solutions for the current densities have to be found which finally lead to the closed-form model.

Chapter 8.

Analytical Closed-form Modeling Approach (ACFMA) for the Currents

The chapter targets to find an explicit solution for the tunneling current density which was presented in chapter 6. The used thermionic current density is already solved in closed form and taken from literature, as explained in the previous chapters. After that the integration of the current densities over the channel cross section has to be solved in closed form as well.

The physics-based two-dimensional analyses in chapter 7 have been performed already. The analyses have shown that the biggest tunneling current density is concentrated in the corners of the device. This result is used to simplify the ANMA from chapter 6 and therefore to concentrate on the main current contributions.

8.1. Tunneling Current Density

The analyses of the tunneling current density from equation (6.11) have shown a two-dimensional influence on the contributions to the product $\mathrm{E(x,y)^2 \cdot T(E,x,y) \cdot f_m(\xi(x))[1-f_s(\xi(x))]}$.

In Fig. 8.1 this influence is shown for $\mathrm{E(x,y)^2 \cdot T(E,x,y)}$ for $\mathrm{V_g}$=0.5 V to 0.8 V and $\mathrm{V_{ds}}$=1 V. As in chapter 7 explained, the biggest tunneling probability $\mathrm{T(E,x,y)}$ can be found in the corners close to the silicon-to-oxide interface as well as at the source boundary. Furthermore, by increasing the gate bias, $\mathrm{E(x,y)^2 \cdot T(E,x,y)}$ is rising due to the increasing electric field and the tunneling probability. The aim should be to predict this behavior accurately by a compact model.

Furthermore, the behavior of the carrier distributions $\mathrm{f_m(\xi(x))[1-f_s(\xi(x))]}$ in Fig. 8.2 have to be described by analytical approximations. One is able to observe that by increasing the gate bias the shape of the carrier distribution at the conduction band is moving towards the source boundary. Additionally, it can be observed that the width of the Gaussian-like shaped carrier distribution is decreasing with the gate bias, as well as a turn of the two-dimensional curvature [192, 193].

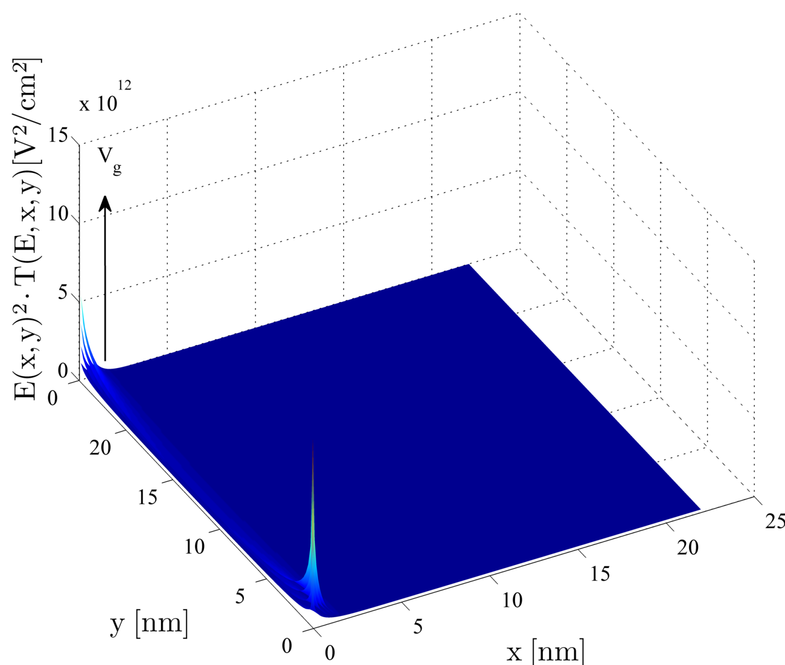

Figure 8.1.: Electric field multiplied by the tunneling probability $\mathrm{E(x,y)^2 \cdot T(E,x,y)}$ for electrons from the ANMA. Results for ϕ_{Bn}=0.28 eV. Device geometry: $\mathrm{l_{ch}}$=22 nm, $\mathrm{t_{ch}}$=10 nm, $\mathrm{t_{ox}}$=2 nm. Bias conditions: $\mathrm{V_{ds}}$=1 V, $\mathrm{V_g}$=0.5 V to 0.8 V with 0.1 V stepping.

Both, $\mathrm{E(x,y)^2 \cdot T(E,x,y)}$ and $\mathrm{f_m(\xi(x))[1-f_s(\xi(x))]}$, finally contribute to the generation rate which is illustrated in Fig. 8.3. As expected, the main concentration is still at the silicon-to-oxide interface but the main contribution is shifted from the source boundary slightly into the channel. Furthermore, the shift is coupled with the gate bias. At the silicon-to-oxide interface, when increasing the gate bias, the influence results in a movement towards the source boundary [192, 193].

By summarizing this extended analyses and dividing the device from gate to gate into several slices along the channel, the contributions within one slice result as shown in Fig. 8.4. For this, in the next sections the components of the generation rate described above will be approximated by analytical functions which in the end allow for integration.

8.1.1. Analytical Approximation of the Tunneling Current Density

To receive an analytical description of the tunneling current density it is necessary to replace its equation by a simplified term which allows integration to find a primitive and in the end a closed-form solution.

Therefore, we assume the following approach [192, 193] to describe the current density for a cut along the channel

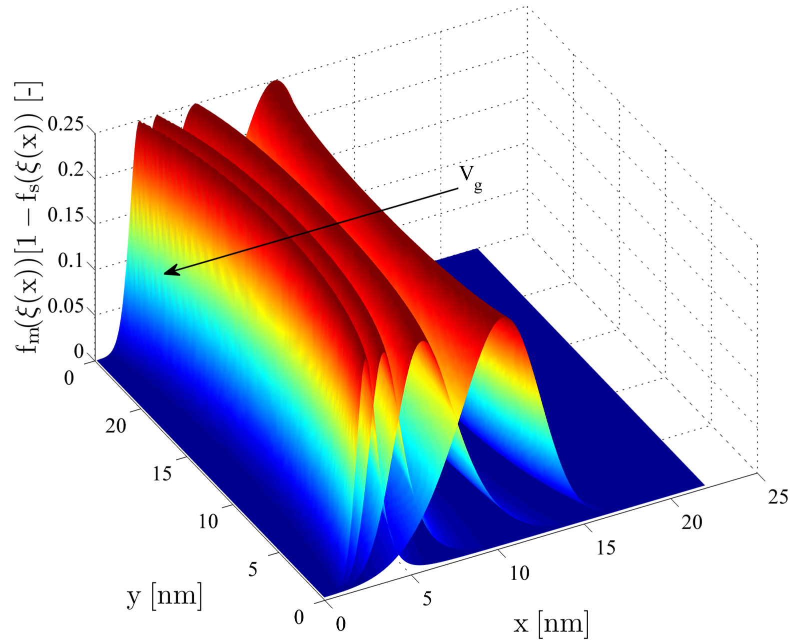

Figure 8.2.: Carrier distribution at the conduction band $f_m(\xi(x))[1-f_s(\xi(x))]$ for electrons from the ANMA. Results for ϕ_{Bn}=0.28 eV. Device geometry: l_{ch}=22 nm, t_{ch}=10 nm, t_{ox}=2 nm. Bias conditions: V_{ds}=1 V, V_g=0.5 V to 0.8 V with 0.1 V stepping.

$$J_{tun}(y) \approx \frac{q\mu N_C}{kT} \int_0^{l_{ch}} \frac{1}{4} \exp\left(-a(x-x_{E_f})^2\right) \cdot b \cdot \exp\left(-cx\right) dx \tag{8.1}$$

where the exponential functions replace the tunneling probability and the carrier distribution in equation (6.11) with x_{E_f}, the position of the Fermi level. Here, using the following analytical approximations

$$E(x,y)^2 \cdot T(E,x,y) \approx b \cdot \exp\left(-cx\right) \tag{8.2}$$

with $b = E(x,y)^2 \cdot T(E,x,y)|_{x=0}$
and $c = -\ln\left(\frac{1}{b}E(x,y)^2 \cdot T(E,x,y)\right)/x_{E_f}|_{x=x_{E_f}}$.

Furthermore, a Gaussian distribution is introduced as approximation of the carrier distribution

$$f_m(\xi(x))[1-f_s(\xi(x))] \approx \frac{1}{4}\exp\left(-a(x-x_{E_f})^2\right). \tag{8.3}$$

8.1.2. Mapping of Distribution Function

The coefficient a in equation (8.3) describes the width (Fig. 8.5) of the carrier distributions [192, 193]. First, a relationship between the carrier distribution and the Gaussian

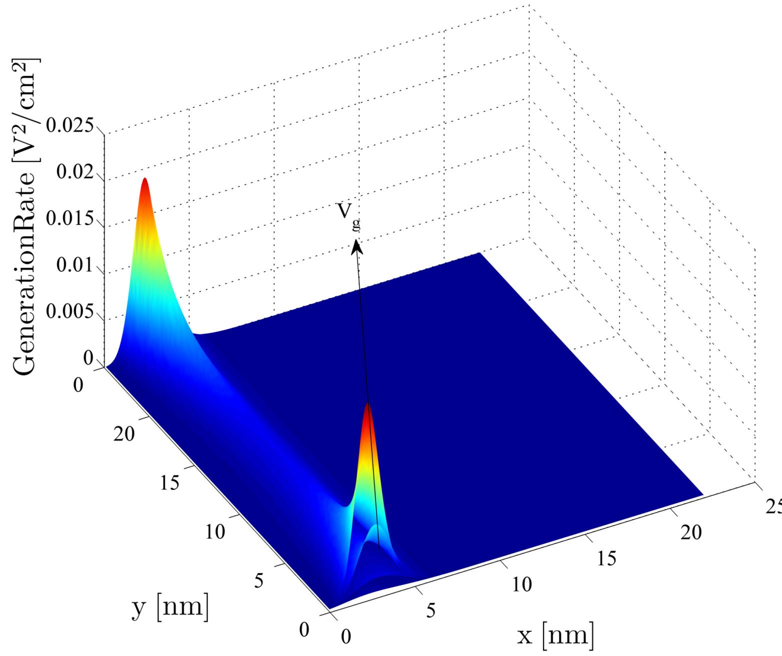

Figure 8.3.: Generation rate $E(x,y)^2 \cdot T(E,x,y) \cdot f_m(\xi(x))[1 - f_s(\xi(x))]$ for electrons from the ANMA. Results for ϕ_{Bn}=0.28 eV. Device geometry: l_{ch}=22 nm, t_{ch}=10 nm, t_{ox}=2 nm. Bias conditions: V_{ds}=1 V, V_g=0.5 V to 0.8 V with 0.1 V stepping.

approximation with respect to the energy is necessary. The carrier distributions from equation (6.11) are described with respect to the energy as

$$f_m(\xi)[1 - f_s(\xi)] = \frac{1}{1 + \exp\left(\frac{\xi - E_f}{kT}\right)} \cdot \frac{1}{1 + \exp\left(\frac{E_f - \xi}{kT}\right)}. \tag{8.4}$$

Equation (8.4) should be approximated by

$$f_m(\xi)[1 - f_s(\xi)] \approx \frac{1}{4} \exp\left(-\widetilde{a}\,(\xi - E_f)^2\right) \tag{8.5}$$

where $\widetilde{a}$ is introduced to describe the width of the distribution in energy space.

Equation (8.4) and equation (8.5) have a different curvature. Nevertheless, a useful relationship between both is obtained. To solve the integral in equation (8.1) the area enclosed by a plot of equation (8.3) is of interest. Therefore, a relationship between the integrals of equation (8.4) and equation (8.5) is developed.

The integral of equation (8.4) is solved for ±∞ which yields

$$\int_{-\infty}^{+\infty} f_m(\xi)[1 - f_s(\xi)] = \int_{-\infty}^{+\infty} \frac{d\xi}{2 + \exp\left(\frac{\xi - E_f}{kT}\right) + \exp\left(\frac{E_f - \xi}{kT}\right)} = kT. \tag{8.6}$$

Afterwards, the integral of equation (8.5) is solved

$$\int_{-\infty}^{+\infty} f_m(\xi)[1 - f_s(\xi)] \approx \int_{-\infty}^{+\infty} \frac{1}{4} \exp\left(-\widetilde{a}\,(\xi - E_f)^2\right) d\xi = \frac{\sqrt{\pi}}{4\sqrt{\widetilde{a}}}. \tag{8.7}$$

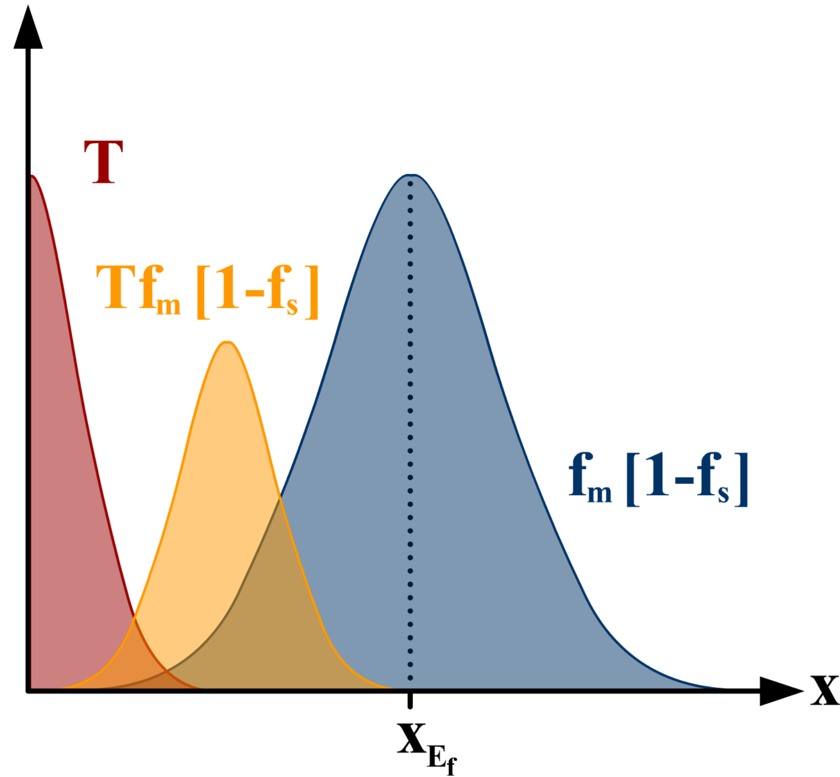

Figure 8.4.: Diagram of the contributions to the two-dimensional tunneling generation rate in one slice from source to drain.

Equating both results from equation (8.6) and equation (8.7) shows that

$$\tilde{a} = \frac{\pi}{16(kT)^2}. \tag{8.8}$$

Now, by using equation (8.3) and equation (8.5) a relation between parameters a and $\tilde{a}$ must be derived. If in equation (8.5) one linearly approximates the relationship between energy and distance x from source close to x_{E_f}, one can write

$$\xi(x) = E_f + \left.\frac{\partial \xi}{\partial x}\right|_{x=x_{E_f}} (x - x_{E_f}). \tag{8.9}$$

Insert equation (8.9) in equation (8.5) and compute it with equation (8.3) which results in

$$\frac{1}{4}\exp\left(-\tilde{a}\left(\left.\frac{\partial \xi}{\partial x}\right|_{x=x_{E_f}} (x - x_{E_f})\right)^2\right) = \frac{1}{4}\exp\left(-a(x - x_{E_f})^2\right). \tag{8.10}$$

Therefore, it follows

$$\tilde{a}\left(\left.\frac{\partial \xi}{\partial x}\right|_{x=x_{E_f}} (x - x_{E_f})\right) = a, \tag{8.11}$$

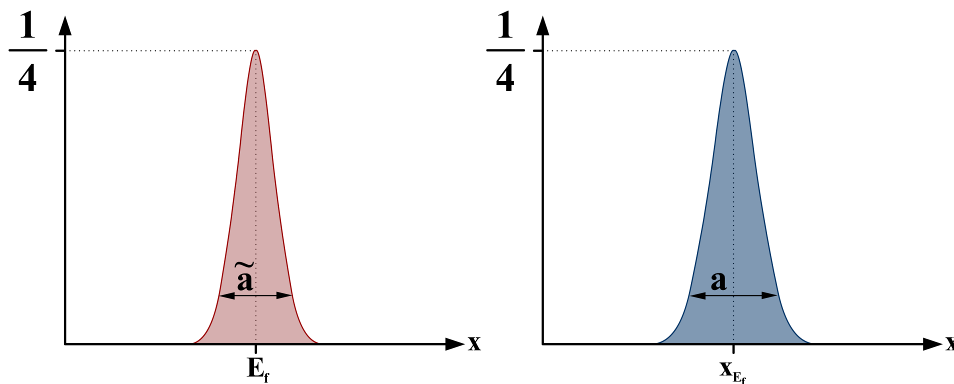

Figure 8.5.: Approximation of the product of the carrier distributions depending on the energy ξ and the coordinate x.

and with equation (8.8) the coefficient a is described as

$$a = \frac{\pi}{16(kT)^2} \cdot q \cdot E(x_{E_f}, y)^2. \tag{8.12}$$

8.1.3. Closed-Form Solution of Tunneling Current Density

All parameters are now defined and the solution of the integral in equation (8.1) with equation (8.2) and equation (8.3) for the tunneling current density results in [192, 193]

$$J_{tun}(y) \approx \frac{q\mu N_C}{kT} \cdot \sqrt{\pi} \cdot b \cdot \exp\left(\frac{c^2}{4a} - cx_{E_f}\right) \cdot \frac{\text{erf}\left(\frac{2a\left(x - x_{E_f}\right) + c}{2\sqrt{a}}\right)}{8\sqrt{a}}. \tag{8.13}$$

This compact solution can be used to calculate explicitly the tunneling current density. The parameters a, b and c in the compact solution are calculated with the ANMA approach for the electric field and the potential from chapter 6 at the points of interest $x = 0$, $x = x - x_{E_f}$ and $x = x_{E_f}$.

Tunneling Current Density Correction

Nevertheless, if the gate bias has the amount of the threshold voltage V_{th} an inaccuracy occurs. It results from the approximation of the carrier distribution which seems to be not accurate enough close to the boundaries for this gate bias range, see Fig. 8.6(a). The Fermi level itself is located somewhere in the middle of the device and the approximation decreases too fast, therefore, parameter a from equation (8.12) is not accurate enough.

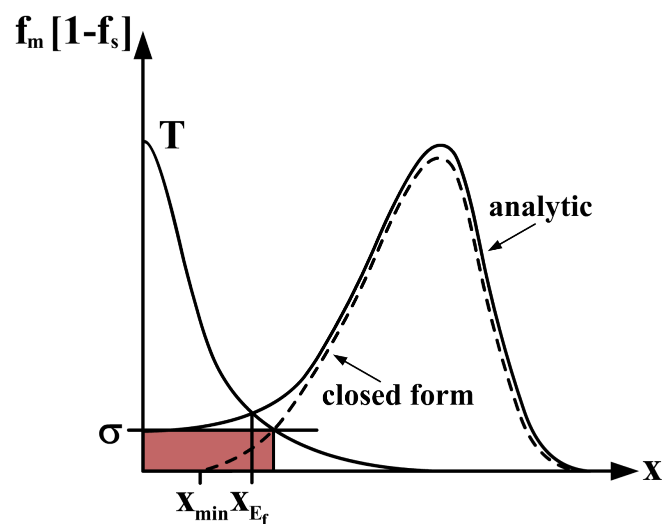

(a)

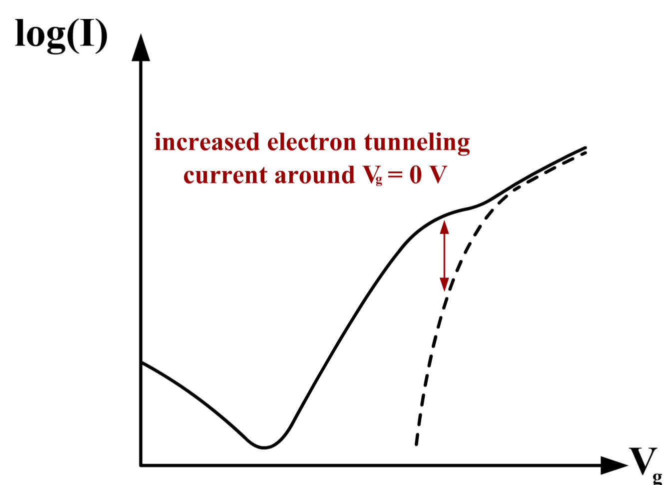

(b)

Figure 8.6.: The closed-form approximation for the carrier distribution in equation (8.13) decreases too fast, therefore the parameter a from equation (8.12) is not accurate enough for a gate bias with the amount of the threshold voltage V_{th} as shown in (a). A correction is developed which compensates the inaccuracy and leads to an improved and increased electron tunneling current around V_{th} as shown in (b).

To compensate this behavior, a correction factor is developed which solves the inaccuracy. From Fig. 8.6(a) the rectangular area has to be added to the carrier distribution. Due to this circumstance from Fig. 8.6(b) the following correction has to be applied. It results in

$$\int_0^\infty \mathrm{f_m}[1-\mathrm{f_s}]_{\mathrm{ANMA}} \cdot \mathrm{b} \cdot \exp\left(-\mathrm{cx}\right) \mathrm{dx} = \int_0^\infty \left(\mathrm{f_m}[1-\mathrm{f_s}]_{\mathrm{ACFMA}} + \sigma\right) \cdot \mathrm{b} \cdot \exp\left(-\mathrm{cx}\right) \mathrm{dx} =$$
$$\int_0^\infty \mathrm{f_m}[1-\mathrm{f_s}]_{\mathrm{ACFMA}} \cdot \mathrm{b} \cdot \exp\left(-\mathrm{cx}\right) \mathrm{dx} + \int_0^\infty \sigma \cdot \mathrm{b} \cdot \exp\left(-\mathrm{cx}\right) \mathrm{dx} = \mathrm{J_{tun}}(\mathrm{y}) + \mathrm{J_{tun,fix}}(\mathrm{y}). \tag{8.14}$$

From equation (8.14) follows as the primitive of $\mathrm{J_{tun,fix}}(\mathrm{y})$

$$\mathrm{J_{tun,fix}}(\mathrm{y}) = \left.\frac{\sigma \cdot \mathrm{b} \cdot \exp\left(-\mathrm{cx}\right)}{-\mathrm{c}}\right|_0^\infty = \sigma \frac{\mathrm{b}}{\mathrm{c}} \tag{8.15}$$

with

$$\sigma = \mathrm{f_m}[1-\mathrm{f_s}]_{\mathrm{ANMA}}\big|_{\mathrm{x}=0} - \mathrm{f_m}[1-\mathrm{f_s}]_{\mathrm{ACFMA}}\big|_{\mathrm{x}=0}$$

where ANMA describes the analytical numerical model and ACFMA the closed-form model.

Adding equation (8.15) to the tunneling current density from equation (8.13), a behavior as shown in Fig. 8.6(b) can be observed and it follows

$$\mathrm{J_{tun,overall}}(\mathrm{y}) = \mathrm{J_{tun}}(\mathrm{y}) + \mathrm{J_{tun,fix}}(\mathrm{y}). \tag{8.16}$$

Taking into account this correction, a compensation for lower voltages is applied while for higher ones the influence of the correction term is negligible.

8.1.4. Estimation of $\mathrm{x_{E_f}}$

Within the analytical tunneling current density approximation the parameter $\mathrm{x_{E_f}}$ describes the peak position of the carrier distribution with respect to the coordinate as shown in Fig. 8.5.

To estimate the peak position $\mathrm{x_{E_f}}$, a polynomial of 4th grade may be sufficient enough to predict the potential distribution. Neither cubic nor quadratic polynomials were able to predict the potential and at least the parameter $\mathrm{x_{E_f}}$ accurately as illustrated in Fig. 8.7, 8.8 and 8.9. If one observes the resulting residuals from the polynomial fit, it is clear that at least a polynomial of 4th grade or higher is necessary to calculate the potential correctly and estimate the peak position $\mathrm{x_{E_f}}$, as one is able to observe from the residuals.

A polynomial of 4th grade delivers

$$\varphi = \mathrm{ax}^4 + \mathrm{bx}^3 + \mathrm{cx}^2 + \mathrm{dx} + \mathrm{e}. \tag{8.17}$$

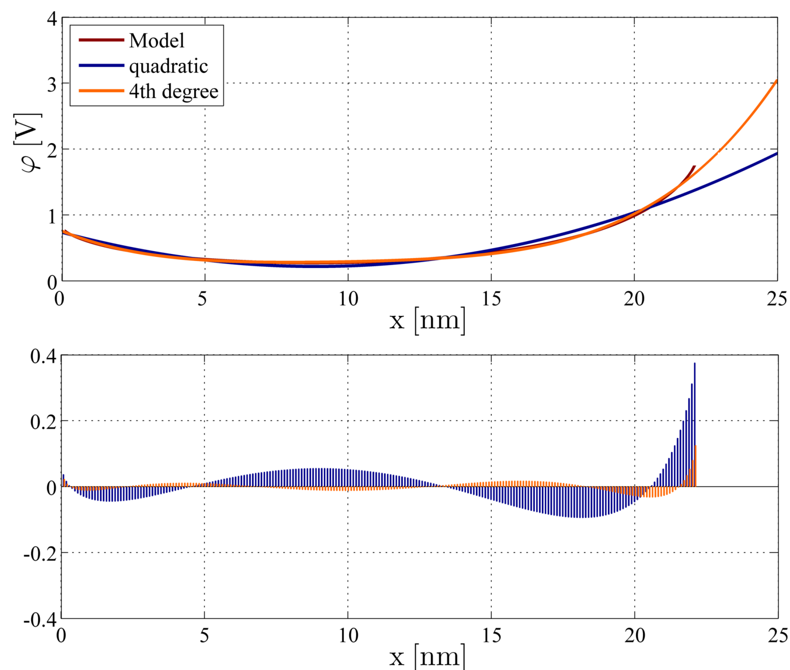

Figure 8.7.: Electrostatic potential φ at the silicon-to-oxide interface in accumulation for a SB-DG-MOSFET. Results for ϕ_{Bn}=0.28 eV. Device geometry: l_{ch}=22 nm, t_{ch}=10 nm, t_{ox}=2 nm. Bias conditions: V_{ds}=1 V, V_g=−0.3 V.

The peak position x_{E_f} is found at the intersection of the potential and the bias condition $\phi_{E_f} = \phi_{bi} + \phi_{Bn}$. Furthermore, constant Fermi level within the channel region is assumed. From equation (8.17) follows

$$ax^4 + bx^3 + cx^2 + dx + e - \phi_{E_f} = 0. \tag{8.18}$$

Here, the real root describes the peak position x_{E_f}. The parameters a,b,c,d and e as well as the roots can be solved numerically.

8.2. Parabolic Current Approximation

In chapter 7 log-scale parabolically shaped tunneling and thermionic current densities with respect to the y axis have been presented. Here, the biggest concentration for the tunneling mechanism is located in the corners and for the thermionic mechanism in the middle of the device. Due to this circumstance a parabolic approximation for the integration in equation (6.12) and equation (6.14) along the y-direction from t_{ox} to $t_{ox} + t_{ch}$ is chosen [193].

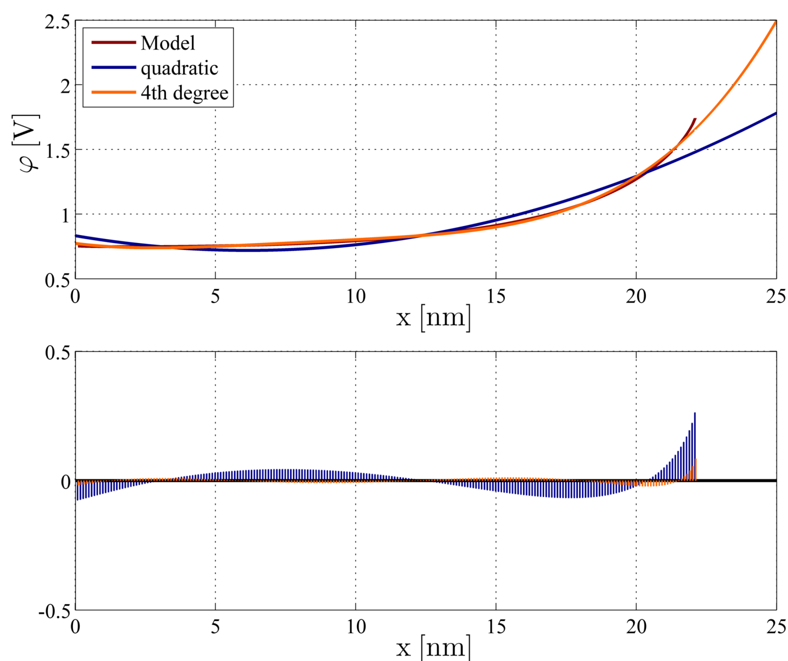

Figure 8.8.: Electrostatic potential φ at the silicon-to-oxide interface in flat band condition for a SB-DG-MOSFET. Results for ϕ_{Bn}=0.28 eV. Device geometry: l_{ch}=22 nm, t_{ch}=10 nm, t_{ox}=2 nm. Bias conditions: V_{ds}=1 V, V_g=0.3 V.

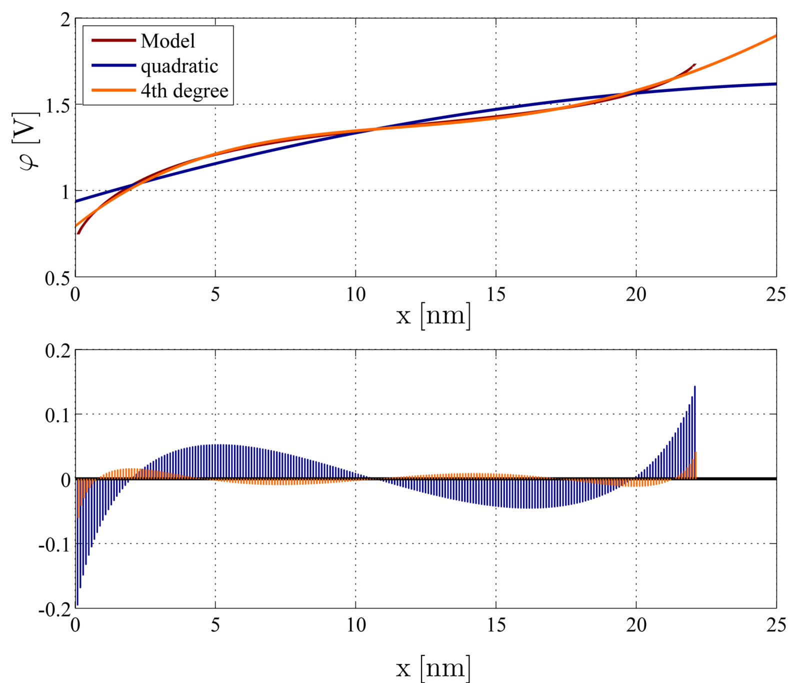

Figure 8.9.: Electrostatic potential φ at the silicon-to-oxide interface in inversion for a SB-DG-MOSFET. Results for ϕ_{Bn}=0.28 eV. Device geometry: l_{ch}=22 nm, t_{ch}=10 nm, t_{ox}=2 nm. Bias conditions: V_{ds}=1 V, V_g=1 V.

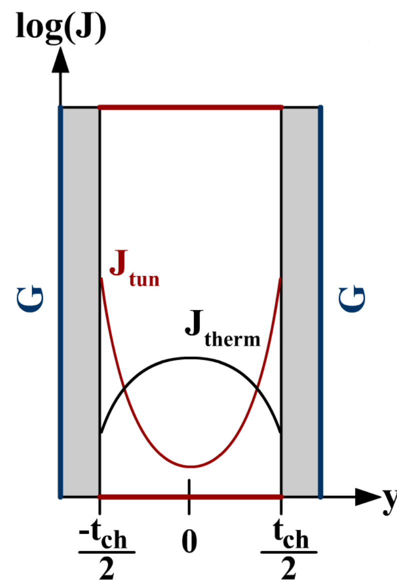

Figure 8.10.: Diagram of the tunneling and thermionic current densities.

Rearranging the coordinates from $-\frac{t_{ch}}{2}$ to $\frac{t_{ch}}{2}$ with the origin in the middle of the channel and assuming the current density to be constant with respect to the z-coordinate, the current can be calculated as (with respect to Fig. 8.10)

$$I = w_{ch} \cdot \int_{-\frac{t_{ch}}{2}}^{\frac{t_{ch}}{2}} \cdot \exp\left(d \cdot y^2 + e\right) dy, \tag{8.19}$$

with $d = -\frac{4}{t_{ch}^2} \cdot \ln\left(\frac{J|_{y=\frac{t_{ch}}{2}}}{J|_{y=0}}\right)$
and $e = \ln\left(J|_{y=0}\right)$.

The coefficients d and e in the approximation $J(y) \approx \exp\left(d \cdot y^2 + e\right)$ in equation (8.19) are solved with the current densities at $J|_{y=0}$ and $J|_{y=\frac{t_{ch}}{2}}$ (Fig. 8.10) with equation (8.13) for the tunneling current densities and with equation (6.13) for the thermionic current densities. With equation (8.19) both components, the tunneling and the thermionic emission, can be calculated.

8.2.1. Closed-Form Solution of Currents

Integrating the obtained solution with respect to y results in [193]

$$I = w_{ch} \cdot \frac{\sqrt{\pi} \cdot \operatorname{erf}\left(\sqrt{d} \cdot y\right) \cdot \exp\left(e\right)}{2\sqrt{d}}. \tag{8.20}$$

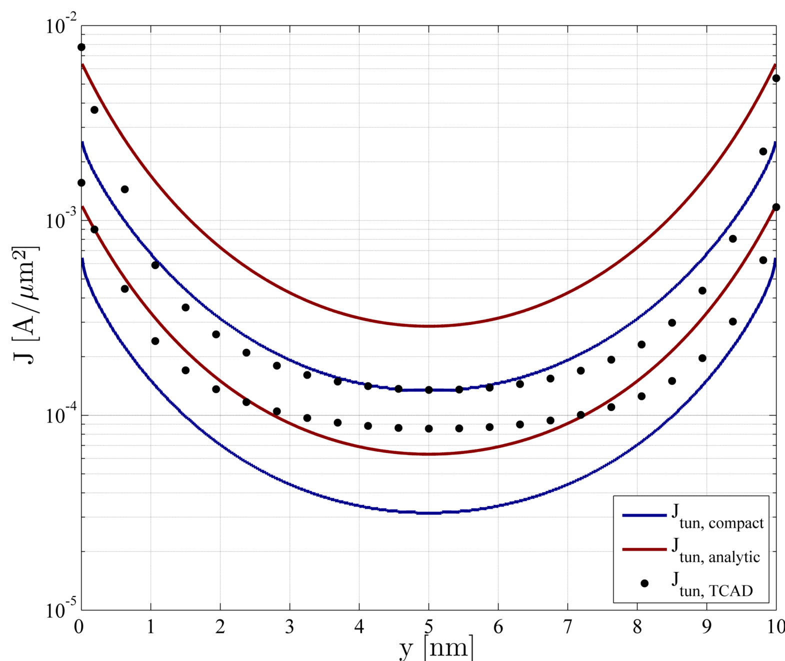

Figure 8.11.: Current Densities $J_{tun,analytical}$ and $J_{tun,compact}$ vs. TCAD. Results for ϕ_{Bn}=0.28 eV. Device geometry: l_{ch}=22 nm, t_{ch}=10 nm, t_{ox}=2 nm. Bias conditions: V_{ds}=1 V, V_g=0.8 V and 1 V.

This solution can be used to solve both, the thermionic and tunneling current. The parameters d and e in the compact solution are calculated with equations (6.13) and (6.11) from the ANMA approach from chapter 6 at the points of interest $y = 0$ and $y = \pm\frac{t_{ch}}{2}$.

8.3. Smoothing; Thermionic to Tunneling Current

In section 6.4 for the analytical numerical modeling approach already a transition between the linear and saturation region or more exactly between the thermionic and the tunneling current has been developed to guarantee a smooth and continuous transition.

This effect has to be taken into account for the analytical closed-from modeling approach as well. Therefore, the following analytical smoothing function is applied [88]

$$V_{gx} = V_{g,trans}\left(1 - \frac{1}{B}\ln\left(\left[1 + \exp\left(A\left(1 - \frac{V_g}{V_{g,trans}}\right)\right)\right]\right)\right) \tag{8.21}$$

with

$$B = \ln\left(1 + \exp\left(A\right)\right) \tag{8.22}$$

where $A \approx 5...10$ and $V_{g,trans}$ defines the point of the continuous smoothing.

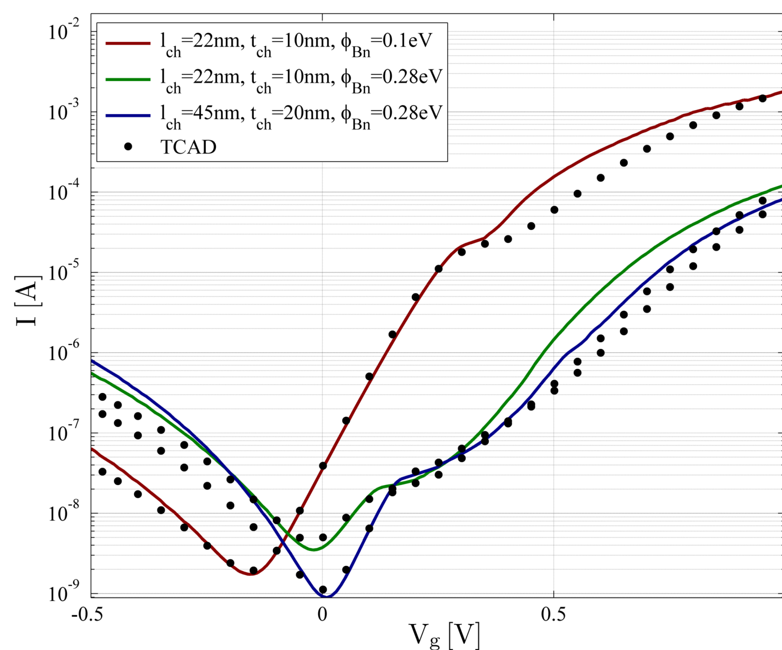

Figure 8.12.: Closed-form current I vs. TCAD. Results for ϕ_{Bn}=0.1/0.28 eV. Device geometry: l_{ch}=22/45 nm, t_{ch}=10/20 nm, t_{ox}=2 nm, w_{ch}=1 µm. Bias conditions: V_{ds}=1 V, V_g=−0.5 V to 1 V with 0.01 V stepping.

8.4. Results

In Fig. 8.11 the result of the tunneling current density for the electrons at the source electrode of the analytical numerical approach [192, 193] is presented compared with the compact solution given by equation (8.13) and TCAD simulation data [64].

One observes that the compact solution is able to predict the current density nearly correctly compared to the analytical numerical solution with numerical integration and TCAD. Especially the shape at the important corners is predicted very well. Furthermore, a constant offset between both solutions can be observed due to the approximations which have been made to receive the explicit equations. This error can be easily compensated by a bias and geometry independent adjustment of parameters (e.g. mobility and density of states).

Fig. 8.12 shows transfer characteristics of the closed-form solution for different device geometries and different Schottky barrier heights for the electrons compared to TCAD simulation data for V_{ds}=1 V and V_g=−0.5 V to 1 V. Finally, the geometry independent fitting parameters of the compact model for several $I_d - V_g$ curves show that only the carrier masses and tunneling mobilities in equations (6.11) and (8.13) have to be adjusted in a small range (e.g. Table 6.3 vs. Table 8.1 for a channel length l_{ch}=22 nm) while the Richardson constant is kept constant. It can be easily observed from the curves that the

Table 8.1.: Adjusted device model parameters for a channel length l_{ch}=22 nm.

Structural	l_{ch}	22	[nm]	channel length
	t_{ch}	10	[nm]	channel thickness
	t_{ox}	2	[nm]	oxide thickness
Mobility	μ_n	1.5 | 1.7	[cm^2/Vs]	elec. tunneling mobility
	μ_p	1.5 | 1.6	[cm^2/Vs]	hole tunneling mobility
Misc	N_B	10^{15}	[cm^{-3}]	substrate doping
	V_{fb}	-0.125 | -0.125	[V]	flatband voltage
	ϕ_{bi}	0.56	[V]	built-in potential s/d
	ϕ_{Bn}	0.28 | 0.1	[eV]	SBH electrons
	A_n^*	82 | 62	[A/cm^{2}K^2]	elec. Richardson constant
	A_p^*	32 | 32	[A/cm^{2}K^2]	hole Richardson constant
	m_n	0.26 | 0.24	[-]	elec. effect. mass
	m_p	0.20 | 0.22	[-]	hole effect. mass

hole tunneling current as well as the thermionic emission current are predicted accurately. The electron tunneling current is also correctly predicted for higher gate biases while an inaccuracy between V_g=0.5 V to 0.8 V can be seen. This inaccuracy might result from the made approximations, e.g. the carrier distribution function, the product of tunneling probability and the square of the electric field. Furthermore, the parabolic approximation [193] is not accurate enough for lower gate biases. If we observe Fig. 8.11, the behavior for lower gate biases of the simulated TCAD tunneling current density has rather a circular than a parabolic shape. Furthermore, at high V_g the model becomes less accurate due to drift-diffusion effects. This effect results from the limitation of the current by drift-diffusion.

8.5. Conclusion

In this chapter a new compact model by an analytical closed-form modeling approach for the current estimation in SB-DG-MOSFETs has been presented. Based on the 2D analyses from chapter 7 analytical approximations have been introduced which describe the main current components and can be solved by explicit closed-form equations. Furthermore, the current densities for the current components of tunneling and thermionic emission are solved by an explicit closed-form equation.

The analytical closed-form current calculations show a very good agreement with TCAD simulation data down to channel lengths of 22 nm. The illustrated results show

UNIVERSITAT ROVIRA I VIRGILI
TWO-DIMENSIONAL ANALYTICAL PREDICTIVE MODELING OF SCHOTTKY BARRIER SOI AND MULTI-GATE MOSFETS
Mike Schwarz
Dipòsit Legal: T.456-2013

that the current components are predicted accurately for a large bias range, several barrier heights and geometries.

Nevertheless, due to the analytical approximations the model parameters, e.g. Richardson constant, tunneling mobility, and effective masses have to be adjusted compared to the analytical numerical modeling approach from chapter 6.

However, the big advantage of the analytical closed-form approach compared to the analytical numerical approach is the fact that for current calculation it requires only the calculation of the electrostatics at a few points, resulting in much less computation time. At least twelve points for the current calculation are needed: Six points for the source related case and six points for the drain related case. A full equation package is given in the Appendix D. The numerical current calculation in a SB-DG-MOSFET device is done at every position in the channel region of the device and depending on the refinement of the coordinates. The computation time is much higher compared to the closed-form approach.

Finally, the closed-form model predicts the current with ambipolar behavior well for various barrier heights and geometries up to a relatively high gate bias. Furthermore, the approach in particular inherently includes 2D effects on the device current.

UNIVERSITAT ROVIRA I VIRGILI
TWO-DIMENSIONAL ANALYTICAL PREDICTIVE MODELING OF SCHOTTKY BARRIER SOI AND MULTI-GATE MOSFETS
Mike Schwarz
Dipòsit Legal: T.456-2013

UNIVERSITAT ROVIRA I VIRGILI
TWO-DIMENSIONAL ANALYTICAL PREDICTIVE MODELING OF SCHOTTKY BARRIER SOI AND MULTI-GATE MOSFETS
Mike Schwarz
Dipòsit Legal: T.456-2013

Chapter 9.

Measurement Data for dopant-segregated SB-UTB-MOSFETs

In chapter 6 the ANMA approach was introduced and discussed in detail. Furthermore, the approach was compared with simulation data from the TCAD Sentaurus device simulator. The results showed a very good agreement for channel lengths down to 22 nm. However, to prove how good a model can predict the behavior of real devices, a comparison with measurement data is necessary. Due to this circumstance the model approaches of chapter 6 are compared to the $I_d - V_g$ measurement data for a SB-UTB device delivered by the Forschungszentrum Jülich [101].

9.1. Device Physics

The understanding of the device physics and the resulting behavior are very important elements during the developing procedure of a model. Therefore, and to concentrate on the main contributions as in Fig. 9.1, the SB-UTB-MOSFET device is simulated in TCAD Sentaurus (Table 9.1) and analyzed in detail [194]. In Fig. 9.2 the electrostatic potential for three different gate potentials is given which range from accumulation to inversion mode, with a gate potential at the bottom $V_{g,bottom}$=0 V.

The behavior is as expected. While one increases $V_{g,top}$ from −0.5 V to 1 V underneath the top oxide the energy bands are bent downwards, see Fig. 9.1. The influence on the bottom channel from the bottom gate is lower compared to the one of the top due to the thicker oxide. Nevertheless, the asymmetric behavior forces that the main contribution to the tunneling current is generated underneath the top oxide [194].

Similar is the influence on the electric field as illustrated in Fig. 9.3. Due to the correspondence between electric field and electrostatic potential, the electric field underneath the top oxide is higher compared to the bottom oxide, Fig. 9.3(a) to 9.3(c). Due to this circumstance the effect of tunneling at the bottom should be less than at the top. This effect may be interpreted based on the WKB approximation [114] used to estimate the

Table 9.1.: Parameter settings of the simulated TCAD device.

l_{ch}	80	[nm]	effect. channel length
t_{ch}	20	[nm]	channel thickness
$t_{ox,top}$	3.5	[nm]	top oxide thickness
$t_{ox,bottom}$	100	[nm]	bottom oxide thickness
ϕ_{Bn}	0.28	[eV]	SBH electrons
N_B	10^{15}	[cm^{-3}]	substrate doping
$\epsilon_{ox,top}$	7	[-]	permittivity top oxide
$\epsilon_{ox,bottom}$	3.9	[-]	permittivity bottom oxide

tunneling probability. If the gradient of the electric field is higher the probability for a charge carrier to tunnel through the channel region is higher, too [194].

Of course more physics than the carrier distribution which describe the generation of tunneling charge as the carrier distributions which are also responsible for the description of the tunneling current, and linked to the electrostatic potential. However, in general the electrostatics are responsible for the tunneling and thermionic mechanisms in the device [194].

The effects described above result in the generation rate of the corresponding charge carriers electrons and holes in the channel, respectively. In Fig. 9.4 and in Fig. 9.5 the electron and hole tunneling generation rates are illustrated for the bias conditions introduced above. From the observations made before the behavior for both is as expected [194].

For electrons follows a movement of the generation rate from the middle or center of the device towards the source junction as shown in Fig. 9.4(a) to 9.4(c). The bands are bent downwards by increasing the gate bias and the tunneling probability for the electrons at the source electrode rises due to the high electric field. Furthermore, it can be observed that the electron generation rate moves from the bottom oxide to the top oxide and concentrates at the top corner close to the source junction [194].

A similar behavior results for the hole generation rate. Due to the existing voltage drop between source and drain, the situation differs slightly. The energy bands (Fig. 9.1) are bent upwards and at the drain junction already a modulated barrier exists which is quite thin enough that holes are able to tunnel into the channel region. The main concentration also exists in the corner of the device, here at the drain junction, as shown in Fig. 9.5(a). Increasing the gate bias results in a decreased bending of the energy bands. Due to this, the barrier becomes thicker at the drain junction and therefore the tunneling probability is reduced which results in a decreased generation of hole charges at the drain electrode, depicted in Fig. 9.5(a) to 9.5(c). Finally, the generation rate

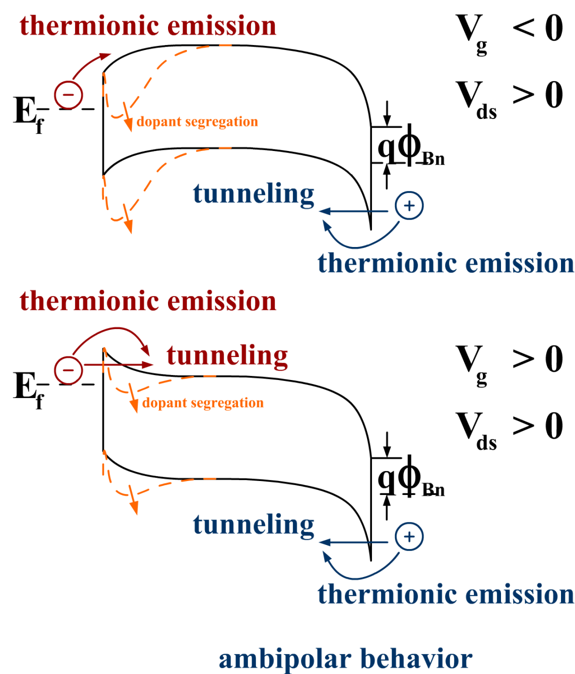

Figure 9.1.: Energy bands of a Schottky barrier MOSFET device, showing the current contribution in accumulation and inversion and the influence of dopant segregation at the source electrode.

moves from the top oxide towards the bottom oxide, cf. Fig. 9.5(c). This effect results in a minor influence due to the small amount of the generated charges [194].

On the other hand, the thermionic emission mechanism is strongly influenced by the maximum of the potential barrier within the channel region. Therefore, the potential distribution is responsible for the thermionic emission current behavior. Depending on the electrostatic potential and operation mode of the device, it is expected for accumulation that the current flow due to the thermionic mechanism concentrates near the bottom oxide and the channel middle of the device where the influence from both gates is low. Here, the potential barrier is lowered by the source and drain junctions. If the device operates in inversion, the barrier determining the thermionic current is the Schottky barrier itself, neglecting the Schottky barrier lowering effect. Furthermore, the main contribution results at the source electrode due to the high Schottky barrier height at the drain junction [194].

To conclude the device behavior, in accumulation, tunneling holes underneath the top oxide are the main contribution to the device current. In subthreshold range thermionic emission of electrons from the source close to the bottom oxide describes the current. In inversion tunneling electrons concentrated underneath the top oxide are the responsible charges for the current [194].

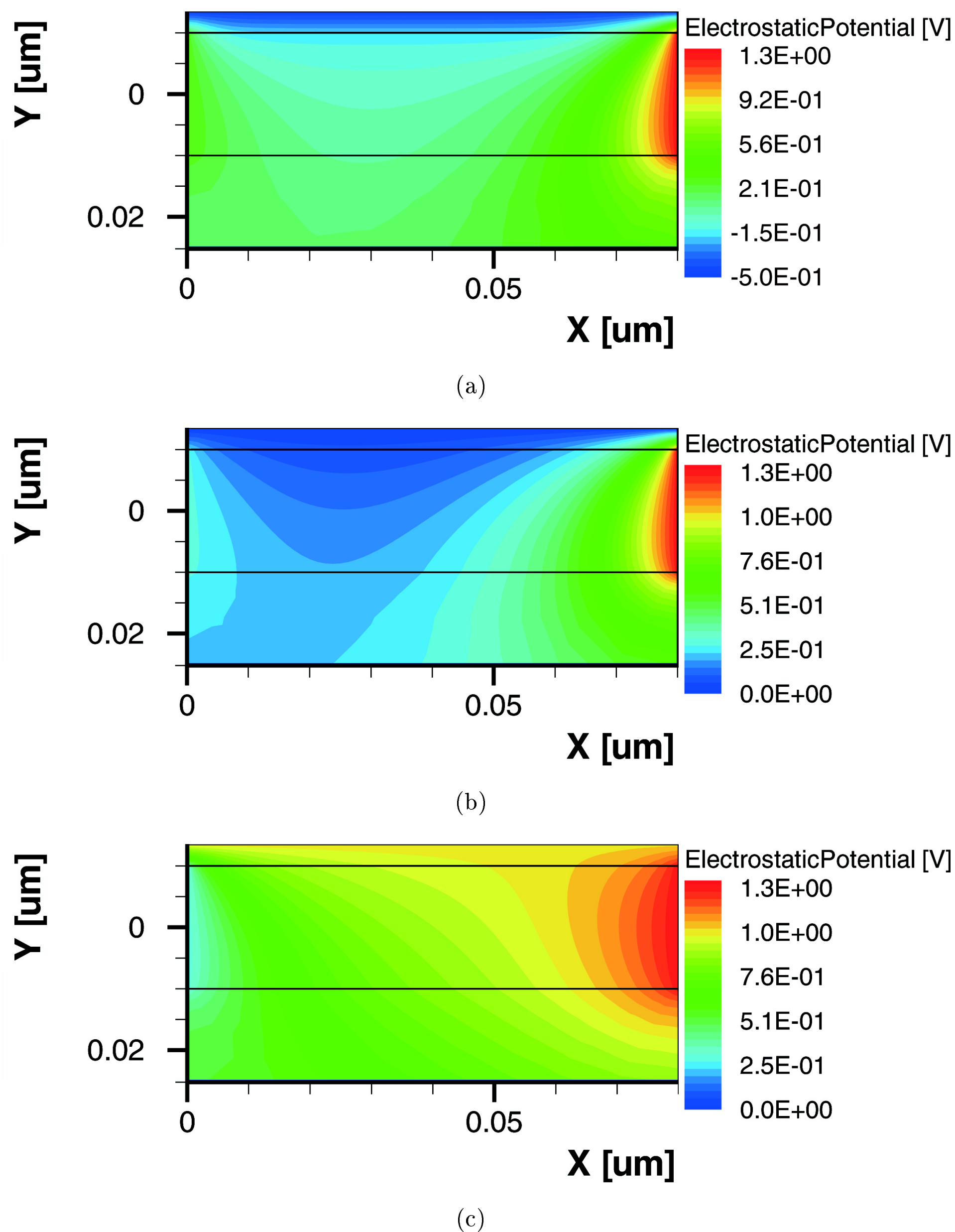

Figure 9.2.: Electrostatic potential φ in (a) at $V_{g,top}=-0.5\,V$, (b) at $V_{g,top}=0\,V$, (c) at $V_{g,top}=1\,V$. Device geometry: $l_{ch}=80\,nm$, $t_{ch}=20\,nm$, $t_{ox,top}=3.5\,nm$, $t_{ox,bottom}=100\,nm$. Bias conditions: $V_{ds}=1\,V$, $V_{g,bottom}=0\,V$.

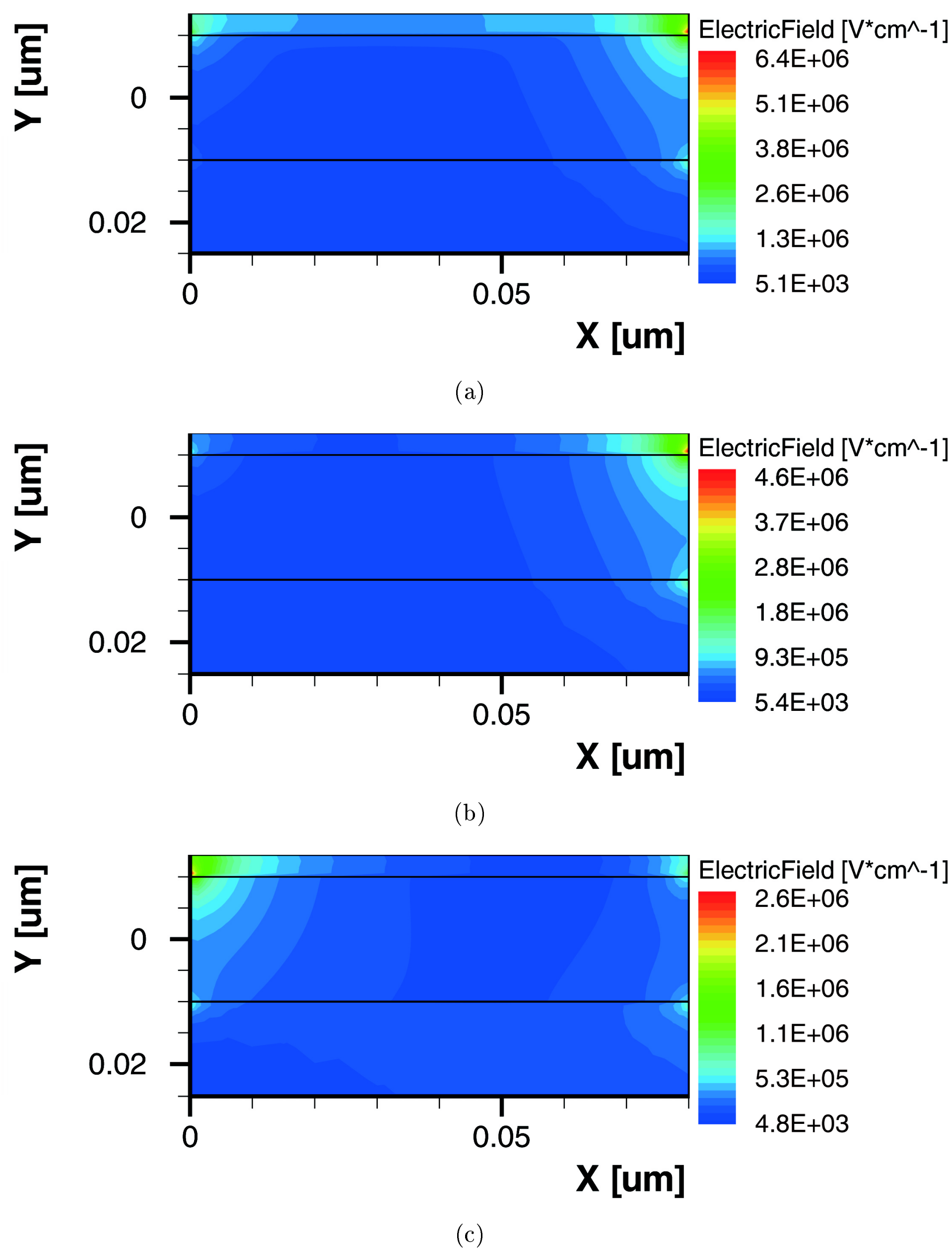

Figure 9.3.: Electric field |E| in (a) at $V_{g,top}=-0.5\,V$, (b) at $V_{g,top}=0\,V$, (c) at $V_{g,top}=1\,V$. Device geometry: $l_{ch}=80\,nm$, $t_{ch}=20\,nm$, $t_{ox,top}=3.5\,nm$, $t_{ox,bottom}=100\,nm$. Bias conditions: $V_{ds}=1\,V$, $V_{g,bottom}=0\,V$.

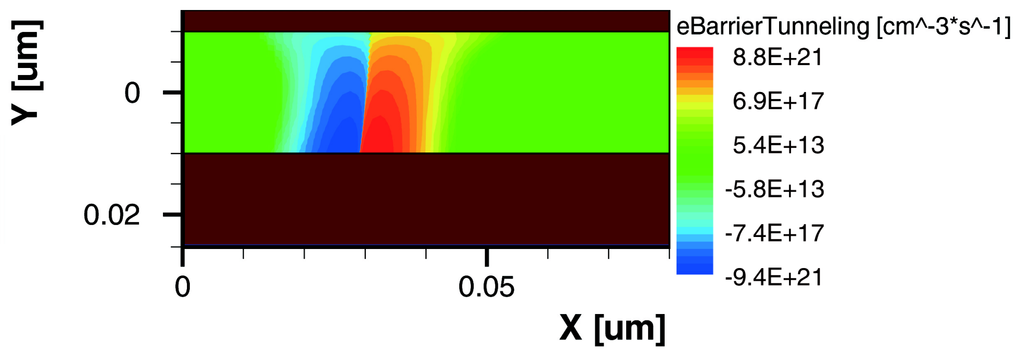

(a)

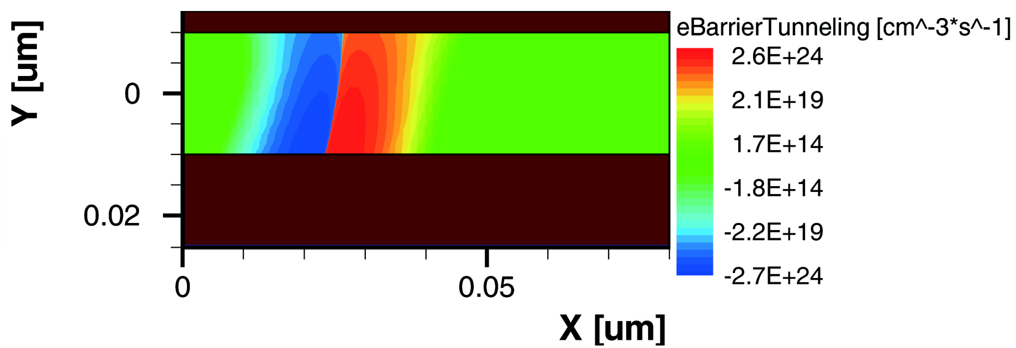

(b)

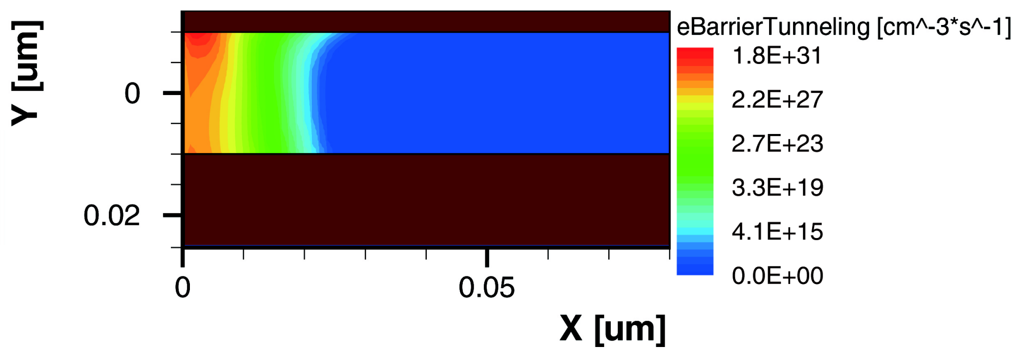

(c)

Figure 9.4.: Electron Tunneling Generation Rate in (a) at $V_{g,top}=-0.5\,V$, (b) at $V_{g,top}=0\,V$, (c) at $V_{g,top}=1\,V$. Device geometry: $l_{ch}=80\,nm$, $t_{ch}=20\,nm$, $t_{ox,top}=3.5\,nm$, $t_{ox,bottom}=100\,nm$. Bias conditions: $V_{ds}=1\,V$, $V_{g,bottom}=0\,V$.

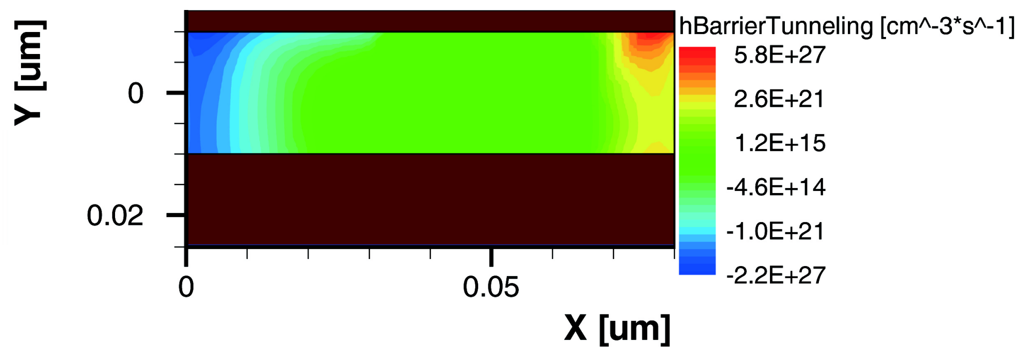

(a)

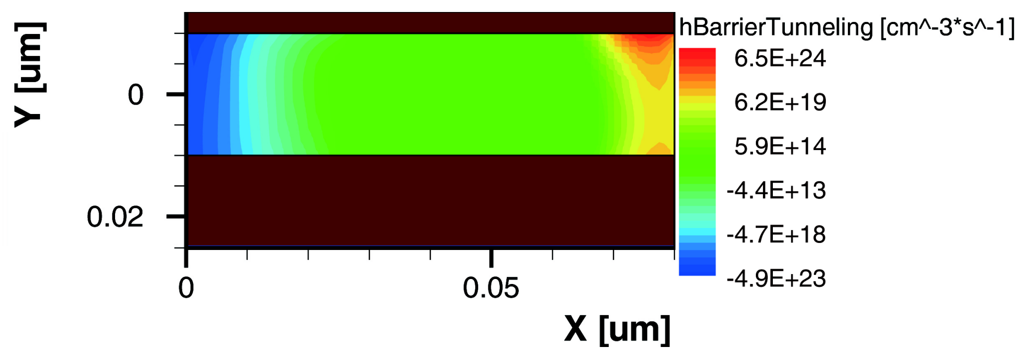

(b)

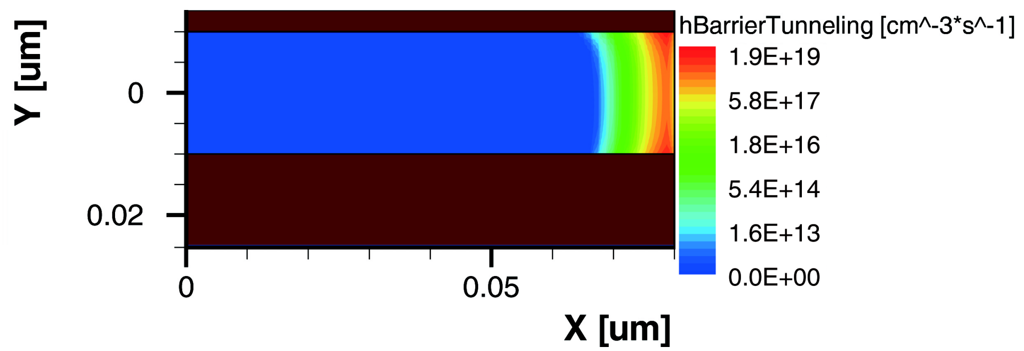

(c)

Figure 9.5.: Hole Tunneling Generation Rate in (a) at $V_{g,top}=-0.5\,V$, (b) at $V_{g,top}=0\,V$, (c) at $V_{g,top}=1\,V$. Device geometry: $l_{ch}=80\,nm$, $t_{ch}=20\,nm$, $t_{ox,top}=3.5\,nm$, $t_{ox,bottom}=100\,nm$. Bias conditions: $V_{ds}=1\,V$, $V_{g,bottom}=0\,V$.

UNIVERSITAT ROVIRA I VIRGILI
TWO-DIMENSIONAL ANALYTICAL PREDICTIVE MODELING OF SCHOTTKY BARRIER SOI AND MULTI-GATE MOSFETS
Mike Schwarz
Dipòsit Legal: T.456-2013

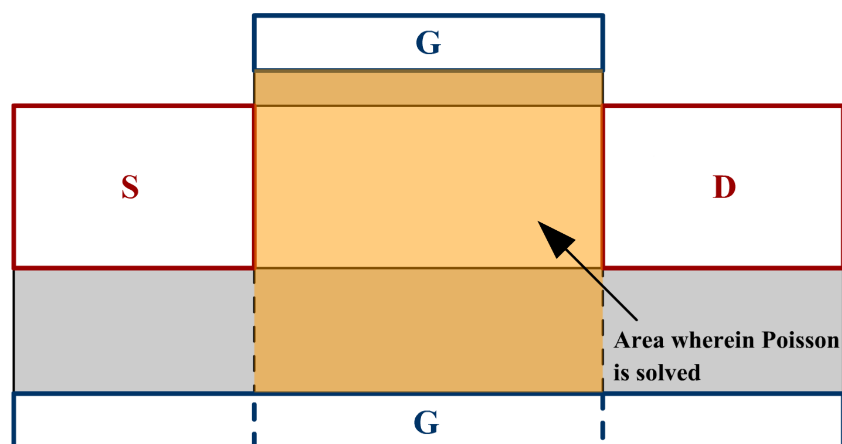

Figure 9.6.: General geometry of a SB-UTB-MOSFET.

For the case of a device with dopant segregation at the Schottky barrier a thin highly doped layer results a the junction which causes a strong band bending, indicated in Fig. 9.1 at the silicide-to-silicon interface. As a result the tunneling probability for the carriers is increased [194].

9.2. Area Definition, Boundary Conditions, Conformal Mapping & Simplifications

As for the Double-Gate device simplifications presented in chapter 4, also for the UTB MOSFET device the basic idea is to describe the device by a simple structure. In Fig. 9.6 the general structure of a SB-UTB-MOSFET is presented. By cutting out the orange shaded rectangle, the region of interest wherein Poisson's equation is solved in 2D, the assumed model structure of the SB-UTB-MOSFET device is shown with the coordinates and boundary conditions in Fig. 9.7. To keep mathematics simple, for the SB-UTB-MOSFET a two corner structure is used.

The applied boundary conditions for the case of a SB-DG-MOSFET was discussed in detail in section 4.3. Here, $V_{g,top}$ represents the top gate potential, and V_{fb} the flat band voltage while V_s and V_d describe the source and drain potentials. The built-in potential at source and drain contacts is represented by ϕ_{bi}. The bottom gate potential $V_{g,bottom}$ is applied to the vertical boundaries starting at a depth corresponding to the position of the bottom gate electrode in the original structure which is an approximation. In the oxides linear boundaries are applied [194].

The origin of the coordinates is set in the left top corner [194]. In the y-direction one has the distance l_{ch} on the top right corner while in x-direction the oxide is represented by the grey region with thickness $\tilde{t}_{ox,top}$. Then the channel begins with thickness t_{ch}

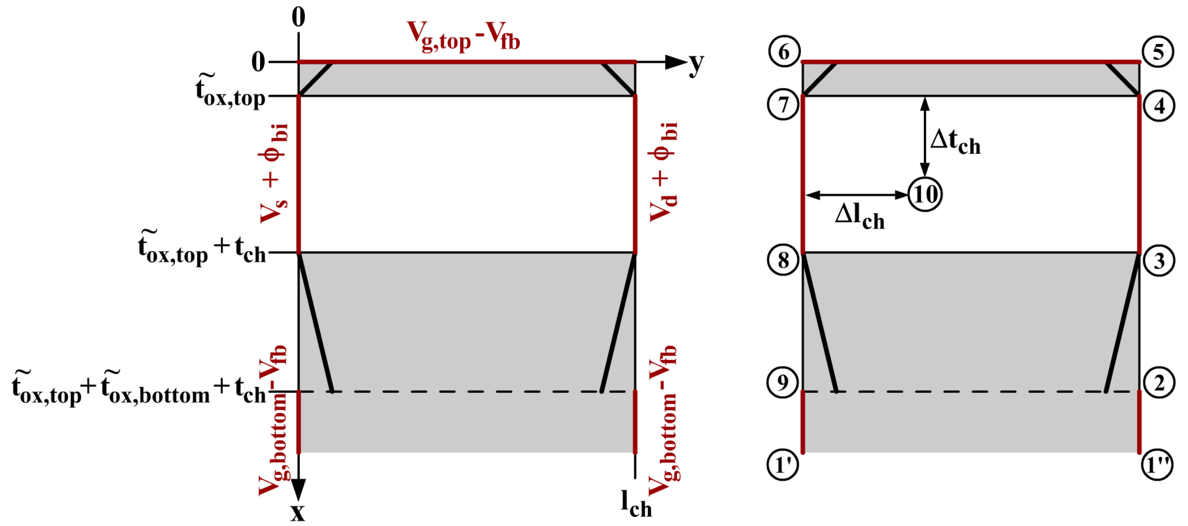

Figure 9.7.: Simplified geometry and definition of boundaries and conformal mapping coordinates of a SB-UTB-MOSFET.

and ends with distance $\tilde{t}_{ox,top} + t_{ch}$. With the oxide on the bottom one receives the distance $\tilde{t}_{ox,top} + \tilde{t}_{ox,bottom} + t_{ch}$. The parameters $\tilde{t}_{ox,bottom}$ and $\tilde{t}_{ox,top}$ are transformed oxide thicknesses which are described in detail in section 4.2.2

$$\tilde{t}_{ox,bottom} = \frac{\epsilon_{Si}}{\epsilon_{ox,bottom}} \cdot t_{ox,bottom},$$
$$\tilde{t}_{ox,top} = \frac{\epsilon_{Si}}{\epsilon_{ox,top}} \cdot t_{ox,top}. \tag{9.1}$$

Several important points along the boundary are defined. They will represent the integration boundaries for the closed-form solutions in equation (5.23), equation (5.25), and equation (5.59). The important points are mapped with equation (5.5), with $\Delta y = l_{ch}$. They represent the piecewise parts of the device, as shown in Fig. 9.7 [194].

Between ⓵'' and ② a constant boundary with the bias condition $V_{g,bottom} - V_{fb}$ prevails. From ② to ③ a linear boundary is applied. Between ③ and ④ we have again a constant boundary with the bias condition $V_d + \phi_{bi}$. As for ② to ③ also a linear boundary exists between ④ and ⑤. From ⑤ and ⑥ a constant boundary with the bias condition $V_{g,top} - V_{fb}$ is applied. A linear boundary exists between ⑥ and ⑦ while from ⑦ and ⑧ a constant boundary with the bias condition $V_s + \phi_{bi}$ prevails. Again, a linear boundary is applied between ⑧ to ⑨. The last boundary is applied from ⑨ to ①'; a constant boundary with the bias condition $V_{g,bottom} - V_{fb}$.

As described, the points ①'' and ①' lie in the infinite region. Considering the infinite for both points in the implementation, the distance in x-direction is set three times higher than, the end of the device, indicated with $\tilde{t}_{ox,bottom}$. This is considered in the following calculations for the important points ①'' and ①'.

$$\begin{aligned}
\overline{u}_{\textcircled{1"}} &= \cosh\left(\frac{\pi\left(\tilde{t}_{ox,top} + t_{ch} + 3\tilde{t}_{ox,bottom} + jl_{ch}\right)}{\Delta y}\right) \\
\overline{u}_{\textcircled{2}} &= \cosh\left(\frac{\pi\left(\tilde{t}_{ox,top} + t_{ch} + \tilde{t}_{ox,bottom} + jl_{ch}\right)}{\Delta y}\right) \\
\overline{u}_{\textcircled{3}} &= \cosh\left(\frac{\pi\left(\tilde{t}_{ox,top} + t_{ch} + jl_{ch}\right)}{\Delta y}\right) \\
\overline{u}_{\textcircled{4}} &= \cosh\left(\frac{\pi\left(\tilde{t}_{ox,top} + jl_{ch}\right)}{\Delta y}\right) \\
\overline{u}_{\textcircled{5}} &= \cosh\left(\frac{\pi\left(0 + jl_{ch}\right)}{\Delta y}\right) \\
\overline{u}_{\textcircled{6}} &= \cosh\left(\frac{\pi\left(0 + j0\right)}{\Delta y}\right) \\
\overline{u}_{\textcircled{7}} &= \cosh\left(\frac{\pi\left(\tilde{t}_{ox,top} + j0\right)}{\Delta y}\right) \\
\overline{u}_{\textcircled{8}} &= \cosh\left(\frac{\pi\left(\tilde{t}_{ox,top} + t_{ch} + j0\right)}{\Delta y}\right) \\
\overline{u}_{\textcircled{9}} &= \cosh\left(\frac{\pi\left(\tilde{t}_{ox,top} + t_{ch} + \tilde{t}_{ox,bottom} + j0\right)}{\Delta y}\right) \\
\overline{u}_{\textcircled{1'}} &= \cosh\left(\frac{\pi\left(\tilde{t}_{ox,top} + t_{ch} + 3\tilde{t}_{ox,bottom} + j0\right)}{\Delta y}\right)
\end{aligned} \tag{9.2}$$

The arbitrary point which represents the point on which the potential or electric field takes influence, is calculated by

$$w_{\textcircled{10}} = \cosh\left(\frac{\pi\left(\tilde{t}_{ox,top} + \Delta t_{ch} + j\Delta l_{ch}\right)}{\Delta y}\right). \tag{9.3}$$

9.3. Electrostatics

With all these preliminaries the electrostatics are solved with the approaches from section 5.3.2 and section 5.4.1 and within the model the non-effective Schottky barrier height ϕ_B included in the built-in potential of the boundary in equation (4.8) is used. For the electrostatic potential equation (5.23) and equation (5.25) and for the electric field equation (5.59) are used, respectively.

UNIVERSITAT ROVIRA I VIRGILI
TWO-DIMENSIONAL ANALYTICAL PREDICTIVE MODELING OF SCHOTTKY BARRIER SOI AND MULTI-GATE MOSFETS
Mike Schwarz
Dipòsit Legal: T.456-2013

9.3.1. Electrostatic Potential Solution

After mapping the defined important points, the solutions for each piece can be applied. In equation (5.23), equation (5.25) function values for the variable z are defined which describe the point of interest. They are inserted as transformed values w calculated from equation (9.3) where $\Delta y = l_{ch}$.

$\underline{\textcircled{1''} \rightarrow \textcircled{2}}$:

$$\varphi_{const}\left(w_{\textcircled{10}}, V_{g,bottom} - V_{fb}, \bar{u}_{\textcircled{1''}}, \bar{u}_{\textcircled{2}}\right) \tag{9.4}$$

$\underline{\textcircled{2} \rightarrow \textcircled{3}}$:

$$\begin{aligned} &\varphi_{const}\left(w_{\textcircled{10}}, V_{g,bottom} - V_{fb}, \bar{u}_{\textcircled{2}}, \bar{u}_{\textcircled{3}}\right) + \\ &\varphi_{lin}\left(w_{\textcircled{10}}, a, b, V_d + \phi_{bi} - V_{g,bottom} + V_{fb}, \bar{u}_{\textcircled{2}}, \bar{u}_{\textcircled{3}}\right) \end{aligned} \tag{9.5}$$

with

$$a = \frac{\bar{u}_{\textcircled{3}} - b}{\left(V_d + \phi_{bi} - V_{g,bottom} + V_{fb}\right)^2}$$

and

$$b = \bar{u}_{\textcircled{2}}$$

where equation (5.25) has to be positive for $V_d + \phi_{bi} \geq V_{g,bottom} - V_{fb}$ and negative for $V_d + \phi_{bi} < V_{g,bottom} - V_{fb}$.

$\underline{\textcircled{3} \rightarrow \textcircled{4}}$:

$$\varphi_{const}\left(w_{\textcircled{10}}, V_d + \phi_{bi}, \bar{u}_{\textcircled{3}}, \bar{u}_{\textcircled{4}}\right) \tag{9.6}$$

$\underline{\textcircled{4} \rightarrow \textcircled{5}}$:

$$\begin{aligned} &\varphi_{const}\left(w_{\textcircled{10}}, V_{g,top} - V_{fb}, \bar{u}_{\textcircled{4}}, \bar{u}_{\textcircled{5}}\right) + \\ &\varphi_{lin}\left(w_{\textcircled{10}}, a, b, V_d + \phi_{bi} - V_{g,top} + V_{fb}, \bar{u}_{\textcircled{4}}, \bar{u}_{\textcircled{5}}\right) \end{aligned} \tag{9.7}$$

with

$$a = \frac{\bar{u}_{\textcircled{4}} - b}{\left(V_d + \phi_{bi} - V_{g,top} + V_{fb}\right)^2}$$

and

$$b = \bar{u}_{\textcircled{5}}$$

where equation (5.25) has to be positive for $V_d + \phi_{bi} \geq V_{g,top} - V_{fb}$ and negative for $V_d + \phi_{bi} < V_{g,top} - V_{fb}$.

$\underline{\textcircled{5} \rightarrow \textcircled{6}}$:

$$\varphi_{const}\left(w_{\textcircled{10}}, V_{g,top} - V_{fb}, \bar{u}_{\textcircled{5}}, \bar{u}_{\textcircled{6}}\right) \tag{9.8}$$

$\underline{\textcircled{6} \rightarrow \textcircled{7}}$:

$$\begin{aligned} &\varphi_{\text{const}}\left(w_{\textcircled{10}}, V_{g,\text{top}} - V_{fb}, \overline{u}_{\textcircled{6}}, \overline{u}_{\textcircled{7}}\right) + \\ &\varphi_{\text{lin}}\left(w_{\textcircled{10}}, a, b, V_s + \phi_{bi} - V_{g,\text{top}} + V_{fb}, \overline{u}_{\textcircled{6}}, \overline{u}_{\textcircled{7}}\right) \end{aligned} \tag{9.9}$$

with

$$a = \frac{\overline{u}_{\textcircled{7}} - b}{\left(V_s + \phi_{bi} - V_{g,\text{top}} + V_{fb}\right)^2}$$

and

$$b = \overline{u}_{\textcircled{6}}$$

where equation (5.25) has to be positive for $V_s + \phi_{bi} \geq V_{g,\text{top}} - V_{fb}$ and negative for $V_s + \phi_{bi} < V_{g,\text{top}} - V_{fb}$.

$\underline{\textcircled{7} \rightarrow \textcircled{8}}$:

$$\varphi_{\text{const}}\left(w_{\textcircled{10}}, V_s + \phi_{bi}, \overline{u}_{\textcircled{7}}, \overline{u}_{\textcircled{8}}\right) \tag{9.10}$$

$\underline{\textcircled{8} \rightarrow \textcircled{9}}$:

$$\begin{aligned} &\varphi_{\text{const}}\left(w_{\textcircled{10}}, V_{g,\text{bottom}} - V_{fb}, \overline{u}_{\textcircled{8}}, \overline{u}_{\textcircled{9}}\right) + \\ &\varphi_{\text{lin}}\left(w_{\textcircled{10}}, a, b, V_s + \phi_{bi} - V_{g,\text{bottom}} + V_{fb}, \overline{u}_{\textcircled{8}}, \overline{u}_{\textcircled{9}}\right) \end{aligned} \tag{9.11}$$

with

$$a = \frac{\overline{u}_{\textcircled{8}} - b}{\left(V_s + \phi_{bi} - V_{g,\text{bottom}} + V_{fb}\right)^2}$$

and

$$b = \overline{u}_{\textcircled{9}}$$

where equation (5.25) has to be positive for $V_s + \phi_{bi} \geq V_{g,\text{bottom}} - V_{fb}$ and negative for $V_s + \phi_{bi} < V_{g,\text{bottom}} - V_{fb}$.

$\underline{\textcircled{9} \rightarrow \textcircled{1'}}$:

$$\varphi_{\text{const}}\left(w_{\textcircled{10}}, V_{g,\text{bottom}} - V_{fb}, \overline{u}_{\textcircled{9}}, \overline{u}_{\textcircled{1'}}\right) \tag{9.12}$$

After the calculation of the piecewise solutions a simple superposition of all components is necessary to predict the overall influence on one specific point in the entire channel region of the device. An interior point (x, y) from the complex z-plane is transformed with the help of equation (9.3) onto the upper half of the complex w-plane. Afterwards, the point $w_{\textcircled{10}}$, a point (u, v) is used to calculate the influence of the piecewise solutions on the electrostatic potential at the corresponding point (x, y). It follows

$$\begin{aligned} \varphi(x, y) = &\varphi_{\text{const},\textcircled{1''}\rightarrow\textcircled{2}+\textcircled{2}\rightarrow\textcircled{3}+\textcircled{3}\rightarrow\textcircled{4}+\textcircled{4}\rightarrow\textcircled{5}+\textcircled{5}\rightarrow\textcircled{6}+\textcircled{6}\rightarrow\textcircled{7}+\textcircled{7}\rightarrow\textcircled{8}+\textcircled{8}\rightarrow\textcircled{9}+\textcircled{9}\rightarrow\textcircled{1'}}(x, y) + \\ &\varphi_{\text{lin},\textcircled{2}\rightarrow\textcircled{3}+\textcircled{4}\rightarrow\textcircled{5}+\textcircled{6}\rightarrow\textcircled{7}+\textcircled{8}\rightarrow\textcircled{9}}(x, y). \end{aligned} \tag{9.13}$$

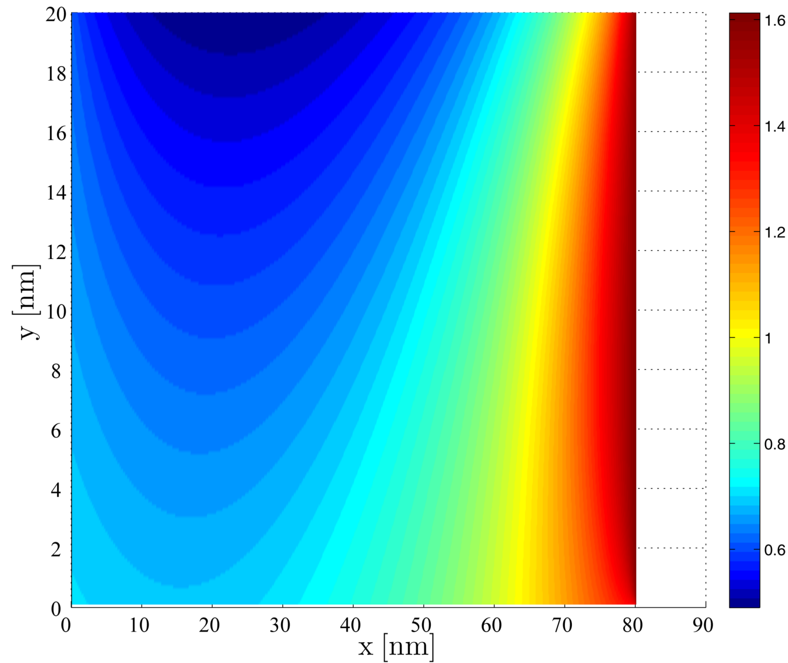

Figure 9.8.: Electrostatic potential φ for a SB-UTB-MOSFET. Results for ϕ_{Bn}=0.6 eV. Device geometry: l_{ch}=80 nm, t_{ch}=20 nm, $t_{ox,top}$=3.5 nm, $t_{ox,bottom}$=100 nm. Bias conditions: V_{ds}=1 V, $V_{g,top}$=−0.5 V, $V_{g,bottom}$=0 V.

From the closed-form solutions of $\varphi(x, y)$ the following results for the electrostatics in a SB-UTB-MOSFET device was calculated. In Fig. 9.8 the electrostatic potential is illustrated [194]. If one compares the potential from Fig. 9.8 with the corresponding simulated potential of TCAD from Fig. 9.2(a) a difference between both solutions can be observed. Especially, at the source junction close to the bottom silicon-to-oxide interface a huge difference between the simulated electrostatic potential of TCAD Sentaurus and the estimated one of the model can be observed [194].

This inaccuracy results from three approximations. The first is neglecting the fringing fields while the structure is simplified as shown in Fig. 9.7. Therefore, the gradient of the potential close to the bottom oxide is influenced and predicted not accurately enough. In general, this influence is low compared to the following approximations [194].

The second reason for the inaccuracy is the transformed oxide in equation (9.1) for the simplification of the conformal mapping technique. Applying the transformed oxide thickness results in an inaccuracy for thick oxides.

The third and last inaccuracy occurs from an analytical approximation of the square root approximation in section 5.3.2 for the case of linear boundary conditions [194].

The influences resulting from all these approximations depend on the gradient of the potential at the bottom oxide. This can be improved by introducing an empirical fitting

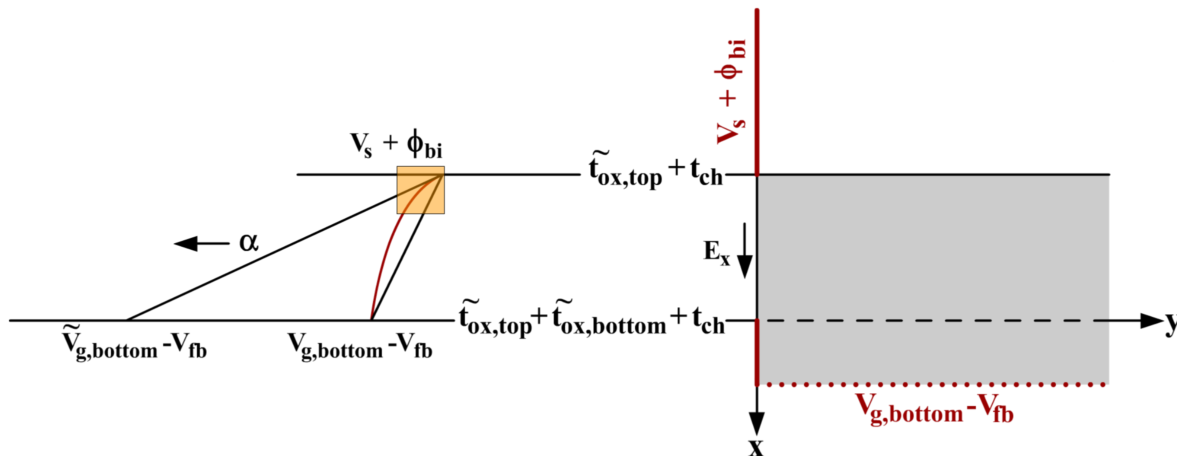

Figure 9.9.: Empirical fitting parameter α corrects the inaccuracy in the gradient and leads to a modified boundary $\tilde{V}_{g,bottom}$. The red curve illustrates the correct boundary as it results from TCAD simulations including fringing fields.

parameter α which modifies the gradient of the potential along the boundary in the oxide and therefore the electrostatic potential, see Fig. 9.9 [194].

It is very important to correct this influence, otherwise the thermionic emission current which is mainly concentrated close to the bottom oxide, saturates too early in the $I_d - V_g$ curve due to the wrong potential. The effect of this behavior on the tunneling currents is of minor interest, because they are mainly concentrated underneath the top oxide where the prediction is accurate [194].

In Figure 9.9, the orange shaded rectangle area shows the region of interest where the most influence from the inaccuracy results. Here, the aim to correct the boundary in the bottom oxide with the empirical fitting parameter which finally leads to a corrected gradient of the potential [194].

Therefore, for the modified boundary condition [194] follows

$$\tilde{V}_{g,bottom} = V_s + \phi_{bi} - \tilde{t}_{ox,bottom} \cdot \tilde{E}_x \tag{9.14}$$

with

$$\tilde{E}_x = \alpha \cdot \frac{V_s + \phi_{bi} - (V_{g,bottom} - V_{fb})}{\tilde{t}_{ox,bottom}}. \tag{9.15}$$

By consideration of the empirical fitting parameter α as in Fig. 9.9, the electrostatic potential results in Fig. 9.10. Comparing the new result with the electrostatic potential from the TCAD Sentaurus simulation in Fig. 9.2(a), one can observe an improvement in the prediction of the potential.

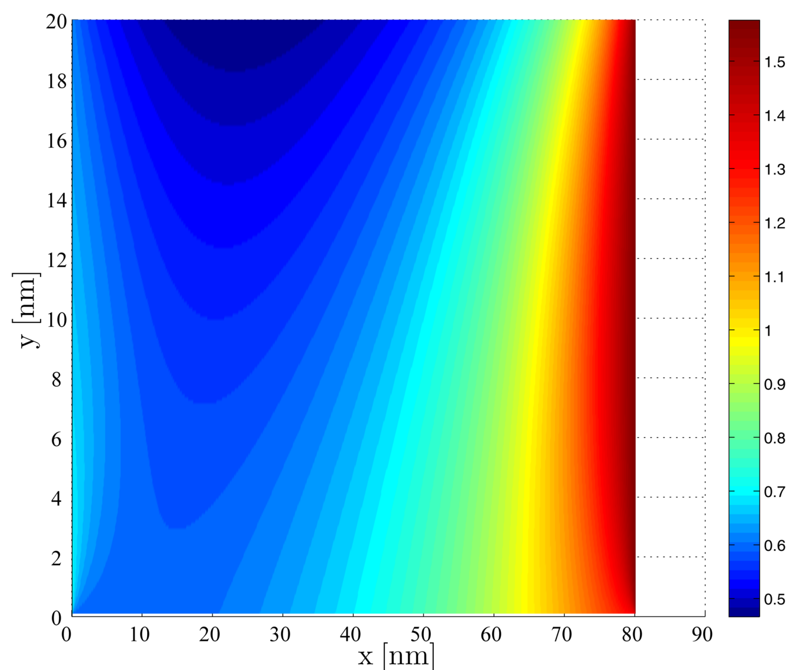

Figure 9.10.: Corrected electrostatic potential φ for a SB-UTB-MOSFET. Results for ϕ_{Bn}=0.6 eV. Device geometry: l_{ch}=80 nm, t_{ch}=20 nm, $t_{ox,top}$=3.5 nm, $t_{ox,bottom}$=100 nm. Bias conditions: V_{ds}=1 V, $V_{g,top}$=−0.5 V, $V_{g,bottom}$=0 V.

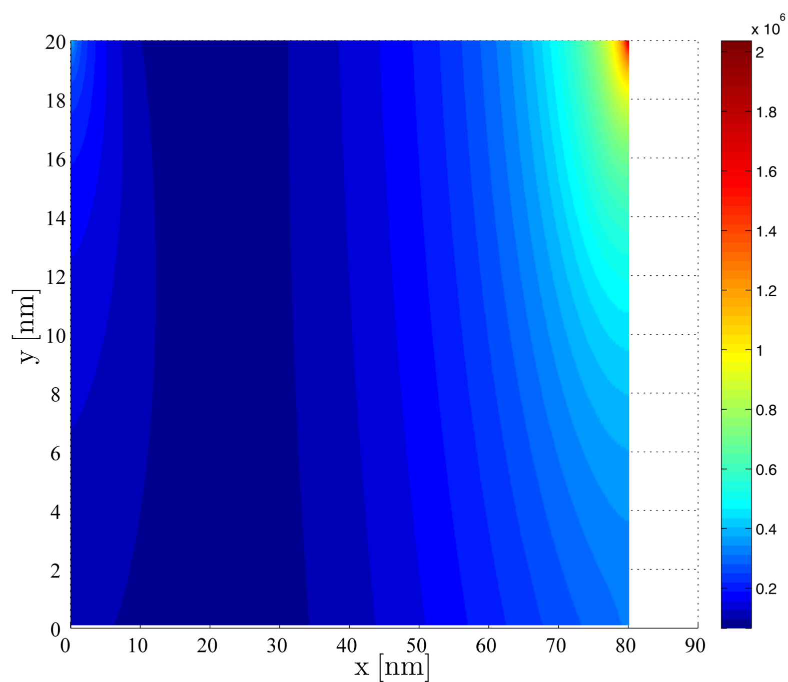

Figure 9.11.: Electric field |E| for a SB-UTB-MOSFET. Results for ϕ_{Bn}=0.6 eV. Device geometry: l_{ch}=80 nm, t_{ch}=20 nm, $t_{ox,top}$=3.5 nm, $t_{ox,bottom}$=100 nm. Bias conditions: V_{ds}=1 V, $V_{g,top}$=−0.5 V, $V_{g,bottom}$=0 V.

9.3.2. Electric Field Solution

After mapping the defined important points, the solutions for each piece can be applied. In equation (5.58) function values for the variable z are defined which describe the point of interest. They are inserted as transformed values w calculated from equation (5.5) where $\Delta y = l_{ch}$.

$\underline{②\rightarrow③}$:

$$\underline{E}\left(w_{⑩}, E_x, \bar{u}_{②}, \bar{u}_{③}\right) \tag{9.16}$$

with

$$E_x = -\frac{V_{g,bottom} - V_{fb} - (V_d + \phi_{bi})}{\tilde{t}_{ox,bottom}}.$$

$\underline{④\rightarrow⑤}$:

$$\underline{E}\left(w_{⑩}, E_x, \bar{u}_{④}, \bar{u}_{⑤}\right) \tag{9.17}$$

with

$$E_x = \frac{V_{g,top} - V_{fb} - (V_d + \phi_{bi})}{\tilde{t}_{ox,top}}.$$

$\underline{⑥\rightarrow⑦}$:

$$\underline{E}\left(w_{⑩}, E_x, \bar{u}_{⑥}, \bar{u}_{⑦}\right) \tag{9.18}$$

with

$$E_x = \frac{V_{g,top} - V_{fb} - (V_s + \phi_{bi})}{\tilde{t}_{ox,top}}.$$

$\underline{⑧\rightarrow⑨}$:

$$\underline{E}\left(w_{⑩}, E_x, \bar{u}_{⑧}, \bar{u}_{⑨}\right) \tag{9.19}$$

with

$$E_x = -\frac{V_{g,bottom} - V_{fb} - (V_s + \phi_{bi})}{\tilde{t}_{ox,bottom}}.$$

Finally, after the calculation of the piecewise parts a superposition takes place to predict the overall influence on one specific point in the entire channel region of the device. An interior point (x, y) from the complex z-plane is transformed with the help of equation (9.3) onto the upper half of the complex w-plane. Afterwards, the point $w_{⑩}$, a point (u, v) is used to calculate the influence of the piecewise solutions on the electric field at the corresponding point (x, y). It follows

$$\underline{E}(x, y) = \underline{E}_{②\rightarrow③}(x, y) + \underline{E}_{④\rightarrow⑤}(x, y) + \underline{E}_{⑥\rightarrow⑦}(x, y) + \underline{E}_{⑧\rightarrow⑨}(x, y). \tag{9.20}$$

Table 9.2.: Device model parameters for a drawn channel length l_{ch}=80 nm.

Structural	l_{ch}	60	[nm]	effect. channel length
	t_{ch}	20	[nm]	channel thickness
	$t_{ox,top}$	3.5	[nm]	top oxide thickness
	$t_{ox,bottom}$	100	[nm]	bottom oxide thickness
Mobility	μ_{n0}	11.0	[cm^2/Vs]	elec. tunneling mobility
	μ_{p0}	1.0	[cm^2/Vs]	hole tunneling mobility
	Θ	0.8	[-]	transverse field dependency
Misc	N_B	10^{15}	[cm^{-3}]	substrate doping
	V_{fb}	-0.56	[V]	flatband voltage
	ϕ_{bi}	0.56	[V]	built-in potential s/d
	$\phi_{Bn,eff}$	0.15	[eV]	effect. SBH electrons
	ϕ_{Bn}	0.6	[eV]	SBH electrons
	A_n^*	62	[A/cm^{2}K^2]	elec. Richardson constant
	A_p^*	32	[A/cm^{2}K^2]	hole Richardson constant
	m_n	0.28	[-]	elec. effect. mass
	m_p	0.30	[-]	hole effect. mass
	α	1.8	[-]	gradient correction parameter

From the closed-form solutions of $\underline{E}(x, y)$ the following result for the electric field in a SB-UTB-MOSFET device was calculated. In Fig. 9.11 the electric field is given. If one compares the prediction with the electric field from TCAD Sentaurus in Fig. 9.3(a), it can be observed that the prediction is in a good agreement with the TCAD simulation results. In contrast to the electrostatic potential the solution of the electric field is solved without the need of an analytical approximation.

9.4. Currents

The currents are calculated with the above corrected solution for the electrostatics and the ANMA approach from chapter 6. The effect of dopant segregation will be accounted for by an effective Schottky barrier height $\phi_{B,eff}$. This height has to be used for the calculation of the tunneling and thermionic current [194].

In equation (6.12) a drift-diffusion mechanism affects the tunneling current via electron effective mobility μ_n. Furthermore, in the tunneling current density model equation (6.11) the mobility degradation is taken into account as in [88]. Thus, the effective mobility may be expressed by formula (9.21) [194]

$$\mu_n = \frac{\mu_{n0}}{1 + \Theta(V_{g,top} - \phi(l_{ch}/2))} \tag{9.21}$$

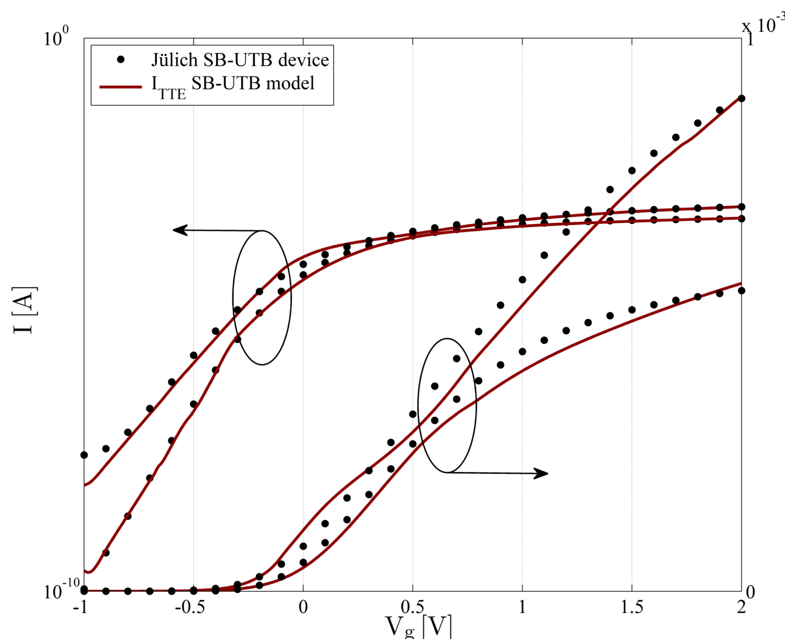

Figure 9.12.: $I_d - V_g$ current I_{TTE} vs. measurement data of the Jülich SB-UTB-MOSFET in log-scale and lin-scale. Results for $\phi_{Bn,eff}$=0.15 eV. Device geometry: l_{ch}=80 nm, t_{ch}=20 nm, $t_{ox,top}$=3.5 nm, $t_{ox,bottom}$=100 nm. Bias conditions: V_{ds}=0.5 V and 1 V, $V_{g,top}$=−1 V to 2 V, $V_{g,bottom}$=0 V.

where Θ is the mobility degradation coefficient and treated as adjusting parameter, $V_{g,top}$ the gate potential and $\phi(l_{ch}/2)$ the channel potential in the middle of the device.

Finally, a smoothing as presented in [195] from the linear to saturation region is applied.

9.5. Results

With the previously explained modeling approach the model is compared with the I_d-V_g measurement data for a SB-UTB-MOSFET device from Jülich [101] in log-scale and lin-scale, as shown in Fig. 9.12. The used model parameters are listed in Table 9.2. As one can observe the model predicts the measured device characteristics quite well. The slope is reproduced accurately and for high V_{ds} a good agreement can be observed. Nevertheless, some inaccuracies exist at close to the V_g=0 V range [194].

These inaccuracies result from the transition between the thermionic and tunneling current and requires further improvements in the smoothing of the model equations. However, the model is able to estimate the behavior of real measurement data for a SB-UTB-MOSFET and is in a good agreement over a large range [194].

UNIVERSITAT ROVIRA I VIRGILI
TWO-DIMENSIONAL ANALYTICAL PREDICTIVE MODELING OF SCHOTTKY BARRIER SOI AND MULTI-GATE MOSFETS
Mike Schwarz
Dipòsit Legal: T.456-2013

9.6. Conclusion

Within this chapter the analytical numerical modeling approach from chapter 6 was applied onto the device structure of a SB-UTB-MOSFET device with dopant segregation. Adapting the electrostatics of chapter 5 and applying the framework on the device structure of a SB-UTB-MOSFET device the tunneling and thermionic currents was calculated.

The analytical current calculations of the $I_d - V_g$ curves show a very good agreement for a comparison with measurement data for the SB-UTB device with a channel length of 80 nm. The result shows that the model is also able to predict the current well compared to real measurements.

However, an empirical parameter had to be introduced to correct the potential at the BOx due to resulting inaccuracy from the piecewise linear solution of the modeling framework. By introducing the empirical parameter a gradient correction of the potential at the BOx results in a correctly predicted thermionic current. If an alternative asymmetrical model is used for the electrostatics, a similar behavior is observed. The current model description predicts the behavior accurately, but is dependent on the accuracy of the electrostatics.

The model is able to predict the current compared to measurements while the approach in particular inherently includes 2D effects on the device current.

UNIVERSITAT ROVIRA I VIRGILI
TWO-DIMENSIONAL ANALYTICAL PREDICTIVE MODELING OF SCHOTTKY BARRIER SOI AND MULTI-GATE MOSFETS
Mike Schwarz
Dipòsit Legal: T.456-2013

Chapter 10.

Conclusion

In the dissertation a package of modeling equations has been developed in order to allow a structure depending description of Schottky barrier Double-Gate MOSFETs with channel lengths down to 22 nm. With a close relationship to the valid physical principal equations in the Schottky barrier Double-Gate transistor and their analytic solution, it could be achieved that the necessary model parameters are given by the process and layout data of the device or at least with a physical relation. Therefore, the relation to the device physics is kept, even for the complexity of the models.

Furthermore, it has been the aim to develop a compact model with explicit modeling equations for further implementations in HDL languages, e.g. Verilog-A. With these compact equations an implementation in a circuit simulator might be possible, because circuit simulators need compact models to estimate the circuit behavior very quickly. Due to this circumstance the aim of a compact model should be to predict the device current in a numerically efficient way compared to finite element methods (FEM) while the complexity of compact models is less.

10.1. Summary

The model development based on a convenient two-dimensional analytical solution obtained using the conformal mapping technique, allows the prediction of the potential distribution and the derivation of model equations which consider short-channel effects.

Within the dissertation fully 2D analytical closed-form solutions for the electrostatics considering 2D effects for channel lengths down to 22 nm have been presented. They are valid for the subthreshold operation region and do not introduce any kind of fitting parameters. All parameters depend on geometry and boundary conditions. The electrostatics show a very good agreement for a comparison with TCAD simulation data for a large range of device biasing, several barrier heights and geometries. Nevertheless, if quantum effects are considered, the 2D analytical closed-form solutions are able to predict the electrostatics for channel lengths below 22 nm for reasonable device geometries.

Based on the 2D analytical closed-form solutions for the electrostatics an analytical numerical modeling approach for the currents has been developed. Instead of solving the device currents with respect to the energy an approach depending on the device coordinates was used for the solving. The WKB approximation, with its less complexity and accuracy, has been used to estimate the tunneling probability for the charge carriers. Furthermore, drift-diffusion effects onto the tunneling current have been taken into account. The analytical numerical current calculations of the $I_d - V_g$ curves show a very good agreement for a comparison with TCAD simulation data. No fitting parameters have been introduced in the modeling approach.

Further 2D analyses of several current contributions as well as the current densities have given an idea of the physical behavior and the primary contributions which have to be taken into account for a closed-form model. From the 2D analyses a Gaussian-like shaped tunneling generation with a concentration in the device corners and a parabolic shape of the density in log-scale results for the tunneling current. The thermionic emission is approximated from the 2D analyses by a current in accumulation with its density concentration in the device middle while in inversion a constant density concentration is observed. In accumulation a parabolic shape of the thermionic current density in log-scale with a negligible thermionic emission for holes is observed.

With the investigation of the essential current contributions a closed-form model for the tunneling and thermionic current is derived. Based on the analyses analytical approximations have been introduced which are able to describe the primary contributions. These analytical approximations can be solved by explicit closed-form equations. Furthermore, the parabolic shape of the current densities for the tunneling and thermionic emission have been solved by an explicit closed-form equation. The analytical closed-form current calculations of the $I_d - V_g$ curves show a very good agreement for a comparison with TCAD simulation data and the analytical numerical modeling approach. Furthermore, no fitting parameters have been introduced in the closed-form modeling approach. The model parameters, e.g. charge carrier masses, tunneling mobility and Richardson constant have to be adjusted in a small range compared to the numerical modeling approach due to the approximations in the analytical equations.

Besides the accurate prediction of the current a further advantage of the analytical closed-form model is the need of at least twelve points for the current calculation at which the analytical solution of the potential and/or the electric field has to be evaluated: six points for the source related case and six points for the drain related case. In terms of computation efficiency, memory consumption, and complexity of the closed-form solution or rather "compact model" is more efficient compared to finite element methods (FEM) which is suitable for circuit simulators. In terms of accuracy, of course the "compact model" is not comparable to finite element methods (FEM) simulators.

UNIVERSITAT ROVIRA I VIRGILI
TWO-DIMENSIONAL ANALYTICAL PREDICTIVE MODELING OF SCHOTTKY BARRIER SOI AND MULTI-GATE MOSFETS
Mike Schwarz
Dipòsit Legal: T.456-2013

For the first time ever, an analytical closed-form model for Schottky barrier Double-Gate MOSFET devices has been demonstrated which is able to calculate the current contributions in a Schottky barrier Double-Gate MOSFET for channel lengths down to 22 nm. Furthermore, for the first time ever, an idea to handle the occurring drift-diffusion effects of the $I_d - V_{ds}$ curves have been given by the introduction of a macro model. Considering the drift-diffusion effects in the $I_d - V_{ds}$ curves, a good agreement for a comparison with TCAD simulation data can be observed.

Finally, the analytical numerical modeling approach was compared with measurement data of a SB-UTB-MOSFET device with dopant segregation. The analytical current calculations of the $I_d - V_g$ curves show a very good agreement for a comparison with measurement data for the SB-UTB device with a channel length of 80 nm. The result indicates that the model is even able to predict the current well compared to real measurements. However, for the measurement comparison it was necessary to introduce an empirical parameter to correct the potential at the BOx due to an inaccuracy in the potential solution for UTB devices. Nevertheless, the model is able to predict the current compared to measurements and in particular inherently includes 2D effects on the device current.

10.2. Future Research Prospects

Further work on the topics presented in this dissertation fall into various subjects which have to be taken into account for improvement of the model. These are including charges for inversion, the Schottky barrier lowering effect, enhancement of the introduced macro model, development of an "explicit" equation for the estimation x_{E_f}, a Verilog-A implementation, ballistic transport mechanism, and quantum confinement.

Concerning charges in the operation region of inversion for the electrostatics, will improve the estimation of the electrostatic potential and the electric field for a higher bias range. Furthermore, the behavior above subthreshold region should be improved, if the charges which "pin" the electrostatic potential, are taken into account. Therefore, the prediction of the tunneling current which is strongly influenced by the electrostatic potential and the electric field, will result in an improvement.

In particular the Schottky barrier lowering effect will improve the predicted model current for the higher bias conditions. Here, the corresponding electric field for the image force might be significantly high and the amount of the lowering effect on the Schottky barrier is not negligible. This results especially in the higher bias conditions in an increased tunneling current due to the increased tunneling probability for the charge carriers. Therefore, including the Schottky barrier lowering will result in adjusted model parameters as masses or tunneling mobility.

UNIVERSITAT ROVIRA I VIRGILI
TWO-DIMENSIONAL ANALYTICAL PREDICTIVE MODELING OF SCHOTTKY BARRIER SOI AND MULTI-GATE MOSFETS
Mike Schwarz
Dipòsit Legal: T.456-2013

Furthermore, as already discussed, an improvement of the introduced macro model is necessary to enhance the output characteristics of the model. Also the equation for the transistor in series which describes the channel behavior, has to be improved. Here, by using a more complex equation, an improvement is to be expected.

With regard to a compact model the development of an efficient equation for the estimation of x_{E_f} is desirable. In the dissertation a method to predict x_{E_f} is explained which might be sufficient enough for the implementation in a circuit simulator. Nevertheless, an explicit description without numerical calculations would be preferred for further implementations. Besides the search of an efficient equation for the estimation of x_{E_f} a further improvement of the parabolic current approximation is necessary, especially for the lower gate biases. Here, a linear or an exponential approximation function for the current density might improve the results.

However, a HDL implementation of the model with relation for further investigations and analyses might be the next step. For example a Verilog-A version of the model might offer further steps for the improvement of the model. Nevertheless, in case of computation time, memory consumption, etc. a HDL implementation indicates a step forward.

Finally, considering state-of-the-art effects like ballistic transport and/or quantum confinement will improve the model especially for channel lengths in the sub-22 nm scale.

10.3. Conclusions

The model developed during the dissertation has shown in analyses that a "compact" current prediction of Schottky Barrier SOI and Multi-Gate MOSFETs including essential two-dimensional effects is possible.

With the developed electrostatics and closed-from current models it was shown for various geometries and boundary conditions that an accurate current calculation of Schottky barrier devices succeeds. This was prototypically shown on the basis of numerous analyses.

The model might be suitable for the implementation in a circuit simulator. With concentration of the primary current contributions and effects in Schottky barrier devices the above described tasks were fulfilled and satisfied - especially, in terms of a significant decreased computation time compared to finite element methods (FEM) simulators.

This is a crucial criterion for circuit simulators, because less computation time of one transistor results in less computation time of a large circuit with millions of transistors. With less computation time of a circuit one receives faster results, therefore a decreased amount of development costs.

UNIVERSITAT ROVIRA I VIRGILI
TWO-DIMENSIONAL ANALYTICAL PREDICTIVE MODELING OF SCHOTTKY BARRIER SOI AND MULTI-GATE MOSFETS
Mike Schwarz
Dipòsit Legal: T.456-2013

Besides the development of the model a huge knowledge transfer within the research group has been achieved. New knowledge about metal-semiconductor junctions, the physics behind and of course the knowledge how to model these effects "compact" was won. All these resources can be used for further research, e.g. analytical modeling of other emerging devices as Tunnel-FETs.

UNIVERSITAT ROVIRA I VIRGILI
TWO-DIMENSIONAL ANALYTICAL PREDICTIVE MODELING OF SCHOTTKY BARRIER SOI AND MULTI-GATE MOSFETS
Mike Schwarz
Dipòsit Legal: T.456-2013

A. The Quantum Mechanical Tunneling Effect

A.1. Infinite Potential Well

First infinite potential wells are investigated. The potential wells are impenetrable, therefore the following boundary condition is defined

$$\psi\left(-\frac{\mathrm{L}}{2}\right) = \psi\left(\frac{\mathrm{L}}{2}\right) = 0. \tag{A.1}$$

With equation (2.7)

$$-\frac{\hbar^2}{2\mathrm{m}} \cdot \frac{\partial^2 \psi(\mathrm{z})}{\partial \mathrm{z}^2} + \mathrm{V}(\mathrm{z}) \cdot \psi(\mathrm{z}) = \xi \cdot \psi(\mathrm{z}) \tag{A.2}$$

follows for the solution in the interval $|\mathrm{z}| > \frac{\mathrm{L}}{2}$

$$\mathrm{V}(\mathrm{z}) = 0. \tag{A.3}$$

The solution in the interval $|\mathrm{z}| < \frac{\mathrm{L}}{2}$ with $\mathrm{V}(\mathrm{z}) = 0$ results in

$$-\frac{\hbar^2}{2\mathrm{m}} \cdot \frac{\partial^2 \psi(\mathrm{z})}{\partial \mathrm{z}^2} - \xi \cdot \psi(\mathrm{z}) = 0. \tag{A.4}$$

With the characteristic polynomial

$$-\frac{\hbar^2}{2\mathrm{m}} \cdot \kappa^2 - \xi = 0 \tag{A.5}$$

and $-\frac{2\mathrm{m}\xi}{\hbar^2} = \kappa^2$ with $\mathrm{k} = \sqrt{\frac{2\mathrm{m}\xi}{\hbar^2}}$ follows

$$\kappa = \pm \mathrm{j}\sqrt{\frac{2\mathrm{m}\xi}{\hbar^2}} = \pm \mathrm{jk}. \tag{A.6}$$

The general solution of the homogeneous partial differential equation

$$\psi(\mathrm{z}) = \mathrm{A}_1 \exp(\mathrm{jkz}) + \mathrm{A}_2 \exp(-\mathrm{jkz}) \tag{A.7}$$

is used and the boundary conditions are insert, it follows

$$\psi\left(\frac{\mathrm{L}}{2}\right) = \mathrm{A}_1 \exp\left(\mathrm{jk}\frac{\mathrm{L}}{2}\right) + \mathrm{A}_2 \exp\left(-\mathrm{jk}\frac{\mathrm{L}}{2}\right) = 0, \tag{A.8}$$

$$\psi\left(-\frac{L}{2}\right) = A_1 \exp\left(-jk\frac{L}{2}\right) + A_2 \exp\left(jk\frac{L}{2}\right) = 0. \tag{A.9}$$

From equation (A.8) follows

$$A_1 = -A_2 \exp\left(-jk\frac{L}{2}\right) \cdot \exp\left(-jk\frac{L}{2}\right) = -A_2 \exp\left(-jkL\right) \tag{A.10}$$

and insert in equation (A.9)

$$A_2\left(\exp\left(jk\frac{L}{2}\right) - \exp\left(-jk\frac{3}{2}L\right)\right) = 0. \tag{A.11}$$

Equation (A.11) results in $A_2 = 0$, no electrons are available. Alternatively, it follows

$$\exp\left(jk\frac{L}{2}\right) - \exp\left(-jk\frac{3}{2}L\right) = \exp\left(-jk\frac{L}{2}\right) \cdot 2\sin(kL) = 0. \tag{A.12}$$

From the roots of sin(kL) are $kL = n\pi$ with $n = 1, 2, 3, ...$ follows the Eigenvalues

$$k_n = \frac{n\pi}{L}. \tag{A.13}$$

Eigenvalues are allowed energy states. It follows

$$\xi_n = \frac{p_n^2}{2m} = \frac{(\hbar k_n)^2}{2m} = \frac{\hbar^2\pi^2 n^2}{2mL^2}. \tag{A.14}$$

Then the allowed energy states for $n = 1, 2, 3, ...$ are

$$\xi_1 = \frac{\hbar^2\pi^2}{2mL^2}, \tag{A.15}$$

$$\xi_2 = \frac{4\hbar^2\pi^2}{2mL^2} = 4\xi_1, \tag{A.16}$$

$$\xi_3 = 9\xi_1. \tag{A.17}$$

For ξ_1 follows with $k_1 = \frac{\pi}{L}$

$$\psi_1(z) = A_1 \exp(jk_1 z) + A_2 \exp(-jk_1 z) \tag{A.18}$$

$$\psi_1\left(\frac{L}{2}\right) = 0 = A_1 \exp\left(j\frac{\pi}{2}\right) + A_2 \exp\left(-j\frac{\pi}{2}\right) = A_1 \cdot j + A_2 \cdot (-j). \tag{A.19}$$

If $A_1 = A_2 \rightarrow A$ it follows

$$\psi_1(z) = A(\exp(jk_1 z) + \exp(-jk_1 z)) = 2A\cos(k_1 z). \tag{A.20}$$

With the normalization follows

$$\int_{-\frac{L}{2}}^{+\frac{L}{2}} |\psi(x,t)|^2 \, dx = 2\,|A|^2\, L = 1, \tag{A.21}$$

UNIVERSITAT ROVIRA I VIRGILI
TWO-DIMENSIONAL ANALYTICAL PREDICTIVE MODELING OF SCHOTTKY BARRIER SOI AND MULTI-GATE MOSFETS
Mike Schwarz
Dipòsit Legal: T.456-2013

and results in

$$|\mathrm{A}| = \sqrt{\frac{1}{2\mathrm{L}}}. \tag{A.22}$$

Then with $\mathrm{k}_1 = \frac{\pi}{\mathrm{L}}$

$$\psi_1(\mathrm{z}) = \sqrt{\frac{2}{\mathrm{L}}}\cos(\mathrm{k}_1\mathrm{z}). \tag{A.23}$$

A.2. Finite Potential Well

Secondly, finite potential wells are investigated. The potential wells are penetrable, therefore the following boundary condition defined

$$\psi\left(-\frac{\mathrm{L}}{2}\right) = \psi\left(\frac{\mathrm{L}}{2}\right) = 0. \tag{A.24}$$

With equation (2.7)

$$-\frac{\hbar^2}{2\mathrm{m}} \cdot \frac{\partial^2\psi(\mathrm{z})}{\partial \mathrm{z}^2} + \mathrm{V}(\mathrm{z}) \cdot \psi(\mathrm{z}) = \xi \cdot \psi(\mathrm{z}) \tag{A.25}$$

follows for the solution in the interval $|\mathrm{z}| > \mathrm{L}/2$

$$\mathrm{V}(\mathrm{z}) = \mathrm{V}_\mathrm{b}. \tag{A.26}$$

The solution in the interval $|\mathrm{z}| < \mathrm{L}/2$ with $\mathrm{V}(\mathrm{z}) = 0$ results in

$$-\frac{\hbar^2}{2\mathrm{m}} \cdot \frac{\partial^2\psi(\mathrm{z})}{\partial \mathrm{z}^2} + (\mathrm{V}_\mathrm{b} - \xi) \cdot \psi(\mathrm{z}) = 0. \tag{A.27}$$

With the characteristic polynomial

$$-\frac{\hbar^2}{2\mathrm{m}} \cdot \kappa^2 + (\mathrm{V}_\mathrm{b} - \xi) = 0 \tag{A.28}$$

and $-\frac{2\mathrm{m}(\xi - \mathrm{V}_\mathrm{b})}{\hbar^2} = \kappa^2$ with $\mathrm{k} = \sqrt{\frac{2\mathrm{m}\xi}{\hbar^2}}$ follows

$$\kappa = \pm \mathrm{j}\sqrt{\frac{2\mathrm{m}(\xi - \mathrm{V}_\mathrm{b})}{\hbar^2}} = \pm \mathrm{jk}. \tag{A.29}$$

Two cases result, for case one $\xi > \mathrm{V}_\mathrm{b}$ follows

$$\kappa = \pm \mathrm{jk}. \tag{A.30}$$

Case two $\xi > \mathrm{V}_\mathrm{b}$ results in

$$\kappa = \pm\sqrt{\frac{2\mathrm{m}(\mathrm{V}_\mathrm{b} - \xi)}{\hbar^2}} = \pm\chi. \tag{A.31}$$

The general solution of the homogeneous partial differential equation results in

$$\psi(\mathrm{z}) = \mathrm{A}_1 \exp(\chi \mathrm{z}) + \mathrm{A}_2 \exp(-\chi \mathrm{z}), \tag{A.32}$$

which is fading exponentially.

UNIVERSITAT ROVIRA I VIRGILI
TWO-DIMENSIONAL ANALYTICAL PREDICTIVE MODELING OF SCHOTTKY BARRIER SOI AND MULTI-GATE MOSFETS
Mike Schwarz
Dipòsit Legal: T.456-2013

B. The WKB Approximation

Beginning from the time-independent Schrödinger equation (2.7), the one-dimensional case results in

$$\left(-\frac{\hbar^2}{2\mathrm{m}}\frac{\partial^2}{\partial \mathrm{x}^2} + \mathrm{V}(\mathrm{x}) - \xi\right)\psi(\mathrm{x}) = 0. \tag{B.1}$$

The following approach is used for the wave function

$$\psi(\mathrm{x}) = \mathrm{R}(\mathrm{x})\exp\left(\mathrm{j}\frac{\mathrm{S}(\mathrm{x})}{\hbar}\right), \tag{B.2}$$

the equations

$$\frac{\partial^2 \mathrm{R}}{\partial \mathrm{x}^2} - \frac{\mathrm{R}}{\hbar^2}\left(\frac{\partial \mathrm{S}}{\partial \mathrm{x}}\right)^2 + \frac{2\mathrm{m}(\xi - \mathrm{V}(\mathrm{x}))}{\hbar^2}\mathrm{R} = 0 \tag{B.3}$$

and

$$\mathrm{R}\frac{\partial^2 \mathrm{S}}{\partial \mathrm{x}^2} + 2\frac{\partial \mathrm{R}}{\partial \mathrm{x}}\frac{\partial \mathrm{S}}{\partial \mathrm{x}} = 0 \tag{B.4}$$

for the real and imaginary part of equation (B.1) can be found. Equation (B.4) can be solved by

$$\frac{\partial \mathrm{S}}{\partial \mathrm{x}} = \frac{\mathrm{C}}{\mathrm{R}^2} \tag{B.5}$$

where C is a constant. With equation (B.5) and equation (B.3) follows

$$\frac{1}{\mathrm{R}}\frac{\partial^2 \mathrm{R}}{\partial \mathrm{x}^2} - \frac{1}{\hbar^2}\left(\frac{\partial \mathrm{S}}{\partial \mathrm{x}}\right)^2 + \frac{2\mathrm{m}(\xi - \mathrm{V}(\mathrm{x}))}{\hbar^2} = 0. \tag{B.6}$$

With the approximation

$$\frac{1}{\mathrm{R}}\frac{\partial^2 \mathrm{R}}{\partial \mathrm{x}^2} << \frac{1}{\hbar^2}\left(\frac{\partial \mathrm{S}}{\partial \mathrm{x}}\right)^2 \tag{B.7}$$

follows

$$\mathrm{S}(\mathrm{x}) \approx \int \sqrt{2\mathrm{m}(\xi - \mathrm{V}(\mathrm{x}))}\mathrm{dx}, \tag{B.8}$$

and $\psi(\mathrm{x})$

$$\psi(\mathrm{x}) = \mathrm{R}(\mathrm{x})\exp\left(\frac{\mathrm{j}}{\hbar}\int \sqrt{2\mathrm{m}(\xi - \mathrm{V}(\mathrm{x}))}\mathrm{dx}\right). \tag{B.9}$$

Considering an energy barrier between the classical turning points x_1 and x_2 with an incoming wave ψ_1 and a transmitted wave ψ_2, and $x_2 > x_1$

$$\begin{aligned} \psi_1(x \leq x_1) \ \exp\left(\frac{j}{\hbar}\int_{-\infty}^{x_1}\sqrt{2m(\xi - V(x'))}dx'\right), \\ \psi_2(x \geq x_2) \ \exp\left(\frac{j}{\hbar}\int_{-\infty}^{x_2}\sqrt{2m(\xi - V(x'))}dx'\right). \end{aligned} \tag{B.10}$$

The transmission probability $T(\xi)$ is proportional to $|\psi_2(x_2)/\psi_1(x_1)|^2$

$$\begin{aligned} T(\xi) = \left|\frac{\psi_2(x_2)}{\psi_1(x_1)}\right|^2 &= \left|\exp\left(\frac{j}{\hbar}\int_{x_1}^{x_2}\sqrt{2m(\xi - V(x'))}dx'\right)\right|^2, \\ &= \exp\left(-\frac{2}{\hbar}\int_{x_1}^{x_2}\sqrt{2m(V(x') - \xi)}dx'\right). \end{aligned} \tag{B.11}$$

It is shown that the WKB approximation is only valid for

$$m\hbar\frac{\partial V(x)}{\partial x} << \sqrt{|2m(V(x) - \xi)|^3}. \tag{B.12}$$

This inequality is fulfilled for points where the variation of the energy barrier is small. The WKB approximation is therefore not valid in the close vicinity of the classical turning points [126].

C. The Square Root Approximation

One investigates the made approximation for the area hyperbolic cosine function in w-plane. Therefore, one applies the general solution for piecewise linear boundary, equation (5.25), with the square root approximation for the linear boundary from ⓵" → ② for a SB-DG-MOSFET and change the length of the linearly shaped boundary Δx between 5 nm and 45 nm. Keeping all other parameters constant one receives the results from Fig. C.1 to C.4 compared to the area hyperbolic cosine function.

From the plots one is able to observe the following behavior for the made approximation. The longer the length Δx becomes, the less the accuracy is, e.g. if the length is 45 nm, as in Fig. C.1 shown. The smaller the length for the linearly shaped boundary solution is, the smaller the error of the function becomes. In Fig. C the length is 5nm and a very good agreement between both functions is observed. This behavior results from the fact that in the w-plane absolute length and in the z-plane the geometry ratio is of interest. Therefore, the presented results are valid for the given geometry.

Nevertheless, it depends on the problem, how accurate the applied general solution for piecewise linear boundary is. In case of the SB-DG-MOSFET where a linear boundary is assumed within the oxide region, the results are very accurate. In Fig. C.5 one made a comparison with the solution of the electrostatic potential and calculated the absolute error $\delta(x, y)$. Again one kept all parameters constant, except the varying parameter for the length, which corresponds here with the oxide thickness t_{ox}. The parameter t_{ox} varies from 4 nm to 2 nm. The results are given in Fig. C.5(a) and C.5(b). The behavior is as expected, the smaller the length, the less the inaccuracy becomes. Furthermore, one is able to observe that the error for the case of t_{ox}=2 nm is less than 2 mV.

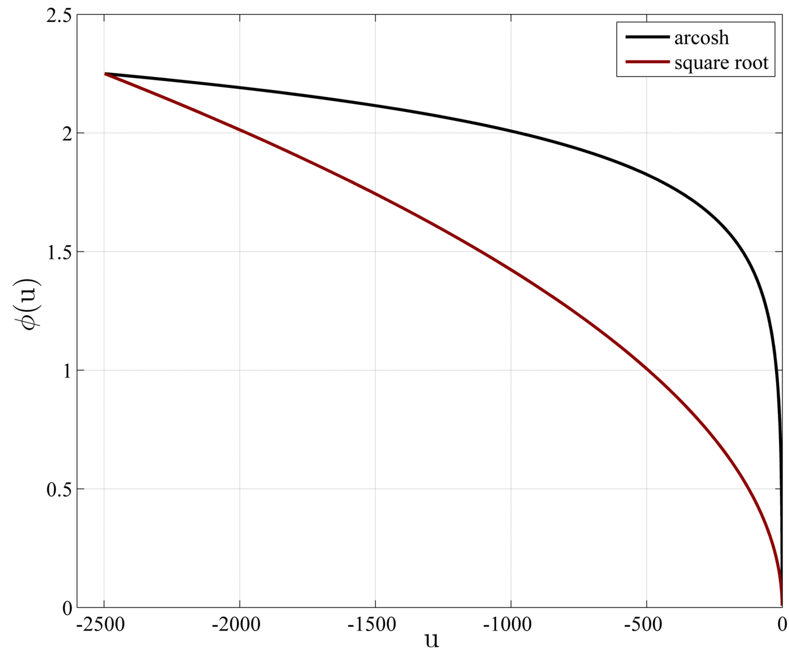

Figure C.1.: Comparison of area hyperbolic cosine function vs. square root approximation for Δx=45 nm.

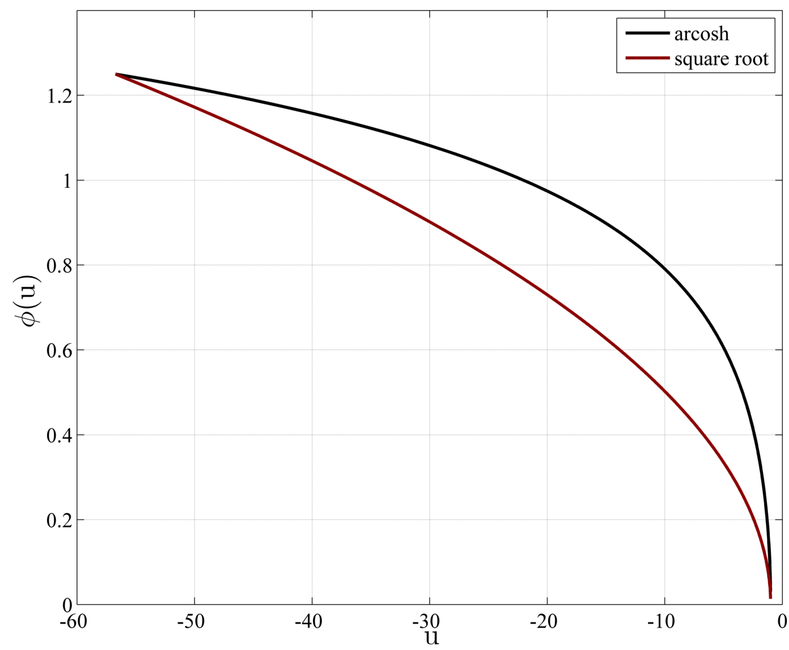

Figure C.2.: Comparison of area hyperbolic cosine function vs. square root approximation for Δx=25 nm.

UNIVERSITAT ROVIRA I VIRGILI
TWO-DIMENSIONAL ANALYTICAL PREDICTIVE MODELING OF SCHOTTKY BARRIER SOI AND MULTI-GATE MOSFETS
Mike Schwarz
Dipòsit Legal: T.456-2013

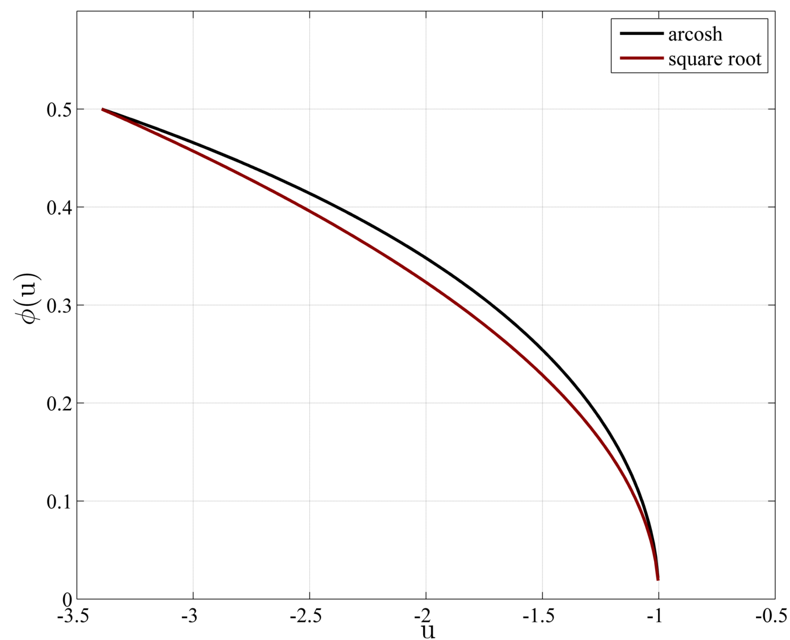

Figure C.3.: Comparison of area hyperbolic cosine function vs. square root approximation for Δx=10 nm.

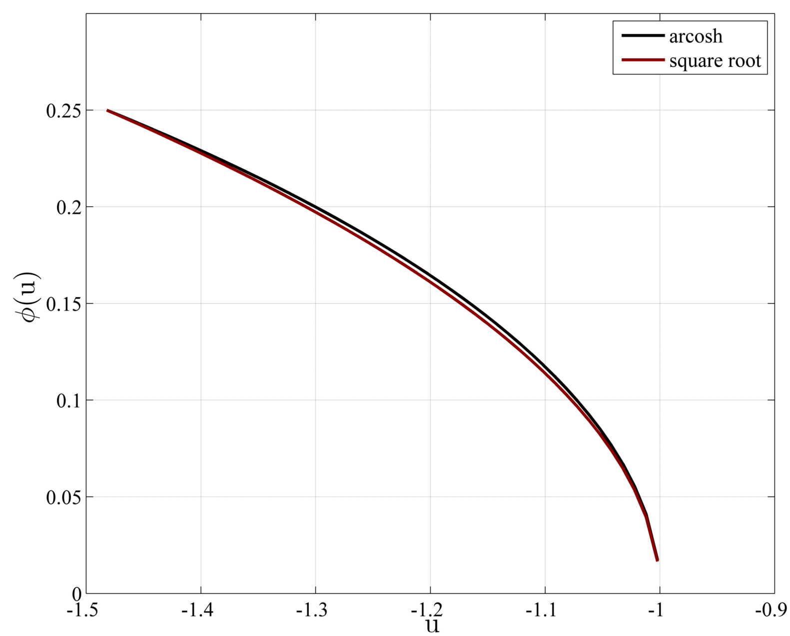

Figure C.4.: Comparison of area hyperbolic cosine function vs. square root approximation for Δx=5 nm.

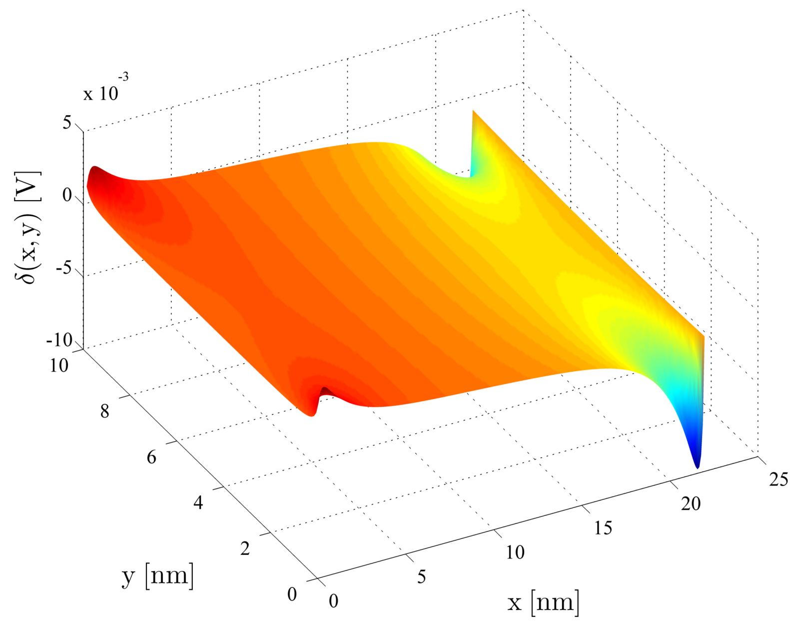

(a)

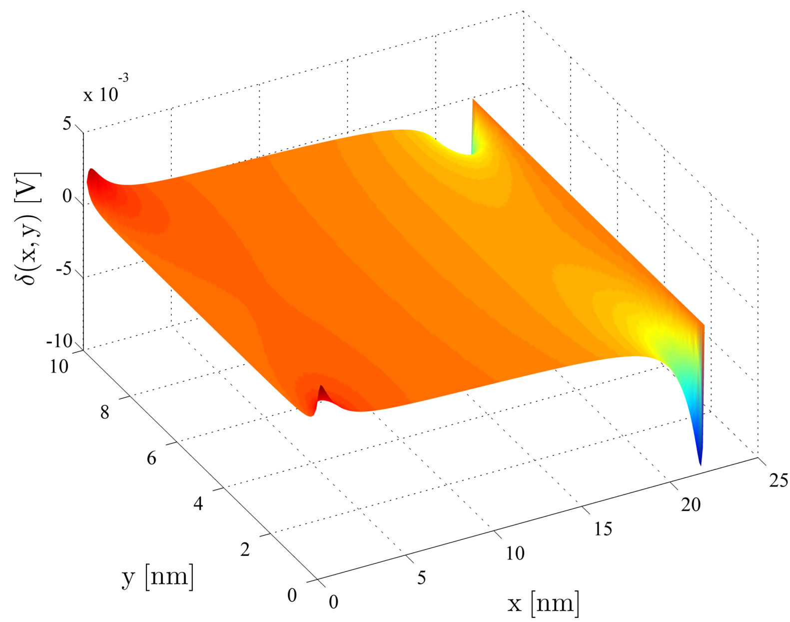

(b)

Figure C.5.: 3D plot of the absolute error $\delta(x, y)$ due to square root approximation for a SB-DG-MOSFET. Results for ϕ_{Bn}=0.4 eV. Device geometry: l_{ch}=22 nm, t_{ch}=10 nm, t_{ox}=2 nm. Bias conditions: V_{ds}=1 V, V_g=0.3 V. Model calculation. (a) t_{ox}=4 nm, (b) t_{ox}=2 nm.

D. Closed-form Equation Package

In the following, the complete set of explicit model equations is summarized. For the analytical closed-form modeling approaches for the currents are six points for each of the source and drain related cases sufficient to predict the current. Therefore, the electrostatics and currents for the following points have to be predicted with

$$
\begin{aligned}
(x_1/y_1) &= \left(0/\tilde{t_{ox}}\right), \\
(x_2/y_2) &= \left(x_{E_f}/\tilde{t_{ox}}\right), \\
(x_3/y_3) &= \left(0/\tilde{t_{ox}} + \frac{t_{ch}}{2}\right), \\
(x_4/y_4) &= \left(x_{E_f}/\tilde{t_{ox}} + \frac{t_{ch}}{2}\right), \\
(x_5/y_5) &= \left(0/\tilde{t_{ox}} + t_{ch}\right), \\
(x_6/y_6) &= \left(x_{E_f}/\tilde{t_{ox}} + t_{ch}\right).
\end{aligned} \tag{D.1}
$$

Scaling of oxide is as follows

$$\tilde{t_{ox}} = \frac{\epsilon_{Si}}{\epsilon_{ox}} \cdot t_{ox}. \tag{D.2}$$

The built-in potential in the Schottky barrier Double-Gate structure is solved as

$$\phi_{bi} = (E_g - \phi_{Bn}) - \left(\frac{E_g}{2} - \phi_p\right) \tag{D.3}$$

where

$$\phi_p = V_t \cdot \ln\left(\frac{N_A}{n_i}\right) = \frac{kT}{q} \cdot \ln\left(\frac{N_A}{n_i}\right). \tag{D.4}$$

The potential in Schottky barrier Double-Gate MOSFET is solved with the solution for the piecewise constant boundary between $\overline{u}_a$ and $\overline{u}_b$

$$\varphi_{const}(z, \phi_{bnd}, \overline{u}_a, \overline{u}_b) = -\frac{\phi_{bnd} \cdot \arctan\left(\frac{u-\overline{u}}{v}\right)}{\pi}\Bigg|_{\overline{u}_a}^{\overline{u}_b}, \tag{D.5}$$

and the solution for the piecewise linear boundary between $\overline{\mathrm{u}}_{\mathrm{a}}$ and $\overline{\mathrm{u}}_{\mathrm{b}}$

$$\varphi_{\mathrm{lin}}(\mathrm{z},\mathrm{a},\mathrm{b},\phi_{\mathrm{bnd}},\overline{\mathrm{u}}_{\mathrm{a}},\overline{\mathrm{u}}_{\mathrm{b}}) = \pm\frac{\mathrm{j}\arctan\left[\frac{1}{\sigma_4}\left(\mathrm{a}\cdot\mathrm{u}\cdot\sigma_1\cdot\sigma_3-\mathrm{a}\cdot\mathrm{b}\cdot\sigma_1\cdot\sigma_3+\mathrm{j}\cdot\mathrm{a}\cdot\mathrm{v}\cdot\sigma_1\cdot\sigma_3\right)\right]\sigma_3}{\pi} + \left.\frac{\mathrm{j}\arctan\left[\frac{1}{\sigma_4}\left(\mathrm{a}\cdot\mathrm{b}\cdot\sigma_1\cdot\sigma_2-\mathrm{a}\cdot\mathrm{u}\cdot\sigma_1\cdot\sigma_2+\mathrm{j}\cdot\mathrm{a}\cdot\mathrm{v}\cdot\sigma_1\cdot\sigma_2\right)\right]\sigma_2}{\pi}\right|_{\overline{\mathrm{u}}_{\mathrm{a}}}^{\overline{\mathrm{u}}_{\mathrm{b}}} \tag{D.6}$$

with

$$\sigma_1=\sqrt{-\frac{\mathrm{b}-\overline{\mathrm{u}}}{\mathrm{a}}},\quad \sigma_2=\sqrt{-\frac{\mathrm{u}-\mathrm{b}+\mathrm{j}\cdot\mathrm{v}}{\mathrm{a}}}$$

$$\sigma_3=\sqrt{\frac{\mathrm{b}-\mathrm{u}+\mathrm{j}\cdot\mathrm{v}}{\mathrm{a}}},\quad \sigma_4=\mathrm{b}^2-2\cdot\mathrm{b}\cdot\mathrm{u}+\mathrm{u}^2+\mathrm{v}^2$$

where

$$\mathrm{b}=\overline{\mathrm{u}}_{\mathrm{peak}} \tag{D.7}$$

and

$$\mathrm{a}=\frac{\overline{\mathrm{u}}_{\mathrm{step}}-\mathrm{b}}{(\phi_{\mathrm{bnd2}}-\phi_{\mathrm{bnd1}})^2}. \tag{D.8}$$

The electric field in Schottky barrier Double-Gate MOSFET is solved between $\overline{\mathrm{u}}_{\mathrm{a}}$ and $\overline{\mathrm{u}}_{\mathrm{b}}$ with

$$\underline{\mathrm{E}}(\mathrm{z},\mathrm{E}_{\mathrm{x|y}},\overline{\mathrm{u}}_{\mathrm{a}},\overline{\mathrm{u}}_{\mathrm{b}})=\frac{1}{\pi}\left|\frac{\mathrm{dw}}{\mathrm{dz}}\right|\mathrm{E}_{\mathrm{x|y}}\left.\left[-\frac{\Delta\mathrm{y}}{\pi}\frac{\sigma}{\sqrt{1-\mathrm{w}^{*2}}}\right]\right|_{\overline{\mathrm{u}}_{\mathrm{a}}}^{\overline{\mathrm{u}}_{\mathrm{b}}} \tag{D.9}$$

with

$$\sigma=\ln\left(\frac{\sqrt{\overline{\mathrm{u}}^2-1}+(\overline{\mathrm{u}}\cdot\mathrm{w}^*-1)\sqrt{\frac{1}{\mathrm{w}^{*2}-1}}}{\overline{\mathrm{u}}-\mathrm{w}^*}\right)$$

where w^* describes the conjugate complex point of point w. $\mathrm{E}_{\mathrm{x|y}}$ the electric field within the oxide. $\Delta\mathrm{y}$ results from the geometry of the device, which is $2\tilde{\mathrm{t}}_{\mathrm{ox}}+\mathrm{t}_{\mathrm{ch}}$. The derivative $\left|\frac{\mathrm{dw}}{\mathrm{dz}}\right|$ results from

$$\left|\frac{\mathrm{dw}}{\mathrm{dz}}\right|=\frac{1}{\left|\frac{\mathrm{dz}}{\mathrm{dw}}\right|} \tag{D.10}$$

where $\left|\frac{\mathrm{dz}}{\mathrm{dw}}\right|$ is expressed by

$$\left|\frac{\mathrm{dz}}{\mathrm{dw}}\right|=\frac{\mathrm{c}}{\sqrt{\mathrm{w}-1}\sqrt{\mathrm{w}+1}}. \tag{D.11}$$

w is received from the conformal mapping and c is calculated with $\mathrm{c}=\left(2\cdot\tilde{\mathrm{t}}_{\mathrm{ox}}+\mathrm{t}_{\mathrm{ch}}\right)/\pi$.

The point of interest z in the solutions for the electrostatics are linked to the coordinates u and v by the conformal mapping as well as the boundary values for $\overline{\mathrm{u}}_{\mathrm{a}}$ and $\overline{\mathrm{u}}_{\mathrm{b}}$. It follows for $\overline{\mathrm{u}}_{\mathrm{a}}$ and $\overline{\mathrm{u}}_{\mathrm{b}}$

UNIVERSITAT ROVIRA I VIRGILI
TWO-DIMENSIONAL ANALYTICAL PREDICTIVE MODELING OF SCHOTTKY BARRIER SOI AND MULTI-GATE MOSFETS
Mike Schwarz
Dipòsit Legal: T.456-2013

$$\begin{aligned}
\overline{u}_{\text{1''}} &= \cosh\left(\frac{\pi\left(3l_{ch} + j\left(2\tilde{t_{ox}} + t_{ch}\right)\right)}{\Delta y}\right)\\
\overline{u}_{2} &= \cosh\left(\frac{\pi\left(0 + j\left(2\tilde{t_{ox}} + t_{ch}\right)\right)}{\Delta y}\right)\\
\overline{u}_{3} &= \cosh\left(\frac{\pi\left(0 + j\left(\tilde{t_{ox}} + t_{ch}\right)\right)}{\Delta y}\right)\\
\overline{u}_{4} &= \cosh\left(\frac{\pi\left(0 + j\tilde{t_{ox}}\right)}{\Delta y}\right)\\
\overline{u}_{5} &= \cosh\left(\frac{\pi\left(0 + j0\right)}{\Delta y}\right)\\
\overline{u}_{\text{1'}} &= \cosh\left(\frac{\pi\left(3l_{ch} + j0\right)}{\Delta y}\right).
\end{aligned} \tag{D.12}$$

It follows for z for the source related case

$$w_{sce} = \cosh\left(\frac{\pi\left(x + j\left(\tilde{t_{ox}} + y\right)\right)}{\Delta y}\right), \tag{D.13}$$

and for the drain related case

$$w_{drn} = \cosh\left(\frac{\pi\left(l_{ch} - x + j\left(\tilde{t_{ox}} + y\right)\right)}{\Delta y}\right). \tag{D.14}$$

Here x and y describe the points where the electrostatics are calculated. The device current is as follows

$$I_{TTE} = I_{tun} + I_{therm}. \tag{D.15}$$

Both currents, the thermionic and tunneling, are described as

$$I = \frac{\sqrt{\pi}\cdot \text{erf}\left(\sqrt{d}\cdot y\right)\cdot \exp\left(e\right)}{2\sqrt{d}} \tag{D.16}$$

with

$$d = -\frac{4}{t_{ch}^2}\cdot \ln\left(\frac{J|_{y=\tilde{t_{ox}}}}{J|_{y=\tilde{t_{ox}}+\frac{t_{ch}}{2}}}\right)$$

and

$$e = \ln\left(J|_{y=\tilde{t_{ox}}+\frac{t_{ch}}{2}}\right).$$

The thermionic current density is as follows

$$J_{therm}(y) = A^*T^2\exp\left(-\frac{q\phi_B(y)}{kT}\right)\left[1 - \exp\left(\frac{-qV_{ds}}{kT}\right)\right] \tag{D.17}$$

with $\phi_B(y)$ the barrier height or maximum barrier.

The tunneling current density is as follows

$$J_{tun}(y) \approx \frac{q\mu N_C}{kT} \cdot \sqrt{\pi} \cdot b \cdot \exp\left(\frac{c^2}{4a} - cx_{E_f}\right) \cdot \frac{\mathrm{erf}\left(\frac{2a\left(x - x_{E_f}\right)+c}{2\sqrt{a}}\right)}{8\sqrt{a}} + J_{tun,fix}(y) \quad \text{(D.18)}$$

with

$$\begin{aligned} a &= \frac{\pi}{16(kT)^2} \cdot q \cdot E(x_{E_f}, y)^2, \\ b &= E(x,y)^2 \cdot T(E,x,y)\Big|_{x=0}, \\ c &= -\ln\left(\frac{1}{b}E(x,y)^2 \cdot T(E,x,y)\right) / x_{E_f}\Bigg|_{x=x_{E_f}}, \end{aligned}$$

and

$$J_{tun,fix}(y) = \sigma \frac{b}{c} \quad \text{(D.19)}$$

where

$$\sigma = f_m[1-f_s]_{ANMA}\big|_{x=0} - f_m[1-f_s]_{ACFMA}\big|_{x=0}.$$

Smoothing the linear-to-saturation region is shown as

$$V_{gx} = V_{g,trans}\left(1 - \frac{1}{B}\ln\left(\left[1 + \exp\left(A\left(1 - \frac{V_g}{V_{g,trans}}\right)\right)\right]\right)\right) \quad \text{(D.20)}$$

with

$$B = \ln\left(1 + \exp\left(A\right)\right) \quad \text{(D.21)}$$

where $A \approx 5...10$ and $V_{g,trans}$ the point of the continuous smoothing.

Bibliography

[1] G. E. Moore, "Cramming more components onto integrated circuits." *Electronics*, vol. 38, April 1965.

[2] M. Kanellos, "Moore's Law to roll on for another decade - CNET News." February 2003.

[3] ITRS, "International Technology Roadmap for Semiconductors." 2012.

[4] J. E. Lilienfeld, "Electric Current Control Mechanism." 1925.

[5] J. E. Lilienfeld, "Method and apparatus for controlling electric currents." 1926.

[6] O. Heil, "Improvements in or relating to electrical amplifiers and other control arrangements and devices." 1935.

[7] B. Davydov, "On the rectification of current at the boundary between two semiconductors." *Compt. Rend. Doklady Acad. Sci.*, vol. 20, pp. 279–282, 1938.

[8] N. F. Mott, "Note on the contact between a metal and an insulator or semiconductor." *Proceedings of Cambridge Philosophical Society*, vol. 34, pp. 568–572, 1938.

[9] W. Schottky, "Halbleitertheorie der Sperrschicht." *Naturwissenschaften*, vol. 26, p. 843, 1938.

[10] B. Lojek, *History of Semiconductor Engineering*. Springer, 2006.

[11] W. Brattain, "Bell Labs logbook." 1947.

[12] J. Bardeen and W. Brattain, "The Transistor, A Semiconductor Triode." *Physical Review*, vol. 74, no. 1, pp. 230–231, 1948.

[13] W. Shockley *Bell Labs lab notebook*, vol. 23, pp. 128–132, 1948.

[14] W. Shockley, "The Theory of p-n Junctions in Semiconductors and p-n Junction Transistors." *Bell System Technical Journal*, vol. 28, p. 435, 1949.

[15] W. Shockley, M. Sparks, and G. K. Teal, "p-n Junction Transistors." *Physical Review*, vol. 83, p. 151, 1951.

[16] J. S. Kilby, "Invention of the integrated circuit." *IEEE Transactions on Electron Devices*, vol. 23, no. 7, pp. 648–654, 1976.

[17] L. Esaki, "Solid State Physics in Electronics and Telecommunications." in *Proceedings of the International Conference on Solid State Physics*, 1958.

[18] M. M. J. Atalla and D. Kahng, "Metal Oxide Semiconductor (MOS) Transistor Demonstrated." 1959.

[19] D. Kahng, "Electric Field Controlled Semiconductor Device." 1960.

[20] F. Wanlass and C. T. Sah, "Nanowatt Logic Using Field-Effect Metal-Oxide Semiconductor Triodes." *International Solid State Circuits Conference Digest of Technical Papers*, 1963.

[21] G. E. Moore, "The role of Fairchild in silicon technology in the early days of Silicon Valley." *Proceedings of the IEEE*, vol. 86, no. 1, pp. 53–62, 1998.

[22] J. S. Koford, G. A. Sporzynski, and P. R. Strickland, "Using a Graphic Data Processing System to Design Artwork for Manufacturing Hybrid Integrated Circuits." in *Proceedings of the Fall Joint Computer Conference*, 1966.

[23] R. M. Holt, "World's First Microprocessor Chip Set." http://www.firstmicroprocessor.com.

[24] S. Augarten, *The Most Widely Used Computer on a Chip: The TMS 1000*. Ticknor & Fields, 1983.

[25] F. Faggin, J. Hoff, M. E., S. Mazor, and M. Shima, "The history of the 4004." *IEEE Micro*, vol. 16, no. 6, pp. 10–20, 1996.

[26] C. Mead and L. Conway, *Introduction to VLSI Systems*. Addison-Wesley Pub, 1979.

[27] nvonews, "Intel Ivy Bridge preview: everything to know about." http://nvonews.com/2012/03/06/intel-ivy-bridge-preview-everything-to-know-about, 2012.

[28] J. Bruner, "Intel 22 nm 3-D Tri-Gate Transistor Technology, News release and press materials (Intel)." http://www.intel.com, 2011.

[29] Intel, "Online in internet." http://www.intel.com, 2012.

[30] Motorola, "Online in internet." http://www.motorola.com, 2012.

UNIVERSITAT ROVIRA I VIRGILI
TWO-DIMENSIONAL ANALYTICAL PREDICTIVE MODELING OF SCHOTTKY BARRIER SOI AND MULTI-GATE MOSFETS
Mike Schwarz
Dipòsit Legal: T.456-2013

[31] AMD, "Online in internet." http://www.amd.com, 2012.

[32] Sony, "Online in internet." http://www.sony.net, 2012.

[33] IBM, "Online in internet." http://www.ibm.com, 2012.

[34] Toshiba, "Online in internet." http://www.toshiba.co.jp, 2012.

[35] nVIDIA, "Online in internet." http://www.nvidia.com, 2012.

[36] T. Sekigawa and Y. Hayashi, "Calculated threshold-voltage characteristics of an XMOS transistor having an additional bottom gate." *Solid-State Electronics*, vol. 27, p. 827, 1984.

[37] R. Chau, B. Doyle, J. Kavalieros, D. Barlage, A. Murthy, M. Doczy, R. Arghavani, and S. Datta, "Advanced Depleted-Substrate Transistors: Single-gate, Double-gate and Tri-gate." in *Extended Abstracts of the International Conference on Solid State Devices and Materials (SSDM)*, 2002.

[38] S. Miyano, M. Hirose, and F. Masuoka, "Numerical analysis of a cylindrical thin-pillar transistor (CYNTHIA)." *IEEE Transactions on Electron Devices*, vol. 39, no. 8, pp. 1876–1881, 1992.

[39] J.-P. Colinge, M.-H. Gao, A. Romano, H. Maes, and C. Claeys, "Silicon-on-insulator 'gate-all-around' MOS device." in *SOS/SOI Technology Conference IEEE*, 1990.

[40] N. Collaert, A. De Keersgieter, A. Dixit, I. Ferain, L. S. Lai, D. Lenoble, A. Mercha, A. Nackaerts, B. J. Pawlak, R. Rooyackers, T. Schulz, K. T. Sar, N. J. Son, M. J. H. Van Dal, P. Verheyen, K. von Arnim, L. Witters, D. Meyer, S. Biesemans, and M. Jurczak, "Multi-gate devices for the 32 nm technology node and beyond." in *ESSDERC*, 2007.

[41] J.-P. Colinge, ed., *FinFETs and Other Multi-Gate Transistors.* Springer Science+Business Media, LLC, 2008.

[42] J.-P. Colinge, "Evolution of SOI MOSFETs: from Single Gate to Multiple Gates." in *MRS Proceedings*, 2003.

[43] S. Cristoloveanu, "Silicon on insulator technologies and devices: from present to future." *Solid-State Electronics*, vol. 45, pp. 1403–1411, 2001.

[44] X. Huang, W.-C. Lee, C. Kuo, D. Hisamoto, L. Chang, J. Kedzierski, E. Anderson, H. Takeuchi, Y.-K. Choi, K. Asano, V. Subramanian, T.-J. King, J. Bokor, and

C. Hu, “Sub 50 nm FinFET: PMOS.” in *IEDM Technical Digest. International Electron Devices Meeting*, 1999.

[45] D. Hisamoto, W.-C. Lee, J. Kedzierski, H. Takeuchi, K. Asano, C. Kuo, E. Anderson, T.-J. King, J. Bokor, and C. Hu, “FinFET-a self-aligned double-gate MOSFET scalable to 20 nm.” *IEEE Transactions on Electron Devices*, vol. 47, no. 12, pp. 2320–2325, 2000.

[46] J.-T. Park, J.-P. Colinge, and C. Diaz, “Pi-Gate SOI MOSFET.” *IEEE Electron Device Letters*, vol. 22, no. 8, pp. 405–406, 2001.

[47] F.-L. Yang, H.-Y. Chen, F.-C. Chen, C.-C. Huang, C.-Y. Chang, H.-K. Chiu, C.-C. Lee, C.-C. Chen, H.-T. Huang, C.-J. Chen, H.-J. Tao, Y.-C. Yeo, M.-S. Liang, and C. Hu, “25 nm CMOS Omega FETs.” in *IEDM Technical Digest. International Electron Devices Meeting*, 2002.

[48] C. Hu, M. Dunga, C. H. Lin, D. Lu, and A. Niknejad, “Compact Modeling for New Transistor Structures.” in *Simulation of Semiconductor Processes and Devices* (T. Grasser and S. Selberherr, eds.), pp. 285–288, Springer, 2007.

[49] J.-P. Colinge and C.-A. Colinge, *Physics of Semiconductor Devices*. Springer, 2002.

[50] M. Lepselter and S. Sze, “SB-IGFET: An insulated-gate field-effect transistor using Schottky barrier contacts for source and drain.” *Proceedings of the IEEE*, vol. 56, no. 8, pp. 1400–1402, 1968.

[51] J. R. Tucker, C. Wang, and P. S. Carney, “Silicon field-effect transistor based on quantum tunneling.” *Applied Physics Letters*, vol. 65, no. 5, pp. 618–620, 1994.

[52] M.-G. Jang, Y.-Y. Kim, M.-S. Jun, C.-J. Choi, T.-Y. Kim, B.-C. Park, and S.-J. Lee, “Schottky Barrier MOSFETs with High Current Drivability for Nano-regime Applications.” *Journal of Semiconductor Technology and Science*, vol. 6, no. 1, pp. 10–15, 2006.

[53] J. M. Larson and J. P. Snyder, “Overview and status of metal S/D Schottky-barrier MOSFET technology.” *IEEE Transactions on Electron Devices*, vol. 53, no. 5, pp. 1048–1058, 2006.

[54] A. Kinoshita, Y. Tsuchiya, A. Yagishita, K. Uchida, and J. Koga, “Solution for high-performance Schottky-source/drain MOSFETs: Schottky barrier height engineering with dopant segregation technique.” in *Symposium on VLSI Technology*, 2004.

UNIVERSITAT ROVIRA I VIRGILI
TWO-DIMENSIONAL ANALYTICAL PREDICTIVE MODELING OF SCHOTTKY BARRIER SOI AND MULTI-GATE MOSFETS
Mike Schwarz
Dipòsit Legal: T.456-2013

[55] B. Black, M. Annavaram, N. Brekelbaum, J. DeVale, L. Jiang, G. H. Loh, D. McCaule, P. Morrow, D. W. Nelson, D. Pantuso, P. Reed, J. Rupley, S. Shankar, J. Shen, and C. Webb, "Die Stacking (3D) Microarchitecture." in *MICRO-39*, 2006.

[56] S. Das, A. Fan, K.-N. Chen, and C. S. Tan., "Technology, Performance, and Computer-Aided Design of Three-Dimensional Integrated Circuits." in *International Symposium on Physical Design*, 2004.

[57] S. Gupta, M. Hilbert, S. Hong, and R. Patti, "Techniques for Producing 3D ICs with High-Density Interconnect." in *21st Intl. VLSI Multilevel Interconnection Conference*, 2004.

[58] G. H. Loh, "3D-Stacked Memory Architectures for Multi-Core Processors." in *35th ACM/IEEE International Conference on Computer Architecture*, 2008.

[59] A. Asenov, "Simulation of statistical variability in Nano MOSFETs." in *Symposium on VLSI Technology*, 2007.

[60] S. Markov, B. Cheng, and A. Asenov, "Statistical Variability in Fully Depleted SOI MOSFETs Due to Random Dopant Fluctuations in the Source and Drain Extensions." *IEE Electron Device Letters*, vol. 33, no. 3, pp. 315–317, 2012.

[61] L. L. Lewyn, T. Ytterdal, C. Wulff, and K. Martin, "Analog Circuit Design in Nanoscale CMOS Technologies." in *Proceedings of the IEEE*, pp. 1687–1714, 2009.

[62] K. Kuhn, "Reducing Variation in Advanced Logic Technologies: Approaches to Process and Design for Manufacturability of Nanoscale CMOS." in *IEDM Technical Digest. International Electron Devices Meeting*, 2007.

[63] SILVACO, Inc., 4701 Patrick Henry Drive, Bldg. 1, Santa Clara, CA 95054, *ATLAS User's Manual Device Simulation Software*, 2010.

[64] Synopsys, *TCAD Sentaurus*. Synopsys, Inc., c-2009.06 ed., 2009.

[65] K.-T. Grasser, *Minimos-NT Device and Circuit Simulator*. Institute for Microelectronics, TU Vienna, 2002.

[66] M. Weidemann, *Analytical Predictive 2D Modeling of Pinch-Off Behavior in Nanoscale Multi-Gate MOSFETs*. PhD thesis, Universitaet Rovira i Virgili, Tarragona, Spain, 2011.

[67] L. W. Nagel and D. Pederson, "SPICE (Simulation Program with Integrated Circuit Emphasis)." Tech. Rep. UCB/ERL M382, EECS Department, University of California, Berkeley, 1973.

[68] G. Hachtel and A. Sangiovanni-Vincentelli, "A survey of third-generation simulation techniques." *Proceedings of the IEEE*, vol. 69, no. 10, pp. 1264–1280, 1981.

[69] L. Nagel and R. Rohrer, "Computer analysis of nonlinear circuits, excluding radiation (CANCER)." *IEEE Journal of Solid State Circuits*, vol. 6, no. 4, pp. 166–182, 1971.

[70] C. Galup-Montoro and M. Schneider, *Mosfet Modeling for Circuit Analysis And Design.* World Scientic, 2007.

[71] Y. Cheng, M.-C. Jeng, Z. Liu, J. Huang, M. Chan, K. Chen, P. K. Ko, and C. Hu, "A physical and scalable I-V model in BSIM3v3 for analog/digital circuit simulation." *IEEE Transactions on Electron Devices*, vol. 44, no. 2, pp. 277–287, 1997.

[72] N. Arora, R. Rios, C.-L. Huang, and K. Raol, "PCIM: A physically based continuous short-channel IGFET model for circuit simulation." *IEEE Transactions on Electron Devices*, vol. 41, no. 6, pp. 988–997, 1994.

[73] K. Joardar, "An improved analytical model for collector currents in lateral bipolar transistors." *IEEE Transactions on Electron Devices*, vol. 41, no. 3, pp. 373–382, 1994.

[74] C. C. Enz, F. Krummenacher, and E. A. Vittoz, "An analytical MOS transistor model valid in all regions of operation and dedicated to low-voltage and low-current applications." *Analog Integr. Circuits Signal Process.*, vol. 8, no. 1, pp. 83–114, 1995.

[75] X. Xi, M. Dunga, J. He, W. Liu, K. M. Cao, X. Jin, J. J. Ou, M. Chan, A. M. Niknejad, and C. Hu, *BSIM4.3.0 MOSFET Model - User's Manual.* Department of Electrical Engineering and Computer Sciences, University of California, Berkeley, 2003.

[76] J. He, J. Xi, M. Chan, H. Wan, M. Dunga, B. Heydari, A. Niknejad, and C. Hu, "Charge-based core and the model architecture of BSIM5." in *Sixth International Symposium on Quality of Electronic Design*, 2005.

[77] X. Niu, Y. Song, B. Li, W. Bian, Y. Tao, F. Liu, J. Hu, Y. Chen, and F. He, "Tests on Symmetry and Continuity between BSIM4 and BSIM5." in *8th International Symposium on Quality Electronic Design*, 2007.

[78] C. Hu, "BSIM Compact MOSFET Modells." in *MOS-AK Workshop, Helsinki*, 2011.

[79] G. Gildenblat, X. Li, W. Wu, H. Wang, A. Jha, R. van Langevelde, G. Smit, A. Scholten, and D. Klaassen, "PSP: An Advanced Surface-Potential-Based MOSFET Model for Circuit Simulation." *IEEE Transactions on Electron Devices*, vol. 53, no. 9, pp. 1979–1993, 2006.

[80] A. Scholten, G. Smit, B. De Vries, L. Tiemeijer, J. Croon, D. Klaassen, R. van Langevelde, X. Li, W. Wu, and G. Gildenblat, "(Invited) The new CMC standard compact MOS model PSP: advantages for RF applications." in *IEEE Radio Frequency Integrated Circuits Symposium*, 2008.

[81] H. Mattausch, M. Miura-Mattausch, H. Ueno, S. Kumashiro, T. Yamaguchi, K. Yamashita, and N. Nakayama, "HiSIM: The first complete drift-diffusion MOSFET model for circuit simulation." in *International Conference on Solid-State and Integrated-Circuit Technology*, 2001.

[82] M. Miura-Mattausch, H. Ueno, J. Mattausch, S. Kumashiro, T. Yamaguchi, K. Yamashita, and N. Nakayama, "HiSIM: Self-Consistent Surface-Potential MOS-Model Valid Down to Sub-100 nm Technologies." in *Technical Proceedings of the International Conference on Modeling and Simulation of Microsystems*, 2002.

[83] M. Miura-Mattausch, H. Ueno, M. Tanaka, H. Mattausch, S. Kumashiro, T. Yamaguchi, K. Yamashita, and N. Nakayama, "HiSIM: a MOSFET model for circuit simulation connecting circuit performance with technology." in *IEDM Technical Digest. International Electron Devices Meeting*, 2002.

[84] H. Mattausch, M. Miyake, D. Navarro, N. Sadachika, T. Ezaki, M. Miura-Mattausch, T. Yoshida, and S. Hazama, "HiSIM2 Circuit simulation - Solving the speed versus accuracy crisis." *IEEE Circuits and Devices Magazine*, vol. 22, no. 5, pp. 29–38, 2006.

[85] D. Vasileska and S. Goodnick, *Computational Electronics.* Morgan & Claypool, 2006.

[86] T. Grasser, *Advanced Device Modeling and Simulation.* World Scientic, 2003.

[87] S. Selberherr, *Analysis and Simulation of Semiconductor Devices.* Springer, 1984.

[88] N. Arora, *Mosfet Modeling for VLSI Simulation: Theory and Practice (International Series on Advances in Solid State Electronics and Technology).* World Scientific Pub Co, 2007.

[89] Y. Tsividis, *Operational Modeling of the MOS Transistor.* McGraw-Hill, 1999.

[90] Y. Tsividis and K. Suyama, "MOSFET modeling for analog circuit CAD: Problems and prospects." in *Proceedings of the IEEE Custom Integrated Circuits Conference*, 1993.

[91] J.-P. Colinge, *Silicon-on-Insulator Technology: Materials to VLSI, 3rd Ed.* Springer, 2004.

[92] C. Wang, J. P. Snyder, and J. R. Tucker, "Sub-40 nm PtSi Schottky source/drain metal–oxide–semiconductor field-effect transistors." *Applied Physics Letters*, vol. 74, no. 8, pp. 1174–1176, 1999.

[93] J. Kedzierski, P. Xuan, V. Subramanian, J. Bokor, T.-J. King, C. Hu, and E. Anderson, "20 nm gate-length ultra-thin body p-MOSFET with silicide S/D." *Superlattices and Microstructures*, vol. 28, no. 5/6, pp. 445–452, 2000.

[94] J. Kedzierski, P. Xuan, E. Anderson, J. Bokor, T.-J. King, and C. Hu, "Complementary silicide source/drain thin-body MOSFETs for the 20 nm gate length regime." in *IEDM Technical Digest. International Electron Devices Meeting*, 2000.

[95] J. Kedzierski, M. Ieong, P. Xuan, J. Bokor, T.-J. King, and C. Hu, "Design analysis of thin-body silicide source/drain devices." in *IEEE International SOI Conference*, pp. 21–22, 2001.

[96] B.-Y. Tsui and C.-P. Lin, "A novel 25 nm modified Schottky-barrier FinFET with high performance." *IEEE Electron Device Letters*, vol. 25, no. 6, pp. 430–432, 2004.

[97] D. Connelly, C. Faulkner, P. A. Clifton, and D. E. Grupp, "Fermi-level depinning for low-barrier Schottky source/drain transistors." *Applied Physics Letters*, vol. 88, no. 1, 2006.

[98] H. Ghoneim, J. Knoch, H. Riel, D. Webb, M. T. Bjork, S. Karg, E. Lortscher, H. Schmid, and W. Riess, "Interface engineering for the suppression of ambipolar behavior in Schottky-barrier MOSFETs." in *Proceedings of ULIS*, 2009.

[99] S. Zhu, J. Chen, M.-F. Li, S. J. Lee, J. Singh, C. X. Zhu, A. Du, C. H. Tung, A. Chin, and D. L. Kwong, "N-type Schottky barrier source/drain MOSFET using ytterbium silicide." *IEEE Electron Device Letters*, vol. 25, no. 8, pp. 565–567, 2004.

[100] M. Zhang, J. Knoch, Q. T. Zhao, A. Fox, S. Lenk, and S. Mantl, "Low temperature measurements of Schottky-barrier SOI-MOSFETs with dopant segregation." *Electronics Letters*, vol. 41, no. 19, pp. 1085–1086, 2005.

UNIVERSITAT ROVIRA I VIRGILI
TWO-DIMENSIONAL ANALYTICAL PREDICTIVE MODELING OF SCHOTTKY BARRIER SOI AND MULTI-GATE MOSFETS
Mike Schwarz
Dipòsit Legal: T.456-2013

[101] C. Urban, M. Emam, C. Sandow, Q.-T. Zhao, A. Fox, J.-P. Raskin, and S. Mantl, "High-frequency performance of dopant-segregated NiSi S/D SOI SB-MOSFETs." in *ESSDERC, Athens, Greece*, 2009.

[102] L. Knoll, A. Schäfer, S. Trellenkamp, K. K. Bourdelle, Q. Zhao, and S. Mantl, "Nanowire and Planar UTB SOI Schottky Barrier MOSFETs with Dopant Segregation." in *Proceedings of ULIS, Grenoble, France*, 2012.

[103] C. Koeneke, S. Sze, R. Levin, and E. Kinsbron, "Schottky MOSFET for VLSI." in *IEDM Technical Digest. International Electron Devices Meeting*, 1981.

[104] J. P. Snyder, C. R. Helms, and Y. Nishi, "Experimental investigation of a PtSi source and drain field emission transistor." *Applied Physics Letters*, vol. 67, no. 10, pp. 1420–1422, 1995.

[105] R. Tsu and L. Esaki, "Tunneling in a finite superlattice." *Applied Physics Letters*, vol. 22, no. 11, pp. 562–564, 1973.

[106] M. Ieong, P. Solomon, S. Laux, H.-S. Wong, and D. Chidambarrao, "Comparison of raised and Schottky source/drain MOSFETs using a novel tunneling contact model." in *IEDM Technical Digest. International Electron Devices Meeting*, 1998.

[107] A. Schenk and G. Heiser, "Modeling and simulation of tunneling through ultra-thin gate dielectrics." *Journal of Applied Physics*, vol. 81, no. 12, pp. 7900–7908, 1997.

[108] R. H. Fowler and L. Nordheim, "Electron Emission in Intense Electric Fields." in *Proceedings of the Royal Society of London. Series A, Containing Papers of a Mathematical and Physical Character*, vol. 119, pp. 173–181, 1928.

[109] E. Zaidman, "Simulation of field emission microtriodes." *IEEE Transactions on Electron Devices*, vol. 40, no. 5, pp. 1009–1016, 1993.

[110] G. Hurkx, D. Klaassen, and M. Knuvers, "A new recombination model for device simulation including tunneling." *IEEE Transactions on Electron Devices*, vol. 39, no. 2, pp. 331–338, 1992.

[111] G. Hurkx, D. Klaassen, M. Knuvers, and F. O'Hara, "A new recombination model describing heavy-doping effects and low-temperature behaviour." in *IEDM Technical Digest. International Electron Devices Meeting*, 1989.

[112] G. Hurkx, H. de Graaff, W. Kloosterman, and M. Knuvers, "A novel compact model description of reverse-biased diode characteristics including tunnelling." in *ESSDERC*, 1990.

UNIVERSITAT ROVIRA I VIRGILI
TWO-DIMENSIONAL ANALYTICAL PREDICTIVE MODELING OF SCHOTTKY BARRIER SOI AND MULTI-GATE MOSFETS
Mike Schwarz
Dipòsit Legal: T.456-2013

[113] A. Schenk, "Rigoroustheory and simplifiedmodel of the band-to-band tunneling in silicon." *Solid State Electronics*, vol. 36, pp. 19–34, 1993.

[114] G. Wentzel, "Eine Verallgemeinerung der Quantenbedingungen für Würfel Zwecke der Wellenmechanik." *Z. Physik*, vol. 38, pp. 518–529, 1926.

[115] H. A. Kramers, "Wellenmechanik und halbzahlige Quantisierung." *Z. Physik*, vol. 39, pp. 828–840, 1926.

[116] L. Brillouin, "La mécanique ondulatoire de Schrödinger; une Méthode Générale de resolution durchschnittliche Näherungswerte successives." *Comptes rendus (Paris)*, vol. 183, pp. 24–26, 1926.

[117] L. Fei, S. Mudanai, Y.-Y. Fan, L. Register, and S. Banerjee, "Compact model of MOSFET electron tunneling current through ultra-thin SiO2 and high-k gate stacks." in *Device Research Conference*, 2003.

[118] L. F. Register, E. Rosenbaum, and K. Yang, "Analytic model for direct tunneling current in polycrystalline silicon-gate metal–oxide–semiconductor devices." *Applied Physics Letters*, vol. 74, no. 3, pp. 457–459, 1999.

[119] H.-H. Park, Z. Jiang, A. G. Akkala, S. Steiger, M. Povolotskyi, T. C. Kubis, J. M. D. Sellier, Y. Tan, S. Kim, M. Luisier, S. Agarwal, M. McLennan, and G. Klimeck, "Resonant Tunneling Diode Simulation with NEGF." 2008.

[120] A. Hazeghi, T. Krishnamohan, and H.-S. P. Wong, "Schottky-Barrier CNFET." 2007.

[121] A. Hazeghi, T. Krishnamohan, and H.-S. P. Wong, "Schottky-Barrier Carbon Nanotube Field-Effect Transistor Modeling." *IEEE Transactions on Electron Devices*, vol. 54, no. 3, pp. 439–445, 2007.

[122] H.-S. Hahm and A. Godoy, "Quantum and Semi-classical Electrostatics Simulation of SOI Trigates." 2008.

[123] F. Garcia Ruiz, A. Godoy, F. Gamiz, C. Sampedro, and L. Donetti, "A Comprehensive Study of the Corner Effects in Pi-Gate MOSFETs Including Quantum Effects." *IEEE Transactions on Electron Devices*, vol. 54, no. 12, pp. 3369–3377, 2007.

[124] T. Binder, K. Dragosits, T. Grasser, R. Klima, M. Knaipp, H. Kosina, R. Mlekus, V. Palankovski, M. Rottinger, G. Schrom, S. Selberherr, and M. Stockinger, *MINIMOS-NT User's Guide*. Institut für Mikroelektronik, Technische Universität Wien, 1998.

[125] V. Palankovski, *Simulation of Heterojunction Bipolar Transistors.* PhD thesis, TU Wien, 2000.

[126] A. Gehring, *Simulation of Tunneling in Semiconductor Devices.* PhD thesis, TU Wien, 2003.

[127] F. Pregaldiny, J.-B. Kammerer, and C. Lallement, "Compact Modeling and Applications of CNTFETs for Analog and Digital Circuit Design." in *IEEE International Conference on Electronics, Circuits and Systems*, 2006.

[128] A. Raychowdhury, S. Mukhopadhyay, and K. Roy, "A circuit-compatible model of ballistic carbon nanotube field-effect transistors." *IEEE Transactions on Computer-Aided Design of Integrated Circuits and Systems*, vol. 23, no. 10, pp. 1411–1420, 2004.

[129] S. Frégonèse, C. Maneux, and T. Zimmer, "A compact model for double gate carbon nanotube FET." in *ESSDERC*, 2010.

[130] S. Frégonèse, C. Maneux, and T. Zimmer, "A Compact Model for Dual-Gate One-Dimensional FET: Application to Carbon-Nanotube FETs." *IEEE Transactions on Electron Devices*, vol. 58, no. 1, pp. 206–215, 2011.

[131] S. Sinha, A. Balijepalli, and Y. Cao, "Compact Model of Carbon Nanotube Transistor and Interconnect." *IEEE Transactions on Electron Devices*, vol. 56, no. 10, pp. 2232–2242, 2009.

[132] G. Zhu, X. Zhou, T. Lee, L. Ang, G. See, and S. Lin, "A compact model for undoped symmetric double-gate MOSFETs with Schottky-barrier source/drain." in *ESSDERC*, 2008.

[133] G. Zhu, X. Zhou, T. S. Lee, L. K. Ang, G. H. See, S. Lin, Y.-K. Chin, and K. L. Pey, "A Compact Model for Undoped Silicon-Nanowire MOSFETs With Schottky-Barrier Source/Drain." *IEEE Transactions on Electron Devices*, vol. 56, no. 5, pp. 1100–1109, 2009.

[134] G. Zhu, X. Zhou, Y.-K. Chin, K. L. Pey, J. Zhang, G. H. See, S. Lin, Y. Yan, and Z. Chen, "Subcircuit Compact Model for Dopant-Segregated Schottky Gate-All-Around Si-Nanowire MOSFETs." *IEEE Transactions on Electron Devices*, vol. 57, no. 4, pp. 772–781, 2010.

[135] J. R. M. Balaguer, B. Iñiguez, "An analytical compact model for Schottky-Barrier Double Gate MOSFETs." in *Proceedings of EUROSOI, Grenoble, France*, 2010.

UNIVERSITAT ROVIRA I VIRGILI
TWO-DIMENSIONAL ANALYTICAL PREDICTIVE MODELING OF SCHOTTKY BARRIER SOI AND MULTI-GATE MOSFETS
Mike Schwarz
Dipòsit Legal: T.456-2013

[136] O. Moldovan, D. Jimenez, J. Guitart, F. Chaves, and B. Iniguez, "Explicit Analytical Charge and Capacitance Models of Undoped Double-Gate MOSFETs." *IEEE Transactions on Electron Devices*, vol. 54, no. 7, pp. 1718–1724, 2007.

[137] E. Weber, *Electromagnetic fields, Vol.I., Mapping of fields.* John Wiley, New York, 1950.

[138] D. Crowdy, "The Schwarz-Christoffel Mapping to Bounded Multiply Connected Polygonal Domains." in *Proceedings of Mathematical, Physical and Engineering Sciences*, vol. 641, pp. 2653–2678, 2005.

[139] H. Lesch, *alpha-Centauri: Was ist der Tunneleffekt?* 2003.

[140] M. Razavy, *Quantum Theory of Tunneling.* World Scientific Publishing Co. Pte. Ltd., 2003.

[141] D. J. M. Yarrison-Rice, "Lecture: Digital optical communications." http://www.cas.muohio.edu/ yarrisjm/S05101incl.html, 2012.

[142] T. Young, *The Bakerian Lecture: Experiments and calculations relative to physical optics.* 1803.

[143] H. Hertz, "Über den Einfluss des ultravioletten Lichtes auf die elektrische Entladung." *Annalen der Physik*, vol. 267 (8), pp. 983–1000, 1887.

[144] L. de Broglie, *Recherches sur la théorie des quanta (Researches on the quantum theory).* PhD thesis, 1924.

[145] V. Mitin, V. Kochelap, and M. Stroscio, *Introduction to Nanoelectronics.* Cambridge University Press, 2008.

[146] K. Goser, P. Glösekötter, and J. Dienstuhl, *Nanoelectronics and Nanosystems - From Transistors to Molecular and Quantum Devices.* Springer, 2004.

[147] A. Kloes, *Lecture: Nanoelectronics.* 2011.

[148] E. Schrödinger, "An Undulatory Theory of the Mechanics of Atoms and Molecules." *Physical Review*, vol. 28, pp. 1049–1070, 1926.

[149] W. Heisenberg, "Über den anschaulichen Inhalt der quantentheoretischen Kinematik und Mechanik." *Zeitschrift für Physik*, vol. 43 (3), pp. 172–198, 1927.

[150] K. K. N. S. M. Sze, *Physics of Semiconductor Devices.* John Wiley & Sons, 2007.

[151] F. Braun, "Über die Stromleitung durch Schwefelmetalle." *Ann. Phys. Chem.*, vol. 153, p. 556, 1874.

UNIVERSITAT ROVIRA I VIRGILI
TWO-DIMENSIONAL ANALYTICAL PREDICTIVE MODELING OF SCHOTTKY BARRIER SOI AND MULTI-GATE MOSFETS
Mike Schwarz
Dipòsit Legal: T.456-2013

[152] A. H. Wilson, "The Theory of Electronic Semiconductors." *Proceedings of Royal Society London*, vol. 133, p. 458, 1931.

[153] H. A. Bethe, "Theory of Boundary Layer of Crystal Rectifiers." *MIT Radiat. Lab. Rep.*, 1942.

[154] R. A. Vega, *Schottky Field Effect Transistors and Schottky CMOS Circuitry.* PhD thesis, Rochester Institute of Technology, Rochester, NY, 2006.

[155] J. Robertson and C. W. Chen, "Schottky barrier heights of tantalum oxide, barium strontium titanate, lead titanate, and strontium bismuth tantalate." *Applied Physics Letters*, vol. 74, no. 8, pp. 1168–1170, 1999.

[156] M. Zhang, *Modelling and fabrication of high performance Schottky-barrier SOI-MOSFETs with low effective Schottky barriers.* PhD thesis, RWTH Aachen, 2006.

[157] C. Crowell, "Richardson constant and tunneling effective mass for thermionic and thermionic-field emission in Schottky barrier diodes." *Solid State Electronics*, vol. 12, no. 1, p. 55–59, 1969.

[158] C. R. Crowell and S. M. Sze, "Current Transport in Metal-Semiconductor Barriers." *Solid State Electronics*, vol. 9, pp. 11–12, 1966.

[159] C. Y. Chang and S. M. Sze, "Carrier Transport across Metal-Semiconductor Barriers." *Solid-State Electronics*, vol. 13, pp. 727–740, 1970.

[160] C. B. Duke, *Tunneling in Solids.* Academic Press, 1969.

[161] W. W. Lui and M. Fukuma, "Exact Solution of the Schrödinger Equation Across an Arbitrary One-Dimensional Piecewise-Linear Potential Barrier." *Journal of Applied Physics*, vol. 60, no. 5, pp. 1555–1559, 1986.

[162] D. C. Hutchings, "Transfer Matrix Approach to the Analysis of an Arbitrary Quantum Well Structure in an Electric Field." *Applied Physics Letters*, vol. 55, no. 11, pp. 1082–1084, 1989.

[163] W. R. Frensley and N. G. Einspruch, *Heterostructures and Quantum Devices.* VLSI Electronics: Microstructure Science, Academic Press, 1994.

[164] M. Schwarz, "Analytical Approaches for 2D Modeling of the Electrostatic Potential in Schottky Barrier Double-Gate MOSFETs." Master's thesis, Universitaet Rovira i Virgili, Tarragona, Spain, 2009.

[165] P. D. O. Greuel, *Komplexe Funktionen und konforme Abbildungen.* BSB B. G. Teubner Verlagsgesellschaft, Leipzig, 1978.

[166] P. D.-I. H. Henke, *Elektromagnetische Felder.* Springer Berlin Heidelberg New York, 2007.

[167] T. Arens, F. Hettlich, C. Karpfinger, U. Kockelkorn, K. Lichtenegger, and H. Stachel, *Mathematik*. Spektrum Akademischer Verlag, 2008.

[168] A. Kloes, *Analytische Modellierung mehrdimensionaler Effekte in Submikron-MOSFETs.* PhD thesis, TU Darmstadt, 1996.

[169] T. Ernst, C. Tinella, C. Raynaud, and S. Cristoloveanu, "Fringing fields in sub-0.1 µm fully depleted SOI MOSFETs: optimization of the device architecture." *Solid-State Electronics*, vol. 46, no. 6, pp. 373–378, 2002.

[170] T. Ernst, R. Ritzenthaler, O. Faynot, and S. Cristoloveanu, "A Model of Fringing Fields in Short-Channel Planar and Triple-Gate SOI MOSFETs." *IEEE Transactions on Electron Devices*, vol. 54, no. 6, pp. 1366–1375, 2007.

[171] Y. Omura, S. Horiguchi, M. Tabe, and K. Kishi, "Quantum-mechanical effects on the threshold voltage of ultrathin-SOI nMOSFETs." *IEEE Electron Device Letters*, vol. 14, no. 12, pp. 569–571, 1993.

[172] M. Schwarz, M. Weidemann, A. Kloes, and B. Iñíguez, "2D Analytical Solution of Potential in Lightly Doped Schottky barrier Double-Gate MOSFET." in *ESSDERC, Athens, Greece*, 2009.

[173] M. Schwarz, M. Weidemann, A. Kloes, and B. Iñíguez, "2D Analytical Model of Potential Distribution in Lightly Doped Schottky barrier DG-MOSFET." in *Graduated Student Meeting, Tarragona, Spain*, 2009.

[174] M. Schwarz, M. Weidemann, A. Kloes, and B. Iñíguez, "2D Analytical Calculation of the Electrostatic Potential in Lightly Doped Schottky barrier Double-Gate MOSFET." *Solid-State Electronics*, vol. 54, no. 11, pp. 1372–1380, 2010.

[175] B. Doris, "ETSOI Technology Tutorial." in *Proceedings of EUROSOI, Granada, Spain*, 2011.

[176] M. Schwarz, T. Holtij, A. Kloes, and B. Iñíguez, "2D Analytical Calculation of the Electric Field in Lightly Doped Schottky Barrier Double-Gate MOSFETs and Estimation of the Tunneling/Thermionic Current." *Solid-State Electronics*, vol. 63, no. 1, pp. 119–129, 2011.

[177] M. Schwarz, T. Holtij, A. Kloes, and B. Iñíguez, "Analytical Compact Modeling Framework for the 2D Electrostatics in Lightly Doped Double-Gate MOSFETs." *Solid-State Electronics*, vol. 69, no. 1, pp. 72–84, 2012.

UNIVERSITAT ROVIRA I VIRGILI
TWO-DIMENSIONAL ANALYTICAL PREDICTIVE MODELING OF SCHOTTKY BARRIER SOI AND MULTI-GATE MOSFETS
Mike Schwarz
Dipòsit Legal: T.456-2013

[178] A. Kloes and A. Kostka, "A new analytical method of solving 2D Poisson's equation in MOS devices applied to threshold voltage and subthreshold modeling." *Solid-State Electronics*, vol. 36, no. 12, pp. 1761–1775, 1996.

[179] M. Schwarz, T. Holtij, A. Kloes, and B. Iñíguez, "2D Analytical Framework for Compact Modeling of the Electrostatics in Undoped DG MOSFETs." in *Proceedings of MIXDES, Gliwice, Poland*, 2011.

[180] M. Schwarz, A. Kloes, and B. Iñíguez, "Analytical 2D Model for the Channel Electric Field in Undoped Schottky Barrier Double-Gate MOSFET." in *Proceedings of MIXDES, Wroclaw, Poland*, 2010.

[181] M. Schwarz, A. Kloes, and B. Iñíguez, "Closed-Form 2D Model for the Electric Field in Lightly Doped Schottky Barrier Double-Gate MOSFET." in *Graduated Student Meeting, Tarragona, Spain*, 2010.

[182] M. Schwarz, T. Holtij, A. Kloes, and B. Iñíguez, "Complex 2D Electric Field Solution in Undoped Double-gate MOSFETs." *IETE Journal of Research*, vol. 58, no. 3, pp. 197–204, 2012.

[183] M. Städele, "Influence of source-drain tunneling on the subthreshold behavior of sub-10 nm double-gate MOSFETs." in *ESSDERC, Firenze, Italy*, 2002.

[184] M. Schwarz, T. Holtij, A. Kloes, and B. Iñíguez, "I-V Model for Lightly Doped Schottky Barrier DG-MOSFETs Including 2D Effects." in *ESSDERC, Hesinki, Finland*, 2011.

[185] N. Ashcroft and N. Mermin, *Solid State Physics.* Harcourt College Publishers, 1976.

[186] M. Schwarz, A. Kloes, and B. Iñíguez, "2D Analytical Calculation of the Tunneling Current in Lightly Doped Schottky Barrier Double-Gate MOSFET." in *ESSDERC, Sevilla, Spain*, 2010.

[187] M. Schwarz, A. Kloes, and B. Iñíguez, "2D Analytical Calculation of the Current in Lightly Doped Schottky Barrier Double-Gate MOSFET." in *Proceedings of EUROSOI, Granada, Spain*, 2011.

[188] M. Schwarz, T. Holtij, A. Kloes, and B. Iñíguez, "2D Analysis of Source/Drain Carrier Tunneling in Lightly Doped Schottky Barrier DG-MOSFETs Using a Fully Analytical Model." in *Proceedings of ULIS, Cork, Ireland*, 2011.

[189] M. Schwarz, T. Holtij, A. Kloes, and B. Iñíguez, "2D Analytical DC Model for Nanoscale Schottky Barrier DG-MOSFETs." in *Proceedings of ISDRS, Stamp Student Union, College Park, University of Maryland, USA*, 2011.

[190] M. Schwarz, T. Holtij, A. Kloes, and B. Iñíguez, "Macro Model for Drift/Diffusion Effects in Short-Channel Undoped Schottky Barrier DG-MOSFETs." in *Proceedings of MOS-AK, Hesinki, Finland*, 2011.

[191] M. Najari, S. Frégonèse, C. Maneux, H. Mnif, N. Masmoudi, and T. Zimmer, "Schottky Barrier Carbon Nanotube Transistor: Compact Modeling, Scaling Study, and Circuit Design Applications." *IEEE Transactions on Electron Devices*, vol. 58, no. 1, pp. 195–205, 2011.

[192] M. Schwarz, T. Holtij, A. Kloes, and B. Iñíguez, "Explicit Model Equations for the Tunneling Current Density in Schottky Barrier Double-Gate MOSFETs." in *Proceedings of EUROSOI, Montpellier, France*, 2012.

[193] M. Schwarz, T. Holtij, A. Kloes, and B. Iñíguez, "Explicit Model for Tunneling and Thermionic Current in Schottky Barrier Double-Gate MOSFETs." in *Proceedings of ULIS, Grenoble, France*, 2012.

[194] M. Schwarz, T. Holtij, A. Kloes, and B. Iñíguez, "Two-dimensional Physics-based Modeling of Dopant-segregated Schottky Barrier UTB MOSFETs." in *Proceedings of MIXDES, Warsaw, Poland*, 2012.

[195] A. Kloes, M. Schwarz, and T. Holtij, "MOS^3: A New Physics-Based Explicit Compact Model for Lightly Doped Short-Channel Triple-Gate SOI MOSFETs." *IEEE Transactions on Electron Devices*, vol. 59, no. 2, pp. 349–358, 2012.

UNIVERSITAT ROVIRA I VIRGILI
TWO-DIMENSIONAL ANALYTICAL PREDICTIVE MODELING OF SCHOTTKY BARRIER SOI AND MULTI-GATE MOSFETS
Mike Schwarz
Dipòsit Legal: T.456-2013

UNIVERSITAT ROVIRA I VIRGILI
TWO-DIMENSIONAL ANALYTICAL PREDICTIVE MODELING OF SCHOTTKY BARRIER SOI AND MULTI-GATE MOSFETS
Mike Schwarz
Dipòsit Legal: T.456-2013